QUANTUM CORRELATIONS OF LARGE PLANAR ION CRYSTALS IN A NOVEL MONOLITHIC RADIOFREQUENCY TRAP

Quantum Correlations of Large Planar Ion Crystals in a Novel Monolithic Radiofrequency Trap

by
Helene Hainzer
August 2024

A thesis submitted to the faculty of
Mathematics, Computer Science and Physics
of the University of Innsbruck,
in partial fulfillment of the requirements for the degree of
Doctor of Philosophy (PhD)

This work was carried out

at the Institute for Quantum Optics and Quantum Information
of the Austrian Academy of Sciences

and the Institute for Experimental Physics
of the University of Innsbruck

under the guidance of

Assoz. Prof. Dr. Christian F. Roos

co-supervised by o.Univ.-Prof. Rainer Blatt

Abstract

Linear ion Coulomb crystals stored in radio-frequency traps have led to state-of-the-art experiments in quantum information science, with outstanding control over the individual particles as well as the interactions between them. This has led to the establishment of linear ion crystals as one of the leading platforms for experiments in the context of quantum computation, simulation, metrology and sensing. However, scaling up these systems beyond $\sim$50 particles while maintaining precise experimental control over them has proven challenging, yet is required for carrying out computations or simulations beyond the capabilities of classical computing, a major goal in experimental quantum information science. This thesis work reports on the setup of a new experimental apparatus for achieving quantum control over ion Coulomb crystals of larger size than previously possible in radio-frequency traps, by moving away from the conventional linear ion crystal configuration and instead trapping planar ion crystals. The approach of harnessing the second spatial dimension opens up ways to mitigate some of the scaling-related technical limitations encountered in linear ion crystals. An additional benefit is the possibility to naturally implement interactions of particles in two dimensions, particularly relevant e.g. for extending the range of models that can be directly investigated in quantum simulation. While previous efforts in quantum control over planar ion Coulomb crystals in radio-frequency traps had been limited to small systems, our work marks the first demonstration of extending this control beyond 100 ions. This thesis work provides evidence that known challenges arising in planar ion Coulomb crystals such as radio-frequency heating, micromotion, and structural phase transitions can be overcome in order to build a robust experimental apparatus for quantum simulation applications. The capabilities of the apparatus are demonstrated in characterization measurements and experiments harnessing quantum correlations, notably entanglement.

Contents

INTRODUCTION

1 Introduction

Quantum mechanics, once merely a subject to be studied, has turned into a valuable tool, its unique phenomena now harnessed for practical applications within the context of quantum technologies. Indeed, the field of quantum technology has experienced rapid progress, from the development of lasers and transistors during the first quantum revolution to the present era, where it has become possible to manipulate individual quantum objects with unprecedented precision. Recent advances in quantum control have allowed fully controlled quantum systems to be engineered in the laboratory for applications such as computation, simulation, communication, metrology and sensing. Here, numerous experimental platforms are explored, among them trapped atomic ions, over which outstanding control has been proven possible [1, 2, 3, 4, 5, 6]. In particular in analog and variational quantum simulation experiments precise manipulation of large ion crystals has been demonstrated, allowing for the study of quantum many-body physics with several tens to hundreds of particles [7, 8, 9, 10, 11, 12]. Here, the quantum system in the laboratory, i.e. the simulator, can be made to mimic the behavior of other inaccessible and complex quantum systems in nature.

Oftentimes, ensembles of interacting spin 1/2 particles are simulated as they can model relevant effects such as magnetism in condensed matter or the transport of excitation in molecules [13, 14]. The dynamics of such ensembles are complex, in particular when long-range interactions between the spins are present, and once the system exceeds a certain size, it is no longer feasible to calculate its dynamics efficiently on a classical computer. At this point quantum simulation becomes particularly relevant: Interesting properties of complex many-body Hamiltonians can be directly observed in the laboratory, while numerical simulations can no longer provide an answer. However, it still remains an outstanding challenge to increase the number of individually controllable particles in the laboratory, to eventually reach such a regime in which numerical simulations would be too elaborate to be carried out by classical computers, while still maintaining the state of the art level of control that is possible over small systems.

So far full quantum control, i.e. establishing coherent global and single-particle control as well as entangling interactions between particles, has been achieved within linear ion Coulomb crystals of up to about 50 particles, which are stored in a 3D linear radio-frequency (RF) Paul trap [15]. Here, ions are arranged along the symmetry axis of the trap to avoid complications from RF-driven micromotion, entangling interactions are realized by coupling to the common motion of the ions via a bichromatic laser field, and single-particle interactions are accomplished with laser beams focused down to spot sizes below the ion-ion distance. In these experimental systems the ion number limit arises from technical challenges due to the extremely anisotropic trapping potentials that are required to keep a long ion crystal linear. As the RF potential responsible for creating transverse confinement of the ions cannot be made arbitrarily high, the potential creating

axial confinement needs to be reduced as the ion number increases, to avoid the ion crystal undergoing a phase transition to a zig-zag structure [16, 17]. As a result, it becomes difficult to maintain sufficiently low temperature along the ion string, where due to weak confinement strong heating effects compete with laser cooling. On the other hand, due to the typical spacing of ions with respect to each other on the order of micrometers, crystals consisting of tens of ions extend over a significant length scale, leading to difficulties in laser-addressing outer ions.

A natural way to facilitate scalability in ion trap systems is to also make use of the second spatial dimension. Penning traps have shown to allow for global manipulation of planar ion crystals consisting of hundreds of particles [7]. However, control of individual ions constitutes a significant challenge as Coulomb crystals in Penning traps rotate at rates of tens to hundreds of kHz, and has only recently been reported for the first time [18, 19]. While arrays of surface (2D) Penning [20, 21] or RF traps[22, 23, 24], where each micro trap confines a single ion, would in principle allow ions to be trapped in nearly arbitrary fixed 2D geometries, technical challenges have so far prevented the scaling of such systems beyond several ions. These challenges include the typically shallow trap depths of surface traps, correlating with high ion loss rates. Furthermore, large surface traps significantly restrict free space optical access and may require the use of integrated optics, a complicated endeavour, in order to reliably deliver laser light to desired locations. Additionally, exposure of the ions to strong surface electric field noise due to their typically small distance to trap electrodes in such micro trap arrays, may cause further complications in the form of strong heating effects.

The key goal of this thesis work was to implement an alternative approach of trapping 2D ion Coulomb crystals in a stationary way and thus facilitate single-particle control, by confining the ions in a single potential well of a 3D RF trap, a strategy also employed by several other research groups [12, 25, 26, 27]. Our work is set in the context of quantum simulation, with the aim to apply the proven methodology for realizing spin models in linear ion crystals, i.e. combining coherent single-ion operations and measurements with engineered spin-spin interactions, mediated by the motional modes of the ion crystal, to directly implement spin Hamiltonians in the system. The motivation for extending the system into the second spatial dimension is not limited to carrying out simulations with larger ion numbers than those previously controlled in RF traps; it also opens up the possibility for directly studying quantum many-body phenomena in two dimensions. However, several experimental challenges emerge in this approach that require mitigation strategies. As most ions in planar crystals are inevitably displaced from the RF null in the trap center, they experience micromotion at the trap drive frequency with possible adverse effects on laser-ion interactions, e.g. a laser beam appearing to be phase modulated in the reference frame of the ion [28]. One strategy to mitigate such complications is to manipulate the ions only with laser beams from directions perpendicular to the micromotion, which in our case necessitates moving away from the conventional 3D linear Paul trap geometry that would restrict optical access from relevant directions. The presence of several structural phases, i.e. lattice configurations in which a planar ion crystal can exist [16, 29], constitutes an additional major challenge. Transitions between structural phases may arise from e.g. background gas collisions or RF heating effects [30, 31, 32]. It is crucial to implement strategies for detecting and controlling these events in order to prevent experimental errors as e.g. individual-ion quantum state detection and manipulation rely on ion positions to remain stable.

This dissertation, along with the thesis of Dominik Kiesenhofer, reports on setting up a new trapped-ion experiment for controlling planar ion crystals beyond 100 particles stored in a RF trap. While previous work with planar crystals in RF traps has been limited to small systems of several ions, e.g. the demonstration of EIT cooling of the out-of plane motional modes of a 2D crystal consisting of 12 $^{171}Yb^{+}$ ions [33] and frustrated quantum magnetism with 10 ions [34], our work marked the first realization of quantum control over significantly larger crystals[1] and as such constitutes a highly-relevant project within the NISQ (noisy intermediate scale quantum) era [37]. It should be noted that the implementation of single-particle control is beyond the scope of this thesis, with the installation of the necessary technical upgrade concluding as this thesis is finalized.

The thesis is structured as follows: Chapter 2 introduces the quantum information concepts essential for understanding this work: starting from basics on storing, manipulating and reading out quantum information, to discussing the role of quantum correlations and concluding with a section on quantum simulation of spin models. In ch. 3 experimental tools for quantum information science with trapped ions are introduced, from ion storage in RF traps to quantum state manipulation and its applications, with these concepts presented generally and specifically for our work with planar crystals of $^{40}Ca^{+}$. Chapters 4 and 5 constitute the technical part of this thesis, encompassing the majority of the work carried out during my PhD. Chapter 4 describes the constituents of the experimental apparatus in detail, i.e. our monolithic linear Paul trap, vacuum system, magnetic field generation and shielding, optical and electronic setups, and experiment control hard- and software. Chapter 5 provides characterization measurements carried out to quantify the performance of the experimental apparatus. More specifically, characteristics of the ion trap, trapping potential and Raman laser system for creating entangling interactions are provided. The stability of the lattice of planar ion crystals consisting of up to 91 ions is investigated and strategies for optimizing the stability are presented, crucial for achieving experimental robustness. Furthermore, ground-state cooling of all out-of-plane motional modes of a 105-ion planar crystal is demonstrated, an important prerequisite for implementing entangling interactions. Chapter 6 presents experiments in which different types of quantum correlations are harnessed for applications in the context of quantum metrology and sensing. In the first part of the chapter correlation spectroscopy is carried out with up to 91 ions, utilizing quantum discord in order to enhance phase estimation tasks [38]. This tool opens up the possibility to measure phase differences across a planar ion crystal precisely, even in the presence of strong collective dephasing, and allows the noise processes giving rise to decoherence to be characterized. Several application examples are given, where correlation spectroscopy is used for characterization and optimization of the experimental apparatus, e.g. for alignment of the Raman laser beams and characterizing the magnetic field environment. While correlation spectroscopy does not require entanglement, the achievable phase uncertainties are compared to the ones expected in entanglement-enhanced phase estimation. In the second part of the chapter, spin squeezing is accomplished in a small 19-ion planar crystal, allowing for measurement precision below the standard quantum limit [39, 40]. At the same time this demonstrates the ability to create entangling interactions between spin

[1] Very recently it was reported in [35] that even larger planar Coulomb crystals of up to 512 $^{171}Yb^{+}$ ions have been trapped in a stable way, with quantum simulations of 2D spin lattices performed on a 300 ion planar crystal. Moreover, the same research group has demonstrated individually-addressed entangling gates in a small planar Coulomb crystal consisting of 4 ions [36].

1/2 particles in our system, which lays the groundwork for quantum simulation tasks in the future. The thesis concludes in ch. 7 with a summary of the work presented and outlook on future upgrades and experimental directions of the apparatus.


QUANTUM INFORMATION

2 Theoretical Framework on Quantum Information Science

Remarkable experimental progress has been made in quantum information science in recent years. The ability to process information in a fundamentally different way, in comparison to classical information processing, opens up significant possibilities such as computational advantage, fundamentally secure communication or enhancement in measurement precision [41, 42]. Here, the unique properties possessed by quantum systems are harnessed, while navigating challenges arising from fundamental limits imposed by quantum physics on reading, copying and storing information [43]. This chapter presents quantum information theory relevant to this thesis work, which is set primarily in a quantum sensing and simulation context. First, in sec. 2.1 and 2.2 the basics on generating and manipulating quantum information, encoded in quantum mechanical two-level systems (qubits), are given, along with information on how interactions of the qubit with the environment can drive the quantum system towards a classical state. Then projective measurements are presented, our tool to read out quantum information, along with fundamental precision limits (sec. 2.3). In systems comprised of multiple qubits correlations can emerge, which play an essential role in many aspects of quantum information science. In particular, sec. 2.4 presents the two types of non-classical correlations entanglement and discord, which are studied experimentally in the last part of this thesis. The chapter concludes in sec. 2.5 with an introduction to quantum simulation, in particular in the context of simulating spin models. The chapter is kept general, with the concepts applicable to any physical system that can be represented by a qubit. The implementation of these concepts in a trapped-ion system, as particularly relevant in the context of this thesis, is then given in the subsequent chapter.

2.1 Encoding Information into Quantum Bits

2.1.1 Single Qubits

In classical information processing, a bit constitutes the basic unit of information, and can take on one of two logical states that are typically expressed as 0 and 1. In analogy, two states of a quantum system $|0\rangle$ and $|1\rangle$[1] can be used to represent a quantum bit or qubit. While in contrast

[1] Here the Dirac notation is used where $|0\rangle = \binom{1}{0}$, $|1\rangle = \binom{0}{1}$, $\langle 0| = (1\ 0)$ and $\langle 1| = (0\ 1)$.

to a classical bit, a qubit can be in a coherent superposition[2] of the two basis states, as represented by the state vector

$$|\Psi\rangle = \alpha|0\rangle + \beta|1\rangle = \begin{pmatrix}\alpha\\ \beta\end{pmatrix}, \tag{2.1}$$

where α and β are complex numbers, a measurement projects the qubit into either $|0\rangle$ or $|1\rangle$, one of the possible outcomes, with respective probabilities $|\alpha|^2$ and $|\beta|^2$. In the laboratory, the values of $|\alpha|^2$ and $|\beta|^2$ can be determined statistically by preparing and measuring the same state many times. More information on the measurement process is given in sec. 2.3.

Equation 2.1 can also be rewritten in spherical coordinates

$$|\Psi\rangle = e^{i\gamma}\Big(\cos(\theta/2)|0\rangle + e^{i\phi}\sin(\theta/2)|1\rangle\Big) \tag{2.2}$$

allowing for the state of a single qubit to be conveniently visualized on a Bloch sphere, shown in fig. 2.1. The real numbers θ and ϕ represent polar coordinates (angles), and γ is a global phase factor which has no observable effect and is thus typically set to 0. In fig. 2.1, the north and south poles of the sphere correspond to the computational basis states $|0\rangle$ and $|1\rangle$ and states that lie in the equatorial plane correspond to equal superpositions of those basis states.

Besides pure quantum states, which can be represented using eq. 2.1 or visually by a point on the surface of the Bloch sphere, there also exist mixed quantum states. Such mixed states lie within the Bloch sphere, and cannot be represented by a single state vector but rather only as a statistical ensemble of different state vectors. In order to mathematically describe pure as well as mixed states, a more general representation of the state of a quantum system is required: The density matrix ρ is used for this purpose, defined as

$$\rho = \sum_i p_i |\Psi_i\rangle\langle\Psi_i| \tag{2.3}$$

where $|\Psi_i\rangle$ are the possible states the system can be in with respective probabilities p_i. Choosing $\{|\phi_m\rangle\}$ as an orthonormal basis, the elements of the density matrix can be written as

$$\rho_{mn} = \langle\phi_m|\rho|\phi_n\rangle = \sum_i p_i \langle\phi_m|\Psi_i\rangle\langle\Psi_i|\phi_n\rangle. \tag{2.4}$$

In quantum information experiments, the density matrix is usually presented in the computational basis, i.e. the states $|\phi_m\rangle$ are the computational basis states of the qubit. In this case, the diagonal elements of the density matrix are referred to as populations of the states. The off-diagonal elements are the coherences which provide information about the phase relationship between the populations. If the trace of the density matrix squared, $\mathrm{tr}(\rho^2)$, i.e. the sum of the diagonal elements of ρ^2, equals 1, the state described by ρ is pure, if the trace is less than one, the state is mixed.

[2] What distinguishes a quantum state from a classical mixture is the presence of coherence, a well-defined phase relationship between the two basis states.

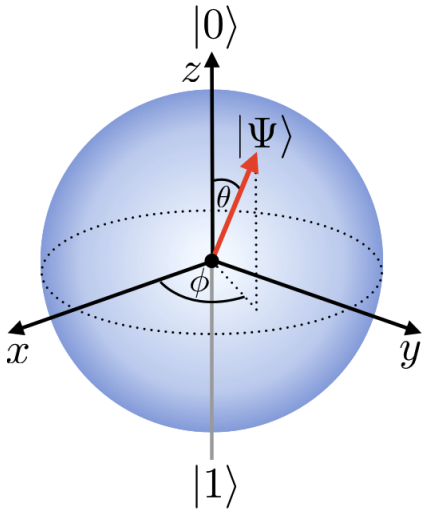

Figure 2.1: The Bloch sphere of a single qubit: A quantum state can be described by its coordinates, i.e. projections onto the x, y and z-axes.

2.1.2 Multi-Qubit Systems

The basis states of a single qubit span the space of states $\mathcal{H}$, which is a Hilbert space. The total state space $\mathcal{H}_N$ of a system composed of n qubits is the tensor product of the state spaces of the individual qubits:

$$\mathcal{H}_N = \mathcal{H}_1 \otimes \mathcal{H}_2 \otimes ... \otimes \mathcal{H}_n \tag{2.5}$$

As the Hilbert space of one qubit is two-dimensional, the Hilbert space of n qubits is 2^n dimensional. A separable product state $|\Psi_n\rangle$ of a system of n qubits can also be represented by the tensor product of the individual qubit states $|\Psi_i\rangle$:

$$|\Psi_n\rangle = |\Psi_1\rangle \otimes |\Psi_2\rangle \otimes ... \otimes |\Psi_N\rangle = |\Psi_1\Psi_2...\Psi_N\rangle \tag{2.6}$$

However, there also exist states that cannot be written as a product of states of its constituents. Such states are called entangled and are presented in sec. 2.4.2.

The density matrix of a multi-qubit system is given also by eq. 2.3, with the individual $|\Psi_i\rangle$ in this case corresponding to the possible multi-qubit quantum states.

2.2 Dynamics of Quantum Systems

Storing and processing quantum information necessitates the ability to change the quantum state of a qubit in a controlled way. Additionally, undesired interactions of the qubit with the environment can affect its quantum state in an uncontrolled way. This section presents how these two processes can be modelled.

2.2.1 Unitary Evolution

In the ideal case, dynamics in a quantum system are described exclusively by unitary operations on the quantum state, mathematically expressed as $\hat{U}|\Psi\rangle$ or $\hat{U}\rho\hat{U}^\dagger$, where

$$\hat{U} = e^{-\frac{i}{\hbar}\hat{H}t}. \tag{2.7}$$

This corresponds to a controlled action on the system over a time t exerted by a classical apparatus, where the qubit dynamics are governed by the Schrödinger equation, an evolution under a Hamiltonian $\hat{H}$. This description of the dynamics, however, is only valid in the case that no information is lost to the enviroment, i.e. the qubit is otherwise perfectly isolated. Non-unitary dynamics due to unwanted dissipative processes however are always present in practice and are introduced in the next subsection.

Unitary operations on a single qubit can be visualized as rotations of its state vector on the Bloch sphere. Rotations by an angle θ about an arbitrary axis of the Bloch sphere, defined by a unit vector $\vec{n} = (n_x, n_y, n_z)$, are mathematically described by[3]

$$\hat{U}_n = e^{-i\frac{\theta}{2}\vec{n}\vec{\sigma}} = \cos(\theta/2)\mathbb{1} - i\sin(\theta/2)(n_x\hat{\sigma}_x + n_y\hat{\sigma}_y + n_z\hat{\sigma}_z). \tag{2.8}$$

Here, the Pauli operators

$$\hat{\sigma}_x = \begin{pmatrix} 0 & 1 \\ 1 & 0 \end{pmatrix} \qquad \hat{\sigma}_y = \begin{pmatrix} 0 & -i \\ i & 0 \end{pmatrix} \qquad \hat{\sigma}_z = \begin{pmatrix} 1 & 0 \\ 0 & -1 \end{pmatrix} \tag{2.9}$$

represent rotations around the x, y and z axis of the Bloch sphere by $180°$ (up to a factor $-i$), respectively. The identity operator

$$\mathbb{1} = \begin{pmatrix} 1 & 0 \\ 0 & 1 \end{pmatrix} \tag{2.10}$$

leaves the original state unchanged. As such, in the context of quantum information processing, these unitary matrices form an elementary set of single-qubit gate operations. Multi-qubit gate operations are introduced in the context of generating entanglement in sec. 2.4.2.

2.2.2 Noise and Decoherence

In the laboratory a quantum system is inevitably exposed to various unwanted, uncontrolled, and non-unitary interactions with its environment, commonly referred to as noise. As a consequence, the quantum system may experience decoherence, leading to the system being driven towards a classical (mixed) state, correlating with the dissipation of quantum information encoded in the state, until it is eventually lost completely.

In the context of this thesis, significant noise processes acting on a qubit are amplitude and phase damping. The reduction of probability of the quantum system being in an excited state is referred to as amplitude damping. For an atomic qubit, this concept describes the decay to the ground state $|1\rangle$ by emission of a photon which carries away any information about the qubit's

[3] Here, Euler's formula $e^{\pm i\varphi\hat{H}} = \cos(\varphi)\mathbf{1} \pm i\sin(\varphi)\hat{H}$ was used, which is valid if $\hat{H}^2 = \mathbf{1}$.

previous superposition state $\alpha|0\rangle + \beta|1\rangle$. All possible qubit states get mapped to the ground state and since the photon is not detected all quantum information is lost. On the other hand, phase damping describes the loss of information about the relative phase between the qubit basis states $|0\rangle$ and $|1\rangle$. This effect can arise from uncontrolled fluctuations of the energy difference between the basis states, or the classical fields the qubit is manipulated with[4]. Effectively, such noise leads to uncontrolled rotations of the qubit about the z axis of the Bloch sphere. All quantum information is lost when the state becomes completely mixed, e.g. taking an initially pure qubit state in the equatorial plane of the Bloch sphere $1/\sqrt{2}(|0\rangle + |1\rangle)$ to the classical mixture of states $1/\sqrt{2}(|0\rangle + |1\rangle)$ and $1/\sqrt{2}(|0\rangle - |1\rangle)$, represented by the density matrix $\rho = 1/2(|0\rangle\langle 0| + |1\rangle\langle 1|)$, which contains no coherences (i.e. the off-diagonal entries of the density matrix are equal to zero).

The coherence time $t_{1,2}$ quantifies how long quantum information can be preserved before it is lost from such decoherence processes. This constitutes a significant measure in any experimental system, setting a limit to the extent in which unitary operations can be carried out on the qubit. Here, t_1 typically corresponds to the limit imposed by spontaneous decay, while t_2 relates to the time it takes for the qubit to dephase. Coherence decay can in many situations be modelled as following an exponential behavior [44][5] and in an experiment this decay can be quantified e.g. by using Ramsey interferometry [45]. Here, a decay in the contrast of an interference pattern is analyzed (see sec. 3.3.4), the coherence time corresponding to the time it takes for the contrast to decrease to $1/e$ or $1/e^2$ of its original value.

When considering multi-qubit systems, noise processes typically act on all qubits and thus their effect is cumulative, making coherent control over large quantum systems particularly challenging. While one would expect the effect of noise to increase in proportion to the number of qubits in the system, in some cases decoherence can also be correlated, leading to a decay that is non-linear in particle number, a key vulnerability of certain entangled states [46].

2.3 Quantum Measurements

In order to determine the state of a qubit, measurements have to be performed on the system. Here, an introduction to projective measurements is provided, capturing the concept of wavefunction collapse and the statistical and non-deterministic interpretation of observables in quantum mechanics. Moreover, the achievable precision limits in quantum measurements are explored, i.e. the standard quantum limit and the fundamental Heisenberg limit.

2.3.1 Projective Measurement

A projective measurement, also known as von Neumann measurement, collapses a quantum (superposition) state ρ, onto an eigenstate of the measured observable[6], while the measurement out-

[4] For an atomic qubit for example, these classical fields can be laser fields interacting with the qubit or magnetic fields which are in the ambient environment.

[5] While coherence decay may generally follow a complex behavior, typical noise processes in many experimental settings may give rise to an exponential decay in coherence. On the other hand, a Gaussian time dependence or power-law models are also possible, as described in [44] and references therein.

[6] An observable is a physical quantity that can be measured and is represented by a Hermitian operator.

come is given by the corresponding eigenvalue. For a general quantum state ρ the expectation value of an observable O is mathematically represented as:

$$\begin{aligned}\langle\hat{O}\rangle = \sum_i p_i \langle\Psi_i|\hat{O}|\Psi_i\rangle = \sum_i p_i \sum_m \langle\Psi_i|\hat{O}|\phi_m\rangle\langle\phi_m|\Psi_i\rangle = \\ = \sum_m \langle\phi_m| \left(\sum_i p_i |\Psi_i\rangle\langle\Psi_i| \hat{O} \right) |\phi_m\rangle = \sum_m \langle\phi_m|\rho\hat{O}|\phi_m\rangle = \mathrm{tr}(\rho\hat{O}),\end{aligned} \tag{2.11}$$

using the completeness relation $\sum_m |\phi_m\rangle\langle\phi_m| = \mathbb{1}$.

Experimentally, since measurement outcomes are probabilistic, measurements have to be performed on repeatedly generated copies of the state ρ, in order to obtain enough statistics to estimate with high confidence the expectation value of $\hat{O}$[7]. In the laboratory it is only possible to measure a qubit in the computational basis, represented by the operator $\hat{\sigma}_z$. In order to fully reconstruct the state of a quantum system, the qubits have to be rotated prior to the measurement to gain access to expectation values in bases other than the computational one (e.g. $\hat{\sigma}_x$ and $\hat{\sigma}_y$). For a rotation $\hat{U}$ the new observable is then given by $\mathrm{tr}(\hat{U}\rho\hat{U}^\dagger\hat{\sigma}_z)$.

2.3.2 Uncertainty from Finite Measurement Statistics

While in an experiment there are many factors which can contribute to the uncertainty in determining the state of a qubit via a projective measurement, such as imperfect state preparation, decoherence or readout errors, there is also an uncertainty associated with the finite number of measurements that are carried out. This uncertainty is referred to as quantum projection noise. The outcome of a single measurement of a qubit's state is either $|0\rangle$ with probability $p \in [0, 1]$ or $|1\rangle$ with probability $1-p$. This essentially corresponds to a coin-flip between the two possibilities. Considering n measurements on repeatedly prepared copies of a quantum state, the outcomes can thus be modelled to follow a binomial distribution [47] with standard deviation $\sqrt{n(p(1-p))}$. In this model, the standard error for the mean of measurement outcomes is given by the equation

$$\sigma_p = \sqrt{\frac{p(1-p)}{n}}, \tag{2.12}$$

which is the definition of quantum projection noise. This expression shows that when a qubit is in an eigenstate of the measurement basis, the outcome of the measurement is certain, while an equal superposition of the basis states corresponds to maximum uncertainty with respect to the measurement basis.

2.3.3 Fundamental Precision Limits

While projection noise represents a limitation of the measurement process, setting a limit to how precisely an observable can be estimated from finite measurements, there also exist other funda-

[7] The expectation value here corresponds to the average of the measured outcomes.

mental limits of the precision with which physical quantities can be determined[8]. In the absence of quantum correlations, which are explained in detail in the subsequent section, the standard quantum limit (SQL) represents the best achievable measurement precision. In the case that quantum projection noise dominates the uncertainty in measurements, it effectively defines the SQL for the specific situation. By harnessing quantum correlations such as entanglement, the SQL can be surpassed, which allows the ultimate Heisenberg limit of precision to be approached. Intuitively this could be understood as the presence of correlations reducing the inherent randomness in the measurement process, thereby allowing for enhanced precision. These ideas have given rise to the field of quantum metrology, an area of research attempting to improve the precision of measurements via the use of quantum effects. More information on strategies to go beyond the SQL is given in sec. 2.4.4.

2.4 Quantum Correlations

Understanding correlation plays a central role in science, as it relates to recognizing underlying patterns in scientific data that may result from a causal relationships between variables. Building on this understanding, hypotheses can be formulated and tested which aim to explain inherent mechanisms governing the physical system that is studied and predictive models can be developed. In a general sense, correlations describe how variables are statistically related to one another, e.g. explaining how they vary in an interdependent way. This section begins with an introduction to statistical tools used throughout this thesis for quantifying correlations. Subsequently, the concept of non-classical correlations is introduced. Quantum correlations are stronger than correlations in a classical system and cannot be explained by classical probability theory. They can arise within a multi-qubit system or between qubits and the environment. In the context of this thesis two important kinds of quantum correlations are relevant: entanglement and discord. Such quantum correlations have various applications in quantum information science, some examples of which are outlined as well as methods on how to verify the presence of non-classical correlations.

2.4.1 Statistical Tools to Quantify Correlations

In order to detect the presence of and quantify correlations various statistical tools are available, which can provide a measure for the degree and type of correlation, e.g. if the correlation is positive or negative, linear or non-linear [48]. Throughout this thesis, covariance and correlation matrices are used to quantify correlations and are thus presented here briefly.

In general, covariance is a measure of a linear relationship between variables and describes how one variable varies with respect to changes in the other. It can be positive or negative, if the vari-

[8] Most notably, the Heisenberg uncertainty principle imposes a limit on the measurement precision of pairs of complementary observables, giving rise e.g. to the linewidths of atomic transitions, an uncertainty in frequency and thus energy.

ables are positively correlated or anti-correlated. Covariance between variables X and Y[9] is mathematically expressed as

$$\mathrm{cov}(X,Y) = \frac{1}{n}\sum_{i=1}^{n}(X_i - \bar{X})(Y_i - \bar{Y}) \tag{2.13}$$

where n is the sample size, X_i and Y_i are the individual measurements and $\bar{X}$ and $\bar{Y}$ are the means of X and Y, respectively.

The covariance matrix is an extension of this concept to multiple variables, quantifying the relationships between each pair of variables in a data set. More specifically, the off-diagonal elements of this matrix are the covariances between pairs of variables, and the diagonal elements are the variances of the individual variables, which corresponds to the covariance of a variable with itself. Considering a data matrix $\mathbf{M}$ which has dimensions $m \times n$, where variables are stored in rows, and individual measurements of these variables are stored in columns, the covariance matrix can be written as[10]

$$\mathbf{K_{MM}} = \frac{1}{n}\mathbf{M}\mathbf{M}^T - \mu_M \mu_M^T \tag{2.14}$$

where μ_M contains expectation values of the variables. $\mathbf{K_{MM}}$ here has dimensions $m \times m$ and characterizes how the rows of $\mathbf{M}$ vary together, thus capturing correlations among the variables. Analogously, the $n \times n$ matrix $\mathbf{M}^T\mathbf{M}$ captures patterns among the different measurements, stored in the columns of $\mathbf{M}$. Each element (i, j) of these two types of covariance matrices is thus given by the covariance between rows or columns i and j of the original data matrix $\mathbf{M}$, respectively. This can be useful e.g. in the context of data dimensionality reduction. Considering that the number of variables m is much smaller than the number of measurements n, the covariance matrix with dimensions $m \times m$ contains information about all correlations which are present among variables in this large data set. More information on tools for data dimensionality reduction is given in sec. 4.7.

The correlation matrix can be considered a normalized version of the covariance matrix. Correlations scale the covariances by the product of the standard deviations of the corresponding variables,

$$\mathrm{cor}(X,Y) = \frac{\mathrm{cov}(X,Y)}{\sigma_X \sigma_Y} \tag{2.15}$$

resulting in values only between -1 and 1. Here the limit values relate to perfect (anti-)correlation between pairs of variables. The diagonal elements of the correlation matrix are always 1, as the perfect correlation of a variable with itself is inevitable.

[9] In our experiments these variables may be e.g. ion positions (see sec. 5.2.3) or different quantum state measurement outcomes of the ions (see sec. 6.1).

[10] Note that the equation for the covariance matrix sometimes contains the normalization factor $1/(n-1)$ rather than $1/n$. This is relevant when calculating the covariance of a sample of the data set, correcting for a bias that would otherwise be introduced.

2.4.2 Entanglement

Definition and Examples

Quantum entanglement describes the phenomenon of two or more quantum objects becoming correlated in a way that the quantum state of one part of the system cannot be described independently of the state of the other part. This holds true regardless of any distance separating the objects, a concept known as nonlocality. The Bell-states

$$|\Phi^{\pm}\rangle = \frac{1}{\sqrt{2}}(|00\rangle \pm |11\rangle) \qquad |\Psi^{\pm}\rangle = \frac{1}{\sqrt{2}}(|01\rangle \pm |10\rangle) \tag{2.16}$$

characterize maximal entanglement in a two-qubit system. When the quantum state of the composite system is determined via projective measurements, the outcomes of the individual qubits are strongly correlated, no matter which basis they are measured in. This can be easily seen e.g. when representing the state Φ^+ in the $\hat{\sigma}_x$ basis, which has the eigenstates $|+\rangle_x = \frac{1}{\sqrt{2}}(|0\rangle + |1\rangle)$ and $|-\rangle_x = \frac{1}{\sqrt{2}}(|0\rangle - |1\rangle)$:

$$|\Phi^+\rangle_x = \frac{1}{\sqrt{2}}\left(\frac{1}{2}(|+\rangle_x + |-\rangle_x)(|+\rangle_x + |-\rangle_x) + \frac{1}{2}(|+\rangle_x - |-\rangle_x)(|+\rangle_x - |-\rangle_x)\right) = \frac{1}{\sqrt{2}}(|++\rangle_x + |--\rangle_x) \tag{2.17}$$

Similarly, in the $\hat{\sigma}_y$ basis with eigenstates $|+\rangle_y = \frac{1}{\sqrt{2}}(i|0\rangle + |1\rangle)$ and $|-\rangle_y = \frac{1}{\sqrt{2}}(-i|0\rangle + |1\rangle)$, the qubits are perfectly anticorrelated, i.e. $|\Phi^+\rangle_y = \frac{1}{\sqrt{2}}(|+-\rangle_y + |-+\rangle_y)$.

From these examples it is also straightforward to see that there is no way to write the entangled state as a tensor product of the states of the individual qubits, which is a formal definition of entanglement. The inability to describe the state of one of the qubits independently from the state of the other manifests mathematically when carrying out the partial trace operation. In a composite system, this operation can be applied in order to obtain the reduced density matrix of a subsystem. Taking again the Bell state Φ^+ and it's corresponding density matrix $\rho_{\Phi+}$ as an example, one could trace over the degrees of freedom associated with the first qubit to extract information only about the second qubit:

$$\mathrm{tr}_1(\rho_{\Phi+}) = \sum_j (\langle j|\mathbb{1})\rho_{\Phi+}(|j\rangle\mathbb{1}) = \frac{1}{2}(|0\rangle\langle 0| + |1\rangle\langle 1|) \tag{2.18}$$

Here, the sum is taken over the computational basis states $\{|j\rangle\}$ of qubit 1, essentially collapsing its state, while the identity operator acts on qubit 2, leaving its state unchanged. While the joint state of the entangled qubits is clearly pure, when looking only at the second qubit its state appears to be maximally mixed, with no information about coherence remaining.

Creation of Entanglement

Entanglement between qubits can be created by applying multi-qubit gate operations that initiate collective spin or phase flips. For two qubits, entangled states can be generated when the system evolves under Hamiltonians of the form $\hat{\sigma}_x^{(1)}\hat{\sigma}_x^{(2)}$, $\hat{\sigma}_y^{(1)}\hat{\sigma}_y^{(2)}$ or $\hat{\sigma}_z^{(1)}\hat{\sigma}_z^{(2)}$, where the superscript denotes which qubit the Pauli operator acts on. Considering as an example a Hamiltonian $\hat{H} = \varphi\hat{\sigma}_x^{(1)}\hat{\sigma}_x^{(2)}$, where φ is some constant that denotes the interaction strength, the time evolution of the state $|11\rangle$ under $\hat{H}$ is given by

$$\hat{U}(t)|11\rangle = e^{-\frac{i}{\hbar}\varphi\hat{\sigma}_x^{(1)}\hat{\sigma}_x^{(2)}t}|11\rangle = \left(\cos\left(\frac{\varphi t}{\hbar}\right)\mathbb{1} - i\sin\left(\frac{\varphi t}{\hbar}\right)\hat{\sigma}_x^{(1)}\hat{\sigma}_x^{(2)}\right)|11\rangle \tag{2.19}$$

Since $\hat{\sigma}_x^{(1)}\hat{\sigma}_x^{(2)}|11\rangle = |00\rangle$, for $\frac{\varphi t}{\hbar} = \frac{\pi}{4}$ the Bell-state $\frac{1}{\sqrt{2}}(|11\rangle - i|00\rangle)$ is created.

A generalization in which this type of interaction is applied to more than two qubits in order to create other and more complex types of entangled states is given in sec. 2.5.2.

2.4.3 Quantum Discord

While entanglement constitutes a specific type of quantum correlation, quantum discord is defined as a measure of the overall "quantumness" of correlations [49]. In other words, discord captures a broader class of quantum correlations which also includes entanglement. The ability of discord to be able to manifest not only in pure but also in separable mixed states provides a significant benefit when harnessing discordant states in quantum information science. Entanglement is oftentimes difficult to create and susceptible to decoherence from environmental noise. Discord, on the other hand, can be even created by environmental noise, the exact mechanism that leads to the fragility of entangled states. More specifically, discord may arise from classically correlated noise processes, such as temporally fluctuating classical fields in the environment of the qubits (e.g. laser or magnetic fields), commonly encountered in experimental setups. The simplicity with which discord can be generated and its greater resistance to dissipative interactions with the environment make discord a valuable resource in quantum information science, which is explained in more detail in the next subsection. It seems natural to assume the presence of discord in most quantum states, unless noise from the environment is entirely spatially and temporally uncorrelated, which may be the case when averaging over prolonged interactions with the environment. States which contain no discord are called pointer states [50].

The mathematical definition of quantum discord is based on the idea that two equivalent ways of measuring correlations within classical information theory are inequivalent when it comes to quantum correlations [51]. More specifically, discord can be defined as the difference between two definitions of the quantum analogs of the classical mutual information. While the exact derivation is omitted here, it is noteworthy that the expressions within the equations for quantum discord involve entropies. These entropies are derived by (partially) tracing over the density matrices of the quantum system or its subsystems. As seen in the previous section, in the context of entanglement, tracing over a part of the quantum system was associated with a loss of information which can hint at the presence of non-classical correlations. And similarly, the von Neumann entropies utilized in the definition of quantum discord capture the information content of quantum states, and thus

provide a quantitative measure of the non-classical correlations between different components of a quantum system.

2.4.4 The Role of Non-Classical Correlations in Quantum Information Science

It is well known that entanglement plays an important role in various aspects of quantum information science. In quantum communication, for example, it serves as a resource for teleportation protocols. In the context of quantum information processing, it has been indicated that entanglement allows for realizing a scalable quantum computer with exponential computational speedup compared to classical devices [52]. Additionally, it plays a role in quantum error correction, where quantum information is protected from noise by distributing it in entangled states of several physical qubits, comprising one logical qubit [53, 54]. In quantum simulation, entanglement is used as a tool for creating interactions between particles, to study quantum systems that are challenging to model classically, as explained in more detail in the subsequent section. Entanglement is also harnessed in quantum metrology, e.g. to improve the signal-to-noise ratio in measurements. Indeed, it has been shown that using entangled states can provide an improvement in measurement precision compared to classical strategies, beating the SQL and approaching the Heisenberg limit [41]. Consequently, much research effort has been on improving the level of control over quantum systems in the laboratory to be able to generate entangled states within larger and larger systems.

However, as discordant states are less sensitive to dissipative environments encountered in experimental setups, it is worth to investigate their role in quantum information science as well. For example, while it has long been assumed that the potential computational speedup of quantum computers is due to entanglement, there are indications that it is indeed discord which is responsible for the speedup [51, 55].

The work that was carried out in this thesis focuses on the role of entanglement and discord in the context of metrology. First, it is shown that the weaker quantum correlations encapsulated by discord also allow for a metrological gain. In particular, in section 6.1, an enhancement in phase estimation based on correlation spectroscopy using discordant states is presented. Furthermore, experiments on spin squeezing [39, 56], a concept related to entanglement [57], are presented in sec. 6.2. In general, squeezing describes the manipulation of the uncertainty in pairs of complementary variables such that the uncertainty in one variable is reduced at the expense of increasing the uncertainty in the other[11]. Squeezed states thus exhibit correlations between the two variables or observables that are stronger than classical and allow for measurement precision beyond the SQL along the squeezed variable.

2.4.5 Detection of Non-Classical Correlations

If the state of a quantum system is completely determined, i.e. all entries of the density matrix are known, the presence and amount of non-classical correlations in the state can be captured by

[11] This concept is often encountered in the context of interferometry, where light is squeezed e.g. in order to enhance precision in gravitational wave detection. Here, tiny path length changes of the interferometer can hint at the presence of gravitational waves. When squeezing is applied in the light's phase quadrature, the interferometer's sensitivity to changes in the phase of the light is improved, allowing for the weak signal from a gravitational wave to be detected, while increasing the uncertainty in the light's amplitude [58].

certain measures, such as concurrence or von Neumann entropy. While it is possible to entirely reconstruct ρ via quantum state tomography, performing measurements on the state in different bases, this method becomes infeasible for large quantum systems as the size of ρ grows exponentially with the number of qubits[12]. On the other hand, there exist alternative and more efficient approaches to investigate the presence of quantum correlations, requiring only the measurement of certain observables on the quantum system (witness operators). An expectation value threshold associated with such a witness operator then distinguishes e.g. the two regimes in which a state is either entangled or separable [51, 60].

Furthermore, as entanglement allows for a unique type of quantum-enhanced measurement precision, metrics which quantify metrological improvements beyond the SQL can indicate the presence of entanglement. Examples of such quantities, which are relevant to this thesis work, are the Quantum Fisher Information [61], a measure for the precision in quantum parameter estimation, or Wineland parameter, which can be used as a measure for the amount of squeezing in a quantum state [62]. More details on these quantities can be found in chapter 6.

2.5 Quantum Simulation

The most ambitious goal in quantum information science is to build a useful, universal and fault-tolerant quantum computer. The interest in building such a device stems from the potential it holds, to carry out specific calculations significantly faster than a classical computer could, opening up the possibility to solve problems currently beyond reach. This is a concept known as quantum advantage. Besides problems that are interesting from a computer science perspective, such as factorizing large prime numbers [63] or efficiently searching vast databases [64], quantum advantage allows for the study of large quantum systems inherent in nature. As the Hilbert space, in which the state of a quatum system exists, is exponentially large in the number of particles, simulating the dynamics of a quantum system on a classical computer becomes impractical beyond a threshold of a few tens of particles. Naturally, using a computer based on the same quantum physical principles as the system to be studied would allow its dynamics to be investigated more efficiently. Quantum simulation constitutes this subfield of quantum information science, where an engineered quantum system in the laboratory mimicks the behavior of another quantum system in nature[13] [65, 66, 67]. In this way, an inherently inaccessible quantum system can be studied in a controlled way, and with the ability to tune system parameters, such as the interaction strength between the individual particles comprising the system. Currently we find ourselves in the NISQ (noisy-intermediate scale quantum) era [37], where small-scale and imperfect quantum systems, consisting of few tens to hundreds of noisy qubits are used to demonstrate initial applications of quantum advantage in computation and simulation [68, 69, 70, 71]. More specifically, already we are witnessing instances of practical quantum advantage, where the computational problems being addressed are relevant practical problems, rather than quantum hardware tests. Significant research effort is dedicated to consistently scale up the size of these engineered quantum systems in

[12] There exist approximations which can reconstruct specific quantum states more efficiently, such as matrix-product state tomography [59].

[13] Beyond that, a quantum simulator also allows for the study of abstract models that are not even realized in any other naturally occuring quantum system.

the laboratory while attempting to maintain precise control over them. The ongoing effort continuously increases the complexity with which quantum simulations can be carried out, which holds the potential to drive significant progress in fields such as quantum chemistry, material science or high-energy physics, where the understanding of the interactions of particles on a microscopic level plays an important role e.g. in the design and development of innovative drugs [72, 73], energy-efficient fertilizers [74] or high-temperature superconductors [75].

2.5.1 Types of Quantum Simulators

Achieving a quantum simulation in the laboratory involves the crucial step of mapping the problem of interest to the experimental system. This requires creating conditions that render the simulator behavior analogous to the natural system we seek to understand. Here, various approaches exist - digital, analog and varitational quantum simulation - each with their own merits and drawbacks [76, 77]. Digital quantum simulation is carried out by a general-purpose quantum computer, the calculation represented by a set of universal quantum gates. Oftentimes, trotterization is employed, a technique to approximate the time evolution under a Hamiltonian of interest, that may not be directly realizable in the laboratory, by decomposing the Hamiltonian into an available elementary gate set [78]. While small noisy quantum computers capable of realizing a universal gate set are available, building them in a larger and fault-tolerant way poses an extremely demanding endeavor, due to the required large number of error-corrected qubits [79] controlled by high-fidelity gate operations. A seemingly more realistic goal is to build quantum simulators which do not necessitate the broad capabilities offered by a universal quantum computer. Diverging from the gate-based approach, and avoiding the complexities of quantum error correction, relates to the concept of analog quantum simulation [66]. While not capable of carrying out arbitrary computations, these simulators excel at efficiently solving a restricted class of complex many-body Hamiltonians which can be directly implemented via the interactions naturally available in the simulator system. A third method of quantum simulation is the variational approach, where a classical computer and quantum simulator operate in a feedback loop to prepare a quantum system in the laboratory in an energy eigenstate of a Hamiltonian of interest [80]. This method is based on iteratively optimizing a set of parameters in order to minimize the difference between the target state and state that is generated in the laboratory[14]. The variational approach offers versatility by not requiring the direct implementation of the Hamiltonian in the laboratory, distinguishing it as a more flexible method compared to analog quantum simulation.

2.5.2 Spin Models

Spin models are oftentimes investigated in quantum simulation as they serve as basic representations of interacting quantum many-body systems, are relatively simple to simulate, in particular in an analog way, and can model a wide range of physical systems that exhibit quantum properties. Examples include the study of quantum magnetism, phase transitions, and other phenomena in condensed matter physics, as well as biology, describing e.g. the transport of energy in molecules within light-harvesting organisms [13, 14]. While there exists a wide variety of spin models, we here consider only spin-$1/2$ particles with two basis states $|\uparrow\rangle$ and $|\downarrow\rangle$, encoded analogously

[14] This optimization process is typically performed using classical optimization algorithms.

as the computational basis states $|0\rangle$ and $|1\rangle$ of a qubit. Essentially, a spin can be visualized as a microscopic magnetic dipole, the magnetic moment either pointing up or down. Well known and important spin models with interaction dimensionalities[15] of 1, 2 and 3, respectively, are the Ising, XY and Heisenberg models. More details on specific spin Hamiltonians relevant to this thesis work and how they can be implemented experimentally[16] are given in sec. 3.2.3. Here, just a short conceptual introduction is presented.

For spin-1/2 particles the Ising model is the simplest of spin models in the sense that it describes interactions only along a single axis. The Hamiltonian describing the transverse-field Ising interaction for N spins has the form:

$$\hat{H}_{\text{Ising}} = \hbar \sum_{i,j}^{N} J_{ij} \hat{\sigma}_x^{(i)} \hat{\sigma}_x^{(j)} + B \sum_i \hat{\sigma}_z^{(i)} \tag{2.20}$$

Here, the first term corresponds to an interaction between pairs of spins i and j along one axis (here x), quantified by collective spin flips $\hat{\sigma}_x^{(i)} \hat{\sigma}_x^{(j)}$ with coupling strength J_{ij}. As seen from sec. 2.4.2, the collective spin flip terms leads to entanglement between spins. The coupling matrix J_{ij} may in the simplest case contain only nearest-neighbor terms, but may in reality contain longer-range interactions giving rise to highly non trivial spin dynamics. The sign of the coupling term relates to neighboring spins aligning parallel (ferromagnetic coupling) or anti-parallel (antiferromagnetic coupling) to each other. In spin systems beyond one spatial dimension, as well as systems with interactions beyond nearest neighbors, spin frustration can emerge, a phenomenon where it is impossible for all interacting spins to align in a way that minimizes the total system energy, e.g. because the geometry of the spins makes it impossible for all of them to align anti-parallel with respect to each other [81]. This gives rise to exotic magnetic states which may be relevant in the search for new materials [82]. The second term of the Hamiltonian in eq. 2.20 is the transverse field, here modelled as an external magnetic field along the z axis, with the field strength given by B. This term competes with the spin-spin interaction along x and polarizes all spins along the z direction. In the limit of large B, i.e. when the second term in the Hamiltonian dominates, the interaction may be formulated as the XY Hamiltonian:

$$\hat{H}_{\text{XY}} = \hbar \sum_{i,j}^{N} J_{ij} (\hat{\sigma}_x^{(i)} \hat{\sigma}_x^{(j)} + \hat{\sigma}_y^{(i)} \hat{\sigma}_y^{(j)}) = \frac{\hbar}{2} \sum_{i,j}^{N} J_{ij} (\hat{\sigma}_+^{(i)} \hat{\sigma}_-^{(j)} + \hat{\sigma}_-^{(i)} \hat{\sigma}_+^{(j)}) \tag{2.21}$$

Here, interactions occur along two axes, x and y, which can be expressed as a flip-flop type interaction via the spin raising and lowering operators

$$\hat{\sigma}_+ = |\downarrow\rangle\langle\uparrow| = \begin{pmatrix} 0 & 0 \\ 1 & 0 \end{pmatrix} \qquad \hat{\sigma}_- = |\uparrow\rangle\langle\downarrow| = \begin{pmatrix} 0 & 1 \\ 0 & 0 \end{pmatrix} \tag{2.22}$$

[15] The term dimensionality in this context refers to along how many axes the interactions occur.

[16] A spin-1/2 particle can be physically represented in an experiment e.g. by a trapped ion, with two electronic states of the ion corresponding to the spin up and down state, respectively. Interactions between spin-1/2 particles can be realized using laser fields coupling to the common motion of the ions.

which, in eq. 2.21, remove excitation in spin i while creating an excitation in spin j and vice versa. This Hamiltonian thus conserves the number of spin excitations present in the system, also known as total magnetization, with additional spin flips being energetically unfavorable[17].

For completeness, the Heisenberg Hamiltonian is provided below, which describes a more general way in which spin-1/2 particles can interact, along three axes x, y and z:

$$\hat{H}_{\text{Heisenberg}} = \hbar \sum_{i,j}^{N} J_{ij} (\hat{\sigma}_x^{(i)} \hat{\sigma}_x^{(j)} + \hat{\sigma}_y^{(i)} \hat{\sigma}_y^{(j)} + \hat{\sigma}_z^{(i)} \hat{\sigma}_z^{(j)}) \tag{2.23}$$

While these spin Hamiltonians are well known, it is challenging to simulate the dynamics of spin systems with more than a few tens of particles, especially when long-range interactions are present, as the state of the system then becomes very complex. Consequently, we rely on the construction of larger quantum simulators to understand the behaviors of such complex spin systems. It is within this context that this thesis work was initiated, with the intention to build a trapped-ion quantum simulator allowing for control over about 100 particles.

[17] Note, that this condition of fixed magnetization is necessary to make the aforementioned approximation of dynamics by the XY Hamiltonian. The approximation is thus valid only within each subspace of constant magnetization. Representation of the entire state space would require the transverse field term to be considered.

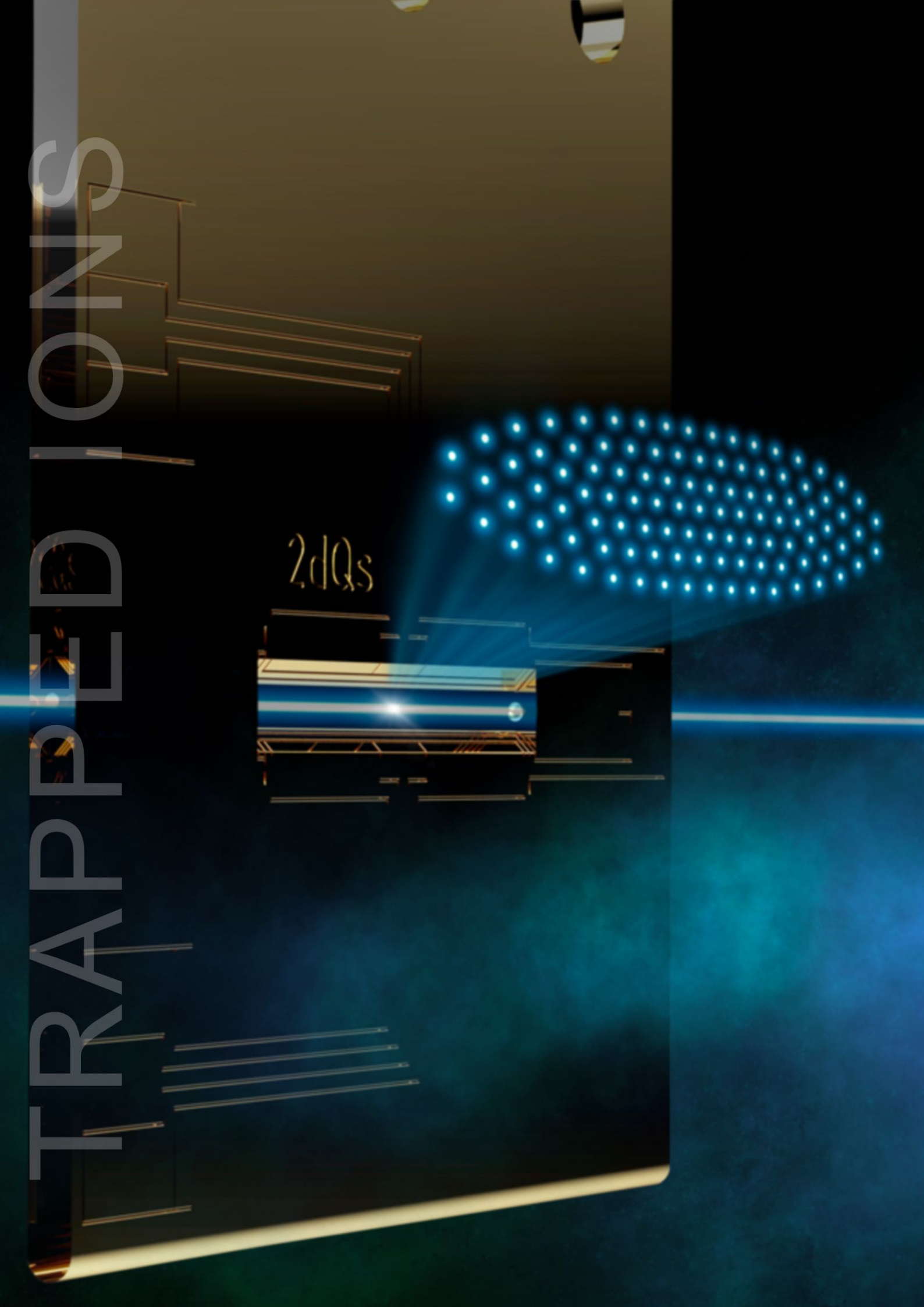
TRAPPED IONS
2dQs

3 Experimental Methods for Quantum Information Science with Trapped Ions

The previous chapter introduced relevant theoretical concepts in the field of quantum information science. In order to harness these concepts experimentally, they need to be implemented in a physical system. The last decades have seen tremendous progress in the control of individual quantum objects in the laboratory, where many experimental platforms, from trapped ions to superconducting qubits, quantum dots, photons and neutral atoms are actively explored, each with their very own benefits and drawbacks. Here, the goal is to establish a fully controlled, engineered quantum system, that can be precisely manipulated to be able to use it for computation, communication, metrology and sensing or just to study quantum phenomena. In this thesis, trapped ions are used as a platform for experiments in the context of quantum sensing and simulation. Trapped ions are among the most precisely controllable quantum systems available, as reflected by the 2012 Nobel prize [83]. They exhibit long coherence and storage times, are addressable individually due to their spacing of a few μm in the trap, their quantum state can be detected efficiently via the electron shelving technique and a toolbox of universal gate operations is available for their manipulation [84]. Moreover, quantum information encoded in trapped ions can efficiently be mapped to a photonic qubit, e.g. using cavity QED techniques, to distribute entanglement between remote systems. Trapped ions thus show promise in satisfying many of the criteria introduced by DiVincenzo as prerequisites for quantum computation and communication [85]. In this thesis a key focus is on the criterion of scalability. Scaling up trapped ion systems while maintaining precise quantum control proves a challenging endeavor. Full quantum control, i.e. entangling interactions as well as manipulation at the single-particle level, has been demonstrated in one-dimensional ion Coulomb crystals with up to 50 particles, stored in a radiofrequency (RF) trap [15]. As 1D ion chains are scaled up beyond such particle numbers, several complications can arise, such as strong heating of the ions along their symmetry axis. In the work presented in this thesis, ions are trapped in two rather than one dimension in a RF trap, which holds the potential to scale the system to higher ion numbers. In the context of quantum simulation, this also allows for the direct implementation of 2D spin models, naturally extending the range of models that can be investigated.

This chapter describes the relevant experimental tools and concepts required for quantum information experiments with trapped ions; from ion storage, manipulation of the quantum state of trapped ions for laser cooling, qubit control and entanglement generation, to characterization tools. The chapter also discusses relevant challenges that need to be overcome, in particular when working with two-dimensional ion crystals.

3.1 Ion Storage

The objective of particle trapping is to hold particles within a defined space using confining fields, while minimizing their interactions with the environment, that could decohere their quantum states. In general, the coupling between the trapping field and particle can occur via several mechanisms, such as through the magnetic or electric (permanent or induced) dipole moments of neutral atoms or molecules, or, in the case of ions, through the particle's charge. The latter generally allows for deeper trap depths and thus longer storage times, a practical advantage of ion trapping. Different types of ion traps make use of various trapping mechanisms. Earnshaw's theorem dictates that it is not possible to confine an ion in three spatial directions by the exclusive use of electrostatic fields. Ion traps overcome this limitation by using a combination of oscillating and static electric fields and magnetic fields to achieve 3D confinement. The two most widely used types of ion traps are Penning traps and Paul traps [86]. The Penning trap employs a combination of static electric and magnetic field, which causes ion crystals to rotate about the axis defined by the magnetic field. As this rotation occurs at a rate on the order of tens to hundreds of kHz, the control over individual ions in such a trap is challenging and has only very recently been demonstrated experimentally for the first time [18, 19]. This section focuses on Paul traps, the ion trap type employed for the experiments carried out in this thesis. A Paul trap combines static with RF voltages to hold the ions in defined positions, which facilitates individual-ion addressing via tightly-focused laser beams. However, RF driven micromotion poses a major challenge in experiments with planar ion crystals.

3.1.1 Operation Principle of Linear Paul Traps

The theory on ions stored in RF traps has been discussed extensively in literature [86, 87, 88, 89]. Thus, this section focuses only on the key points to provide a concise understanding. A RF trap is essentially an arrangement of electrodes which can be classified as RF and DC electrodes. As such they utilize both static and time-varying electric fields within the RF range, applied to the DC and RF electrodes, respectively, to establish an average confining potential. The potential is modeled as harmonic, representing the ideal scenario where ions may be trapped in a stable way, their motion predictable. More specifically, within a harmonic potential the ions experience a restoring force proportional to their displacement from the trap center, allowing them to be treated as simple harmonic oscillators. In reality, it is difficult to achieve a purely harmonic potential. The effect of anharmonic contributions is neglected for the moment and discussed later on in sec. 3.1.3.

Mathematical Description of the Trapping Potential

A three dimensional (x, y, z) harmonic potential can be modelled as

$$\Phi = \gamma_x x^2 + \gamma_y y^2 + \gamma_z z^2 \tag{3.1}$$

where parameters γ_i quantify the potential's curvatures along the three spatial directions x, y and z. From the Laplace equation $\Delta\Phi = 0$, it follows that $\gamma_x + \gamma_y + \gamma_z = 0$, i.e. when applying only static fields to create the potential the curvatures along x, y and z cannot all be positive, a concept known as Earnshaw's theorem [90]. To overcome this problem, of the potential

exhibiting negative curvature and thus being anti-confining along at least one direction, in RF traps an oscillating electric field is employed which dynamically traps the ions. The total trapping potential can then be expressed as

$$\Phi(t) = \Phi_{RF}(t) + \Phi_{DC} \tag{3.2}$$

where the dynamic part, dependent on time t, is given by

$$\Phi_{RF}(t) = \frac{V_{RF}}{2d_{RF}^2}(\alpha_x x^2 + \alpha_y y^2 + \alpha_z z^2)\cos(\Omega_{RF} t) \tag{3.3}$$

and the static contribution can be written as

$$\Phi_{DC} = \frac{V_{DC}}{2d_{DC}^2}(\beta_x x^2 + \beta_y y^2 + \beta_z z^2). \tag{3.4}$$

In these equations, the potential's curvature scales with parameters V, denoting a voltage amplitude or strength, and geometric factors, which depend on the trap geometry and electrode shapes. Here we have on one hand d, the distance between the center of the trap and the electrodes which create the confinement[1], and parameters α_i and β_i containing dimensionless factors that describe how much of the voltage applied to the trap is actually translated into curvature of the potential ("trap efficiency"[2]). The sum of the curvatures must again obey Laplace's equation. However, from eq. 3.3 one can see that for times $t = 0$ and $t = \pi/\Omega_{RF}$, the confining and anti-confining directions of the trapping potential are exchanged. When the voltage is switched sufficiently fast[3], an ion cannot escape the trapping potential and remains confined to the trap.

Single Ion Trajectory and Stability Regime

The starting point for the derivation of the trajectory that a cold[4] ion of mass m and charge Q follows in the potential of a RF trap is

$$F_i = m\ddot{r_i} = -\frac{d}{dr_i} Q\Phi(t). \tag{3.5}$$

Here, we consider the force F_i on the ion along direction r_i, where $r_i \in \{x, y, z\}$. The expression can be rewritten in the form of the Mathieu equation

[1] While expressing the potential in terms of V and d provides a convenient intuition to how the confinement scales linearly with the voltage and inversely with the square of the trap size, note that the situation may be more complicated in reality. These equations represent a simplified scenario, in that they model e.g. a standard linear Paul trap, where pairs of electrodes, symmetrically placed around the trap center and carrying the same voltage, produce the RF or DC potential, respectively. For a trap with more DC electrodes, which is the case in this thesis and most situations describing surface traps, carrying different voltages and having different distances to the trap center, the curvatures created by all electrodes will have to be added up accordingly, which is not reflected by eq. 3.4. Taking this into account will consequently also modify the expression for the a-parameter given in eq. 3.7.

[2] The trap efficiency is maximized for traps with hyperbolic electrode shapes, however this is oftentimes not practical as it restricts optical access required for laser beams to manipulate the ions.

[3] Here, for a given voltage amplitude, the rate at which the voltage must be switched to create a stable confinement depends on the ion's mass and charge.

[4] For the ion's motion to be quantized we require it to be laser-cooled to the Lamb Dicke regime (see sec. 3.3.3).

$$\frac{d^2 r_i}{d\xi^2} + (a_i - 2q_i \cos(2\xi)) r_i = 0 \tag{3.6}$$

where $\xi = \Omega_{RF} t/2$ and

$$a_i = \frac{4Q\beta_i U_{DC}}{m d_{DC}^2 \Omega_{RF}^2} \tag{3.7}$$

$$q_i = \frac{2Q\alpha_i V_{RF}}{m d_{RF}^2 \Omega_{RF}^2}. \tag{3.8}$$

These a- and q-parameters have physical significance, defining a regime in which the ions' motion is bounded and they can thus be trapped in a stable way. Ion traps are usually operated in the lowest stability regime where $|a_i|, q_i^2 \ll 1$[5].

The solutions to the Mathieu equation can be found via a Floquet-Ansatz, where the leading order term is given by

$$r_i(t) \approx (A_{i0} + \underbrace{A_{i1} \cos(\omega_i t)}_{\text{secular motion}})(1 + \underbrace{\frac{q_i}{2} \cos(\Omega_{RF} t)}_{\text{micromotion}}) \tag{3.9}$$

This expression constitutes a good approximation (within the lowest stability regime) of the motion of a trapped ion at position A_{i0}[6]. The motion is comprised of a slowly varying (secular) motion, represented in pseudopotential approximation[7] by a harmonic oscillation with frequency

$$\omega_i = \frac{\sqrt{a_i + q_i^2/2}}{2} \Omega_{RF}, \tag{3.10}$$

and a fast oscillation at the RF drive frequency, called micromotion. The secular frequencies are also referred to as trap frequencies, with those two terms used interchangeably within this thesis, and characterize the strength of the confinement of an ion in the trap. Micromotion, which is discussed in more detail in sec. 3.1.3, can have adverse effects on experiments where an ion's quantum state is coherently manipulated via laser fields. Consequently, the amplitude of micromotion should be kept as small as possible by placing the ions in the RF null in the trap center ($A_{i0} = 0$), where the effect of the switching RF field on the ions is minimized, and operating the trap at low q parameters, e.g. by increasing Ω_{RF}.

[5] When additionally $|a_i| \ll q_i$ is considered, the q-parameter is upper-bounded by ~ 0.9. In practice, though, q-parameters below about 0.5 are used as higher values can lead to instabilities in the presence of higher-order terms in the trapping potential (see also sec. 3.1.3).

[6] Note, that for the potential described above $A_{i0} = 0$, with the ion confined to the center of the trap. A non-zero value of A_{i0} would require an additional potential with a linear position dependence (i.e. a stray field).

[7] See the next subsection for an explanation of the pseudopotential approximation. Note, that in reality the frequency might slightly deviate from this value.

Pseudopotential Approximation

In order to simplify the description of the RF potential, it is possible to approximate it by its average effect, a static "pseudopotential", in units of energy given by

$$Q\Phi_{RF,pseudo} = \frac{Q^2|E(r)|^2}{4m\Omega_{RF}^2}. \tag{3.11}$$

Here E denotes the electric field generated by the trap electrodes, which can e.g. be determined from finite-element simulations for a specific ion trap model. The 3-dimensionally confining total potential $Q\Phi_{tot} = Q(\Phi_{RF,pseudo} + \Phi_{DC})$ consisting of the pseudopotential and the potential created by the DC electrodes, can also be expressed in terms of the trap frequencies

$$Q\Phi_{tot} = \frac{m}{2}(\omega_x^2 x^2 + \omega_y^2 y^2 + \omega_z^2 z^2), \tag{3.12}$$

corresponding to the potential of a three dimensional quantum harmonic oscillator[8]. Within the pseudopotential approximation the trap depth can be defined, which relates to the kinetic energy that a particle initially at rest in the trap center has to gain in order to escape the trap. It can be calculated by taking the potential energy difference of $Q\Phi_{tot}$ at the point at which the potential becomes anti-confining and at the trap center. In three dimensional[9] RF traps the trap depth is usually on the order of a few to several tens of eV, which is high compared to the thermal energy of atoms, such that collisions of the ions with background gas do in most cases not lead to ion loss.

The pseudopotential approximation constitutes a useful tool, that simplifies the modelling of trapped ion dynamics. Several calculations throughout this thesis rely on this approximation, such as the simulations carried out during the ion trap design process, presented in sec. 4.1.1. Later on in sec. 5.2.3 the deviations between the potential created by our ion trap and a model derived from pseudopotential approximation are investigated experimentally.

Linear Paul Trap Characteristics

RF traps can exist in various geometries, and in this thesis a linear Paul trap is employed. The standard linear Paul trap, as shown in fig. 3.1a, consists of two pairs of blades[10], creating a 2-dimensional RF quadrupole that confines the ions along the two "radial" trap directions, and endcap electrodes, to which a positive DC voltage is applied in order to confine the ions along the symmetry axis of the trap ("axial direction"). The benefit of using this geometry compared to a 3D Paul trap is that here the RF null extends along a line in the trap center and is not limited to a single point. Thus, micromotion can be minimized for any ion placed along this line. The RF

[8] Note, that this simple expression provides a good representation of the trapping potential along the main axes typically only near the trap center. Further away from the center the harmonic representation may no longer be sufficient to describe the potential (see e.g. fig. 4.4). Moreover, the potential will become anti-confining at some point along some direction, which limits the achievable trap depth.

[9] In contrast, surface traps usually have trap depths of below 1 eV and are thus more prone to ion loss.

[10] Here, oftentimes, RF is only applied to one pair of blades while the other pair is kept at ground potential or a DC potential which lifts the degeneracy of the confinement along the two radial directions. This may be necessary for efficient laser cooling of the trapped ions.

potential is ideally characterized by the parameters $\alpha_x = -\alpha_y$ and $\alpha_z = 0$ (see eq. 3.3), where x and y are the radial and z the axial trap direction. However, in reality small deviations are present, e.g. due to applying RF voltage only to one pair of blades, non-symmetric electrode geometries, or the finite length of the trap, which may introduce a small RF contribution along the z direction.

3.1.2 Ion Coulomb Crystals

An ion Coulomb crystal forms from a collection of trapped ions when they are laser-cooled (see sec. 3.3.3) to sufficiently low temperatures on the order of mK[91]. It manifests as an ordered structure which the ions arrange themselves in, reflecting the underlying shape of the external trapping potential, tunable via the RF and DC voltages applied to the trap. This section focuses on the different shapes that ion crystals can take on when stored in a linear Paul trap and the many harmonic modes of motion that ions in such crystals share.

Linear and Planar Ion Crystals in RF Traps

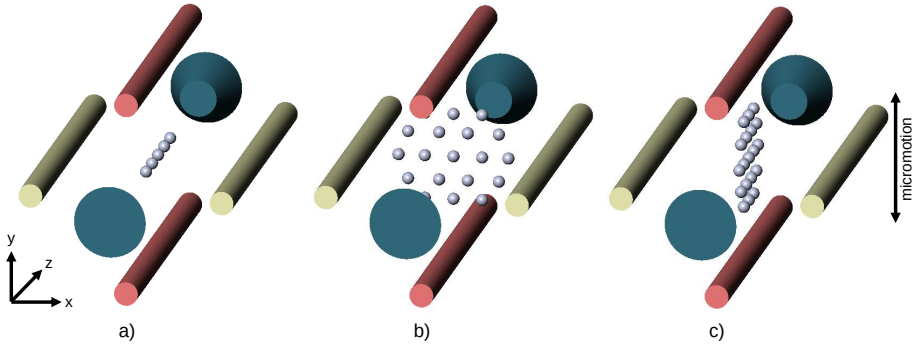

Figure 3.1: Schematic illustration of ion crystal configurations in a linear Paul trap: A standard linear Paul trap consists of two RF electrodes (pink) and two DC electrodes (yellow), generating the RF confinement, as well as two endcap DC electrodes (blue) for confining the ions along the symmetry axis of the trap. In this type of trap, directions x and y are typically referred to as radial directions, while z is denoted as the axial direction. a) A linear ion crystal is stored along the RF-null line. b) and c) show the two primary possibilities of storing a planar ion crystal in a linear Paul trap. In b) micromotion is present along both directions in which the crystal is extended, whereas in c) micromotion occurs to first order only along y.

The shape of the trapping potential, characterized by the trap frequencies, dictates the shape of an ion crystal in the trap. This section focuses on linear and planar ion crystals[11]. In a linear ion crystal, the ions are trapped along the RF null, to minimize micromotion for all ions. Here, complete quantum control of long crystals comprised of up to about 50 particles has been demonstrated experimentally [15]. However, scaling up 1D systems to larger numbers of individually controllable particles becomes challenging at some point, as structural phase transitions from a

[11] Experiments in quantum information science with 3D crystals are impractical, e.g. due to the challenge of imaging ions which are in different layers.

one dimensional to a two dimensional phase have to be suppressed [12]. For an ion crystal to remain linear, the condition

$$\omega_t/\omega_a > 0.77\frac{N}{\sqrt{\log(N)}} \tag{3.13}$$

must hold, where ω_t is the trap frequency along the transverse (radial) directions, ω_a along the axial trap direction and N is the number of ions [92, 93]. For e.g. $N = 50$ particles, we require $\omega_t/\omega_a > 19.47$. From this example it is straight forward to see that very anisotropic potentials are required to keep an ion crystal linear which gives rise to significant complication when scaling up trapped ion systems: The transverse confinement, set by the RF voltage, cannot be made arbitrarily high, such that the axial confinement needs to be lowered in order to maintain the linearity condition. This can lead to strong heating of the ions' axial motion, detrimental to laser cooling and entangling interactions[13]. Moreover, it can become challenging to laser-address individual ions at the edge of long ion strings spanning several hundreds of micrometers [94].

In 2D there exists one direction of strong confinement ω_s in which the crystal is compressed, and two directions of weak confinement $\omega_{w1,2}$, in which the crystal expands. The planarity condition, preventing an ion crystal from undergoing a phase transition to a three-dimensional structure, is given by [92]

$$\omega_s/\omega_{w1,2} > 1.23N^{1/4}. \tag{3.14}$$

Using the same example of $N = 50$ as before, here a ratio of trap frequencies of only 3.27 is required for keeping an ion crystal planar, scaling much more favorably with increasing ion number than the linearity condition. While this facilitates scaling up to larger ion crystal sizes, there are also downsides to taking this approach: Since the RF null extends along a line in the trap center, all ions which are displaced from this line will experience excess micromotion. Moreover, structural phase transitions can occur between several 2D lattice configurations[14] that are similar in energy, triggered by e.g. background gas collisions or RF heating, which is discussed in detail in sec. 3.1.3.

A planar ion crystal can be oriented within a linear Paul trap in two primary ways: Either the weak directions that span the crystal plane are chosen along both radial trap directions, as shown in fig. 3.1b or along one of the radial and the axial trap direction, illustrated in fig. 3.1c. The necessary asymmetry of the trap frequencies can be achieved via DC voltage control on the pair of DC blades and endcap electrodes, to compress the crystal into the desired plane. One benefit of the second approach is that micromotion only occurs along a single direction. Thus, in principle, an entire plane is available from which the ions can be laser-addressed to first order free of micromotion[15]. In terms of RF power requirements, none of the two configurations provide an advantage, as the following brief calculation based on pseudopotential approximation shows. The q-parameter is upper-bounded by a value q_m to keep the micromotion amplitude low. The

[12] Structural phase transitions are discussed in detail in sec. 3.1.3.

[13] Entangling interactions are mediated via the common motion of the ions, which is presented in sec. 3.2.3.

[14] These structural phase transitions are different than the ones occuring between phases of different dimensions in that they happen within an ion crystal for a fixed number of ions, held at a specific trapping potential.

[15] In practice, the trap electrodes restrict this optical access. For this reason, the linear Paul trap developed in this thesis work is of a modified geometry, compared to the standard design, as will be explained in sec. 4.1.1.

potential is characterized by the three secular frequencies ω_i with $i \in x, y, z$, which, assuming that in a linear trap $q_x = q_y = q$ and $q_z = 0$, can be expressed as

$$\omega_{x,y} = \frac{\Omega_{RF}}{2}\sqrt{\frac{q^2}{2} + a_{x,y}}, \quad \omega_z = \frac{\Omega_{RF}}{2}\sqrt{a_z}. \tag{3.15}$$

As the a parameters sum up to $a_x + a_y + a_z = 0$, the sum of the square of the secular frequencies is given by $\sum_i \omega_i^2 = q^2\Omega^2/4$. This condition lower-bounds the value of the angular drive frequency Ω_{RF} to

$$\Omega_{RF}^2 = \frac{4}{q^2}\sum_i \omega_i^2 \geq \frac{4}{q_m^2}\sum_i \omega_i^2. \tag{3.16}$$

As eq. (3.16) does not depend on the orientation of the planar crystal in the trap, the minimum RF power required to generate the desired set of secular frequencies is the same for both geometries. However, as will be presented in sec. 3.1.3, the two crystal orientations differ in their sensitivity to RF power fluctuations.

Ion Equilibrium Positions

The equilibrium positions of the ions within a Coulomb crystal arise from a balance of the repulsive forces from the Coulomb interaction between the ions and the force exerted on them by the trapping potential. The exact structure and stability of an ion Coulomb crystal depends on a variety of factors, besides the strength of the trapping fields, such as the number and type of ions, and their temperature. In our experiments the distance between ions is typically on the order of a few micrometers, which allows for spatially resolved fluorescence detection and laser addressing.

Calculation of the equilibrium positions of N ions can be done in the following way [93, 95]: The potential is modeled according to eq. 3.12. For N ions the potential energy of a Coulomb crystal can be written as

$$V = \sum_i^N \frac{1}{2}m(\omega_x^2 x_i(t)^2 + \omega_y^2 y_i(t)^2 + \omega_z^2 z_i(t)^2) + V_{Coulomb} \tag{3.17}$$

where

$$V_{Coulomb} = \frac{Q^2}{8\pi\epsilon_0}\sum_{i,j=1,i\neq j}^N \frac{1}{|\vec{r}_i(t) - \vec{r}_j(t)|} \tag{3.18}$$

represents the Coulomb repulsion between the individual ions i and j which are located at positions $\vec{r}_i(t) = (x_i(t), y_i(t), z_i(t))$ and $\vec{r}_j(t)$. Here, ϵ_0 is the permittivity of free space.

When the ions are sufficiently cold, their position $\vec{r}_i(t)$ can be approximated as

$$\vec{r}_i(t) \approx \vec{r}_i^0 + \vec{\xi}_i(t), \tag{3.19}$$

$\vec{r}_i^0$ representing the equilibrium positions and $\vec{\xi}_i(t)$ being a small time-dependent displacement.

To obtain the equilibrium positions the partial derivative of the potential V is taken with respect to the ion positions and equated with 0:

$$\frac{\partial V}{\partial r_i}|_{r_i=r_i^0} = 0 \tag{3.20}$$

For few ions this calculation can be done analytically while for higher ion numbers a numerical calculation is required [95].

Motional Modes

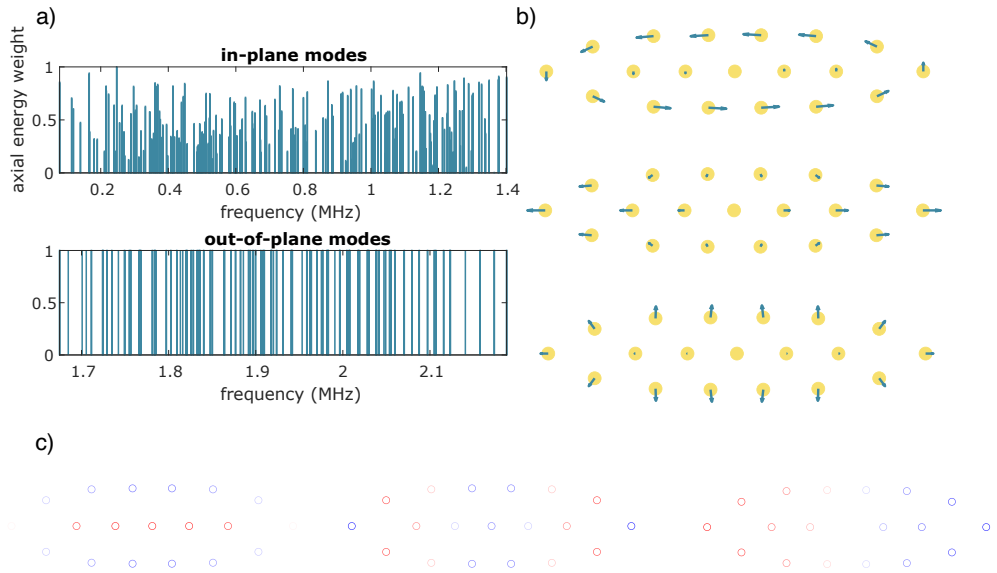

Figure 3.2: Motional modes of planar ion Coulomb crystals: a) The mode spectrum of a 105-ion planar crystal is calculated in pseudopotential approximation for trapping parameters $(\omega_x, \omega_y, \omega_z) = 2\pi(2188, 528, 247.2)$ kHz. With these trapping parameters the ion crystal extends, by our definition, along one radial and the axial direction of a linear Paul trap, as in fig. 3.1c. The top graph shows all in-plane motional modes, with the height of the mode representing the normalized axial energy weight, a parameter quantifying the ability to laser-cool the respective mode with a beam propagating along the axial trap direction. A clear energy separation between the in- and out-of-plane motional modes is visible. The latter modes are shown in the bottom plot. See fig. 5.6 for the experimentally measured out-of-plane mode spectrum for these trapping parameters. Images in b) and c) each illustrate three in-plane and out-of-plane motional modes, respectively, of a smaller 19-ion planar crystal, such as the one used in experiments in sec. 6.2. While the displacement of ions within the plane is illustrated via arrows in b), the back and forth movement out of the plane is illustrated via colors red and blue in c).

Considering the displacement of ions from their equilibrium positions, it is clear that their displacement will be coupled, due to the Coulomb interaction between them. For a sufficiently cold N ion crystal this motion is quantized and represented by $3N$ motional modes, N for each of the spatial dimensions. The mode in which all ions oscillate with the same amplitude and phase is called the center of mass (COM) mode and its frequency corresponds to the trap frequency along the respective direction[16]. Other motional modes are characterized by different tilting or sheering movements. For a 2D crystal, the modes can be divided into in-plane and out-of-plane modes. Figure 3.2 presents simulations in pseudopotential approximation on the motional mode structure of a 105-ion and 19-ion planar crystal, which experiments later on in this thesis are based on. Figure 3.2a shows the full simulated mode spectrum of the 105-ion crystal while 3.2b and c show the displacement of ions, visualizing a few distinct motional modes of the 19-ion crystal.

Methods for calculating the mode frequencies are e.g. given in [95] and in the thesis of Dominik Kiesenhofer. As micromotion may lead to a modification of the mode frequencies, performing such calculations in pseudopotential approximation may lead to inaccurate resuts. Methods which take the full RF dynamics into account, such as a Floquet-Lyapunov approach or Fourier transform of the ions' motion were studied in the thesis of Dominik Kiesenhofer, but did for the most part not provide a significant improvement to pseudopotential calculations when compared to experimental data. The motional modes of ion crystals can be used to mediate interactions between ions, which is discussed in sec. 3.2.3. This forms the basis for creating entanglement and is thus an important tool in the context of trapped-ion quantum information science.

3.1.3 Experimental Challenges and Mitigation Strategies

While the models presented so far in this chapter represent an ideal scenario, the experimental reality may not be accurately portrayed by these models. Experimental challenges can arise from different effects, some of which are particularly severe when working with planar ion crystal. This section focuses on these challenges and mitigation strategies which we apply in our experiments.

Anharmonic Trapping Potentials

The information in this subsection is mainly based on [96], where the author has provided a comprehensive summary of the effects of anharmonic contributions to the trapping potential. An ideal Paul trap produces a harmonic trapping potential where only terms of the form x^2 contribute, which is difficult to achieve in reality. Terms that are lower or higher order in x (e.g. octopole $\propto x^4$ hexadecapole $\propto x^8$) may also be present in a realistic Paul trap due to electrode misalignment or the use of approximations to the ideal hyperbolic electrode geometry, i.e. simpler electrode shapes which allow for better optical access. If the potential includes anharmonic contributions, the ion motion can become complex and even chaotic due to the non-linear relationship between the force acting on the ions and their displacement. This results in unpredictable normal

[16] Note that this is only the case for ion crystals which consist of identical ions. Also, measuring the COM mode of an ion crystal or determining the secular frequency of a single ion for the same trapping parameters might in practice produce a small deviation due to anharmonic terms in the trapping potential that become relevant for the length scales over which the ion crystal extends.

mode frequencies and amplitudes [97], a coupling between the motion along different axes[17], and in general a lack of control over the ion motion, characterized by heating and in the worst case ejection of ions from the trap due to nonlinear resonances [98, 99]. In experiments with linear ion strings in macroscopic linear Paul traps, the ions are confined to a small region in the trap close to the RF null, where higher order terms are usually negligible. However, when non-conventional trap geometries are used, much larger deviations from the ideal can arise. On top of that, when ions are far displaced from the RF null, which is the case when storing large planar ion crystals in a RF trap, adverse effects arising from higher-order terms may be much more severe, which has been observed e.g. in mass spectrometry.

Micromotion

Micromotion at the RF drive frequency is always present in RF traps and has adverse effects on the precision with which the trapped ions can be controlled, e.g. relating to increased motional heating and structural phase transitions, effects which are explained in more detail later on in this section. Moreover, the quantum states of trapped ions are manipulated via laser light, as presented in sec. 3.2, and micromotion can have adverse effects on these light-matter interactions. In particular, micromotion leads to a phase[18] modulation of the laser light in the reference frame of the ion. On narrow transitions, coupling strength may be lost to sidebands rather than the desired carrier transition. On broad transitions, such as the one used for laser cooling, the lineshape may be Doppler-broadened, making laser cooling less efficient.

As can be seen from eq. 3.9 the micromotion amplitude scales linearly with the q-parameter and the distance of an ion from the trap center. In experiments with linear ion chains, micromotion can thus be kept at low levels, by placing the ions along the RF null line. In practice, this involves cancelling the effect of stray electric fields that would displace ions from the trap center, by applying compensation voltages on designated electrodes. In this case, remaining micromotion due to the secular motion of the ions, which slightly displaces the ions from the RF null, is low and does not impose any experimental restrictions. However, in 2D ion crystals most ions are inevitably displaced comparatively far from the RF null. For crystals which extend over several tens of micrometers, this can easily result in micromotion amplitudes for the outermost ions on the order of micrometers, and thus on the order of the inter-ion spacing. Operating the ion trap at low q-parameters is one strategy to decrease the micromotion amplitude. Additionally, in order to mitigate adverse effects of micromotion in planar ion crystals, ions should be manipulated with laser beams only from directions that are perpendicular to the micromotion. In this way, undesired effects on laser-ion interactions are suppressed to first order[19]. This strategy is employed in this thesis work: The crystal configuration is chosen according to fig. 3.1c, with the crystal extending along the axial and one of the radial trap direction. Here, micromotion ideally occurs only along a single direction. In order to gain laser access from relevant directions, perpendicular

[17] A coupling of different motional modes may be problematic as this might cause an energy transfer from a hot mode to a ground-state cooled one.

[18] For laser beams which are strongly focused onto a single ion also amplitude modulation of the laser light may be present due to micromotion.

[19] To first order here means that, as the ions are coupled via their Coulomb interaction, micromotion along one direction perpendicular to the laser beam may also lead to a small motion in another direction, not necessarily perpendicular to the laser beam.

to the micromotion direction, the standard linear Paul trap design was modified, as presented in sec. 4.1.1. An approach to minimize the micromotion along undesired directions and the achievable level of residual micromotion along those those directions in our apparatus is discussed in sec. 5.2.2.

Residual Background Gas and Langevin Collisions

In order to operate an ion trapping experiment, vacuum conditions around the trap have to be established. Limitations to the vacuum quality arise from e.g. material outgassing or residual contaminants within the vacuum vessel, resulting in the presence of residual gas atoms or molecules which can collide with the trapped ions. Such "Langevin" collisions pose challenges, restricting the lifetime of an ion Coulomb crystal via several mechanisms. First of all, a collision may result in a chemical reaction between a trapped ion and background gas particle, leading to the formation of a "dark" ion. Here, the lasers for imaging the atomic ions (see sec. 3.3.3) are no longer resonant with the resulting molecule's transitions, causing the ion to appear dark. Note that dark ions can also occur in the absence of a collision, when a background gas particle is ionized and captured by the trapping potential. Upon the formation of a dark ion, it may be necessary to empty the trap and reload the ion crystal, unless the dark ion is molecular, in which case it may be possible to dissociate it via laser light in a deterministic way. Another problem that can arise from Langevin collisions is the loss of an ion from the trap. Here, the ion gains sufficient kinetic energy via the collision, also potentially aided by heating mechanisms (as described in the subsequent subsection), to exceed the trap depth. This issue is more common in surface traps, with typical trap depths below 1 eV. In 2D ion Coulomb crystals, collisions can additionally cause structural phase transitions, such as to a melted phase or between different configurations of the crystal lattice, as discussed in detail in subsequent subsections.

Establishing excellent vacuum conditions is imperative for minimizing the rate of Langevin collisions and thereby reducing the likelihood of dark ions, ion loss and structural phase transitions. This is particularly important in experiments involving large ion crystals, given that the collision rate scales linearly with the number of ions. Cryogenic systems facilitate establishing and maintaining such high-quality vacuum conditions. This is attributed to the decreased vapor pressure of substances at low temperatures, leading to fewer molecules evaporating into the gas phase (reduced outgassing) and the effective removal of background gases present inside the vacuum vessel by condensation onto the chamber walls. Additionally, the thermal motion of background gas particles is reduced, such that collisions not only occur less frequently but also at lower energies, making them less harmful to the ion crystals. However, cryogenic systems come with certain drawbacks, such as increased operational complexity, potential vibrations that can adversely affect laser-ion interactions where phase stability on the length scale of a small fraction of the light's wavelength is required, and high costs. Alternatively, it is possible to achieve good vacuum conditions around 10^{-11} mbar at room temperature by taking the following measures: All materials inside the vacuum vessel should have good outgassing properties. Substances such as polymers or glues should thus be avoided, as they usually exhibit a high level of outgassing. Moreover, metals such as titanium or aluminium are preferable over stainless steel, especially for the vacuum vessel itself, due to lower hydrogen outgassing. All in-vacuum parts should be cleaned thoroughly in ultra-sonic baths of ultraclean solvents in order to eliminate hydrocarbons which

are detrimental to vacuum pressures. The parts should furthermore be properly vented to avoid virtual leaks. Heat treatments such as vacuum firing, air baking and vacuum baking should be applied in order to reduce the outgassing of metals and eliminate water inside the vessel. The vacuum system should be designed in a way that allows for effective pumping, with non-evaporative getters (NEGs) and ion pumps sustaining vacuum conditions over time. In the end, the pressure inside the chamber should be dominated by hydrogen, specifically H_2, a light particle which in collisions is less detrimental to the ion crystals' stability than heavier ones.

Ion Heating

In order to manipulate ions at the quantum level, they need to be cooled to sufficiently low temperatures by means of laser cooling, which is discussed in sec. 3.3.3. However, cooling is counteracted by heating mechanisms. Strong heating may result in the breakdown of the crystal structure, causing ions to enter a melted phase or even escape the trapping potential. In less severe cases, heating may disrupt the ions' adherence to the Lamb-Dicke regime that is necessary for harnessing the shared motion of the ions in the trap for e.g. entangling interactions (see sec. 3.2.3). Related to this, heating may limit the coherence (motional and electronic [100]), and thus the timescale of experiments investigating the dynamics of interacting spin-1/2 particles.

Several heating mechanisms exist which transfer energy to the ions. One model is based on electric field noise coupling to the ion's charge and exciting the secular motion of the ions. Such electric field noise can arise from a combination of different origins, most commonly technical noise, Johnson noise or surface noise. Noise which is present in the voltage supply of the ion trap or may be picked up from the laboratory environment can be summarized by the term technical noise. It can be reduced by ensuring a clean electrical environment in the laboratory free of ground loops[20], and using low-noise power supplies and electronics in combination with filters and active stabilization. Johnson noise, also known as Nyquist noise, arises from the random motion of electrons in electronic components at non-zero temperature. The random movement of the electrons results in random voltage fluctuations which manifest as noise across a wide range of frequencies. Since the magnitude of Johnson noise is proportional to temperature, operating ion traps at cryogenic temperatures is beneficial. Moreover, its magnitude is dependent on resistance, requiring a smart design of electronics which are within the voltage network of the ion trap, such as the filters typically employed to reduce ripple on the trap's DC electrodes. Surface noise is not well understood but attributed to microscopic processes on the surface of the ion trap.

The electric field noise produced by these processes is characterized by its spectral density S_E, oftentimes modeled as

$$S_E \propto \omega^{-\alpha} d^{-\beta} T^{+\gamma}. \tag{3.21}$$

Here, ω is the motional frequency of the ion, d is the distance between ion and trap electrode and T is the surface temperature of the trap, while α, β and γ are positive constants that quantify the power-law behavior [101]. While this relation is sometimes disputed [101], it can provide an intuitive understanding and in many situations may agree well with experimental data within a reduced parameter space. The proposed scaling for surface noise is oftentimes on the order of

[20] Our approach to avoiding ground loops, where the interconnection of devices gives rise to noise components at the frequency of the AC mains hum, is presented in sec. 4.8.1.

d^{-4}, meaning that an electrode-ion distance that is as large as possible is desired. The frequency dependence is typically modelled between $1/\omega^{-1}$ and $1/\omega^{-2}$, in our setup we have observed a scaling of about $1/\omega^{-2}$. Higher secular frequencies are thus desired to decrease heating effects.

An additional heating mechanism is RF heating, an effect that is not related to fluctuating electric fields but arises from the trapping RF field itself. Here, energy is transferred from the RF field to the trapped ions [30, 31]. In planar crystals this effect may be more severe, compared to linear crystals, as the ions that are placed far from the RF null experience more significant acceleration from the RF field. Again, operating the trap at low q parameters is a good strategy for mitigating these effects. RF heating can also be aggravated by other mechanisms, e.g. Langevin collisions of the ions with background gas particles. Here, energy is first transferred to the ions via the momentum kick through the collision, with additional energy supplied by RF heating, which may induce transitions into a non-crystalline phase and give rise to heating dynamics as observed in [31].

Structural Phase Transitions of the Crystal Lattice

In contrast to linear ion crystals, planar crystals can exist in different structural configurations, within a given trapping potential. A prerequisite for a transition to take place between these distinct configurations, is the availability of structural phases which are close in energy to each other, such that the energy gap can be bridged by e.g. heating effects or Langevin collisions of the ions with background gas. This phenomenon of structural phase transitions is well-known in the context of barely two-dimensional zig-zag crystals with two mirror-symmetric, energetically-degenerate ground-state configurations [16, 17]. In larger and less elongated planar ion crystal, more lattice configurations are possible. The thesis of Dominik Kiesenhofer presents a thorough investigation of lattice configurations of ion Coulomb crystals trapped in our apparatus and compares the experimental observations with expected configurations, determined via simulated annealing.

Transitions between different lattice configurations are undesired in the experiment as quantum state readout and manipulation is in many cases ion-specific, and shifting of ion positions thus leads to errors. Moreover, these transitions may modify the motional mode structure of the crystal, which affects entangling interactions. Besides having established excellent vacuum conditions in our apparatus in order to reduce the rate of Langevin collisions, we employ several strategies to practically eliminate the effect of structural phase transitions on our experiments. These include selecting specific ion numbers and trap anisotropies, for which the crystal lattice is intrinsically more stable, stabilizing the trap frequencies (see also next subsection), and detecting configuration changes during experimental measurement sequences such that the corresponding data can be excluded. These strategies are presented in more detail in sec. 5.3.2.

Trapping Potential Instabilities

Fluctuations in the voltages supplying the ion trap give rise to several undesirable effects. As discussed in sec. 3.1.3 noise on the DC electrodes can result in heating of the trapped ions. However, stabilizing DC voltages is generally easier than stabilizing RF voltages[21], leading us to consider RF

[21] In an electrical environment free of ground loops, off-the-shelf low-noise DC power supplies in combination with lowpass filters close to the trap are usually sufficient to bring the noise level on the DC electrodes down to acceptable

stability as a potential limiting factor in the experiment. According to equations 3.10 and 3.8, the trap frequencies are linearly dependent on the amplitude of the RF voltage. Thus, voltage fluctuations may result in changes of the mode structure of the ion crystal, which is problematic in the context of entangling interactions, where stability of the mode frequencies with respect to the frequency of the laser creating the interaction is crucial, to maintain a constant coupling strength throughout the experiment. At the same time, changes in trap frequencies may lead to changes of the aspect ratio of the ion crystal, potentially increasing the likelihood of structural phase transitions to occur. As discussed previously, there are two primary configurations of trapping a planar ion Coulomb crystal in a linear Paul trap, with the option of the crystal extending along the axial and one of the radial direction (fig. 3.1c) having the benefit of micromotion only occurring along a single direction. Here, the two possible options are compared in terms of their sensitivity to RF voltage fluctuations.

Starting from eq. 3.15, the dependence of the secular frequencies on the q-parameter can be calculated via

$$\frac{d\omega_i}{dq} = \frac{\Omega}{4}\frac{q}{\sqrt{\frac{q^2}{2}+a_i}} = \frac{\Omega^2 q}{8\omega_i} = \frac{1}{2q\omega_i}\sum_{n=1}^{3}\omega_n^2 \quad , i \in 1,2 \tag{3.22}$$

$$\frac{d\omega_3}{dq} = 0. \tag{3.23}$$

These expressions show that the secular frequency along the axial trap direction does not change with changing RF power and thus, trapping a planar crystal within the radial plane of the trap (as in fig. 3.1b) is the best option to suppress coupling strength variations of the laser creating entangling interactions. On the other hand, while the secular frequencies of a crystal trapped in a plane spanned by one radial and the axial trap direction are not insensitive to RF power fluctuations, the effect is still a factor of two weaker than for a linear ion crystal with the same maximum secular frequency. Thus, a crystal confined to the axial-radial plane may still be suitable for experiments in which entanglement is mediated via motional modes, when establishing sufficient frequency-stability of those modes with respect to the interaction beam via a state-of-the-art RF power stabilization unit. In terms of sensitivity of the crystal aspect ratio with respect to changes in the trap frequencies, a crystal in the radial plane also provides a benefit. In this case both in-plane directions are affected equally by RF power fluctuations, leading to a ”breathing” effect of the crystal. This correlates with a reduced chance of structural phase transitions to occur, compared to a crystal trapped in the radial-axial plane, for which RF power fluctuations do alter the crystal aspect ratio.

levels. For RF electronics the situation is much more difficult since here a signal oscillating on the order of tens of MHz has to be stabilized in frequency and amplitude. This requires a combination of custom active-stabilization electronics, sophisticated pickup schemes for the reference signal as well as excellent temperature and humidity control around the experiment.

3.2 Controlling the Quantum State of Trapped Ions

In order to perform trapped-ion experiments in a quantum information context, the quantum states of the ions need to be precisely manipulated, to allow for storing, processing and reading out quantum information. In principle, any approximation of a two-level quantum system can be employed to encode a physical qubit. A multi-level quantum system can be used in the case that two states can be sufficiently decoupled from the others, which is often the case for the internal (electronic or hyperfine levels) of an atom or ion. This section focuses on how precisely timed control fields can be used to manipulate the quantum states of trapped ions. This manipulation forms the basis of performing single qubit gates, or more generally, arbitrary rotations around the Bloch sphere. Moreover, manipulating the external (motional) degrees of freedom of the trapped ions by means of laser fields can create entangling interactions within an ion crystal, forming the basis of multi-qubit quantum operations.

3.2.1 Coherent Interactions

The electronic and hyperfine levels of an atom are non-uniformly spaced, allowing them to be addressed individually through radiation with a frequency matching their respective energy splitting. Laser, microwave, or RF fields may be employed for this purpose. Here, laser fields offer advantages as their high spatial coherence, correlating with strong spatial confinement, allows for the resolution required for manipulating the quantum state of individual ions within a Coulomb crystal. Moreover, lasers are able to couple to the ions' motion, required for creating entangling interactions, which is presented in the next sections. Besides manipulating ions with lasers, in this thesis work ions are also manipulated via magnetic RF fields. While spatial resolution was mentioned as a benefit of laser-driven interactions, the Gaussian beam profile of a laser may lead to undesired coupling strength variations in global operations on the ion crystal. Here, RF fields in principle allow for a more homogeneous interaction and also prevent unwanted coupling to the ions' motion in situations where it is not desired. Moreover, RF sources with excellent amplitude and phase stability are commercially available while stabilizing lasers in amplitude and phase can be technically very demanding, but is a requirement for the high-fidelity manipulation of the ions' quantum states.

In the following, the coupling between a trapped ion and laser fields is described, with the first part about resonant interactions also applicable to RF fields. Later on in sec. 3.2.2 the theory is extended to interactions within a harmonic trapping potential, to describe the coupling between a laser and an ion's motion.

The energy of an ion described in terms of two quantum states, e.g. representing the basis states of a physical qubit, can be expressed as the Hamiltonian

$$\hat{H}_{\text{atom}} = \frac{\hbar\omega_0}{2}\hat{\sigma}_z. \tag{3.24}$$

Here, the two states have eigenenergies $\pm\hbar\omega_0/2$, thus $\hbar\omega_0$ corresponding to the energy difference between the two states. In simple terms, radiation at frequency ω_0 can be used to couple the two energy levels, i.e. to excite or de-excite the ion from one to the other state (population transfer of e.g. an electron from one energy state to the other). During the interaction a laser field, which can

be modelled classically as a sinusoidal travelling wave at frequency ω_l and phase $\phi_l = \vec{k_l}\vec{r} + \phi$, where $\vec{k_l}$ is the laser wavevector, $\vec{r}$ the position vector and ϕ some phase offset, interacts with the ion for a time t. The coherent population dynamics are then described by the time evolution under a Hamiltonian, as discussed in sec. 2.2.1. The Hamiltonian describing this coupling can be expressed as

$$\hat{H}_{\text{coupling}} = \hbar\Omega \cos(\omega_l t - \phi_l)(\hat{\sigma}_+ + \hat{\sigma}_-) \tag{3.25}$$

where $\hat{\sigma}_\pm$ are the raising/lowering operator defined in eq. 2.22 and Ω is the Rabi frequency which quantifies the coupling strength, i.e. the speed at which population is transferred between the two states.

The Rabi Frequency

The Rabi frequency is a measure for the coupling strength on an atomic transition and depends on several parameters, such as the type of transition, the intensity of the driving field, as well as polarization and direction of the laser beam with respect to the magnetic field axis[22] [94]. For example, in dipole transitions the Rabi frequency is proportional to the dipole transition matrix element multiplied with the electric field amplitude of the driving field. In contrast, for quadrupole transitions it is dependent on the gradient of the electric field which couples to the quadrupole moment of the ion. Moreover, the Clebsch-Gordan coefficients are relevant in this context, which describe the possible coupling strength between two specific angular momentum states. The Rabi frequency also depends on light polarization and geometric factors based on the angle between laser beam and quantization axis[23]. Here, it is useful to consider an atom's spatial absorption/emission characteristics during a transition, illustrated e.g. in fig. 2.2 and 2.3 of [102], which demonstrate the constraints on laser beam direction and polarization in order to achieve coupling. More quantitatively, these geometric factors are provided in [94, 103] for the quadrupole transitions in $^{40}Ca^{+}$[24]. When setting up laser beams in the experiment, these geometric factors should be considered to maximize the coupling on the desired transition. In the given example of $^{40}Ca^{+}$, for driving $\Delta m = 0$ transitions, it is beneficial for the laser to propagate at a 45 degree angle with the quantization axis with a polarization that is linear (π-polarization) within the plane spanned by the laser and magnetic field axis. On the other hand, for driving transitions in which the magnetic quantum number should change by $\Delta m = 1$, maximum coupling can be achieved when a laser beam with circular polarization propagates along the magnetic field axis. Here, σ^+ and σ^- denote circular light polarizations driving transitions where Δm changes by +1 and -1, respectively.

Transformation into the Interaction Picture

The total Hamiltonian describing the atom and its coupling to the light field is given by $\hat{H}_{\text{atom}} + \hat{H}_{\text{coupling}}$. We are interested in the dynamics which are initiated by $\hat{H}_{\text{coupling}}$. It is thus convenient to change into the interaction picture via the transformation $\hat{H}_{\text{int}} = e^{\frac{i\hat{H}_{\text{atom}}t}{\hbar}} \hat{H}_{\text{coupling}} e^{-\frac{i\hat{H}_{\text{atom}}t}{\hbar}}$,

[22] These concepts are related to the selection rules for atomic transitions that describe which transitions are allowed in general and the conditions that must be satisfied for a certain transition to occur.

[23] The quantization axis corresponds to the axis of magnetic field in the experiment. This axis provides a reference for the atom's directional transition characteristics. Note, that in the case of dipole transitions the angle between the beam and the quantization axis does not enter the expression for the Rabi frequency directly but only has an influence on the allowed polarization vectors.

[24] These transitions can couple an optical qubit, as discussed in sec. 3.3.4.

where the evolution of the unperturbed atom is separated from the evolution due to the laser-driven interaction. Additionally, the rotating wave approximation is applied, which neglects terms $\propto (\omega_l + \omega_0)t$ in the Hamiltonian that oscillate rapidly, and thus average out over the time scale of the interaction[25]. This leads to the interaction Hamiltonian

$$\hat{H}_{\text{int}} = \hbar\frac{\Omega}{2}\left(e^{i\chi}\hat{\sigma}_+ + e^{-i\chi}\hat{\sigma}_-\right) \tag{3.26}$$

where $\chi = \phi_l - \Delta t$ and $\Delta = \omega_l - \omega_0$ is the frequency detuning of the laser from the atomic transition frequency.

Resonant driving

Here the case where the detuning $\Delta = 0$ is considered, i.e. the laser's frequency exactly matches the frequency of the atomic transition. In this case, the dynamics are described by the unitary evolution

$$\hat{U}(t) = e^{\frac{-i\hat{H}_{\text{int}}t}{\hbar}}. \tag{3.27}$$

The population dynamics of the ion's energy states under this unitary evolution are described by the optical Bloch equations (without damping). Here, the populations evolve as sinusoidal oscillations at the Rabi frequency (Rabi oscillations). This can be illustrated as rotations of the state vector around the Bloch sphere about an axis within the equatorial plane that is set by ϕ_l. Here, the amount of rotation the state vector experiences is proportional to the interaction time t via $\theta = \Omega t$. Laser pulses of a duration that cause a complete population transfer between the qubit basis states, from $|0\rangle$ to $|1\rangle$ and vice versa, are referred to as π-pulses as here $\theta = \pi$. This effectively realizes e.g. a $\hat{\sigma}_x$ or $\hat{\sigma}_y$ gate operation, depending on the value of ϕ_l. Pulses of a duration that map an original state $|0\rangle$ or $|1\rangle$ onto an equal superposition state of $|0\rangle$ and $|1\rangle$ are referred to as $\pi/2$-pulses.

The optical Bloch equations also allow for decoherence effects to be included in the model for population dynamics in an atomic two-level system, via the introduction of damping terms. This effect of damping Rabi oscillations becomes visible in the experiment when averaging over many projective measurements.

Non-Resonant Laser-Ion Interactions

In the case of $\Delta \neq 0$, i.e. the laser frequency not being resonant with the atomic transition frequency, the population dynamics increase in speed, the effective Rabi frequency given by

$$\Omega_{\text{eff}} = \sqrt{\Omega^2 + \Delta^2} \tag{3.28}$$

while the ability to transfer population from one state to the other is reduced by $\Omega^2/\Omega_{\text{eff}}^2$. Resonance thus seems to be a natural requirement in order to perform rotations of the qubit state with high fidelity. However, off-resonant operations are also crucial as they allow for $\hat{\sigma}_z$ rotations to be performed, an operation not easily accessible with resonant pulses. This ability is based on the

[25] However, situations exist in which these terms do become relevant, such as ultrafast excitation of the atom with high-intensity laser pulses.

AC Stark effect and can be derived by changing into a different, albeit less intuitive, interaction picture than previously. Now, the total Hamiltonian $\hat{H}_{\text{atom}} + \hat{H}_{\text{coupling}}$ is divided into the two parts

$$\hat{H}_0 = \frac{\hbar\omega_l}{2}\hat{\sigma}_z \tag{3.29}$$

and

$$\hat{H}_1 = -\frac{\hbar\Delta}{2}\hat{\sigma}_z + \hbar\Omega\cos(\omega_l t - \phi_l)(\hat{\sigma}_+ + \hat{\sigma}_-). \tag{3.30}$$

The transformation into the new interaction picture $\hat{H}_{\text{int'}} = e^{\frac{i\hat{H}_0 t}{\hbar}}\hat{H}_1 e^{-\frac{i\hat{H}_0 t}{\hbar}}$ and applying a rotating wave approximation yields

$$\hat{H}_{\text{int'}} = -\frac{\hbar\Delta}{2}\hat{\sigma}_z + \frac{\hbar\Omega}{2}\hat{\sigma}_x. \tag{3.31}$$

From this equation it is easy to see that when the first term dominates at large detuning the dynamics under $\hat{U}'(t) = e^{\frac{-i\hat{H}_{\text{int'}}t}{\hbar}}$ result is an effective rotation around the z-axis of the Bloch sphere. In the process, the atomic energy levels are light-shifted by

$$\Delta_{\text{AC Stark}} = -\frac{1}{2}\Delta \pm \frac{1}{2}\sqrt{\Omega_{\text{eff}}^2 + \Delta^2}. \tag{3.32}$$

Besides the usefulness of AC-Stark pulses within the context of creating phase gates on qubits, Stark shifts which are fluctuating in time relate to phase fluctuations of the qubit and thus lead to decoherence. In a real atom, which consists of many more energy levels than the two considered here, a light field can couple off-resonantly to all of them, making the control of AC Stark shifts challenging. Moreover, more complications may arise due to Stark shifts not necessarily being spatially homogeneous due to a laser beam's Gaussian intensity profile.

Raman Transitions using two Laser fields

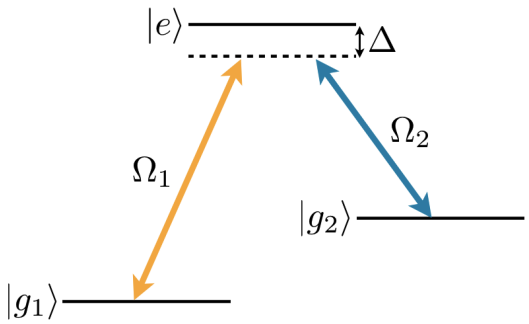

Figure 3.3: Three-level Λ-type system: $|g_1\rangle$ and $|g_2\rangle$ represent two long-lived states, which are off-resonantly (detuning Δ) coupled to a short-lived excited state $|e\rangle$ using two laser fields with Rabi frequencies Ω_1 and Ω_2. This Raman process creates resonant coupling between the the ground states $|g_1\rangle$ and $|g_2\rangle$.

Raman transitions allow for two energy states of an atom to be coupled via a third state, offering a convenient way of driving transitions, for which lasers are unavailable. Theory on Raman transitions is provided in detail e.g. in [104, 105, 106, 107], with the most important concepts explained in the following. We consider a "Λ-type" three-level system, as shown in figure 3.3. $|g_1\rangle$ and $|g_2\rangle$ represent two long-lived ground states between which population is coherently transferred, by off-resonantly coupling them via a short-lived excited state $|e\rangle$ using two laser fields. The respective Rabi frequencies of the laser fields are denoted as Ω_1 and Ω_2, while the detuning from the excited state is represented by Δ. For the Raman process to be resonant, the frequency difference of the two laser fields has to match the transition frequency between $|g_1\rangle$ and $|g_2\rangle$[26]. Another requirement for the coherent population transfer between the ground states is that $\Delta >> \Omega_1, \Omega_2, \Gamma$, to suppress population of $|e\rangle$ and spontaneous decay from this excited states that would lead to decoherence. Here, Γ corresponds to the total spontaneous emission rate, representing the two possible decay channels from the excited state in the three-level system[27]. In this Raman process, the population oscillates between $|g_1\rangle$ and $|g_2\rangle$ with an effective Rabi frequency of

$$\Omega_{\text{eff}} = \frac{\Omega_1 \Omega_2}{2\Delta}, \tag{3.33}$$

while the effective scattering rate from the excitated state scales as $1/\Delta^2$ [108, 109]. Consequently, as the off-resonant scattering rate drops quadratically with detuning, while the effective Rabi frequency decreases linearly with it, the ratio $\Gamma/\Omega_{\text{eff}}$ can be minimized by detuning further from the excited state. However, high laser power densities may be necessary in order to sustain sufficient coupling strengths at large detunings.

3.2.2 Coupling Internal and Motional States

Coupling the electronic and motional states of an ion forms the basis for many important tools commonly used in trapped-ion experiments, such as laser cooling and creating entangling interactions. For creating entanglement, precise control over the ions' motion is required, meaning that the ion must first be laser-cooled to sufficiently low temperatures. Here, a fundamental requirement is that a quantized description of the ion motion is applicable, the ion being represented by a quantum harmonic oscillator whose energy states represent the phonon occupation. Additionally, the approximations which are made in this section rely on more stringent requirements. In this context, the Lamb-Dicke parameter constitutes an important metric, defining the relevant temperature regime and additionally quantifying the coupling between a laser and the ion motion.

For a single ion the Lamb-Dicke parameter is defined as

$$\eta = |\vec{k_l}| x_0 \cos(\vartheta) = |\vec{k_l}| \sqrt{\frac{\hbar}{2m\omega}} \cos(\vartheta) \tag{3.34}$$

[26] In reality, the energy shifts on the atomic levels due to the AC Stark effect, induced by off-resonant driving, have to be considered.

[27] In a real atom, with more energy states, all possible decay channels have to be considered.

where m is the mass of the ion, that is confined in a harmonic potential characterized by the trap frequency ω, x_0 represents the extent of the wave packet of the ion's harmonic motion in the ground state and ϑ is the angle between the laser's wavevector and the axis of oscillation of the ion. The Lamb-Dicke approximation is valid when the ion's wave packet is much smaller than the laser wavelength, quantified by the condition

$$\eta^2(2\bar{n}+1) \ll 1, \tag{3.35}$$

with $\bar{n}$ being the mean phonon number present in the system. In this regime, coupling between the laser and ion motion is simplified to single quanta dynamics, meaning that transitions which change the number of phonons by more than one are suppressed. While the condition $\eta^2(2\bar{n}+1)$ should be small, it is not desired that η itself is small, as the coupling strength between the ion's motion and laser field is proportional to η, which is shown further down in this section. As η depends linearly on the wavevector and thus inversely on wavelength, there is effectively no coupling between an ion's motion for realistic trapping frequencies and long-wavelength radiation, e.g. in the RF range, while laser fields in the optical domain have a significant Lamb-Dicke parameter and thus allow for motional interactions. In order to combine the benefits of RF transitions, such as long qubit lifetimes, with the possibility of motional coupling, Raman transitions can be employed. In such a Raman process the effective wave vector is given by the difference in k vectors of the individual beams contributing to the transition:

$$\vec{k}_{\text{eff}} = \vec{k}_{l2} - \vec{k}_{l1} \tag{3.36}$$

This has to be considered in the expressions where $\vec{k}_l$ is relevant, such as ϕ_l and η.

In the following, the atom-light interaction Hamiltonians including motional coupling are derived. Additional to the Hamiltonian used in describing an atom and its coupling to a laser field in the previous section, here another term is added, representing the oscillation of an ion in the trap in terms of one of the harmonic motional modes at frequency ω. The Hamiltonian describing the energy of an ion in the trap is thus given by

$$\hat{H}_{\text{atom, trap}} = \frac{\hbar\omega_0}{2}\hat{\sigma}_z + \hbar\omega\left(\hat{a}^\dagger\hat{a} + \frac{1}{2}\right), \tag{3.37}$$

where $\hat{a}$ and $\hat{a}^\dagger$ are the annihilation and creation operators which lower or increase the number of phonons in the mode by one. The interaction Hamiltonian for a trapped ion is given by

$$\hat{H}_{\text{int}} = \hbar\frac{\Omega}{2}\left(e^{i\chi}\hat{\sigma}_+ e^{i\eta\left(\hat{a}e^{-i\omega t}+\hat{a}^\dagger e^{i\omega t}\right)} + h.c.\right) \tag{3.38}$$

where $h.c.$ represents the hermitian conjugate. For typical experimental situations, where $\bar{n} < 20$, the exponential in eq. 3.38 can be approximated via a Taylor-expansion

$$e^{i\eta\left(\hat{a}e^{-i\omega t}+\hat{a}^\dagger e^{i\omega t}\right)} \approx 1 + i\eta\left(\hat{a}e^{-i\omega t} + \hat{a}^\dagger e^{i\omega t}\right), \tag{3.39}$$

which allows the interaction Hamiltonian to be expressed as

$$\hat{H}_{\text{int}} = \hbar\frac{\Omega}{2}\Big(e^{i\chi}\hat{\sigma}_+\Big(1 + i\eta\Big(\hat{a}e^{-i\omega t} + \hat{a}^\dagger e^{i\omega t}\Big)\Big) + h.c.\Big). \tag{3.40}$$

Considering a resonant laser beam where $\Delta = 0$ and performing a rotating wave approximation, yields a Hamiltonian of a similar form as given in sec. 3.2.1, i.e.

$$\hat{H}_{\text{car}} = \hbar\frac{\Omega}{2}\Big(e^{i\phi_l}\hat{\sigma}_+ + e^{-i\phi_l}\hat{\sigma}_-\Big). \tag{3.41}$$

This Hamiltonian describes "carrier transitions", which leave the motional state unchanged and couple $|1, n\rangle \longleftrightarrow |0, n\rangle$. Previously, when evaluating matrix elements, the motional state was not considered, and the coupling strength was assumed to be independent of the motional quantum number. However, when including the motional state of the ion in the calculation, a dependence of the coupling strength on the motional quantum number n has to be considered. For example, when the Hilbert space is restricted to the two-dimensional subspace spanned by the states $|1, n\rangle$ and $|0, n\rangle$, the coupling strength effectively scales as $\Omega_n = (1 - \eta^2 n)\Omega_0$, where Ω_0 is the coupling strength at $n = 0$.

"Sideband transitions", which are detuned from the carrier by the trap frequency, allow for the description of operations that simultaneously manipulate an ion's internal states as well as motional degrees of freedom. A red sideband transition, detuned by $\Delta = -\omega$ from the carrier, couples $|1, n\rangle \longleftrightarrow |0, n-1\rangle$. As the detuning in this case corresponds exactly to the energy of a phonon, one quantum of motion is annihilated every time the ion is excited[28]. Applying a rotating wave approximation, the Hamiltonian describing the red sideband transition can be written as

$$\hat{H}_{\text{red}} = i\hbar\eta\frac{\Omega}{2}\Big(e^{i\phi_l}\hat{a}\hat{\sigma}_+ - e^{-i\phi_l}\hat{a}^\dagger\hat{\sigma}_-\Big). \tag{3.42}$$

Here, the states $|1, n\rangle \longleftrightarrow |0, n-1\rangle$ are coupled with an effective coupling strength that scales as $\Omega_{n,n-1} = \eta\sqrt{n}\Omega_0$. Equivalently, a blue sideband transition can be driven, where one phonon is added in the process, requiring a positive laser detuning of $\Delta = \omega$ from the carrier. The Hamiltonian for blue sideband transitions is given by

$$\hat{H}_{\text{blue}} = i\hbar\eta\frac{\Omega}{2}\Big(e^{i\phi_l}\hat{a}^\dagger\hat{\sigma}_+ - e^{-i\phi_l}\hat{a}\hat{\sigma}_-\Big), \tag{3.43}$$

Here, when coupling states $|1, n\rangle \longleftrightarrow |0, n+1\rangle$, the coupling strength effectively scales as $\Omega_{n,n+1} = \eta\sqrt{n+1}\Omega_0$. Figure 3.4 shows the three different resonances in a diagram.

[28] This forms the basis of resolved sideband cooling, as explained in sec. 3.3.3.

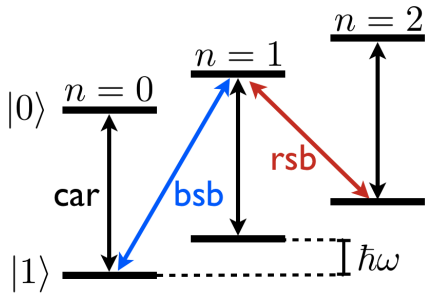

Figure 3.4: Carrier (car), red sideband (rsb) and blue sideband (bsb) transitions: The top levels represent the excited state whereas the bottom levels represent the ground state of the qubit for different motional states with n phonons. The energy difference between the motional states correponds to the detuning required to drive sideband transitions.

3.2.3 Entangling Interactions

This section describes theory on creating entangling interactions within an ion Coulomb crystal in the electronic degrees of freedom of the ions, via coupling to the harmonic modes of motion of the crystal. First, the Mølmer-Sørensen (MS) interaction of the form $\hat{\sigma}_x\hat{\sigma}_x$ is introduced, describing the simple model of two ions coupled via a single vibrational mode [110]. The model is then extended to multiple ions, still coupled via a single vibrational mode. For this type of interaction the interaction range is infinite, meaning that all ions in the crystal couple to each other with the same strength. This provides a benefit in contrast to other experimental platforms in quantum information science, where all-to-all connectivity cannot be directly implemented. The MS interaction requires a bichromatic laser field with symmetric detunings from the red and blue motional sidebands to illuminate the ions. However, by introducing an additional asymmetric detuning of the laser frequencies with respect to the red and blue sidebands, it is possible to create transverse-field Ising-type and XY-type interactions, as relevant in the context of spin models (see sec. 2.5.2.). Additionally, in the experiments presented in this thesis, rather than coupling to a single vibrational mode of an ion crystal, the bichromatic laser field couples to many modes at the same time [29], which allows interactions to be realized ranging from all-to-all couplings to couplings whose strengths decay algebraically with the distance between the ions.

Mølmer-Sørensen interaction

In the case of two qubits, the state $|11, n\rangle$ is initially prepared with the ions sharing a motional excitation of n phonons in the trap[30]. The bichromatic laser field driving the interaction consists of two superimposed frequencies with symmetric positive and negative detuning from the carrier transition. The two frequencies of the light are chosen near the first red and blue sideband, respectively, as $\nu \pm \omega \pm \delta$ where ν is the carrier transition frequency, ω is the trap frequency and δ is a detuning from the sideband frequencies. In the following, we consider the interaction to be me-

[29] In particular, the laser field couples off-resonantly to all of the out-of-plane motional modes of our planar crystals.
[30] Typically, the ions are cooled as close as possible to their motional ground state, i.e. $\bar{n} \approx 0$.

diated via the center-of-mass mode of motion. For a single ion, interaction with the bichromatic light field is described by the Hamiltonian

$$\begin{aligned}\hat{H}_{\text{bic}} = \hat{H}_{\text{red}} + \hat{H}_{\text{blue}} = i\hbar\eta\frac{\Omega}{2}\left(\left(e^{i\phi_r}\hat{a}\hat{\sigma}_+ - e^{-i\phi_r}\hat{a}^\dagger\hat{\sigma}_-\right) + \left(e^{i\phi_b}\hat{a}^\dagger\hat{\sigma}_+ - e^{-i\phi_b}\hat{a}\hat{\sigma}_-\right)\right) = \\ = \hbar\eta\frac{\Omega}{2}\left(\left(e^{i(\phi_r+\frac{\pi}{2})}\hat{a}\hat{\sigma}_+ + e^{-i(\phi_r+\frac{\pi}{2})}\hat{a}^\dagger\hat{\sigma}_-\right) + \left(e^{i(\phi_b+\frac{\pi}{2})}\hat{a}^\dagger\hat{\sigma}_+ + e^{-i(\phi_b+\frac{\pi}{2})}\hat{a}\hat{\sigma}_-\right)\right) = \\ = \hbar\eta\frac{\Omega}{2}\left((\hat{a}+\hat{a}^\dagger)\left(\hat{\sigma}_x\cos\left(\frac{\phi_b-\phi_r}{2}\right)\cos\left(\frac{\phi_r+\phi_b+\pi}{2}\right) - \hat{\sigma}_y\cos\left(\frac{\phi_b-\phi_r}{2}\right)\sin\left(\frac{\phi_r+\phi_b+\pi}{2}\right)\right)\right. \\ \left. + i(\hat{a}^\dagger-\hat{a})\left(\hat{\sigma}_x\sin\left(\frac{\phi_b-\phi_r}{2}\right)\cos\left(\frac{\phi_r+\phi_b+\pi}{2}\right) - \hat{\sigma}_y\sin\left(\frac{\phi_b-\phi_r}{2}\right)\sin\left(\frac{\phi_r+\phi_b+\pi}{2}\right)\right)\right)\end{aligned} \tag{3.44}$$

where $\phi_r = \phi_l + \delta t$ and $\phi_b = \phi_l - \delta t$. Here, the coupling strengths of the red and blue sideband Hamiltonians are assumed to be equal and are denoted by Ω. In the case of $\phi_r + \phi_b = \pi$, equation 3.44 simplifies to

$$\hat{H}_{\text{bic}} = -\hbar\eta\frac{\Omega}{2}\left((\hat{a}+\hat{a}^\dagger)\cos(\delta t)\hat{\sigma}_x + i(\hat{a}^\dagger-\hat{a})\sin(\delta t)\hat{\sigma}_x\right) = -\hbar\eta\frac{\Omega}{2}\left(\hat{a}^\dagger e^{-i\delta t} + \hat{a}e^{i\delta t}\right)\hat{\sigma}_x. \tag{3.45}$$

Extending this expression to two qubits leads to the MS Hamiltonian

$$\hat{H}_{\text{MS}}^{2\text{ qubits}} = -\hbar\eta\frac{\Omega}{2}\left(\hat{a}^\dagger e^{-i\delta t} + \hat{a}e^{i\delta t}\right)\hat{S}_x \tag{3.46}$$

where $\hat{S}_x = \sigma_x^{(1)} + \sigma_x^{(2)}$. The time evolution under this Hamiltonian is given by

$$\begin{aligned}\hat{U}(t) = e^{-\frac{i}{\hbar}\int_0^t \hat{H}_{\text{MS}}(t')\mathrm{d}t'} = \lim_{m\to\infty}\prod_{j=1}^{m} e^{-\frac{i}{\hbar}\hat{H}(j\Delta t)\Delta t} = \\ \lim_{m\to\infty}\hat{D}\left(-i\eta\frac{\Omega}{2}e^{-i\delta\frac{t}{m}}\hat{S}_x\right)\cdot\ldots\cdot\hat{D}\left(-i\eta\frac{\Omega}{2}e^{-i\delta t}\hat{S}_x\right)\end{aligned} \tag{3.47}$$

where $\Delta t = \frac{t}{m}$, and the displacement operator $\hat{D}(\alpha) = e^{\alpha\hat{a}^\dagger - \alpha^*\hat{a}}$ has been defined. This operator describes the displacement in phase space of the harmonic oscillator representing the motion of the two-ion crystal, e.g. the center of mass mode, by an amount α. Using the Baker-Campbell-Hausdorff formula $\hat{D}(\alpha)\hat{D}(\beta) = \hat{D}(\alpha+\beta)e^{i\Im(\alpha\beta^*)}$, where $\Im$ denotes the imaginary part, the unitary evolution in eq. 3.47 can be represented by

$$\begin{aligned}\hat{U}(t) = \hat{D}\left(-\int_0^t i\eta\frac{\Omega}{2}e^{-i\delta t'}\mathrm{d}t'\hat{S}_x\right)e^{-i\Im\left(\int_0^t \eta\frac{\Omega}{2}e^{-i\delta t'}\mathrm{d}t'\int_0^{t'}\eta\frac{\Omega}{2}e^{i\delta t''}\mathrm{d}t''\hat{S}_x^2\right)} = \\ \hat{D}\left(\eta\frac{\Omega}{2\delta}(e^{-i\delta t}-1)\hat{S}_x\right)e^{-i\eta^2\frac{\Omega^2}{4}\Im\left(\frac{t}{i\delta}-\frac{e^{-i\delta t}-1}{\delta^2}\right)\hat{S}_x^2} = \\ \hat{D}\left(\eta\frac{\Omega}{2\delta}(e^{-i\delta t}-1)\hat{S}_x\right)e^{-i\eta^2\frac{\Omega^2}{4\delta^2}(\sin(\delta t)-\delta t)\hat{S}_x^2}.\end{aligned} \tag{3.48}$$

This evolution represents an off-resonantly driven harmonic oscillator, which, in analogy to the classical case, returns to its initial state after times $t = N\frac{2\pi}{|\delta|}$, where $N \in \mathbb{N}$. At these times eq. 3.48 reduces to

$$\hat{U}(t = N\frac{2\pi}{\delta}) = \hat{D}(0)e^{i\eta^2\frac{\Omega^2}{4\delta^2}2\pi N\,\mathrm{sign}(\delta)\hat{S}_x^2} = e^{i\eta^2\frac{\Omega^2}{4\delta^2}2\pi N\,\mathrm{sign}(\delta)\hat{S}_x^2}. \tag{3.49}$$

As $\hat{S}_x^2 = (\hat{\sigma}_x^{(1)} + \hat{\sigma}_x^{(2)})^2 = (\hat{\sigma}_x^{(1)})^2 + (\hat{\sigma}_x^{(2)})^2 + 2\hat{\sigma}_x^{(1)}\hat{\sigma}_x^{(2)} = 2\mathbb{1}^{(1)}\mathbb{1}^{(2)} + 2\hat{\sigma}_x^{(1)}\hat{\sigma}_x^{(2)}$, the effective Hamiltonian describing the dynamics can then be written as

$$\hat{H}_{\text{eff}} = -\hbar J\hat{\sigma}_x^{(1)}\hat{\sigma}_x^{(2)}, \tag{3.50}$$

the time evolution under this Hamiltonian creating an entangled state as shown in sec. 2.4.2. Here,

$$2\pi J = 2\pi\eta^2\frac{\Omega^2}{2\delta^2}\mathrm{sign}(\delta) \tag{3.51}$$

is the effective coupling strength of the entangling interaction[31].

The phase space diagram offers a convenient way of visualizing the MS interaction. To see how the qubit states evolve in phase space, the single-qubit case is first considered: The ground state of a single qubit is given by a product state of the electronic ground state $|1\rangle$ and the motional ground state or vacuum state $|\text{vac.}\rangle$ and can be written in the $|+\rangle_x/|-\rangle_x$ basis as

$$|1\rangle|\text{vac.}\rangle = \frac{1}{\sqrt{2}}(|+\rangle_x - |-\rangle_x)|\text{vac.}\rangle \tag{3.52}$$

where the states $|+\rangle_x$ and $|-\rangle_x$ are the electronic eigenstates of the displacement operator. The displacement from a bichromatic light field generates a motional Schrödinger cat state

$$\hat{D}(\alpha)|1\rangle|\text{vac.}\rangle = \frac{1}{\sqrt{2}}(|+\rangle_x|\alpha\rangle - |-\rangle_x|-\alpha\rangle) \tag{3.53}$$

where the coherent states $|\alpha\rangle$ and $|-\alpha\rangle$ are entangled with the internal qubit states $|+\rangle_x$ and $|-\rangle_x$. In fig 3.5a and b the phase space diagram[32] in a rotating reference frame is provided for the resonant case where $\hat{H} \propto (\hat{a} + \hat{a}^\dagger)\hat{\sigma}_x$ and the off-resonant case where $\hat{H} \propto (\hat{a}e^{i\delta t} + \hat{a}^\dagger e^{-i\delta t})\hat{\sigma}_x$, respectively. In the off-resonant case the displacement results in a circular trajectory (analogous to the trajectory of an off-resonantly driven harmonic oscillator) with the oscillator returning to its initial state after a certain time. In the two qubit case, the MS interaction, mediated via the center-of-mass mode, leads to the two states $|++\rangle_x$ and $|--\rangle_x$ being entangled with the motion. This is illustrated again in a rotating reference frame in fig. 3.5c, where these states exhibit a circular trajectory in phase space and return to their original state at $t = n\frac{2\pi}{|\delta|}$, at which point the internal

[31] In the following, J is used generally to represent spin-spin coupling strength, but may require different pre-factors depending on the exact scenario.

[32] The momentum p and location x are the imaginary and real part of α.

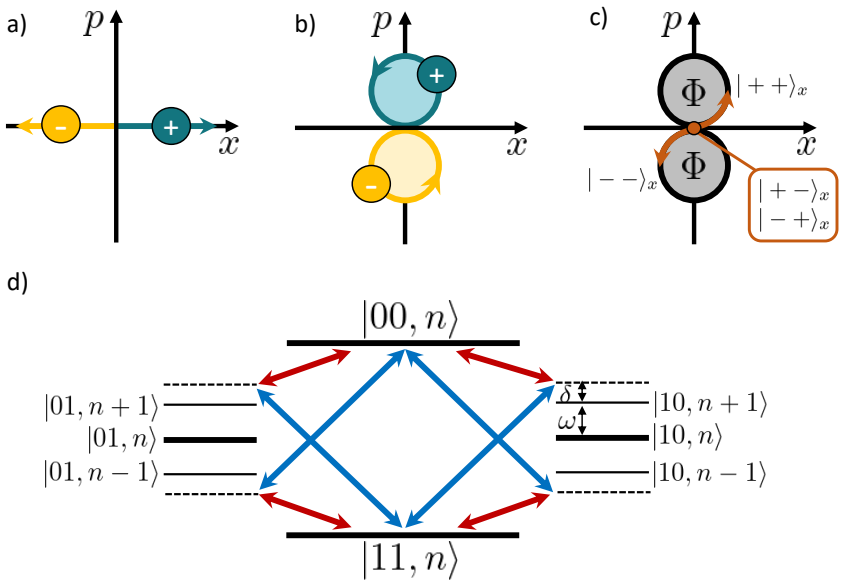

Figure 3.5: Visualization of the MS interaction: Displacement in phase space of the states $|+\rangle_x$ (bluegreen) and $|-\rangle_x$ (orange) in a rotating reference frame: a) In the resonant case, in the context of the bichromatic laser field being resonant with the motional sidebands, the two states are displaced in opposite directions in phase space, analogous to a resonantly driven harmonic oscillator. b) In the off-resonant case the states exhibit a circular trajectory in phase space analogous to an off-resonantly driven harmonic oscillator. c) The illustration presents the phase space diagram of the evolution under the MS interaction as derived in eq. 3.48, for two ionic qubits. The states $|++\rangle_x$ and $|--\rangle_x$ are displaced in phase space and pick up a geometric phase as given in eq. 3.54, eventually returning to the initial state after a time $t = n\frac{2\pi}{|\delta|}$. The states $|+-\rangle_x$ and $|-+\rangle_x$, on the other hand, remain stationary. d) The MS interaction for two qubits can also be visualized via the energy levels relevant in the process. The transition from $|11\rangle$ to $|00\rangle$ can be driven via the intermediate states $|01, n \pm 1\rangle$ and $|10, n \pm 1\rangle$.

and motional states become disentangled again. The area enclosed by the trajectory corresponds to a geometric phase

$$\Phi(t) = -\eta^2 \frac{\Omega^2}{4\delta^2}(\sin(\delta t) - \delta t) \tag{3.54}$$

which is picked up by these states. On the other hand, the states $|+-\rangle_x$ and $|-+\rangle_x$ do not couple to the motion. The displacement in phase space in opposite directions of the $|+\rangle_x$ and $|-\rangle_x$ states results in the trajectory of $|+-\rangle_x$ and $|-+\rangle_x$ being stationary. No phase is accumulated as the enclosed area equals zero. This scenario corresponds to a conditional phase gate.

The MS interaction can also be visualized considering the different interaction paths that connect the states $|11\rangle$ and $|00\rangle$, which are shown in 3.5d. When the bichromatic laser field acts on the qubits, the transition from $|11\rangle$ to $|00\rangle$ can be driven via the intermediate states $|01, n \pm 1\rangle$ and $|10, n \pm 1\rangle$. If the detuning δ is sufficiently large but still small enough so that coupling to other motional modes is prevented, population of the intermediate states (i.e. the generation of phonons) is negligible.

The derivation of the MS interaction for two ions can be generalized to an arbitrary number of ions N by exchanging $\hat{S}_x$ with $\hat{S}_x^N = \sum_{i=1}^N \hat{\sigma}_x^{(i)}$. This results in a unitary of the form

$$\hat{U}(t = n\frac{2\pi}{|\delta|}) = e^{i\eta^2 \frac{\Omega^2}{4\delta^2} 2\pi n \,\mathrm{sign}(\delta) \sum_{i\neq j} \hat{\sigma}_x^{(i)} \hat{\sigma}_x^{(j)}}. \tag{3.55}$$

Transverse-Field Ising Model and XY-Hamiltonian

Section 2.5.2 introduced the transverse field Ising and XY-Hamiltonian, which are relevant in the context of spin models. While it has been shown in the previous subsection that the MS interaction allows for couplings of the type $\hat{\sigma}_x\hat{\sigma}_x$, this interaction has to be modified in order to realize the desired spin Hamiltonians. In order to achieve this, an additional detuning is introduced that is asymmetric with respect to the red and blue motional sidebands, called center-line detuning δ_c. Here, we still consider the case of coupling to a single motional mode of the ion crystal, where the detuning from the red and blue sidebands is now given by $\nu \pm (\omega + \delta) + \delta_c$ with $\delta \gg \delta_c$.

The relevant derivations are presented in detail in [111], here only the most important steps are discussed. In analogy to the previous section, an effective Hamiltonian for a single ion in a bichromatic light field with center-line detuning can be derived in rotating wave approximation:

$$\hat{H}_{\mathrm{bic},\delta_c} = -\hbar\eta\frac{\Omega}{2}(\hat{a}e^{i\delta t} + \hat{a}^\dagger e^{-i\delta t})(\hat{\sigma}_+ e^{-i\delta_c t} + \hat{\sigma}_- e^{i\delta_c t}) \tag{3.56}$$

For multiple ions, considering equal coupling for all of them via the center-of-mass mode, the interaction Hamiltonian is then given by

$$\hat{H}^N_{\mathrm{bic},\delta_c} \propto -\hbar\eta\frac{\Omega}{2}(\hat{a}e^{i\delta t} + \hat{a}^\dagger e^{-i\delta t})(\hat{S}_+ e^{-i\delta_c t} + \hat{S}_- e^{i\delta_c t}) \tag{3.57}$$

where $\hat{S}_\pm = \sum_i^N \hat{\sigma}_\pm^{(i)}$ are the collective spin operators for N ions. Under the assumption that $\eta\Omega \gg \delta$, i.e. the adiabatic limit is considered where the coupling strength on the motional sideband is much weaker than the detuning from it, the previous expression leads (see appendix B1 of [111]) to the Hamiltonian

$$\hat{H}_{\text{Spin-Spin}} = \frac{J}{2}\sum_{i,j}^{N}(\hat{\sigma}_+^{(i)}\hat{\sigma}_+^{(j)}e^{-2i\delta_c t} + \hat{\sigma}_+^{(i)}\hat{\sigma}_-^{(j)} + \hat{\sigma}_-^{(i)}\hat{\sigma}_+^{(j)} + \hat{\sigma}_-^{(i)}\hat{\sigma}_-^{(j)}e^{2i\delta_c t}). \tag{3.58}$$

A major difference to the MS interaction can be seen when considering the phase space picture as previously. In the present case, the circular trajectory in phase space is small, which means that the internal and motional states of the ions are essentially disentangled during the entire dynamics, not just at the fixed gate time which corresponds to the circular trajectory having returned to its origin.

For $\delta_c = 0$ we recover the MS-Hamiltonian and for $\delta_c \neq 0$ we distinguish two different regimes in which different types of interactions manifest: For $\delta_c \approx J$ the transverse field Ising Hamiltonian

$$\hat{H}_{\text{Ising}} = \hbar J \sum_{i,j}^{N} \hat{\sigma}_x^{(i)} \hat{\sigma}_x^{(j)} + B \sum_i \hat{\sigma}_z^{(i)} \tag{3.59}$$

emerges after transforming into the interaction picture with respect to the Hamiltonian $B \sum_i \hat{\sigma}_z^{(i)}$, where $B = \delta_c/2$ represents an effective magnetic field. On the other hand, when $\delta_c \gg J$, a rotating wave approximation can be applied to neglect terms oscillating at δ_c. This leads to the XY-Hamiltonian

$$\hat{H}_{\text{XY}} = \hbar J \sum_{i,j}^{N} (\hat{\sigma}_+^{(i)} \hat{\sigma}_-^{(j)} + \hat{\sigma}_-^{(i)} \hat{\sigma}_+^{(j)}). \tag{3.60}$$

As discussed previously in sec. 2.5.2, approximation by this Hamiltonian is valid only in each subspace with fixed magnetization and considering the entire Hilbert space requires the transverse field term to be added.

Tunable-Range Entangling Interactions

In sec. 3.2.3 a general method for creating entanglement across an ion crystal was presented, where a single motional mode, specifically the center-of-mass mode, was employed to mediate the interaction between ions. In this way, an infinite range entangling interaction is established, where all ions are coupled in an equal way to all other ions in the Coulomb crystal. On the other hand, coupling to multiple motional modes at the same time, and thus driving several MS interactions in parallel, allows for more complex entangled states to be created. Effectively, this type of coupling between the bichromatic light field and many motional modes leads to an interaction with tunable range. Here, the range, quantified by the coupling strength J_{ij}, depends on the laser detuning δ from the M motional sidebands which are at frequencies ω_M. More specifically, the coupling between the two ions i and j within a Coulomb crystal is given by [112]

$$J_{ij} = \frac{\Omega^2 \hbar k^2}{4m} \sum_M \frac{b_{i,M} b_{j,M}}{(\omega + \delta)^2 - \omega_M^2}, \tag{3.61}$$

where the Rabi frequency of ion i and j are assumed equal and $b_{i,M} b_{j,M}$ are the eigenvectors of the motional modes, which are contained in the Lamb-Dicke parameter. As before, $\omega + \delta$ represents the laser detuning from the carrier transition. While for the situation considered so far, where coupling was mediated by the center-of-mass mode, with an equal Lamb-Dicke parameter for all ions, here we have to consider the ion i and mode M specific Lamb-Dicke parameters, modified from the expression in eq. 3.34 to

$$\eta_{i,M} = \vec{k} \cdot \vec{b}_{i,M} \sqrt{\frac{\hbar}{2m\omega_M}}. \tag{3.62}$$

The coupling strength between ions can be approximated as a power law with respect to $|i-j|$, i.e. the distance between them:

$$J_{ij} \propto \frac{1}{|i-j|^{\alpha}} \tag{3.63}$$

Here, α represents the interaction range, which can be tuned by changing the detuning of the laser beam with respect to the motional modes. This effectively modifies the relative contribution of each mode to the coupling with the two extreme cases emerging in the limits of small and large δ: For small δ the laser couples mainly to the center-of-mass mode, recovering the effect of the MS interaction where $\alpha = 0$. On the other hand, when δ is large, the laser couples to all motional modes (e.g. all radial modes in 1D Coulomb crystals or all out-of-plane modes in planar Coulomb crystals) equally, leading to an effective dipolar interaction where $\alpha \approx 3$[33].

3.3 Controlling $^{40}Ca^{+}$ Ions in our Apparatus

The previous sections introduced experimental tools, relevant when employing trapped ions as a platform for experiments in quantum information science. The present section focuses on how these building blocks are combined in our experimental apparatus with the goal to establish quantum control over planar ion Coulomb crystals consisting of $^{40}Ca^{+}$ ions. The section introduces the relevant electronic level scheme of $^{40}Ca^{+}$, our approach to loading ions into the trap and laser-cooling them to different temperature regimes. Information is given on how a physical qubit is encoded into each $^{40}Ca^{+}$ ion, and how these ionic qubits are manipulated. The section further presents relevant characterization tools to determine ion temperature and coherence time and concludes with our approach to implement tunable-range spin-spin interactions in planar ion crystals. The focus here is on presenting concepts and tools, with the specific technical implementations to be found in the subsequent chapter.

3.3.1 Atomic Structure of $^{40}Ca^{+}$

Atoms used for ion trapping are typically of the alkaline-earth kind, found in group two of the periodic table. When singularly-ionized, a single outer valence electron remains attached to the atom, giving rise to a comparatively simple hydrogen-like structure. The energy states of this valence electron can be manipulated for different purposes e.g. using laser fields. While two long-lived states have proven suitable for the implementation of a physical qubit, short-lived states may e.g. be used for laser cooling. One of the leading ionic species in experimental quantum information science is $^{40}Ca^{+}$, with numerous state-of-the art experiments carried out in Innsbruck and other research groups around the world in the past decades. Figure 3.6 provides an overview of the electronic energy levels of $^{40}Ca^{+}$ that are relevant in our experiments. These states are described via the notation $n^{2s+1}l_j$ where n represents the principal quantum number, s the absolute value of the spin of the electron, l the orbital angular momentum and $j = |l \pm s|$. A magnetic field of a few Gauss lifts the degeneracy of the Zeeman manifold and establishes a quantization axis, defining requirements in terms of laser beam direction and polarization for driving transitions

[33] Note, that those extreme cases are difficult to achieve experimentally.

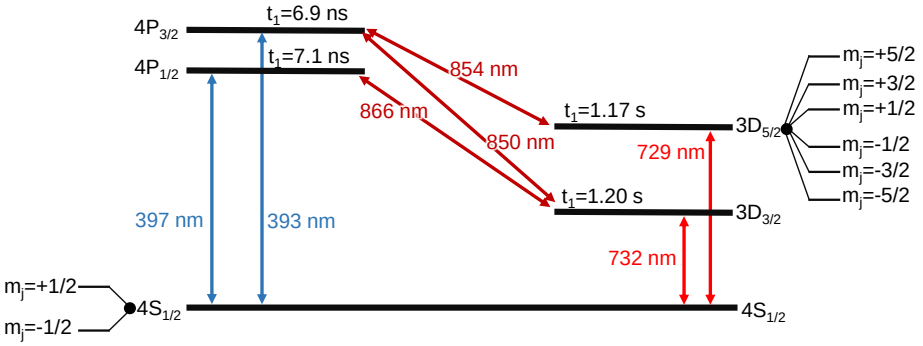

Figure 3.6: Electronic levels of $^{40}Ca^{+}$ used in our experiments: A qubit is encoded either in the $4^2S_{1/2}$ ground state and the $3^2D_{5/2}$ metastable excited state (optical qubit), or the two Zeeman states of the $4^2S_{1/2}$ ground state manifold. State detection as well as Doppler cooling is performed on the electric dipole transition $4^2S_{1/2} \longleftrightarrow 4^2P_{1/2}$ at 397 nm with repump laser at 854 nm and 866 nm which remove population from the long lived $3^2D_{3/2}$ and $3^2D_{5/2}$ states by coupling them to $4^2P_{1/2}$ and $4^2P_{3/2}$, respectively. Ground state cooling is either performed on the optical qubit transition (sideband cooling) or blue detuned from the 397 nm transition (EIT cooling). Furthermore, the optical qubit transition is used for optical pumping to initialize a qubit state at the beginning of an experiment. The lifetimes t_1 of the excited states are taken from [113] (D states) and [114] (P states).

selectively [34]. The Zeeman splitting is illustrated in fig. 3.6 for the relevant D and S levels, showing the possible values of the magnetic quantum number m_j. For the magnetic field strengths typically applied in the experiment, a frequency splitting of the states on the order of MHz is obtained. The following subsections provide information on the use of the individual transitions illustrated in fig. 3.6 in the experiment. However, a short summary is also provided in the figure caption.

3.3.2 Ion Loading

Several different methods exist for loading ions into a RF trap, commonly involving neutral atoms to be brought into the vicinity of the trap center where they are ionized and subsequently caught in the trapping potential. A relatively simple approach involves resistively heating a piece of material, in our case calcium, causing it to evaporate into the trapping region. The loading process by such an atomic oven has several disadvantages, such as it being generally slow[35] and correlating with insufficient control over the ion number. The amount of calcium that is evaporated relates to the current that is applied to the oven, but the process remains stochastic. Given our work with large ion Coulomb crystals, a deterministic and fast loading scheme is crucial. Here, laser ablation emerges as a simple solution. In this approach, a pulsed laser vaporizes material from a solid

[34] Due to the electronic levels' sensitivity to magnetic fields, decoherence may arise from magnetic field noise. Thus, it is crucial to establish a well-controlled and stable magnetic field environment on long and short timescales (see also sec. 4.3).

[35] Another team in our research group working with long strings of ions has experienced extended loading times of up to half an hour for Coulomb crystals of few tens of particles. Given the need for repetition of the loading process at least once a day in their setup, this poses a severe limitation in efficiency.

target, the particles flying into the trapping region. If the power of the ablation pulse is above a certain threshold, this process already ionizes the calcium atoms. However, it is desirable to work at lower powers, such that predominantly neutral atoms are ablated, which are then ionized in an isotope-selective way. Then, no ionic species other than $^{40}Ca^{+}$ is loaded into the trap. In our case, the ablated calcium atoms are photo-ionized via two laser beams that propagate through the trap center: A 422 nm laser couples one of the valence electrons on a cycling transition to an excited state (not shown in fig. 3.6), from which the electron is detached by 375 nm laser light. As described in sec. 4.4.3, which also presents further technical details, this method of loading, in combination with precise control over the trapping potential, allows ion Coulomb crystal with desired ion numbers to be loaded on a timescale of about one minute, such that preparation time for experiments remains low.

3.3.3 Laser Cooling

Laser cooling forms the basis of achieving precise quantum control over the ions in the trap. It allows them to transition from their initial thermal motion, ions at room temperature exhibiting speeds of few hundred meters per second, to temperatures in the mK range, at which point they are frozen into an ion Coulomb crystal. The requirement for such low temperatures extends beyond spatial localization of the ions, but is necessary for high-fidelity manipulation of the ions' quantum states. For example, a laser driving an electronic transition may couple to a wide thermal distribution of motional states with varying coupling strengths, resulting in damping of Rabi oscillations when averaging over many experiments. This means that at some point population cannot be transferred with high fidelity between the qubit basis states anymore. More stringent requirements to the ions' temperature arise in the context of entangling interactions. Here, the ions must remain close to the ground state of motion in the modes employed for the interaction, for the Lamb-Dicke approximation to hold during the entire dynamics. A variety of cooling techniques is available for trapped ions, addressing different temperature regimes. For a hot (thermal) ion, Doppler cooling is employed, which allows ions to crystallize and remain in the Lamb-Dicke regime. Ground-state cooling methods such as sideband cooling and electromagnetically-induced transparency (EIT) cooling allow the motion in particular mode(s) to be frozen out completely, bringing the ions into the motional ground state with high probability. How these cooling techniques are applied in our experimental system is explained in the following subsections.

A prerequisite for the success of these cooling processes is the overlap of the cooling laser beam with the direction of motion to be cooled. Trapped ions can be Doppler-cooled with a single beam given that it overlaps with all three directions of motion simultaneously[36]. In ground-state cooling, where typically only a specific set of motional modes is targeted, the lasers need to be set up to align with the respective direction(s). Information regarding the cooling beam geometry with respect to the ion crystal plane as well as the optical setups is presented in the subsequent chapter (see in particular fig. 4.9 and sec. 4.4.4).

[36] However, it has been demonstrated in our apparatus, that in planar crystals it is sufficient for the cooling laser to have overlap with only two directions (see sec. 4.4.4).

Doppler Cooling

Doppler cooling effectively lowers the ions' temperature by scattering many off-resonant photons, necessitating a short-lived and closed cycling transition. In our experiments with $^{40}Ca^{+}$ the $4^2S_{1/2} \longleftrightarrow 4^2P_{1/2}$ dipole transition is selected for this purpose, where the excited state has a lifetime of about $t_1 = 7.1$ ns [114]. The 397 nm laser coupling the cooling transition is red-detuned, such that ions moving towards the laser beam become more resonant with the light, absorb a photon, and scatter it in an arbitrary direction during the spontaneous decay process. In this way, a net cooling effect emerges when averaging over many absorption-emission cycles, with the minimum achievable temperature set by the Doppler limit, where heating and cooling mechanisms are in equilibrium. For a $^{40}Ca^{+}$ ion confined at a trap frequency of $\omega = 1$ MHz and Doppler cooled at 397 nm, the minimum achievable mean phonon number is about 10 phonons [115][37].

In order to establish continuous cooling, the transition needs to be closed, meaning that the electron spontaneously decays exclusively back to the $4^2S_{1/2}$ ground state. However, there is a small probability for the electron to end up in the long-lived $3^2D_{3/2}$ state, which interrupts the cooling process. Thus, a "repump" laser at 866 nm, coupling the $3^2D_{3/2} \longleftarrow 4^2P_{1/2}$ states, returns the electron into the cooling cycle. Moreover, a 854 nm laser repumps electronic population from the $3^2D_{5/2}$ by establishing a coupling to the short-lived $4^2P_{3/2}$ state from which the electron decays back to the $4^2S_{1/2}$ ground state. It may be useful in certain situations to employ Doppler cooling beams at multiple frequencies, red-detuned by different amounts from the 397 nm transition. In our apparatus the "primary" Doppler cooling beam is about 10 MHz red-detuned, i.e. half the natural linewidth of the cooling transition, in order to achieve the lowest possible temperature. Introducing a second, far-red detuned beam that is resonant with faster ions can shorten the initial cooling time when loading new ions into the trap and allows for fast recrystallization after an ion crystal melts due to e.g. a collision with background gas.

The 397 nm light that is scattered by the ions serves an additional purpose in the experiment: a fluorescence signal, by which to detect the ions. The fluorescence signal not only indicates the presence of an ion but also allows for reading out the quantum state of a qubit as explained in sec. 3.3.4.

Ground-State Cooling

Once the ions are pre-cooled via means of Doppler cooling, it is possible to cool them further and bring them close to the motional ground state. Achieving such low temperatures in specific motional modes of an ion crystal is required if they are to mediate entangling interactions. In our planar crystals, the N out-of-plane motional modes are used for this purpose, necessitating them to be prepared close to the motional ground state. In our apparatus, two ground-state cooling techniques are available: resolved-sideband cooling as well as EIT cooling. Sideband cooling is generally applied to a small number of ions, as cooling is performed sequentially for each individual mode, or a few modes whose frequencies lie within the frequency range where sideband

[37] This number is based on the condition that the laser is red-detuned from the cooling transition by half the transition linewidth $\Gamma = 2\pi \cdot 21.57$ MHz. The mean phonon number $\bar{n}$ and the minimum achievable temperature T_D can be determined from the equation $k_B T_D = \hbar\Gamma/2 = \bar{n}\hbar\omega$ where k_B the Boltzmann constant, assuming a two-level system, which is not the case for $^{40}Ca^{+}$. However, considering well-chosen Doppler cooling parameters, the expected temperature should be close to $\hbar\Gamma/2$.

cooling is effective for the chosen parameters. This method thus becomes impractical for larger ion crystals and the corresponding large number of modes to be cooled. EIT cooling, on the other hand, is a multimode-cooling technique, allowing for fast and simultaneous cooling of many motional modes.

Resolved Sideband Cooling

Resolved-sideband cooling is based on the ability to couple ions on the red motional sideband, as described in sec. 3.2.2 and illustrated in fig. 3.4, by detuning the laser beam from the carrier transition by the motional frequency, effectively removing a quantum of motion in the process. In order to resolve the sidebands, a narrow transition with respect to the motional frequency has to be chosen. For this reason, e.g. the dipole transition employed for Doppler cooling is not suitable as its linewidth is larger than the typical trap frequencies. In our apparatus, resolved-sideband cooling is thus implemented on the $4^2S_{1/2} \longleftrightarrow 3^2D_{5/2}$ quadrupole transition at 729 nm. A 729 nm laser pulse will ideally take the excitation from $|S, n\rangle$ to $|D, n-1\rangle$, where n is the number of phonons. As spontaneous decay from the long-lived $3^2D_{5/2}$ state would take too long, the electronic excitation is transferred to the $4^2P_{3/2}$ ($|P, n-1\rangle$) state by an 854 nm laser pulse ("quenching"), from which the electron rapidly decays to the $|S, n-1\rangle$ state[38], enabling the cycle to start from the beginning. With every cycle the number of phonons is reduced by up to one until the specific motional mode that was addressed by the 729 nm laser is prepared in the ground state with high probability[39]. This probability is limited by heating processes which act on the ions already during the cooling process. While mean phonon numbers as low as $\bar{n} = 0.001$ [116] have been reported for a single ion, the slowness of the cooling process and the inability for multimode cooling pose a significant disadvantage of this cooling technique. Due to the weak coupling on the quadrupole transition, resolved-sideband cooling of a single motional mode requires several milliseconds of cooling time in our setup. Since every motional mode of the ion crystal requires a specific detuning of the laser to be resonant with the motional sideband transition, modes need to be cooled consecutively, previously cooled modes heating up while cooling other modes. In our apparatus, sideband cooling has been set up to cool the out-of-plane direction but has been used only once throughout this thesis, to determine the heating rate of a single ion (see sec. 5.1.2)[40]. Here mean phonon numbers on the order of $\bar{n} = 0.008$ were achieved, as shown in fig. 5.3.

Electromagnetically-Induced Transparency (EIT) Cooling

EIT cooling, which is presented in more detail in the thesis of Dominik Kiesenhofer, has been demonstrated with a single ion [103], long strings of ions [117], and 2D ion Coulomb crystals in Penning [118] and RF traps [33]. This technique offers notable advantages over resolved sideband cooling, due to it being faster and offering the possibility of cooling multiple motional modes close to the ground state at the same time. Moreover, while the temperatures achievable with EIT cooling are not as low as with sideband cooling [116], it is superior to other multimode-techniques such as polarization gradient cooling, which fails to reduce the mode temperatures to the low level possible with EIT cooling.

[38] While it is not impossible to decay back to $|S, n\rangle$ the probability to decay to $|S, n-1\rangle$ is higher than the probability to add a phonon back into the system, resulting in a net cooling effect.

[39] When the ground state is reached it is no longer possible to drive a red sideband transition.

[40] For a single ion the term out-of-plane does not have any meaning, which is why this direction is also referred to as the "strongly confined" one.

In general, EIT is an effect where a laser beam is able to propagate through a medium as if it were transparent. This relates to suppressed photon scattering, a dominant heating mechanism in other cooling schemes, and thus the ability to cool to low temperatures. EIT cooling is realized within an atomic three-level system, as described in sec. 3.2.1, with two ground states coupled to a short lived excited state. Two laser beams are thus required to implement this cooling scheme, the first of which creating dressed states due to its high intensity. When scanning the frequency of the second laser of weak intensity, a Fano-like absorption profile emerges. The shape of the Fano profile gives rise to an asymmetry in excitation probability, strongly favoring red sideband transitions to be driven over blue sidebands and suppressing excitation on carrier transitions.

In our apparatus EIT cooling is implemented in the two Zeeman sublevels of the $4S_{1/2}$ manifold, which are coupled off-resonantly via the $4P_{1/2}$ level. Thus, the 397 nm laser used for Doppler cooling is also used for EIT cooling, but at a different frequency, here blue-detuned from the $4^2S_{1/2} \longleftrightarrow 4^2P_{1/2}$ transition. A larger detuning corresponds to a lower phonon number that can be achieved, but at the same time a more narrow cooling range, limiting the frequency spread of modes that can be cooled efficiently. For our trapping parameters and an ion Coulomb crystal consisting of about 100 ions, the out-of-plane motional modes are spread in frequency by several hundreds of kHz[41]. Thus, the detuning of the EIT beams should be chosen accordingly, about 110 MHz blue-detuned from the carrier transition. In order to couple the two ground states to the $4P_{1/2}$ level, two perpendicular beams at 397 nm are used, one π polarized and one σ^- polarized beam, each having a k-vector at an angle of 45° with respect to the crystal plane. In this way, the effective k-vector aligns with the out-of-plane motional modes. The σ^- polarized light strongly couples the $4S_{1/2}$ $(m = +1/2) \longleftrightarrow 4P_{1/2}$ $(m = -1/2)$ transition, generating dressed states, while the weak π polarized probe beam couples on the $4S_{1/2}$ $(m = -1/2) \longleftrightarrow 4P_{1/2}$ $(m = -1/2)$ transition. The Fano profile has to be set at the correct frequency, corresponding to the mode(s) to be cooled, by adjusting the beam power and thus the light shift induced by the σ^- light. Here, the center of the out-of-plane mode spectrum is chosen, in order to optimize the overlap between all motional modes and the cooling range. EIT cooling results for a large planar ion crystal are presented in sec. 5.4.

Ion Thermometry

Different schemes exist for quantifying the temperature of trapped ions. At higher temperatures, where the ions are not cooled close to the motional ground state, the temperature can be estimated e.g. via determination of the Doppler-broadened linewidth of a transition. At lower temperatures information about the motional state can be mapped to the electronic state and read out via spectroscopic techniques. Here, the sideband-ratio method is widely used for estimating the mean phonon number of a single ion. The method is based on the fact that near the ground state, where mean phonon numbers are low, a strong asymmetry can be observed when measuring excitation

[41] The out-of-plane modes are the only ones relevant in this context. As they are used for mediating entangling interactions they need to be ground-state cooled. A measured frequency spectrum of these modes is presented in sec. 5.4 for a 105-ion planar crystal.

probabilities on red and blue sideband transitions, respectively. The mean phonon number $\bar{n}$ in the respective vibrational mode is given by [89]

$$\bar{n} = \frac{p_{\text{rsb}}}{p_{\text{bsb}} - p_{\text{rsb}}}, \tag{3.64}$$

where p_{rsb} (p_{bsb}) is the excitation probability on the first red (blue) motional sideband. In practice these excitation probabilities can be measured by scanning a narrow-band laser over the motional sideband frequencies and determining the sideband height via a fit. This approach is employed in sec. 5.1.2 in order to measure the heating rate of our ion trap. However, the sideband-ratio method has limitations, such as when near the ground state the red sideband excitation is barely visible, making the application of a reliable fit to the data challenging. Thus, a new thermometry method was developed [119], which is presented in detail in the thesis of Dominik Kiesenhofer. This method is based on measuring the excitation dynamics on the red and blue motional sidebands, i.e. the shape of the Rabi oscillations. Besides single ions, this method is also applicable to larger ground-state cooled ion crystals. For such cold crystals suitable methods for quantifying the temperature were previously not available, traditional methods such as the sideband-ratio scheme failing due to many-body interactions within the ion crystal.

3.3.4 Qubit Operations

In our apparatus we have the option to encode a qubit in two different ways, which we distinguish as optical qubit and ground state qubit. The two basis states $|1\rangle$ and $|0\rangle$ of the optical qubit are defined as one of the $4^2\text{S}_{1/2}(m = \pm 1/2)$ ground states and one of the $3^2\text{D}_{5/2}(m = -5/2... + 5/2)$ metastable states[42]. The excited state has a lifetime of about $t_1 = 1.168\,\text{s}$ [113], rendering this qubit a suitable choice for storing and processing quantum information, with the time it takes to perform gate operations with established methods (typically in the range of 10 to 100 μs) being significantly shorter than t_1. In order for the t_2 time not to be limited by laser phase noise, a frequency-stable 729 nm laser with a linewidth on the order of the linewidth of the quadrupole transition, i.e. about 1 Hz, is required for qubit manipulation. Achieving such precision in frequency stabilization poses a significant technical challenge, necessitating the use of a high-finesse optical cavity as a frequency reference. The ground-state qubit offers in principle infinite t_1 time, the t_2 time, however, limited by sensitivity to magnetic field noise. The ground-state qubit's basis states are defined as $|1\rangle = 4^2\text{S}_{1/2}(m = -1/2)$ and $|0\rangle = 4^2\text{S}_{1/2}(m = +1/2)$, which are split in frequency by 11.4 MHz in our apparatus due to the application of a magnetic field of about 4 Gauss.

Initialization

At the start of an experiment, the qubit has to be prepared in a defined initial state, one of the two Zeeman states of the S manifold. In our apparatus the $m = -1/2$ is typically chosen

[42] Several choices exist for coupling the ground state to the D state, which differ in their coupling strengths, as well as sensitivity to magnetic field noise. For example, transitions for which the magnetic quantum number m is the same for both states are less sensitive to magnetic field variations. While magnetic-field sensitivity is a source of decoherence, it can sometimes be desired in sensing applications.

as the qubit $|1\rangle$ state. The state preparation is accomplished via optical pumping, a process in which population is transferred from $m = +1/2$ into the target state $m = -1/2$. The target state represents a dark state, from which no coupling to the pumping light is possible, such that once population is transferred there, it remains there. Two methods of optical pumping can be employed in our setup to initialize the qubit in the target Zeeman state, harnessing the transitions' selection rules and the polarization of the laser driving the transition. The first option is to optically pump via circularly-polarized σ^- light at 397 nm which drives transitions where the magnetic quantum number changes by $\Delta m = -1$. Electronic population is transferred from $4^2\mathrm{S}_{1/2}(m = +1/2) \longrightarrow 4^2\mathrm{P}_{1/2}(m = -1/2)$, from which it can decay to the desired $4^2\mathrm{S}_{1/2}(m = -1/2)$ state. Population in $4^2\mathrm{S}_{1/2}(m = -1/2)$, however, does not couple to the σ^- light. While this approach allows for a fast qubit initialization, the downside is that it is difficult to achieve perfect σ^- polarization such that the chance of coupling out of the target state is not zero. Therefore, optical pumping is typically performed at 729 nm. Here, population is transferred from $4^2\mathrm{S}_{1/2}(m = +1/2) \longrightarrow 3^2\mathrm{D}_{5/2}(m = -3/2)$ and subsequently transferred to the $4^2\mathrm{P}_{3/2}(m = -1/2, -3/2)$ states, from which, due to the selection rules of the transition, the electron can decay only into the target ground state $m = -1/2$.

Manipulation

In the case of the optical qubit, we employ a frequency-stable 729 nm laser to realize coherent operations on the electronic quadrupole transition. Control of the ground-state qubit, on the other hand, does not require a narrowband laser system. Here, the qubit can be coherently manipulated either by applying a magnetic RF field oscillating at 11.4 MHz (for technical details see sec. 4.5) or via a stimulated Raman transition. The latter approach has the advantage of allowing for coupling to the motion of the ions and thus for establishing entanglement between ground-state encoded qubits, as described in sec. 3.3.5. The technical details of the Raman laser system at 395.8 nm are provided in sec. 4.4.5. While the Raman laser does not need to be frequency-stabilized to a high-finesse cavity, the two Raman laser beams need to be phase-stable with respect to each other, requiring interferometric stability within the optical setup.

Note that all operations on the qubits performed in the context of this thesis are global. The control of individual ions in an ion Coulomb crystal was not yet possible when this thesis work was carried out, but the optical setup for this purpose has very recently been built and will be presented in the upcoming PhD thesis of Artem Zhdanov. This optical setup allows for tightly focusing down a 729 nm laser beam to a spot size on the order of a micrometer, and for the beam to be steered in two dimensions via two acousto-optic deflectors, in order to carry out addressed operations on specific ions within a planar crystal.

Readout

As described in sec. 3.3.3, the fluorescence signal from the cooling laser at 397 nm allows for the detection of ions and the quantum states of the qubits encoded in them. Here, a high-numerical aperture (NA)[43] objective collects a fraction of the scattered light, emitted towards the objective.

[43] The NA is a measure for the range of angles over which light can be collected by the objective. It is determined by $\mathrm{NA} = n \sin\theta$, where n is the index of refraction of the medium, in our case air, and θ is the half-angle of the

This light is then guided to a device for measuring the fluorescence, e.g. a photo-multiplier tube (PMT) or camera, allowing for spatially-resolved detection. For reading out the qubit states, the electron shelving method is employed [120, 121, 122]: Ions will only scatter 397 nm light if the transition $4^2S_{1/2} \longleftrightarrow 4^2P_{1/2}$ can be excited. If the electron occupies another state, such as one of the long lived D states, then the ion will remain dark. In this way a distinction between the two basis states of the optical qubit can be made. In the case that the qubit is in a superposition of the states $4^2S_{1/2}$ and $3^2D_{5/2}$, the presence of 397 nm light[44] projects the qubit either into the $4^2S_{1/2}$ or $3^2D_{5/2}$ state. This procedure corresponds to performing a projective measurement, as conceptually introduced in sec. 2.3.1. During detection, the 866 nm repump laser remains on to prevent population of the $3^2D_{3/2}$ state, which would result in detection errors. At the end of the detection process, the 854 nm repump laser is additionally switched on in order to pump out the metastable $3^2D_{5/2}$ state, enabling the fast initiation of a new experimental cycle.

Reading out the ground state qubit is done in the same way, but requires an additional step of first mapping the ground state qubit to the optical qubit. Here, population from one of the $4^2S_{1/2}$ Zeeman states has to be transferred to the $3^2D_{5/2}$ state, using several shelving pulses at 729 nm which address different Zeeman levels of the $3^2D_{5/2}$ manifold[45]. Since Δm cannot exceed 2, there are 5 transitions available for shelving.

Detecting the individual qubit states from a camera image of many ions may be challenging, given the low level of detected light during short imaging times as well as light from one ion spilling over to locations of other ions (crosstalk). Section 4.7 introduces our algorithm, based on machine learning techniques, which allows for the distinction of the quantum states of individual ions within an ion crystal with high fidelity.

Characterizing Qubit Coherence via Ramsey Interferometry

Spectroscopic methods offer the possibility to quantify the coherence of a qubit. Here, Rabi spectroscopy represents a fundamental tool, the damping of Rabi oscillations indicating how the state of a qubit becomes mixed from decoherence mechanisms such as laser phase or magnetic field noise[46]. The timescale of damping is thus a measure for the coherence time of the qubit. In this thesis, Ramsey interferometry is used for the determination of coherence time, which constitutes a more precise tool for this purpose. Here, the interaction time of qubit and drive field (local oscillator) is divided into two intervals, where the phase of the qubit's superposition state evolves

maximum cone of light that can enter the objective. The NA and resolution of the objective are inversely related by $\lambda/2\text{NA}$. A large NA is thus desirable as it relates to a higher photon collection efficiency and a better resolution in ion detection on camera images. Additionally, the objective can be used to focus down laser beams for individual-ion control. Here, a higher NA allows for smaller achievable spot sizes. In practice, the NA will be limited by the spatial restrictions imposed by the experimental setup.

[44] In principle, the $4^2S_{1/2} \longleftrightarrow 4^2P_{3/2}$ transition would also be a suitable choice for Doppler cooling and detection. However, this would be incompatible with the choice of optical qubit encoding in the $4^2S_{1/2}$ and $3^2D_{5/2}$ levels: The cooling and detection laser would couple to one of the qubit states which would spoil the readout process.

[45] Different transitions are coupled as it was found that this improves the shelving fidelity.

[46] Note, that e.g. insufficient laser cooling can also be a reason for damping of Rabi oscillations but as laser cooling is not present during the coherent manipulation of the qubit it is not considered a decoherence mechanism. Insufficient laser cooling results in insufficient control over the motional state initialization, which in turn results in the coupling strength on the optical qubit transition becoming a random variable through its dependence on the motional state. When averaging over many experimental realizations this manifests as damping of Rabi oscillations.

freely during the period in between the two interaction pulses. While the measurement protocol is presented in detail below, the essential idea is that the method allows the phases of the qubit's superposition state and the phase of the driving field, both of which are sensitive to noise, to be compared. The phase coherence of these two entities with respect to each other on the timescale of the free evolution time is quantified in the contrast of the Ramsey signal. Here, the coherence time t_2 of the qubit corresponds to the time at which the contrast has dropped to $1/e^2$[47].

Ramsey spectroscopy techniques are not exclusively performed on the electronic transitions of an ionic qubit, but can also be applied to superpositions of motional states. In this way, the motional coherence time can be investigated, which limits the timescale of entangling interactions. The motional coherence is typically restricted by the frequency stability of the motional modes, dependent on power fluctuations in the RF signal that drives the ion trap.

Ramsey experiments are applied several times throughout this thesis, e.g. in sec. 5.5 to determine the optimum achievable coherence time of the ground-state qubit in our apparatus. Besides the determination of coherence time, Ramsey interferometry also provides the ability to characterize any mechanisms giving rise to phase differences between a qubit and drive field, e.g. frequency detunings from drifts of the magnetic field or laser[48]. Here, long free evolution times are beneficial, allowing for the accumulation of a larger phase difference between the two oscillators (ion and drive field), and in turn enabling the resolution of smaller detunings. However, the coherence time poses a limit to how long the ion can be probed for on the respective transition. In sec. 6.1, measurements on correlation spectroscopy are presented, where Ramsey interometry is applied to many qubits simultaneously and quantum correlations emerging between the qubits are harnessed to determine transition frequency differences with probe times much longer than the coherence time of a single ion.

Ramsey Experiment Protocol

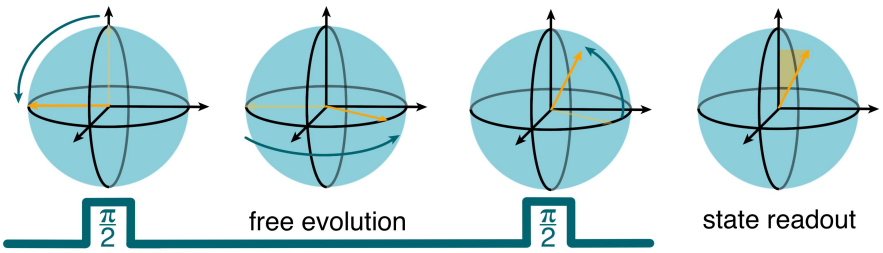

Figure 3.7: Schematic illustration of a Ramey experiment: After initialization of the qubit in the ground state, a first $\pi/2$ pulse prepares the qubit in the equatorial plane of the Bloch sphere. During the free evolution time the qubit superposition state evolves within the equatorial plane at a rate given by the energy difference between the qubit basis states. A second $\pi/2$ pulse maps the qubit state back into the measurement basis, where it is eventually read out in a projective measurement.

[47] In some cases, $1/e$ or even $1/\sqrt{e}$ is also used to define the coherence time.

[48] In order to distinguish whether these phase changes are due to a drift of the atomic energy levels from unstable magnetic fields, or a drift of the local oscillator, Ramsey measurements are performed in several transitions of different magnetic sensitivity.

The experimental protocol for Ramsey interferometry is illustrated in fig. 3.7. Initially, an ionic qubit is prepared in the $|1\rangle$ ground state. An equal superposition of the qubit basis states is then created by applying a $\pi/2$ pulse. This is followed by a wait time ("free evolution time") during which no interaction occurs between the ion and the local oscillator. During this time the phase of the qubit's superposition state evolves at a rate given by the energy difference between the qubit basis states[49]. Meanwhile, the phase of the local oscillator ideally evolves at the same frequency, i.e. the local oscillator keeps track of the phase of the ion. Finally, a second $\pi/2$ pulse maps this phase information back into the measurement basis, from which it is read out via a projective measurement. In this ideal scenario, the second $\pi/2$ pulse in the Ramsey sequence will add to the first one, resulting in a π pulse, flipping the state of the qubit from $|1\rangle$ to $|0\rangle$. However, in reality, noise processes are acting on the qubit as well as the drive field during the free evolution time, such that the two oscillators run out of phase with each other. Decoherence emerges when their phase difference varies for each experimental realization: When averaging over these repeatedly determined states of the qubit at the end of the Ramsey sequence, this phase noise will manifest as mixedness, quantified in the contrast of the Ramsey fringe. A Ramsey fringe is measured by repeating the Ramsey experiment for a fixed free evolution time at different phases of the second Ramsey pulse with respect to the first one. Determining the contrast of the Ramsey fringe for different free evolution times allows the coherence time to be extracted.

Extension to a Spin-Echo Sequence

The noise that contributes to the decay in contrast of Ramsey fringes can be classified into two different timescales: fast and slow noise. While fast noise gives rise to coherence decay that cannot be mitigated, slow noise, which is stable over an experimental cycle, can be compensated by a spin-echo experiment, which has the potential to significantly extend the coherence time. Here, the difference in the measurement protocol compared to an ordinary Ramsey experiment is that an additional π pulse is added in the middle between the two $\pi/2$ pulses, effectively splitting the free evolution time into two sections. During the first free evolution, the qubit's state vector may rotate within the equatorial plane due to slow noise processes. During the second free evolution time, of equal length as the first, the state vector rotates within the equatorial plane by the same amount as during the first evolution, given that the noise process giving rise to this rotation remains constant over the timescale of the experiment. However, as the state vector was flipped via the π pulse, the Bloch vector rotates back to its original position, essentially leading to a rephasing. Such π rotations may be performed around different axes of the Bloch sphere, e.g. around an axis perpendicular to the state vector, flipping it around by 180°within the equatorial plane. Alternatively, it is possible to use an echo pulse whose rotation axis is aligned with the Bloch vector. Here, the vector remains in the same place, while the noise phase changes sign during the second free evolution. Dynamical decoupling constitutes a generalization of the spin echo technique, where multiple π pulses are applied instead of a single one.

[49] This oscillation on the order of 10^{14} Hz is significantly faster than the laser driven dynamics. The interaction picture which was defined in eq. 3.26 allows these two timescales to be separated, effectively rotating along with the fast oscillation such that only the dynamics caused by the interaction pulses are observed.

3.3.5 Creation of Spin-Spin Interactions with Raman Beams

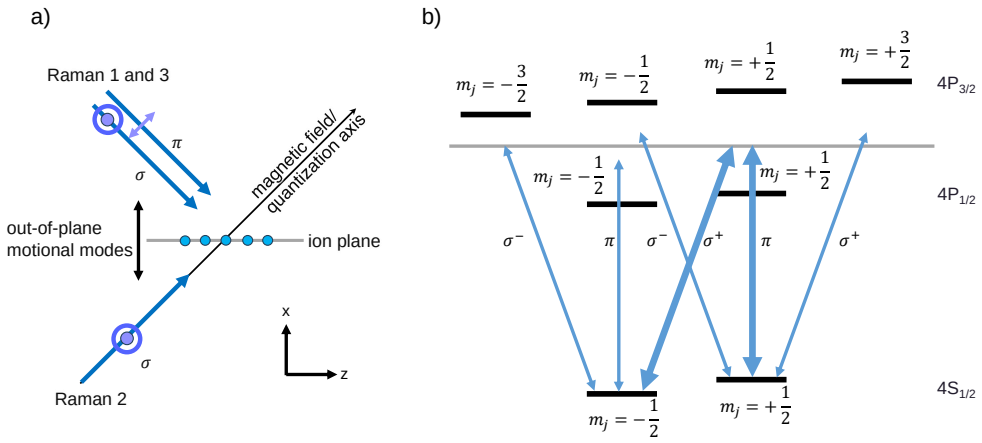

Figure 3.8: Details on the Raman laser beams which couple the ground-state qubit transition and mediate entangling interactions: a) The schematic illustrates the spatial arrangement and polarization of the Raman laser beams in the experiment with respect to the ion Coulomb crystal and quantization axis (top view). b) The diagram shows the energy levels contributing to the Raman transition and possible coupling between them, which depends on the light polarization. The grey line represents the magic wavelength at which the laser is operated, with the Raman interaction path shown in bold. The presence of both σ^+ and σ^- light cancels out differential Stark shifts on the spin states.

Section 3.2.3 introduced theory on creating entangling interactions in ion Coulomb crystals. The present section provides information on how these entangling interactions are realized in our apparatus to create spin-spin interactions with tunable interaction strength. Here, entanglement is mediated via the out-of-plane motional modes of our planar crystals, as they oscillate at higher frequencies than the in-plane modes, allowing for lower heating and faster interactions, and additionally they do not align with the direction of micromotion. For encoding the spin states $|\downarrow\rangle$ and $|\uparrow\rangle$, we have the option of using the optical or the ground state qubit basis states. The ground state qubit approach is the one taken for the experiments presented in this thesis. As described in sec. 3.3.4 the ground state qubit provides the benefit of longer t_1 time and not requiring an ultra-narrow laser for driving the qubit transition. Given the transition frequency in the MHz range it is not possible to drive the ground state transition directly via a laser field. As driving the transition via a RF signal would result in an insufficient Lamb-Dicke parameter for coupling to the motional modes, a Raman transition needs to be employed for this purpose. This Raman transition is implemented at 395.8 nm, off-resonantly coupling the two ground-state spin states via the $4^2P_{1/2}$ and $4^2P_{3/2}$ states[50]. This specific wavelength is chosen as it corresponds to a "magic

[50] In contrast to the Raman process introduced in sec. 3.2.1, here a four-level scheme is considered, where the coupling via both excited states adds up to the total Raman coupling strength. On the other hand, also the decay from both those excited state needs to be considered.

wavelength" where differential Stark shifts between the $4^2S_{1/2}$ and $3^2D_{5/2}$ states cancel out, i.e. intensity fluctuations of laser beams shift the S and D levels equally only at this wavelength[51].

Using a Raman transition in the UV for implementing spin-spin coupling rather than the quadrupole transition at 729 nm offers an additional advantage besides being able to make use of the long t_1 time. As demonstrated e.g. in eq. 3.61 the spin-spin coupling strength scales with the square of the Lamb-Dicke parameter and thus with the square of the laser's wave vector $\vec{k}$. Since the wave vector is inversely proportional to the wavelength of the light, using the shorter wavelength of 395.8 nm corresponds to η being almost a factor of two larger compared to when using 729 nm light. Also, since the Raman transition effectively constitutes a two photon process, the momentum transferred to the ion is even higher. This can be quantified by the effective wave vector $\vec{k}_{\text{eff}}$, as introduced in eq. 3.36, leading to an additional increase in coupling strength by a factor of up to 2. In our experimental setup, due to geometric constraints (see below), this gain is reduced. However, considering the same effective Rabi frequency and the same number of motional modes to be coupled, the Raman approach at 395.8 nm correlates with a 13.6 times higher spin-spin coupling strength compared to using the 729 nm quadrupole transition. On the other hand, the Raman approach also gives rise to challenges. First of all, off-resonant photon scattering from the P states during the interaction can lead to decoherence through amplitude damping. Second, fluctuating Stark shifts due to the off-resonant light field being unstable in intensity can also lead to decoherence through phase damping. Third, decoherence may also arise from the two Raman beams not being phase stable with respect to each other. And lastly, the high-power UV light, required to achieve sufficient coupling strengths at the given large detuning, may destroy optics or create charges on the ion trap which could give rise to the creation of dark ions and stray electric fields. The technical implementation of the Raman setup and strategies to mitigate these challenges are presented in sec. 4.14, with experimental characteristics of the Raman beams to be found in sec. 5.5.

Raman Beam Geometry

The Raman beam geometry in our apparatus with respect to the ion crystal plane is shown in fig. 3.8a. Here, we have the option of driving Raman transitions via two pairs of beams, co-propagating Raman fields where the two beams propagate in parallel[52] and counter-propagating beams, where the beams propagate at an angle of 90 degrees with respect to each other. In order for the light to couple to the motion of the ion crystal, the effective k vector, i.e. the difference in k vectors of the individual beams, has to overlap with the direction of motion. In our case we want the light field to couple to the out-of-plane motional modes for the implementation of entangling interactions. Here, the counter-propagating beam configuration is used, for which $\vec{k}_{\text{eff}}$ aligns with the desired direction, enabling a maximum coupling to the out-of-plane modes

[51] This approach, however, does not mitigate differential Stark shifts between the two ground states and the associated decoherence from laser intensity fluctuations. As discussed further down, those differential Stark shifts are cancelled by employing only linearly polarized beams for the interaction. However, for the S to D transition, differential Stark shifts are also present for π polarized light, except at the magic wavelength of 395.8 nm. While in the context of this thesis spins are encoded in the ground states, avoiding these shifts is relevant for harnessing the optical qubit transition in a phase-sensitive way, e.g. in experiments encoding some spins in the optical qubit states.

[52] The option of co-propagating beams was later on removed due to lack of necessity as also a RF drive is available for coupling carrier transitions.

while minimizing undesired coupling to in-plane modes. On the other hand, the co-propagating Raman beams allow transitions between the spin states to be driven with no possible coupling to the ion motion as here $\vec{k}_{\text{eff}} = 0$.

Raman Beam Polarization

In order to drive transitions between the ground states, the polarizations of the Raman beams need to be chosen appropriately with respect to the magnetic field axis. A transition from the $m = -1/2$ ground state to the $m = +1/2$ ground state requires one Raman beam to drive a $\Delta m = 1$ and the other beam to drive a $\Delta m = 0$ transition. It thus seems natural to employ one circularly (σ^+) polarized and one linearly (π) polarized beam, in order to maximize the coupling strength on the Raman transition. However, this scenario is not ideal as the circularly polarized light induces differential Stark shifts on the spin states. This means that the states $4^2S_{1/2}(m = 1/2)$ and $(m = -1/2)$ are shifted by different amounts from the off-resonant light field, beam power instabilities leading to decoherence. Employing only linearly polarized laser beams, instead, constitutes a solution to this problem: The linear polarization represents a superposition of σ^- and σ^+ light, where the presence of both those polarization components effectively cancels differential Stark shifts[53]. This is illustrated in fig. 3.8b with the beam polarizations also shown in a. Here, the "σ" beams are vertically polarized and the π beam, propagating perpendicular to the quantization axis as required to achieve $\Delta m = 0$ coupling, is horizontally polarized. The downside of this approach is that half the power of the σ beam is not used as one of the possible transitions cannot be driven, leading to a lower Raman Rabi frequency than would in principle be possible with the available laser power.

Spin-Spin Interactions

In order to establish tunable-range entangling interactions mediated by the out-of-plane motional modes of our planar crystals, Raman beams 1 and 2 are employed, which are detuned from the out-of-plane motional modes of the crystal, as described in sec. 3.2.3. Here, Raman beam 1 (π) constitutes the "interaction beam" that is driven in a bichromatic way, in order to couple off-resonantly to the red as well as blue motional sidebands simultaneously.

[53] In reality, unfortunately, due to the focusing of the Raman beams into the trap, undesired polarization components may occur, giving rise to Stark shifts that cannot be compensated.

APPARATUS

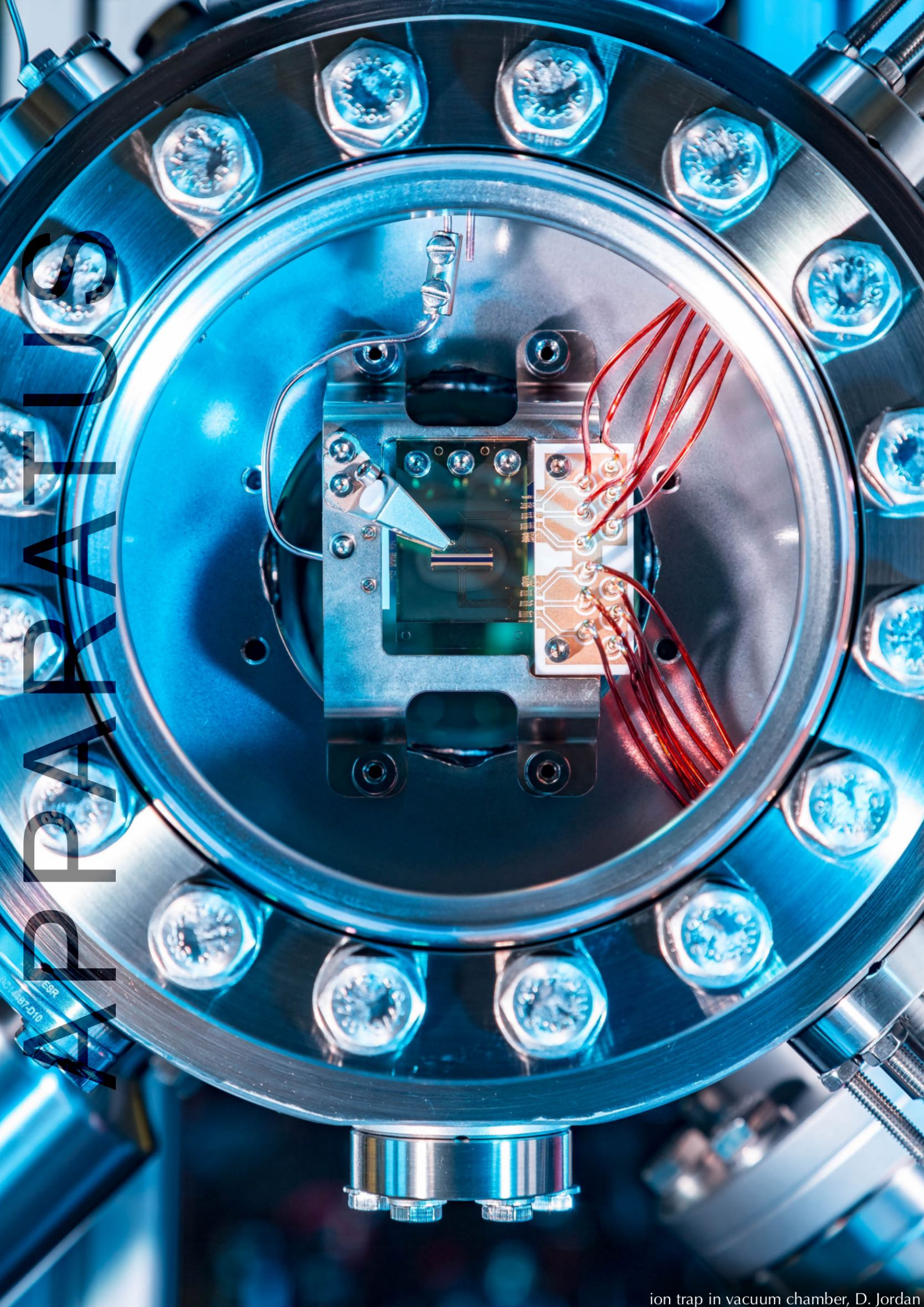

ion trap in vacuum chamber, D. Jordan

4 Setup and Control of the Experimental Apparatus

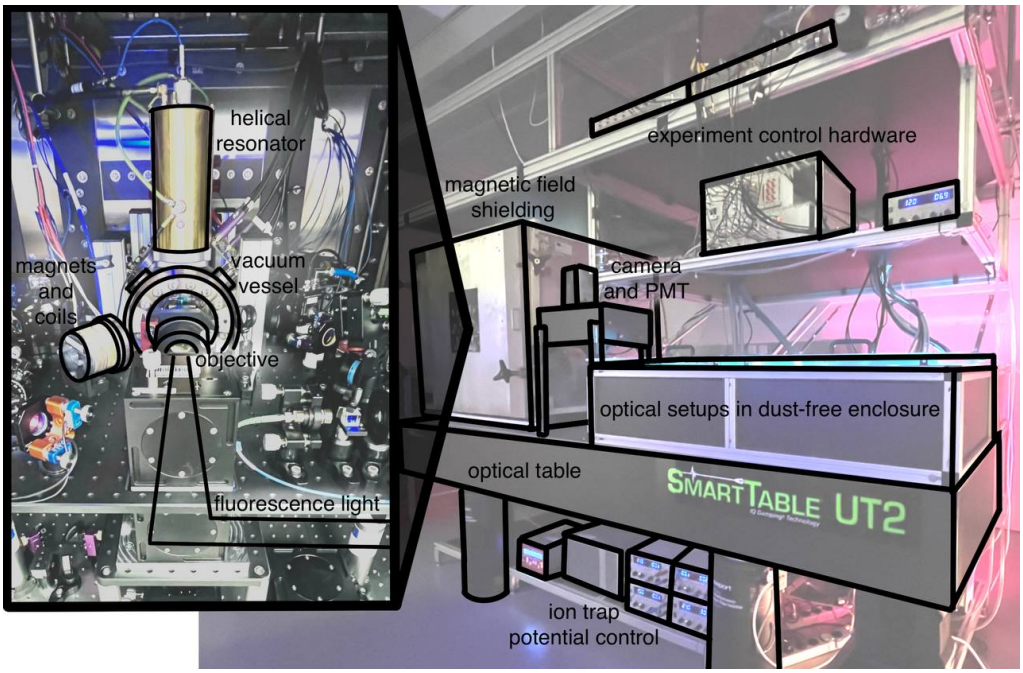

Figure 4.1: Experimental apparatus for controlling 2D ion Coulomb crystals: This image presents an overview of the components comprising the experimental apparatus, which are discussed in this chapter. Here, one of the two optical tables is shown, the main experimental table on which the ion trap setup rests. The left part of the image shows the inside of the magnetic field shielding. Details on the individual components can be found in the main text. More detailed information on the vacuum setup as well as the ion trap potential control electronics can be found in the thesis of Dominik Kiesenhofer.

The experimental setup presented in this thesis was built with the goal of gaining quantum control[1] over large planar $^{40}Ca^{+}$ ion crystals, consisting of around 100 particles. Here, it is essential to on one hand provide a well-controlled environment for the trapped ions, in particular by shielding them from ambient noise in order to sustain long coherence times, and on the other hand to be able to precisely interact with the ions by means of magnetic or laser fields to manipulate

[1] Quantum control encompasses cooling to sufficiently low temperatures and coherently manipulating the ions.

their quantum states. For this purpose a sophisticated experimental setup has been built, whose key components are described in this chapter. In particular, an overview of the design, construction and functionalities of the various subsystems comprising the apparatus is described, as well as the interconnection between them. The core piece of the apparatus is a novel monolithic ion trap, described in sec. 4.1, providing a stable confinement for planar ion crystals while allowing for generous optical access for ion imaging and manipulation via laser light. Section 4.2 presents the ion trap's installation inside a UHV chamber, ensuring the required low-pressure environment. The creation of a highly stable and clean magnetic field in order to achieve qubit coherence times of hundreds of milliseconds is described in the following sec. 4.3. For cooling and high-fidelity manipulation of the ion's quantum states, several laser systems (sec. 4.4) as well as a radiofrequency antenna (sec. 4.5) are available. Section 4.6 presents the imaging system for detecting the ions' fluorescence light. To extract relevant information from the acquired images, such as the number of ions, ion-specific quantum state readout or crystal lattice configurations, the analysis tools presented in sec. 4.7 are applied. The chapter concludes in sec. 4.8 with a presentation of the experiment control system, consisting of hardware and software required to operate the experimental apparatus, i.e. establishing control of and communication between various subsystems. This includes the precisely-timed generation of RF signals to apply experimental sequences to the ions as well as the communication with various devices such as laser controllers or electronics required for creating the trapping potential.

4.1 A Monolithic Linear Paul Trap for Planar Ion Crystals

As discussed in sec. 3.1.2 there exist two particular possibilities for orienting a planar ion crystal within a linear Paul trap: the crystal spanning either across the radial directions of the trap or along one radial and the axial direction. To summarize the comparison made in sec. 3.1, the benefit of the first option is a reduced crystal lattice instability as the crystal aspect ratio does not change from RF power fluctuations. The benefit of the second option is that micromotion occurs only along a single direction, such that an entire plane is available for laser addressing of the ions, to first order free of micromotion. As the problem of RF power instabilities can be addressed with a suitable stabilization scheme, the second option is chosen in our setup. This section presents our segmented linear Paul trap, designed for storing large planar ion Coulomb crystals. More specifically, the section describes information on the trap's electrode arrangement, that allows for optical access from relevant directions for laser access and imaging. Furthermore, information is given on the microfabrication of the trap via a subtractive 3D printing technique on a fused silica wafer. This technique allows for significantly more precise electrode structures to be realized compared to other methods that rely on the hand-assembly of machined parts. High precision in this context is particularly relevant when working with planar ion crystals as small electrode alignment imperfections can be detrimental, potentially making it impossible to perform experiments with or even trap large 2D crystals in a stable way. The reason for these challenges, as discussed in sec. 3.1.3, are e.g. nonlinear resonance effects that could lead to ejection of ions from the trap, especially when ions are far displaced from the RF null. The section concludes with information on the creation of a stable trapping potential using home-built and commercially available RF and DC electronics.

4.1.1 Design and Simulations

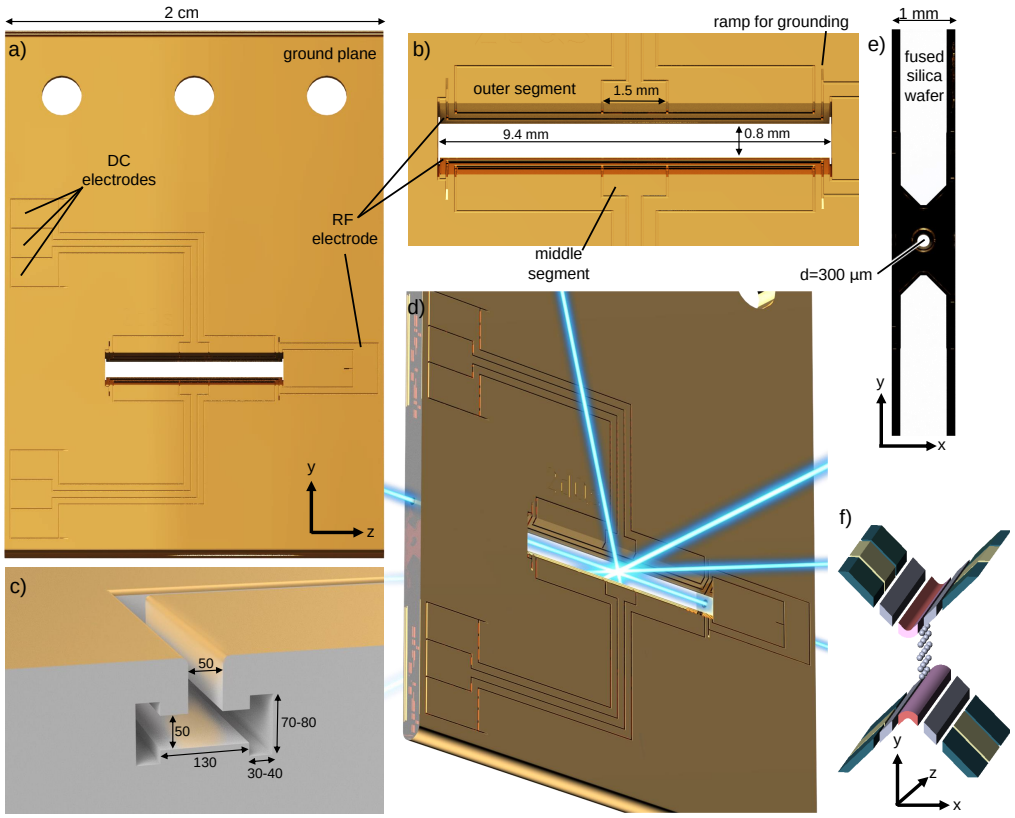

Figure 4.2: Our novel monolithic linear Paul trap for storing planar ion Coulomb crystals: a) A CAD model of the entire trap chip is shown from the side which contains the RF electrode pad. The other side that is not visible contains 6 DC electrodes in mirror symmetry. Note, that the actual trap deviates from this CAD model in that the chip extends a bit further on the bottom (uncoated), with two holes in the chip whose only purpose was to allow for secure shipping. b) Zoom in to the central trap region. c) Dimensions in µm of the trenches used for separating electrodes: Note that dimensions are approximate as they depend on the local geometry and its effect on the etching process. d) Laser beam access in the horizontal (xz) plane: Here, access from 8 directions towards the trap center is possible, including the axial trap direction, where holes in the trap chip allow for optical access. e) Side view of the central section of the monolithic trap. f) Schematic illustration of the electrode structure of the monolithic trap and planar ion crystal. Ion crystals are stored in the trap (yz) plane in the trap center. RF electrodes are shown in pink, the DC electrodes in yellow and the endcap electrodes in bluegreen. The grey electrodes next to the RF rails are grounded. This electrode arrangement offers general optical access in the horizontal (xz) plane that is perpendicular to micromotion (along y), as well as from 45 degrees with respect to the crystal plane from top and bottom for spectroscopy laser beams.

In a standard linear Paul trap design, as shown schematically in fig. 3.1, the DC electrodes obstruct optical access within the horizontal plane as required for imaging and laser addressing of the

planar ion crystal. Thus, in our apparatus the trap geometry is modified in order to gain optical access from the relevant directions perpendicular to micromotion and crystal plane. Our electrode structure can be seen in fig. 4.2f and effectively realizes a three-layer trap. Compared to a standard linear Paul trap, the DC blades are split and projected to the top and bottom. The DC electrodes are segmented into three adjoined parts. This allows for confinement of the ions along the axial trap direction, when applying higher voltages to the outer segments than are applied to the inner segments. Recession of the DC electrodes with respect to the RF electrode in vertical direction enables optical access at a 45°angles from top and bottom with respect to the crystal plane. Despite overlap with the ions' micromotion, laser beams from these directions may be used for spectroscopy of in-plane motional modes. A ground electrode is additionally introduced into the electrode structure, placed between the RF and DC electrodes for shielding purposes: When applying RF voltage to the RF electrodes a small RF potential along the axial trap direction additionally emerges due to the segments slits in the DC electrodes[2]. By placing a ground electrode in between the RF and DC electrodes, this potential and thus micromotion along the axial trap direction can be reduced, such that, as desired, micromotion can be approximately constrained to a single direction.

In order to determine the exact dimensions of the electrode structures, finite element simulations were carried out using COMSOL Multiphysics. Here, it is sufficient and computationally less expensive to conduct static simulations: First, the RF potential is determined by simulating the application of a DC voltage to the RF electrodes of the trap model, where the magnitude of the DC voltage represents the RF voltage amplitude. The dynamic effect for a specific drive frequency is then obtained via eq. 3.11 in pseudopotential approximation. In a second simulation, DC voltages are applied to the DC electrodes of the trap model. The results from the two simulations are then added as $Q(\Phi_{\mathrm{RF,pseudo}} + V_{\mathrm{static}})$, to obtain the full trapping potential.

Such simulations were performed for various electrode geometries, most importantly varying the width of the RF electrodes and the distance between them, as well as dimensions of the DC electrodes and their placement, to find a configuration which allows for a good balance between all relevant parameters. The design process is described below in detail. But in summary, the parameters that are balanced against each other include the achievable secular frequencies and q parameter for a given voltage and RF drive frequency, while at the same time maintaining good optical access from relevant directions. Moreover, sufficient tunability of the DC potential has to be ensured in order to allow for precise control of the crystal's shape and orientation, while sustaining low axial micromotion. When designing a trap one should first make assumptions about the maximum voltage that can be applied. In our case, the limitations of the ion trap in terms of voltage handling capability were not completely known during the design stage and were estimated to be somewhere in the range between 1 and 2 kV. An indication of the possible RF voltage handling capability was an electrical test performed by another ion-trapping team in our institute. They applied RF voltage to simple fused-silica test wafers where electrodes were separated by 50 µm gaps. Up to 1200 V peak-to-peak at $\Omega_{\mathrm{RF}} = 2\pi \cdot 46$ MHz drive were applied without the occurrence of any voltage breakdowns. We based our assumption regarding voltage handling capability as well as the geometry of the trenches for electrode separation, shown in fig. 4.2c,

[2] The small RF potential along the axial trap direction emerges because the segment slits in the DC electrodes influence the path of the electric field lines.

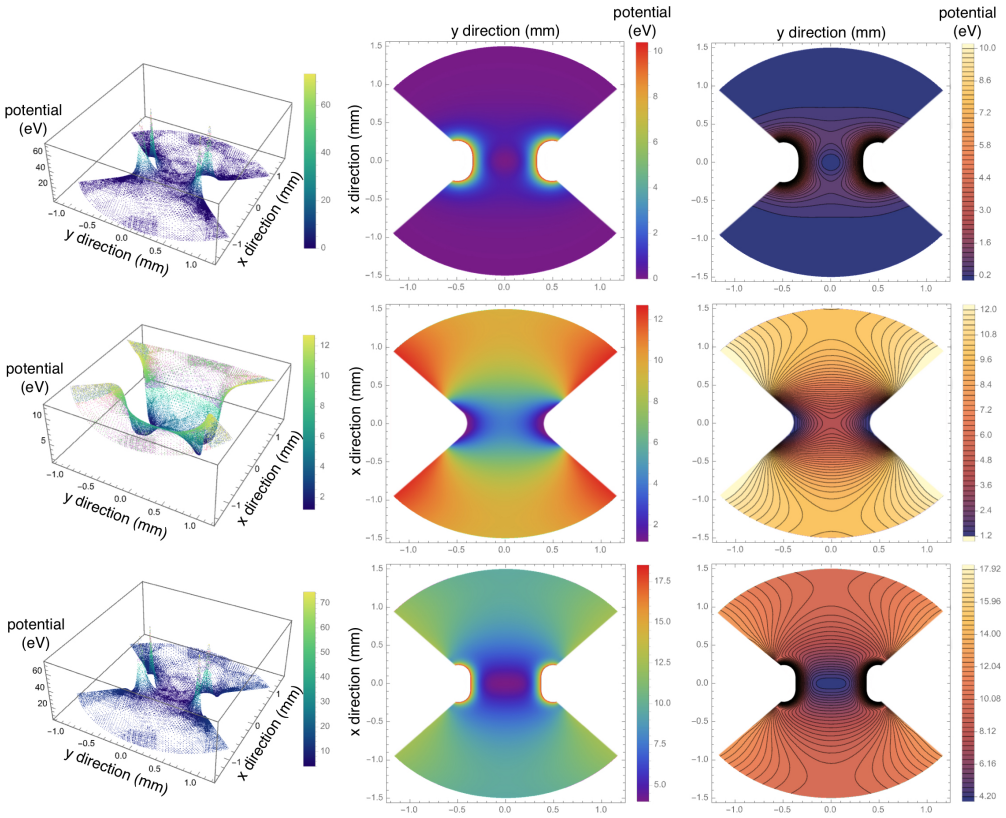

Figure 4.3: Simulated trap potential for voltages similar to our experimental parameters. Shown here are the RF, DC and combined potentials, in the radial (xy) plane through the trap center. The first column shows a side view of the potential landscape, with the second column showing a view of the radial plane from the z direction, which is shown again as a contour plot in the third column, making the potential structure better visible. The top row shows the potential that is created by 1000 V peak-to-peak applied to the RF electrodes of the trap model at a $\Omega_{\mathrm{RF}} = 2\pi \cdot 45\,\mathrm{MHz}$ drive frequency. One can see that the RF potential in the trap center is rather symmetric, relating to a degeneracy of the two secular frequencies in this plane. The second row represents the DC potential when applying 13 V on the middle segments of the trap electrodes and 24 V on the outer segments. In the last row the two potentials are combined. Here, it can be seen that the DC voltages give rise to an anisotropy of the potential, where one direction corresponds to the strongly confined one (x), along which a planar ion crystal is squeezed flat, while the other direction corresponds to the weakly confined one (y), along which the crystal is extended.

on these results. In terms of trap frequencies, higher is better as then the ions are more tightly confined, relating to lower heating and faster entangling interactions, crucial for quantum simulation tasks. In particular, the aim was for the out-of-plane secular frequency to be at least on the order of a few MHz. To satisfy the planarity condition in eq. 3.14, the in-plane secular frequencies should, depending on crystal size, be a factor 3 to 4 times lower than the out-of-plane secular frequency. Moreover, the in-plane frequencies should be on the order of a few hundred kHz to reduce in-plane motional heating. From equations 3.7, 3.8 and 3.10 it follows that the

trap frequencies scale with RF voltage amplitude and inversely with Ω_{RF} and the square of the electrode-ion distance d. Thus, as the maximum voltage that can be applied safely is restricted, a strategy for achieving high secular frequencies is the use of low Ω_{RF} and small d. However, while maintaining high secular frequencies is important, other factors should not be neglected: Keeping the q parameter low is crucial in experiments with 2D ion crystals as the micromotion amplitude scales linearly with it, as can be seen from eq. 3.9. Achieving a low q parameter relates again to a higher drive frequency according to eq. 3.8. Moreover it is beneficial to keep d large to reduce anomalous heating effects, as discussed in sec. 3.1.3. Data in [101, 123] suggests that an ion-electrode distance of more than 300 µm should allow for heating rates below 10 phonons/s per ion confined at a secular frequency of 1 MHz in a room temperature setup. Due to the many relevant parameters that have to be considered when designing the trap, it is not a trivial task to find a good balance of all of them. In the end, the distance d between electrode and ion was chosen as 400 µm, a compromise of being large enough to reduce heating, while being small enough to obtain out-of-plane frequencies on the order of 2 MHz when applying RF voltages around 1 kV peak-to-peak at a $\Omega_{\mathrm{RF}} = 2\pi \cdot 45$ MHz drive frequency. The latter keeps the q parameter low around 0.1. Further design considerations for the ion trap include the width of the RF electrode, a smaller width corresponding to higher secular frequencies resulting from a faster voltage drop in the vicinity of the trap center. As aforementioned, a ground electrode was introduced between RF and DC electrodes in order to reduce micromotion along the axial trap direction that results from the slits separating the DC electrodes. Additionally, the finite length of the trap can give rise to micromotion along this direction. To reduce this effect the trapping region is designed to be 9.4 mm, shown in fig. 4.2b. It is challenging to quantify the axial micromotion from simulations as the small potential curvatures arising along the axial direction when applying voltage to the RF electrodes are hard to resolve. However, an estimation yields a curvature ratio on the order of 10^{-5}, two orders of magnitude better than QSIM[3] has determined experimentally[4]. For shaping the DC potential it is beneficial to keep the central electrode segments short as this reduces the required voltages on the outer segments. The central segment length was chosen as 1.5 mm which allows for tilting of an ion crystal's principal axes, important for micromotion compensation, by application of reasonably low asymmetric voltages on the outer electrodes.

The simulated trapping potential is presented in fig. 4.3 and 4.4. In fig. 4.3 the potential is shown in 2D, for a slice through the trap center along the radial trap directions (x and y). The simulation in fig. 4.4 represents the trapping potential along three lines through the trap center, along the three principal axes. In these simulations voltages are applied which are close to the experimental values used in subsequent chapters, i.e. 1000 V peak-to-peak of RF voltage at 45 MHz, 13 V DC voltage on the inner electrode segments and 24 V DC voltage on the outer electrode segments. The DC voltages used here are on the lower side and represent conditions that allow for trapping a planar 19 ion crystal, which has a structure as shown in fig. 3.2. The simulated trap frequencies $2\pi(2070, 668, 349)$ kHz corresponding to these voltages are obtained by applying a

[3] The QSIM apparatus is run by another team in our institute. They carry out quantum simulation experiments with long strings of trapped ions stored in a standard linear Paul trap[15].

[4] In general, applying a symmetric RF drive, i.e. opposite polarity to two pairs of RF electrodes rather than applying RF only to one pair of RF electrodes while keeping the other pair at ground potential, allows for better results in this context. However, even without symmetric RF drive, we achieve good simulation results by careful design considerations of the trap electrode structure and dimensions.

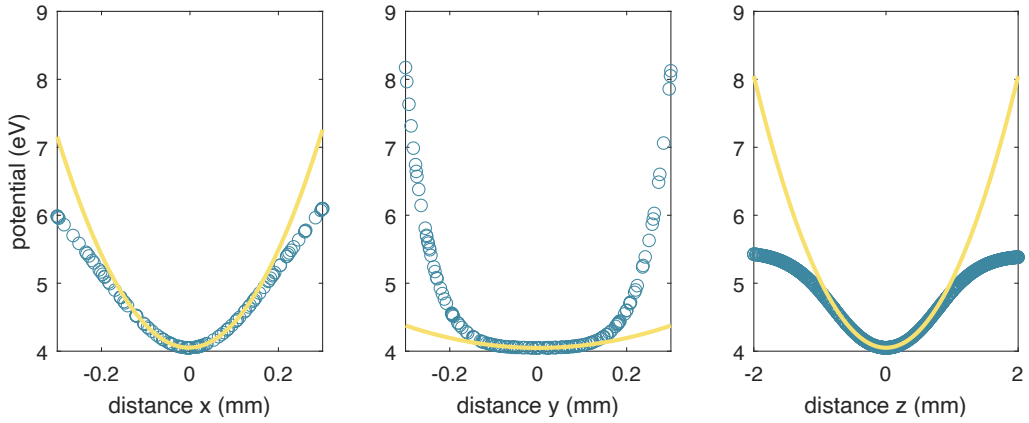

Figure 4.4: Potentials along lines through the trap center. The points represent simulated data along the x direction (perpendicular to the crystal plane), y direction (along the direction of the RF electrodes), and along the z direction (axial trap direction). Yellow lines represent quadratic fits to the central potential region, from which trap frequencies are determined.

quadratic fit to the simulated data in fig. 4.4. The fit is applied only to the central region of the trapping potential, where the potential is harmonic. Clearly, the harmonic region extends beyond the anticipated dimensions of the ion crystals, suggesting that any adverse effects resulting from anharmonicities are expected to be minimal, unless imperfections in the actual trap geometry give rise to stronger anharmonicities. From the simulated data in fig. 4.3 a trap depth of about 4 eV is found as the energy difference between the point where the potential becomes anticonfining along some direction and the potential minimum.

4.1.2 Fabrication

The trap was microfabricated by the company Translume via a subtractive 3D printing process called selective laser-induced etching (SLE). Previous applications of this technology in the context of manufacturing ion traps were employed in [124, 125]. The ion-trap fabrication can be divided into three stages: First, a fused silica wafer is processed by a pulsed laser. The laser locally changes the chemical composition of the glass due to intense heating and thus writes the design into the wafer. More specifically, here the chemical etchability is locally modified. In the next stage, the material that was previously illuminated by the laser light is etched away in a bath of e.g. potassium hydroxide or hydrofluoric acid. Finally, the wafer is metallized in order to produce the required conducting layer on the chip. The benefit of this technique is the ability to produce nearly arbitrary electrode structures with outstanding precision, on the order of submicrometer. Moreover, trenches which extend underneath the surface[126, 127] can be realized, which enable electrical isolation for larger gap sizes between electrodes, thus increasing voltage handling capabilities of the chip.

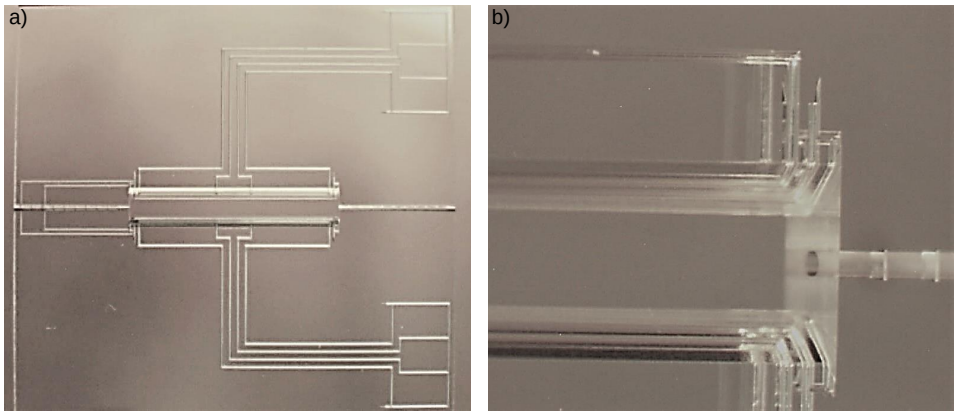

Figure 4.5: Ion trap fabrication from selective laser-induced etching (photographs taken by the manufacturer Translume): a) Unmetallized trap chip with the electrode structures as well as tunnels for axial laser beam access etched into the glass. b) Close up of the right part of the central trap region: Here, the periodic openings from the tunnels to the chip surface can be seen, as required for efficient etching of these structures. Moreover, one of the ramps that connects the bottom of the trench for separating electrodes to the trap surface can be seen in the top right corner. These ramps allow for a well-defined potential also on surfaces on the bottom of the trenches, which may be important for establishing a well-controlled trapping potential.

Material

Glass has proven to be a suitable material in microfabriaction techniques based on SLE, due to its optical transparency over a wide range of wavelenghts and chemical inertness ensuring a controlled etching process. Fused silica is the most widely used material in this context, however, there are disadvantages of using fused silica for ion traps. In RF electronics, the loss tangent of a material is an important parameter, describing how much RF power propagating through a material is dissipated. In fused silica and other (mostly dielectric) materials used typically as substrates for microstructured ion traps, such as sapphire, diamond or silicon, the loss tangent is significant, relating to RF losses in the substrate, power inefficiency and potential heating of the chip. For the substrates used for our ion trap, a loss tangent of <0.00002 at 10 MHz and 25 °C and <0.0001 at 100 °C was provided by the manufacturer. While sapphire or diamond have similar loss tangents as fused silica, the superior heat conductivity of these materials would allow heat to be carried away from the trapping region more effectively. At the time of constructing our experimental apparatus fused silica was the only material available for SLE that could be processed with sufficient precision and reliability for our purposes. However, there has been recent progress on the use of sapphire in SLE, which might open up the possibility to use this material for ion traps in the future [128].

Design Constraints for SLE

In SLE the selectivity of the material describes the etching rate ratio of unmodified and modified regions. For fused silica the selectivity is in the range of 500 to 1000 [129]. As a result of this finite ratio, very deep features which take a long time to etch, cannot be etched without losing dimensional accuracy on the structures which should remain unprocessed. This is relevant in

our trap design for the long tunnels with a length of about 5.3 mm and outer width of 300 µm, that can be seen in fig. 4.2 and 4.5, providing optical access for laser beams along the axial trap direction. Thus, periodic openings of the tunnels towards the trap plane are implemented (see fig. 4.5b, to shorten the etching time of the tunnels. In terms of accuracy, the roughness after etching is on the order of a few 100 nm. Rounding of edges with a radius of curvature of a few micrometers occurs automatically during the etching process.

Electrode Separation

A conventional method of creating separation between individual electrodes is to create slits in a wafer and then metallize the wafer at an angle. For sufficiently deep slits, no metal coating will reach the bottom of the trench, such that electrically-isolating areas remain within the structure. However, when high voltages are applied, larger distances between electrodes are required, in order to avoid voltage breakdown between electrodes. The wider the slits, the deeper they have to be to sustain electrical isolation, which at some point becomes infeasible. However, the SLE process offers a convenient method for separating electrodes [126, 127], as e.g. depicted for our specific case in fig 4.2c. Here, trenches extending to the sides underneath the surface are used, enabling the realization of larger gap sizes, compared to straight slits, without the need for excessive depth. In principle, for any direction used for metallization there remain uncoated areas within the structure creating electrical isolation. In practice, however, some technical challenges need to be overcome. Short circuits can be a result of debris accumulation inside the gaps. This is complicated also by the fact that trenches deep within the structure take a long time to etch and other design features have to be adjusted accordingly. We are grateful to Translume for their efforts in optimizing the trench shapes, finding that H shaped trenches were more effective in preventing shorts than the previously established T shaped trenches. Additionally, ramps were incorporated into the design that connect the bottom of the trenches, that would otherwise be on a floating potential, to the ground plane of the chip, to establish well-defined potentials in close proximity to the ions throughout the trap structure.

Metallization

Metallizing an ion trap to obtain a conducting layer for the electrodes can be accomplished using various methods, such as evaporation, sputtering, and electroplating. Evaporation provides directional coating, while subsequent electroplating helps achieve a more consistent and thicker gold layer, although variations can still occur based on certain parameters: The lateral growth associated with electroplating may cover smaller defects in the initial sputtered layer and reduce surface roughness, but it can also contribute to the formation of shorts. Sputtering is generally less directional than evaporation but can be applied faster in order to produce thicker layers without additional electroplating. The surface roughness of a sputtered piece is typically the same as the roughness of the bare piece prior to coating.

The coating thickness should be comparable to the skin depth (d_S) of the metal at the RF drive frequency that is used. This parameter describes the penetration depth of the RF voltage into the

material. A metal layer thinner than the skin depth will thus increase resistance, and heating of the chip, and reduce power efficiency. The skin depth is defined as

$$d_S = \sqrt{\frac{2\rho}{\Omega_{\mathrm{RF}}\mu_r\mu_0}} \tag{4.1}$$

where ρ is the resistivity of gold[5], μ_r is the relative permeability of gold and μ_0 is the permeability of free space, which results in $d_S \approx 11$ micrometers of skin depth at 45 MHz. While a thick gold layer is also beneficial in the context of carrying away heat faster than through the fused silica substrate, it is in practice not always feasible to implement, especially in microstructured traps, where a significant amount of structural resolution may be lost that could lead to shorts.

At the time of constructing the experimental setup, the company Translume offered the possibility of sputtering and electroplating to metallize the trap chip. Unfortunately, it proved challenging to sustain electrical isolation of the RF electrode throughout the plating process. Therefore, the entire trap chip was metallized exclusively via sputtering: an adhesion layer of titanium was first applied (30 nm), followed by about 3 µm of gold.

4.1.3 Trapping potential generation

For the generation of a stable and well-controlled 3D trapping potential several homebuilt and commercially available electronic devices are employed.

RF Network

The ion trap needs to be supplied with high and stable RF voltage. In numbers this means a RF voltage of more than 1000 V peak-to-peak with a stability of below 10^{-6}, correlating with motional mode frequencies that are stable on the order of a few Hz. In order to produce this high voltage, the signal from a frequency generator[6] is amplified using an RF amplfier[7] and resonantly enhanced by a factor ~ 25 using a helical resonator[130] consisting of a macroscopic coil[8] in a cylindrical enclosure and the trap, which acts as an additional capacitance. Its resonance frequency depends on the trap capacitance as well as on the resonator's inductance, dominated by the coil. A resonance at about 43 MHz is found. From observing the shift in resonance frequency when attaching different capacitances to the resonator it is possible to find an upper limit for the capacitance of the trap of about 12 pF.

It is crucial to keep the RF power at a constant value, in particular in experiments with planar crystals, as instabilities result in an increased number of configuration changes of the crystal lattice, as discussed in sec. 3.1.3. Moreover, when the motional modes of an ion crystal are used to mediate entangling interactions across the system, frequency stability of those modes needs to be maintained to reduce coupling strength variations caused by unstable laser detuning from the

[5] Usually gold is chosen as a preferred coating material for ion traps due to its resistance to oxidation. Copper for example has a better conductivity, but oxidation on the surface could increase the trap's heating rate.

[6] Rohde& Schwarz SMB-100A

[7] Minicircuits LZY-22+

[8] 40.4 mm diameter, 5 mm wire thickness, 10 mm winding pitch, and 70 mm coil height, made of silver-coated (30 µm) and gold coated (0.5 µm) copper

sidebands. On long timescales, typically a mode drift of several kHz over a few minutes, caused by temperature fluctuations around the experiment, needs to be corrected for. But stabilization is also relevant on short timescales, to increase the motional coherence time which poses a limit to the interaction time that spin dynamics can be observed for[9]. A home-built proportional-integral (PI) controller is used for RF power stabilization. It is ethernet controlled and besides stabilization allows the RF potential to be tuned and attenuated precisely[10], enabling e.g. the removal of single ions from a crystal. The feedback signal for the stabilization circuit was initially picked off capacitively and later on inductively at the helical resonator coil. The inductive pickup provides the benefit of leaving the ground of the helical resonator unaffected, as no connection is required, enabling increased stability with respect to environmental factors like temperature and mechanical stress. Here, on one hand, the inductive pickup does not rely on temperature-sensitive capacitances, which can significantly influence the splitting ratio of a capacitive divider. On the other hand, also impedance matching may be affected by temperature variations as well as mechanical stress, with the inductive pickup offering a convenient solution: when using an antenna with a low Q for impedance matching, the reactive part of the impedance cancels out on resonance such that even when electronic components are affected by temperature or mechanical stress, impedance matching does not change. Other measures taken by us to improve RF power stability was the enclosure of all components contributing to the RF network in a closed box, improving temperature stability of the electronics, as well as implementing an active temperature stabilization of the PI circuit.

In order to estimate the RF voltage that is applied to the trap, three different methods can be employed: First, when picking off a fraction of the RF signal at the helical resonator coil with a capacitive divider, the splitting ratio depends on the electronic components of the circuit. Here, a small fraction on the order of 1/500 to 1/1000 is typically used e.g. as a feedback signal for the RF stabilization circuit. This splitting ratio can be calculated as well as measured, which afterwards allows one to infer how much RF power is applied to the trap by measuring the small fraction. Second, the RF voltage applied to the trap can be determined by multiplying the input voltage, created via the frequency generator, with the gain of the RF network, consisting of RF amplifier and helical resonator gain. The gain of the RF amplifier is known from its specifications, the gain of the helical resonator can be determined from the frequency and FWHM of the resonance. Third, a measurement of the secular frequencies of an ion stored in the trap can be compared to simulations in order to estimate the RF voltage, which typically yields the most accurate result.

DC Voltages

In order to generate stable DC voltages a 16-channel high voltage module[11] is used. The voltages required for creating a suitable potential are rather low, on the order of few tens of volts. Thus, voltage dividers with a division ratio of 1:11 are used to harness the benefits of operating this device at high voltages, i.e. lower voltage drift rates and noise levels. The voltages are further filtered via first-order lowpass filters at cutoff frequencies of 300 Hz to suppress noise in the secular fre-

[9] Here, we obtain values of about 50 ms using a spin echo sequence. The PID controller was, however, also tested integrated into other setups with a lower heating rate where a motional coherence time of up to 200 ms was achieved.
[10] 18/20 bit DAC corresponds to about 16/4 Hz mode frequency resolution
[11] ISEG EHS F2 20p_SHV, maximum voltage 2kV DC

quency regime while allowing for the possiblity of fast DC voltage control on millisecond time scales[12]. The shape of the trapping potential is controlled via application of voltage sets to the 12 segmented DC electrodes of the ion trap. These voltage sets allow certain actions on the ion crystal to be performed, decoupled from other actions, e.g. increasing the confinement along one of the principal axes, and shifting/rotating the ion crystal along and around those axes for micromotion compensation. The calculation of these voltage sets is based on the simulations presented in sec. 4.1.1, and solving an inversion problem to link the required action on the ions to the voltages that need to be applied on the individual electrodes [131]. For more information on these voltage sets see the thesis of Dominik Kiesenhofer.

4.2 Vacuum System

Photographs and CAD drawings of our vacuum setup are shown in fig. 4.6. As discussed in sec. 3.1.3, Langevin collisions of the ions with background gas can result in a variety of problems when working with trapped ions, among them melting and structural phase transitions of the crystal lattice. Therefore, a lot of effort was on trying to establish excellent vacuum conditions in our setup. One option for achieving this would be to operate the ion trap in a cryogenic environment, where reduced outgassing of volatile substances and the lower vapor pressure of gases at low temperatures facilitates reaching pressures below 10^{-12} mbar. However, cryogenic systems are intricate, expensive and may introduce mechanical vibrations that compromise laser-ion interaction relying on phase stability. A room temperature ion trap setup is thus a more convenient option, but it is more challenging to achieve excellent vacuum conditions there. In our setup several measures were taken for this purpose: First, the custom-designed stainless steel vacuum vessel was low-hydrogen annealed ("vacuum-fired") by the manufacturer. In this process the vessel is baked in a vacuum oven at 1050°C for two hours, after which hydrogen outgassing is reduced significantly: in [132] two orders of magnitude improvement were reported compared to untreated stainless steel chambers. Moreover, any solder and glue in vacuum is avoided: all electrical connections are plugged, crimped or clamped. Metallic in-vacuum parts were plasma-polished, air-baked and designed in a way which allows for sufficient venting to avoid virtual leaks. All in-vacuum parts[13] were thoroughly cleaned in an ultrasonic bath in multiple stages using degreaser and distilled water, acetone (except for copper parts), isopropanol and methanol. A vacuum-bake of the complete system at 200°C for several days concluded the system assembly. In order to maintain good vacuum conditions a combined non-evaporative getter (NEG) Ion-Pump module[14] as well as an additional NEG close to the trap are employed.

In vacuum the ion trap is mounted onto a Titanium frame which provides thermal anchoring as well as electrical ground (see e.g. 4.6a and b). Attached to the frame are also two alumina printed circuit boards (PCBs), that serve as an interface between the wires coming from the electrical vacuum feedthroughs and the golden wirebonds connecting to the trap (50 µm diameter). A calcium ablation target is held by a titanium aperture ("funnel") which reduces the spatial extend of the atomic beam during ablation loading to avoid coating the trap and viewport with calcium.

[12] Fast control has not been necessary in the experiments conducted in the course of this thesis but may be useful e.g. for resolving metastable configurations of the crystal lattice.
[13] Note, that the ion trap was not cleaned by us, besides blowing away dust particles from its surface.
[14] SAES NexTorr D500-5

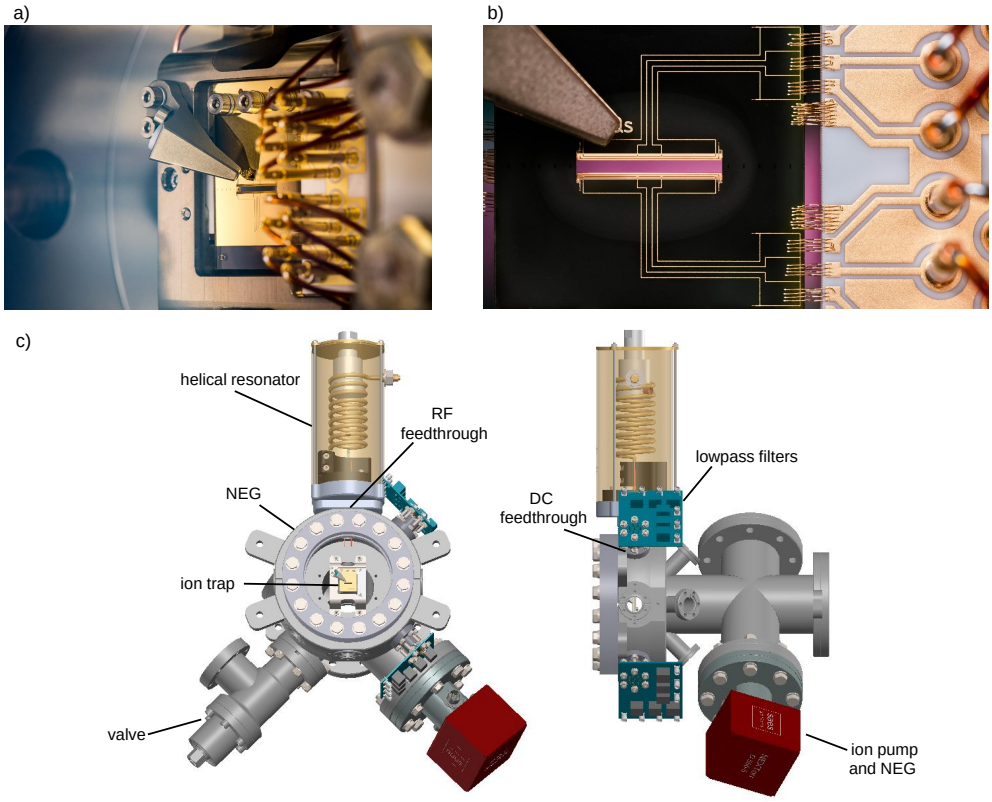

Figure 4.6: Ultra-high vacuum setup: a) Ion trap side view: The trap is attached to a titanium frame on which an ablation target is mounted with a funnel aperture to reduce the extent of the atomic beam. The photograph is taken from the side corresponding to the direction from which Doppler cooling lasers are applied. The 0.3 mm aperture in the funnel, through which calcium atoms fly into the trap center, is visible in the reflection on the trap surface. b) Ion trap front view: Here the wirebonds are well visible connecting the trap's DC electrodes to one of the alumina interposer boards on the right. Attached to the board are pins which are connected to Kapton insulated wires which in turn are connected to the vacuum feedthroughs. These two photographs were taken by David Jordan. c) Vacuum setup CAD model front and side view: Four (two) plates with through holes are welded to the front (back) of the chamber to attach it to an aluminium profile structure. On top of the chamber the golden helical resonator is shown, directly attached to the RF vacuum feedthrough. Two filter boards shown in blue are attached to the DC vaccum feedthroughs that are mounted onto the right diagonal flanges of the octagon. Excellent vacuum conditions in the setup are sustained by the NexTorr module, shown in red as well as an additional NEG in the octagon (left top flange). All other flanges are closed by viewports for laser beam access. Not shown in the rendering: in-vacuum electrical connections, viewports.

The geometry of the vacuum chamber can be seen in fig. 4.6c and d. The trap is installed in the center of a six inch spherical octagon chamber which possesses eight CF16 flanges in the corpus. The trap is placed at a distance of 28 mm from a CF100 viewport allowing for ion imaging with a

high numerical-aperture (NA) objective. On the back side of the trap the octagon is welded onto a CF63 tube, through which vacuum pumping is achieved. Four CF16 flanges in the back allow for optical access from 45° directions with respect to the main axes.

4.3 Magnetic Field

In contrast to other ionic species such as $^{43}Ca^{+}$, making use of e.g. hyperfine ground-state levels to encode qubits, the electronic states in $^{40}Ca^{+}$ ions are much more sensitive to magnetic fields. It is thus essential to provide a stable and low-noise magnetic field environment for the trapped ions, in order to achieve sufficient control over their quantum states: to lift degeneracy of the Zeeman states, the manifold is split up with a well-defined and stable magnetic field. This field establishes a quantization axis, allowing the selective excitation of the ions' electronic state on specific transitions via laser fields of suitable direction and polarization (see sec. 3.2.1). Stability of the magnetic field environment is on one hand crucial on short timescales in order to sustain coherence, i.e. maintain a stable phase relation between the drive field and the atomic qubit during qubit manipulation. On the other hand, stability is also required on longer timescales to maintain resonance between the drive field and atomic transition. In our system a stable magnetic field environment is ensured by employing permanent magnets to create the quantization field, and placing the vacuum system inside a magnetic field shielding box, protecting the ions from external magnetic field noise generated in the laboratory environment.

4.3.1 Quantization Field

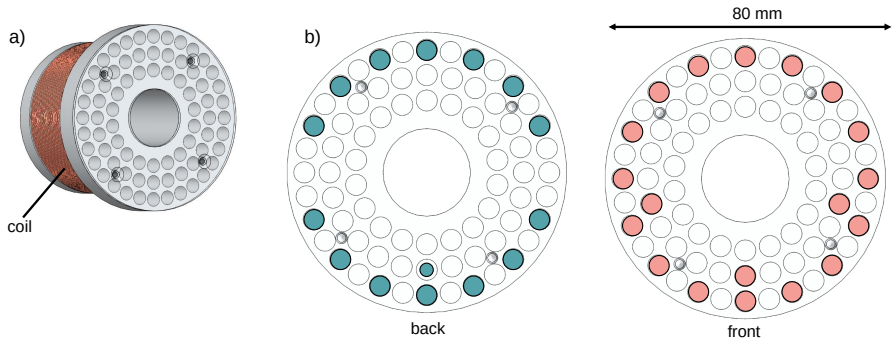

Figure 4.7: Creation of the quantization field: a) Combined holder for permanent magnets and current-driven gradient-compensation coils. b) Configuration of permanent magnets producing the quantization field. This configuration was found empirically when attempting to produce a field of roughly 4 G in the trap center while minimizing the magnetic field gradient present across an ion crystal. One of the circles in the back holder is not entirely filled as here it was necessary to use a 2/3 piece of a magnet rather than a whole one, in order to optimize the field gradient.

The quantization axis is defined by 33 and 2/3 cylindrical[15] Samarium Cobalt (Sm_2Co_{17}) magnets, creating a magnetic field of approximately 4 G in the trap center. The magnets are placed into

[15] diameter: 6 mm, length: 10 mm

holders in three concentric rings[16], as shown in fig. 4.7. Asymmetric placement of the magnets into the two holders partially compensates a field gradient along the y and z directions, such that only low currents on gradient compensation coils are necessary for optimization (see below). The magnet holders are placed symmetrically around the trap at a distance of 125 mm from the trap center. The orientation of the magnetic field is set within the horizontal plane at a 45°angle with respect to the main trap axes, as shown in fig. 4.9.

The advantage of using permanent magnets for creating the quantization field over using current-driven coils is an increased stability due to absence of noise from current drivers, typically dominated by 50 Hz noise. In order to quantify the improvement constituted by permanent magnets, the QSIM team performed Ramsey experiments within the $3^2D_{5/2}$ manifold[17], coupling the $m_j = -3/2$ and $m_j = 5/2$ states before and after replacing their current driven coils with permanent magnets. An improvement of coherence time from 7.9(3) ms to 123(7) ms was observed on this transition [133]. Due to the low sensitivity to temperature changes of Sm_2Co_{17} (reversible temperature coefficient of about 0.03 % per K, according to the manufacturer), the magnetic field produced by the magnets is also expected to be less sensitive to temperature fluctuations than a field created by current-driven coils. The magnet holders in our apparatus do, however, also incorporate two pairs of coils[18]. One pair of coils in anti-Helmholtz configuration[19] compensates the residual magnetic field gradient in the trap center, to avoid transition frequency differences across the ion crystal. Here, a current of about 10 mA[20] is sufficient to minimize the gradient to a transition frequency shift of the ground-state qubit of about 10 Hz across a 91-ion crystal that extends over up to 40 µm along y and 110 µm along z. An additional coil pair in Helmholtz configuration offers the possibility for e.g. feed-forward compensation of periodic external magnetic field noise [134], such as 50 Hz. However, this has not been necessary as the magnetic-field shielding in combination with a clean electrical environment in the lab provide sufficient noise suppression. More importantly, though, these coils will likely be used in the future for compensation of global low frequency magnetic fields, caused by a tram line that is approximately 80 m away from the laboratory and gives rise to ground state qubit transition frequency shifts on the order of 30 Hz on time scales of 10 s when a tram is passing by (see also next subsection).

4.3.2 Magnetic-Field Shielding

Any change in magnetic field that the ions are exposed to results in transition frequency shifts according to the Zeeman effect. Low-frequency magnetic field drifts, e.g. generated by a near-by elevator or tram line, may result in the inability to maintain resonance between e.g. a laser and the respective electronic transition, making constant re-calibration during long measurements necessary. Higher frequency magnetic field noise, on the other hand, may lead to decoherence. Here it is expected that 50 Hz and multiples are the dominant noise source, created by the mains hum. Section 4.8.1 presents strategies on how to reduce the effect of mains hum on the ions, by avoiding

[16] radii 35 mm, 27.75, 20.5 mm
[17] In this case only the magnetic field would contribute to decoherence as the laser frequency approximately drops out.
[18] coil inner diameter 39 mm, outer diameter 65 mm, width 20 mm, wire diameter 0.9 mm, about 340 windings.
[19] Space constraints on the breadboard limit the possible radii and thus prevent implementation of an ideal Helmholtz coil pair geometry.
[20] Power supply CAENEL Easydriver1020

the occurrence of ground loops in the laboratory. However, a magnetic field shielding is still required to provide a stable magnetic field environment for the ions over the complete range range of relevant frequencies. The magnetic field shielding, shown in fig. 4.8a, is manufactured by the company Imedco AG. It consists of several layers of mu-metal and aluminium which attenuate DC and AC magnetic fields (see frequency dependence in fig. 4.8b) created in the vicinity of the experiment. The shield allows the ground state qubit coherence to be increased to about 130 ms without spin echo and 370 ms with spin echo (see sec. 5.5), respectively, while without shield and taking care to avoid ground loops, coherence was completely lost within several ms. Unfortunately, the DC attenuation of the shield is not sufficient in order to protect the ions from the magnetic field created by the tram line, which is on the order of 1 mG, measured on the outside of the shield close to its surface. Before inserting the experimental setup into the magnetic field shielding, a degaussing/demagnitization procedure was performed in order to reset the DC attenuation. For this purpose, coils along the three principal axes of the shield were installed by the manufacturer to which a current of several amperes was applied in several cycles over a timescale of about a minute.

The weight of the experimental setup must not rest on the mu-metal as mechanical stress would negatively affect the shielding performance. Thus, the shield possesses five holes in the bottom, for aluminium posts on which the experimental setup rests on. More specifically, the setup is mounted onto a honeycomb breadboard, resting on vibration-isolating sorbothane pads, that are connected to the aluminium posts.

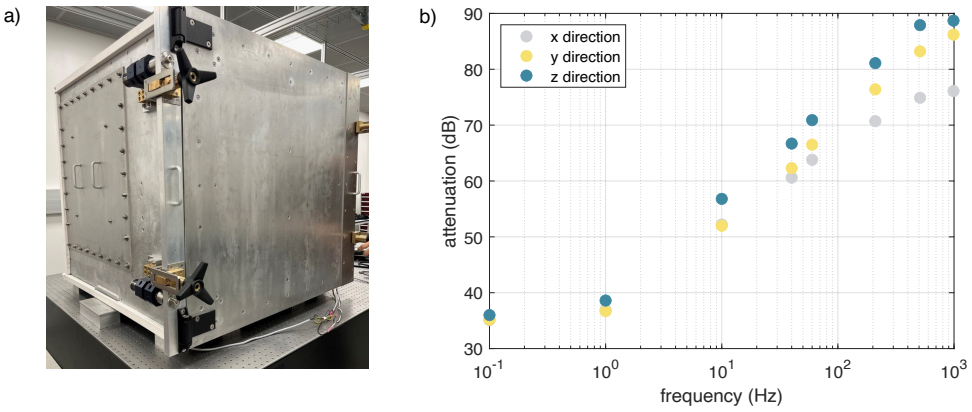

Figure 4.8: a) Magnetic field shielding manufactured by Imedco AG. The front door is aligned with the x-direction defined previously. Windows on all other sides offer access to the experimental setup. b) The attenuation of the shield was measured by the manufacturer Imedco AG along three spatial directions and is found to be within specifications.

4.4 Laser Systems and Optical Setups

In order to create ions, cool them and control their quantum states, a variety of laser systems is used. This section provides an overview of the lasers as well as the optical setups to generate,

frequency- and phase-control and precisely time laser pulses. The experiment control hardware to drive the acousto-optic elements within the optical setups is presented later on in sec. 4.8.3.

4.4.1 Overview of Laser Systems and Beams

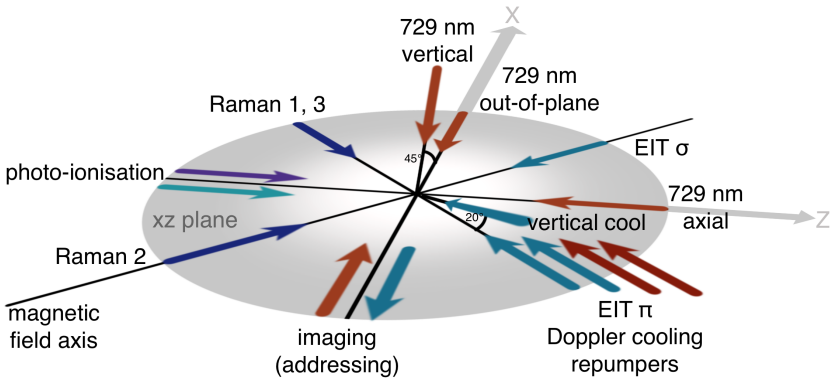

Figure 4.9: Overview of all the laser beams used in the experiment: Ions are trapped in the yz plane. Most laser beams are within the xz (horizontal) plane, with the exception of the vertical 729 nm and cooling beam, which have a 45 degree and $\sim$ 20 degree angle with the xz plane, respectively. Not shown in this image is the ablation laser beam for ion loading, which comes from the bottom along the y direction.

Figure 4.9 illustrates all directions used for optical access in the experiment, to image and laser-address the ion Coulomb crystals, with most laser beams lying within the horizontal xz plane. All beams within this plane are perpendicular to the micromotion of the ions, which aligns with the vertical (y) direction. In order to image the ions an objective is placed close to the front viewport of the vacuum chamber. More details on the imaging can be found in sec. 4.6. After this thesis work is concluded, the objective is also used to address individual ions in the crystal with tightly focused laser beams, which will be presented in the thesis of Artem Zhdanov. Photoionization beams at 422 nm and 375 nm are focused through the holes of the trap chip along the axial (z) direction. The ions are Doppler cooled (397 nm cooling laser with repump lasers at 854 nm and 866 nm) from a direction orthogonal to the quantization axis, from which coupling to all in- and out-of-plane motional modes of the crystal is possible, with the exception of the vertical center-of-mass mode[21]. EIT cooling of the out-of-plane motional modes of the ion crystals is achieved via two beams at 397 nm, a circularly polarized beam that is propagating along the quantization axis, and a linearly polarized one[22] that is propagating perpendicular to it. Two 729 nm laser beams are available in the horizontal plane, to coherently manipulate the ions on the optical qubit transition for shelving and spectroscopy, or couple to the crystals' motional modes: one beam from the back that allows for coupling to the out-of-plane motion and can be used for sideband cooling, and one beam from the axial direction. Lastly, there are three Raman laser beams, used for ground

[21] Cooling of all motional modes of ion crystals consisting of a few ions and more is still possible from this direction. The reason for this is so far not understood.

[22] More specifically, the beam's polarization is within the plane spanned by the beam's k vector and magnetic field axis.

state qubit manipulation as well as realization of entangling interactions via coupling to the out-of-plane motional modes. Similarly to the EIT beams, they propagate along and perpendicular to the quantization axis, respectively. However, in order to avoid differential Stark shifts, both Raman beams are linearly polarized, one horizontally and one vertically, as explained in sec. 3.3.5.

Laser beams which are not within the horizontal plane are indicated with angles in fig. 4.9. A 729 nm beam at a 45°angle with the horizontal plane can be used to couple to both in- as well as out-of-plane motional modes of the crystal. This beam has overlap with the micromotion and can be used for compensation purposes or to perform spectroscopy on in-plane modes that are not accessible from other directions. A second Doppler cooling beam at a $\sim$ 20°angle with the horizontal plane allows for cooling of the y direction ("vertical cooling"), which is needed when trapping small Coulomb crystals and single ions. The ablation laser beam for loading calcium ions into the trap comes from the bottom (not shown in the figure).

All beams in the horizontal plane are set up with a small vertical angle in order to avoid back reflections of laser light which can result in experimental errors. Such errors may e.g. result from changes in laser-ion coupling depending on the phase difference between the incident and reflected light field giving rise to intensity maxima and minima. Piezo-controlled mirror mounts[23] are used for remote-controlled and precise beam alignment when the magnetic field shielding is closed. Photodiodes[24] monitor the power of the beams, which can be used to intensity-stabilize the light directly via our experiment control hardware (see sec. 4.8.3).

Table 4.1: Overview of all laser systems used in the experiment.

Laser System	Wavelength /nm	CW	Purpose	Stability
Coherent Flare NX 515-0.6-2	515	pulsed	ablation loading	free running
Toptica iBeam smart-S	375	CW/pulsed	photo-ionization	free running
Toptica MDL pro HP	422	CW	photo-ionization	WM locked
Toptica MDL pro HP	397	CW	laser cooling	WM locked
Toptica MDL pro	854	CW	repump	WM locked
Toptica MDL pro	866	CW	repump	WM locked
Toptica TA-SHG pro	396	CW	Raman	WM locked
MSquared SolsTis	729	CW	optical qubit	high-finesse cavity

An overview of all laser systems used in the experiment is given in tab. 4.1. With the exception of the ablation laser, all lasers are operated in continous-wave (CW) mode. The Toptica MDL are rack-mounted laser systems, the light of which is guided to the optical setups via optical fibers. All other lasers are installed directly on optical tables, resting on pneumatic vibration isolators. To monitor the frequency of the laser light, a wavelength meter is used. Moreover, MDL and DL lasers are frequency-stabilized to the wavelength meter, as described in the following section. The 729 nm laser requires a higher stability, i.e. a linewidth on the order of 1 Hz, and is thus locked to an optical cavity using a Pound-Drever-Hall laser locking scheme [135].

[23] Liop-Tec PiezoStar with piezos from Physik Instrumente (PI) GmbH & Co. KG
[24] Thorlabs PDA10A2

4.4.2 Laser Wavelength Measurement and Stabilization

In order to measure the wavelength and frequency of all laser systems, as well as stabilize[25] some of them, a HighFinesse wavelength meter model WS8-10 is employed. The wavelength meter measures the frequency of the lasers interferometrically (Fizeau interferometer) with a precision < 10 MHz. One port of the wavelength meter is used for regular automated frequency calibration, using frequency-stable 729 nm laser light.

When a laser is frequency-stabilized to the wavelength meter, a feedback bandwidth of 12 Hz can be achieved in switching mode, the normal operation where multiple lasers are stabilized simultaneously. In order to estimate the linewidth and drift rate of our rack-based lasers, locked to the wavelength meter, a frequency beat measurement of our 854 nm laser with a laser locked to a reference cavity was performed. The beat linewidth was 200 kHz over a timescale of 100 ms, constituting a sufficiently narrow result for our purposes. Additionally, a slow drift of the beat signal of 200 kHz within 15 minutes was observed. However, on top of that, frequency jumps on the order of a few MHz can be caused by vibrations or air pressure fluctuations.

For the diode laser parameter tuning and frequency stabilization, a control program was written where the connection between the Toptica digital laser controller (DLC) and the wavelength meter is established via a server. From the user interface it is possible to control PID values, and wavelength set points.

4.4.3 Ion Creation

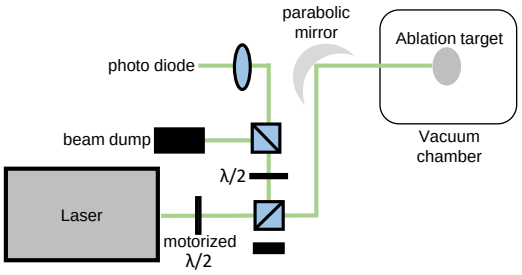

Figure 4.10: Setup of the ablation laser. The power of the ablation pulses is controlled via the motorized waveplate in combination with the subsequent PBS. A small fraction of the light reflected at this PBS is guided to a photodiode which produces a trigger signal for the 375 nm photoionization laser. The ablation light transmitted at the PBS is focused onto the ablation target with a parabolic mirror.

For loading calcium ions into the trap, three lasers are used: an ablation laser, producing an atomic beam of calcium directed towards the trap center, and two photo-ionization beams to ionize the calcium atoms. The ablation laser is a 515 nm pulsed laser system[26], which allows single pulses to be triggered, as well as to be operated in continuous pulse mode with repetition rates of up to 2 kHz. The maximum pulse energy is around 300 µJ. In our case, the laser is typically

[25] A PID loop controls the laser's piezo voltage.
[26] Coherent Flare NX

operated in a way where single or few pulses are triggered. The optical setup for ablation control is shown in fig. 4.10. Here, the laser is focused precisely onto the calcium target via a parabolic mirror[27] in order to achieve a spot size of about 100 µm, such that only about a fifth of the maximum pulse energy is needed for effective ion loading. The power of the ablation pulses is fine-tuned via a motorized waveplate in combination with a polarizing beam splitter (PBS) and is set sufficiently low to mostly ablate neutral atoms from the calcium target. Consequently, we do not directly load ions from the ablation laser but rather rely on photo-ionization of neutral atoms. In this way, isotope selectivity during the ionization process can be ensured by means of frequency-control of the 422 nm laser. More specifically, two laser beams are used to photo-ionize neutral calcium atoms in the trap center: a 422 nm laser driving a cycling transition to an excited state of the desired isotope ^{40}Ca ($4s4p\,^1P_1$), and a 375 nm laser which excites the electron further to the continuum and thus detaches it from the atom. The 375 nm laser is operated in a pulsed way after an ablation pulse is fired. Here, a photodiode in the ablation setup creates the trigger signal such that the 375 nm laser is switched on 10 µs after the ablation. This is implemented for two reasons: First of all due to isotope and Doppler shifts, the 422 nm laser is resonant with fast Ca^{44} atoms as well as the desired slow Ca^{40} atoms. Second, in order to expose the trap to as little as possible 375 nm light which could create charges on the trap electrodes, leading to problems as increasing the number of dark ions or potentially pushing the ions away from the trap center. The atomic beam and the photo-ionization lasers cross at a 45 °angle, which has the benefit of being able to exploit the Doppler shift to select slower atoms from the velocity distribution.

In summary, this method of loading ions into the trap, in combination with control over the ion trap's RF potential, allows fast and deterministic trapping of Coulomb crystals with a desired ion number: The power of the ablation pulses can be set precisely, such that per pulse either a single ion or many ions can be loaded into the trap. In the case that too many ions are loaded into the trap the RF potential can be precisely attenuated to then remove single ions from a crystal. A typical timescale for obtaining a crystal with a desired ion number is on the order of one minute, keeping the preparation time for an experiment low.

4.4.4 Laser Cooling and Quantum State Detection

The possible cooling methods in our experimental setup include Doppler, EIT and sideband cooling. This section presents the laser setups for Doppler and EIT cooling, as sideband cooling is performed on the optical qubit transition using 729 nm light and the optical setup for this laser is discussed in the subsequent section. For Doppler cooling, light at 397 nm is used, red detuned from the $4^2S_{1/2} \longleftrightarrow 4^2P_{1/2}$ transition. To enable continuous cooling, additional repump lasers at 854 nm and 866 nm remove population from the long-lived $3^2D_{5/2}$ and $3^2D_{3/2}$ states. A fraction of the 397 nm light scattered by the ions is collected with an objective for quantum state detection via the electron shelving technique, as described in sec. 3.3.4. During detection only the 866 nm repump laser is switched on along with the 397 nm laser. Ground state cooling via EIT is also performed at 397 nm, the laser light in this case however is blue detuned by about 110 MHz from the $4^2S_{1/2} \longleftrightarrow 4^2P_{1/2}$ transition. The optical setups for the 397 nm laser and repump lasers are shown in fig. 4.11 and fig. 4.12, respectively.

[27] Thorlabs MPD169-P01, silver coated with effective focal length of 152.4 mm.

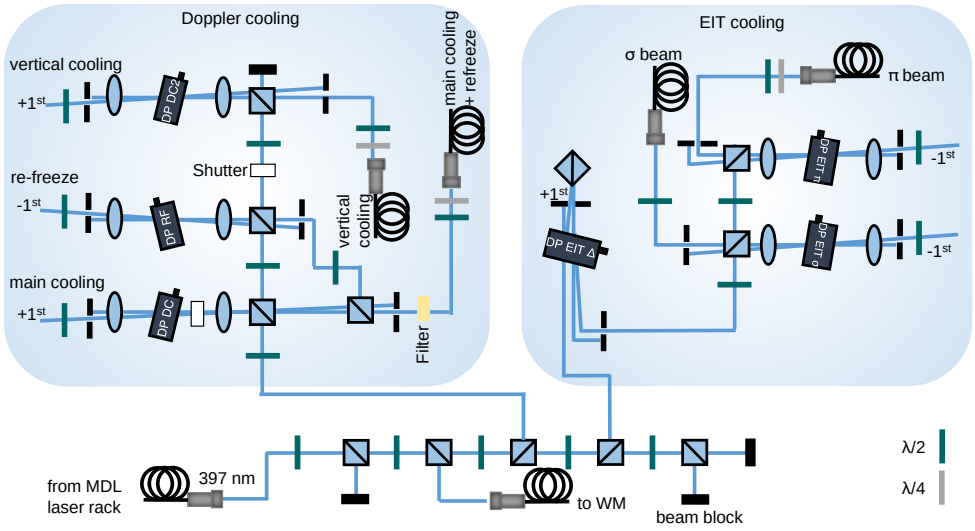

Figure 4.11: Optical setup of the 397 nm laser system. The left part of the setup controls the three Doppler cooling beams (main cooling, vertical cooling and re-crystallization), while the right part controls the EIT cooling beams. More information on the optical and electronic elements comprising the setup can be found in the main text.

397 nm setup

Light from the rack-based MDL laser system is out-coupled and split into several parts. A small fraction is coupled into a fiber to the wavelength meter for wavelength monitoring and stabilization. The rest of the light is subsequently split into two paths leading to setups for controlling the Doppler cooling and EIT light, respectively. In the Doppler cooling setup three AOMs[28] in double pass configuration provide frequency control and switching for three Doppler beams. Two Doppler beams (main cooling and vertical cooling) have the same frequency, approximately 10 MHz red-detuned from the $4^2S_{1/2} \longleftrightarrow 4^2P_{1/2}$ transition. Two shutters in the setup block leaking light from one cooling beam when using the other one. An additional far-red detuned refreeze beam approximately 330 MHz from the $4^2S_{1/2} \longleftrightarrow 4^2P_{1/2}$ transition is used to re-crystallize the ions in case of a melting event. The re-crystallization light is coupled into the same fiber as the main cooling light and sent to the trap setup. Before the fiber coupler, a bandpass filter is placed[29] to attenuate light at 393 nm emitted from the 397 laser in a process of amplified spontaneous emission, which lead to significant unwanted coupling on the $4^2S_{1/2} \longleftrightarrow 4^2P_{3/2}$ transition. This would lead to detection errors, as the electron can end up in the $3^2D_{5/2}$ state, and should thus be avoided. The light for the vertical cooling beam is coupled into a separate optical fiber.

In the EIT cooling setup, an AOM[30] in a double pass configuration is used to adjust the detuning of the EIT light from the $4^2S_{1/2} \longleftrightarrow 4^2P_{1/2}$ transition. This AOM contains a quartz

[28] Gooch&Housego 3080-125, at 80 MHz center frequency, TeO_2 crystal
[29] Alluxa F97-396 subnanometer bandpass filter, center wavelength 396.92 nm, bandwidth <0.45 nm
[30] Intraaction ASM-2002B8, center frequency 200 MHz

crystal that requires vertical polarization in order to diffract light. For this reason it is not possible to operate it in a "typical" double pass configuration, where the separation of in and output beams is based on them having different polarizations[31]. Thus, the beam has to be reflected back into the AOM via a prism, that creates a small (horizontal) displacement between in and output beam that enables their separation at the output with a small D-shaped mirror. Two additional AOMs[32] in double-pass configuration allow frequency control and switching of the individual EIT beams. In summary, the frequency shifts add up to a blue detuning of roughly 110 MHz from the $4^2S_{1/2} \longleftrightarrow 4^2P_{1/2}$ transition. The two EIT beams (σ and π beam) are coupled into two optical fibers through which the light is sent to trap.

Repump Laser Setup

The repump laser setup consists of components to control the 854 nm and 866 nm beams. Fiber beam splitters attached to the rack-based lasers couple $\sim 5\,\%$ of the light directly to the wavelength meter, while the remaining light is coupled out on the optical table. The light of the two individual lasers is frequency shifted and switched by their respective double-pass AOMs[33], then overlapped and coupled into a single optical fiber which guides it to the ion trap setup.

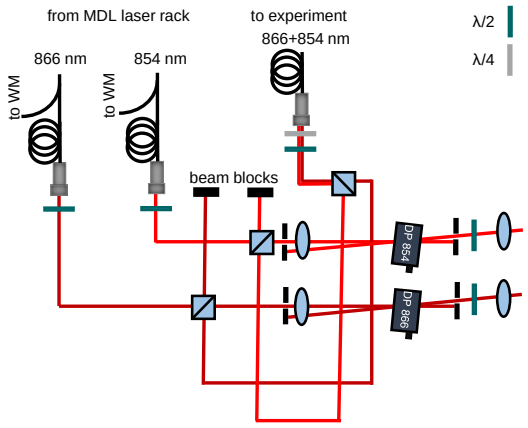

Figure 4.12: Optical setup of the repump lasers. While outcoupling the light onto the optical table, a fraction is split off with a fiber beam splitter guiding the light to the wavelength meter. The 854 nm and 866 nm laser are switched via an AOM in double-pass configuration, overlapped and coupled into a single optical fiber, guiding the light to the ion trap setup. All lenses have a focal length of 200 mm.

[31] When using polarization-insensitive AOMs, the light with vertical polarization would pass through the AOM one time, after which its polarization is converted to circular via a quarterwaveplate. Reflection at a mirror causes the circular polarization to switch to the opposite direction, the beam passes the quarterwaveplate again and is converted to horizontal polarization. After the second pass through the AOM, the in and output beams can then be easily separated with a PBS.

[32] Gooch&Housego 3080-125, center frequency 80 MHz, TeO_2 crystal

[33] Gooch&Housego 3200-124, center frequency 200 MHz, TeO_2 crystal

4.4.5 Coherent Manipulation

Two laser systems are available for coherent manipulation of the quantum state of the ions. A 729 nm laser allows for manipulation on the $4^2S_{1/2} \longleftrightarrow 3^2D_{5/2}$ optical qubit transition. In order to manipulate the ground state qubit, a laser system at 395.8 nm is employed, coupling the two Zeeman states of the $4^2S_{1/2}$ manifold off-resonantly via a Raman transition. By detuning the laser close to the out-of-plane motional modes of the crystal this laser interaction creates entanglement between the ions.

Optical Qubit

Light from frequency-stable lasers at 729 nm is kindly provided to us from other ion-trapping teams in neighboring labs. Most measurements were performed using the Titanium-Sapphire laser of the Distributed Quantum Systems team, with the light sent to our experiment through a 20 m long optical fiber. The laser is locked via a Pound-Drever-Hall laser locking scheme, to an intrinsically stable reference cavity with a finesse of about 160000. This setup achieves stabilization to a laser linewidth on the order of a few Hz [135]. Due to unreliable performance of this laser, in particular the pump laser, it will soon be replaced by a diode laser system, which, containing an intracavity EOM for high bandwidth feedback and supported by a filter cavity, should provide sufficiently low-noise laser light. In the meantime, diode laser light at 729 nm from another laboratory focused on quantum information experiments (AQTION), was used. No fiber noise cancellation was implemented on the fiber link with a length of tens of meters, such that the laser linewidth on our side is on the order of about 10 kHz. While this broad linewidth would not be suitable for some of the measurements presented in this thesis (e.g. high resolution spectra, thermometry), it suffices for optical pumping and shelving operations during quantum state detection, e.g. in the measurements presented in sec. 6.2. For these purposes it is more important that the lock is stable and no frequency components are present outside the laser linewidth which could e.g. couple resonantly to motional modes.

The optical setup controlling 729 nm light in our laboratory is shown in fig. 4.13. A distribution setup splits the light arriving from the remote laboratory into paths for the wavemeter, and two tapered amplifiers (TAs). The amplified light from the TAs is fiber-outcoupled and sent to two AOM networks. The first network controls the light that will be used for individual-ion adressing, which is not yet implemented during writing of this thesis and is thus omitted here. The second network is used for frequency control and switching of three 729 nm beams: the out-of-plane, axial and vertical beam. Here, we use a high-bandwidth AOM[34] in double pass configuration to bridge the frequency of all Zeeman transitions from the $4^2S_{1/2}$ to the $3^2D_{5/2}$ manifold as well as the micromotion sideband, about 43 MHz detuned from the carrier transition. For switching of the in-plane and vertical beam two single-pass AOMs[35] are used. The out-of-plane beam is switched with a fiber AOM[36] which allows for the possibility of applying a bichromatic drive without changing fiber coupling. After guiding the light to the ion trap setup through optical fibers, there are about 70 mW of power available per beam to manipulate the ions, which results in a Rabi frequency of up to about 200 kHz.

[34] Brimrose TEF-270-100-729, center frequency 270 MHz, bandwidth 100 MHz, TeO_2 crystal
[35] Gooch&Housego 3080-125, center frequency 80 MHz, TeO_2 crystal
[36] Gooch&Housego MM080-1C2V14-5-F2SH-B

In the context of this thesis, operations on the optical qubit transition are used for various purposes, such as: spectroscopy of the motional sidebands e.g. to determine the trapping confinement and for qualitative and quantitative thermometry measurements, micromotion compensation, sideband cooling, optical pumping to prepare a well-defined Zeeman ground state at the start of an experiment, and quantum state readout[37].

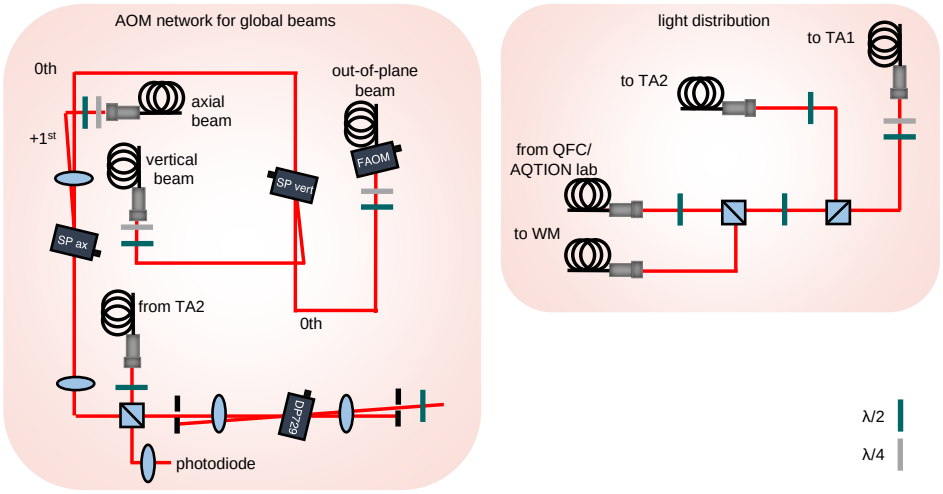

Figure 4.13: Optical setup to control 729 nm light. The light (tens of mW) arrives from a neighboring laboratory through an optical fiber and is then split into paths to the wavelength meter and two TAs which amplify the light to several hundred mW (setup on the right side). Light from TA2 is sent to the AOM network shown on the left for switching and frequency-controlling three 729 nm laser beams (out-of-plane, vertical and axial beam). For the out-of-plane beam a fiber-AOM is used.

Raman Laser

To create light at 395.8 nm[38] for coupling the ground-state qubit on a Raman transition, we initially installed a frequency-doubled Titanium-Sapphire laser. Such laser systems provide high output powers in the UV, a prerequisite for driving far-detuned and at the same time fast interactions in order to create strong coupling of spins in quantum simulation experiments. However, problems with the pump laser and frequency-doubling stage resulted in the purchase of a replacement laser, a custom diode laser system from Toptica. The Toptica system contains a TA and frequency-doubling stage (fundamental at about 792 nm) and provides an output power of 1.5 W at 395.8 nm. A benefit of the new laser apart from its experimental robustness is that water cooling, which can be intricate, is not required, and motorized ultrastable mirror mounts inside the laser allow for automatized internal alignment and output power optimization. While the free-running laser linewidth of below 50 kHz on a timescale of 5 µs is narrow for a Toptica diode

[37] Quantum state readout of the ground state qubit requires it to be mapped to the optical qubit via a 729 nm pulse, followed by fluorescence detection at 397 nm to distinguish bright and dark states.

[38] This is the "magic wavelength" at which differential Stark shifts between the S and D states cancel, as discussed in sec. 3.3.5

laser system, due to the use of a longer laser resonator, a Titanium-Sapphire laser would provide an intrinsically lower linewidth, typically on that order over a timescale of 100 µs. However, in the case of Raman transitions this is irrelevant due to the following arguments: First, the Raman transition is driven with far off-resonant laser beams (about 0.4 THz detuned), i.e. small frequency fluctuations on the order of MHz do not significantly alter the coupling strength. Second, frequency noise of the laser is not harmful if the noise is common-mode to both Raman beams. However, the optical setup needs to be interferometrically stable to ensure phase stability of the Raman beams with respect to each other. To this end, we employ a single laser to generate both Raman beams and ensure that the interferometer formed by the two paths is balanced to a precision far below the respective frequency fluctuations. The optical path length of the two Raman beams differs by less than 10 cm due to the way in which the optics are set up. In order for a relative phase shift between the two beams to be a small fraction of π, the relative path length should not change by more than a few ten nm.

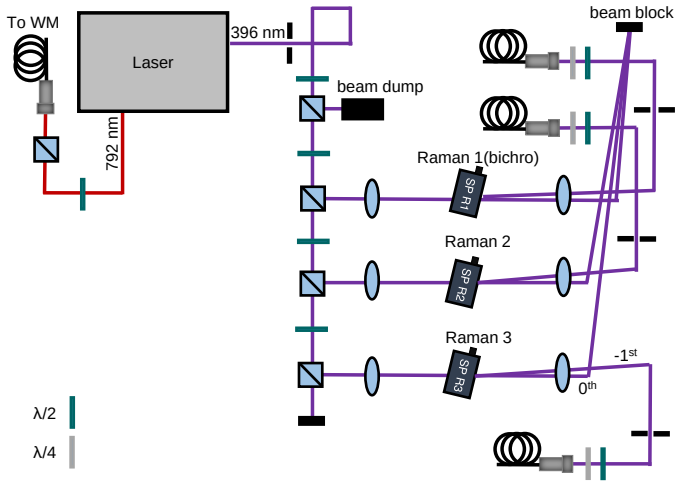

Figure 4.14: Optical setup of the Raman laser: The fundamental light is coupled into a fiber guiding it to the wavelength meter for frequency monitoring and stabilization. The frequency-doubled light is aligned in free space into three AOMs in single pass configuration. Here, AOM 1 controls the interaction beam and is thus driven in a bichromatic way. All lenses in the setup have a focal length of 300 mm. The light diffracted at the AOMs is coupled into three optical fibers via home-build and sealed couplers and guided to the ion trap setup. Note that the third Raman beam was removed during the writing of this thesis as the RF antenna presented in the next subsection suffices for driving carrier trasitions on the ground-state qubit.

The optical setup to control the Raman laser beams is shown in fig. 4.14. The fundamental light is sent to the wavelength meter for frequency monitoring and stabilization. The frequency-doubled light is split into 3 different arms, one for each Raman beam, and switched with single-pass AOMs[39]. These AOMs are based on crystalline quartz, able to sustain the high powers in the

[39] Gooch & Housego, I-M110-3C10BB-3-GH27, AOM 1 operated at about 96 MHz driven with a bichromatic RF signal for the generation of entangling interactions, AOMs 2 and 3 operated at about 107.4 MHz, to create resonance on the ground state qubit transition at 11.4 MHz.

UV of several hundred mW that they are exposed to. In general, throughout the optical setup, high-quality polarization optics[40] suitable for intense powers are in use. The light diffracted at the AOMs is coupled into three optical fibers, guiding it to the ion trap setup. Here, great care is taken to cope with the high power densities which can easily damage optics and fibers, in particular fiber facets: End-capped fibers[41] reduce the beam intensity at the fiber's air-to-glass interface, decreasing the chance for damage there. Moreover, dust within the fiber coupling stage, which could burn onto optics (focusing lens and fiber facet) and thus exacerbate damage, is reduced via home-built sealed fiber couplers. But, there is still the chance of solarization within the fiber, i.e. UV-induced color-centre formation, which can attenuate light passing through. By only sending light through the fiber during experimental sequences its lifetime is thus extended. A second problem, besides the damage to optics due to high UV powers, is that UV light scattered at the trap might result in charging effects that could perturb the trapping potential or lead to the detachment of atoms which subsequently form dark ions. To ensure a beam profile as clean as possible, only few optical elements of high quality are used before the trap. For example, the lens for fiber out-coupling also focuses the laser beam onto the ion crystal[42].

The Raman beam waist in the trap center is about 500 µm, which for powers of about 300 mW per beam, results in Raman Rabi frequencies around $2\pi \cdot 200\,\mathrm{kHz}$. Some other characteristics of the Raman beams such as scattering rate and coherence when probing the ground-state qubit transition are given in sec. 5.5.

As described in sec. 3.3.5, the three Raman beams can be used in different combinations in order to drive different types of interactions. Here, specific polarizations of the beams are required: The polarization of the beam propagating along the magnetic field axis should be circularly polarized in order for $\Delta m = 1$ transitions to be driven. However, this would result in differential Stark shifts which affect the Zeeman ground state levels by a different amount such that the qubit would acquire an additional phase. Intensity noise would then lead to phase noise on the qubit and thus to decoherence. To circumvent this problem only linearly-polarized beams are used, where the differential Stark shift is zero. The beam propagating along (perpendicular to) the magnetic field axis is vertically[43] (horizontally) polarized using Glan-Laser polarizers[44]. The differential Stark shift was measured to be only about 200 Hz across a 91-ion crystal, instead of the 120 kHz that would be expected if circularly polarized light was used at this intensity. The small residual differential Stark shifts are likely caused by beam focusing, which may introduce additional polarization components beyond the intended linear polarization.

[40] Bernhard Halle Nachfl. GmbH

[41] OZ Optics

[42] Note, that the Raman optical setup for focusing the beams onto the ions has been under constant development over the last year and many components have been tested to find the optimum. Details on these optics will thus be given in the upcoming PhD thesis of Artem Zhdanov.

[43] The linear vertical polarization can be considered as a superposition of σ_+ and σ_- polarizations, but only one of the transitions is possible. The coupling strength is thus reduced by a factor of $\sqrt{2}$ due to half of the intensity of the beam not contributing to the coupling.

[44] Thorlabs GLB10-405

4.5 Radiofrequency Antenna

Besides coupling the ground-state qubit optically on a Raman transition, it can also be coupled directly via an RF field, oscillating at approximately 11.4 MHz. Benefits of driving interactions without laser beams include typically good global control of the ion crystal that is unaffected by beam intensity profiles, no unwanted coupling to the ions' motion and less phase noise compared to using lasers due to the longer wavelength of the radiation. This section presents the electrical design of the RF antenna which generates the magnetic RF field to drive the ground state transition. The antenna essentially consists of a wire loop outside the vacuum chamber directly at the front viewport, as seen in fig. 4.15a, which along with a capacitance forms an LC resonator. Additionally, an impedance matching network maximizes the transfer of RF power into the antenna. A simplified circuit is shown in fig. 4.15b. The loop dimensions are: 35 mm coil diameter, 0.8 mm wire diameter, number of windings 5, and inductance of about $L =\approx 2\,\mu\text{H}$[45]. The resonance condition at around $f = 1/(2\pi\sqrt{LC}) = 11.4\,\text{MHz}$ is achieved by placing a capacitor of about $C = 98\,\text{pF}$ in series with the coil. The Q of this resonator is about 18, determined via the resonance frequency and FWHM. From $Q = 1/R\sqrt{L/C}$, an effective resistance of about $R_{loss} = 8\,\Omega$ can be estimated. This resistance results from parasitic loss and is hard to determine a priori. However, its influence on the resonator Q has important implications: it limits the power efficiency of the resonator. Impedance matching in order to maximize the power of the RF signal is achieved via passive components summarized as $L_M = 244\,\text{nH}$ and $C_M = 231 - 271\,\text{pF}$ (variable capacitance). Obtaining suitable values for these components required a combination of an analytical calculation and empirical process, i.e. testing different values and observing the power transfer/reflections.

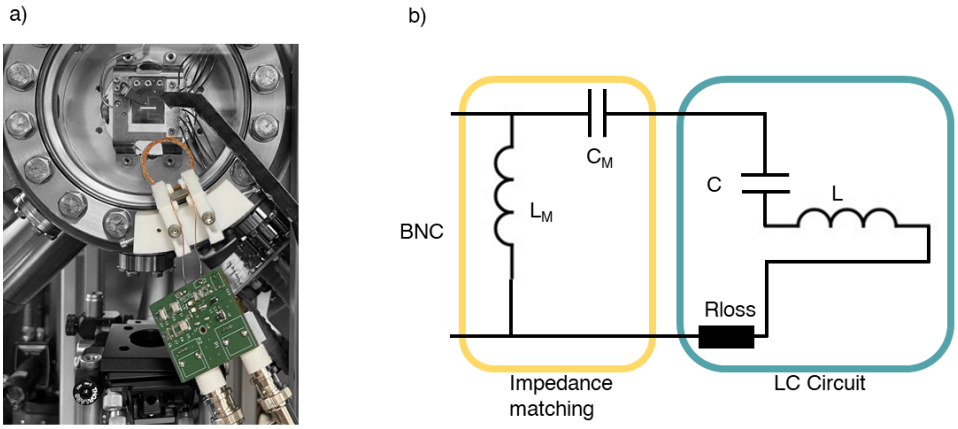

Figure 4.15: RF antenna for producing the magnetic field oscillating at 11.4 MHz to drive the ground-state qubit transition: a) Image of the RF antenna installed at the vacuum chamber front viewport. The wire loop can be seen in copper in front of the glass, with the circuit board for impedance matching shown in green. b) Simplified circuit diagram of the RF antenna with impedance matching network. The values of the capacitances and inductances are $L_M = 244\,\text{nH}$, $C_M = 231 - 271\,\text{pF}$, $R_{loss} = 8\,\Omega$, $C = 98\,\text{pF}$ and $L \approx 2\,\mu\text{H}$

[45] Here it was important to avoid large coil inductance that relates to requiring tiny capacitances to achieve the desired resonance frequency.

The RF signal supplying the circuit is provided via a DDS[46] within the experiment control hardware system (see sec. 4.8.3). The signal is further amplified[47] and galvanically isolated with a transformer[48] to reduce ground loops. In order to increase suppression of the DDS an additional switch[49] is used in the connection line.

In the end, the achievable Rabi frequency when coupling the ground-state qubit with a RF signal created by this setup is about 100 kHz, without any decay of oscillations on timescales of hundreds of ms. In terms of the homogeneity of the interactions, the Rabi frequency varies by 3.5 percent over a large crystal comprised of 91 ions.

4.6 Ion Fluorescence Detection and Imaging

The fluorescence light emitted by the ions during Doppler cooling carries relevant information about their state. For example, it allows us to determine information about ion positions, localization and thus temperature, and quantum state. As a consequence, the most important tools for optimizing experimental parameters as well as data taking rely on fast and reliable detection of the ions' fluorescence. This sections presents the optics, in particular the objective used for collecting the ions' fluorescence light, as well as the devices for recording it, i.e. the EMCCD camera and PMT.

4.6.1 Imaging Optics

An objective manufactured by the company Sill Optics GmbH[50], that had been available from a previous experimental setup from 15 years ago, was used for the majority of the experiments presented in this thesis. However, the imaging quality of our objective was sub-par, due to aberrations, different objectives from the same production batch seemingly displaying significant quality differences. Moreover, an NA of only 0.289 is not ideal, relating to a low photon collection efficiency. An example of an image taken with the Sill Optics objective is given in fig. 4.16a, showing a 105-ion planar crystal trapped in our apparatus. A high level of light-scattering crosstalk is present in the image, i.e. fluorescence light from an ion, in the shape of flares towards the right side, overlapping with other ions in the crystal. This effect could not be removed by translating the objective. An image with minimal aberrations is, however, useful in order to distinguish with high fidelity bright and dark states of individual ions that are only a few micrometers apart. Due to the higher number of neighboring ions in planar crystals compared to linear ones, excellent imaging quality becomes even more important. Thus, a new objective was custom-designed and installed recently. The new objective was manufactured by the company Photon Gear and was used for measurements carried out in sec. 6.2. An image of a 91-ion crystal taken with this new objective is shown in fig. 4.16b. In comparison with the old objective in 4.16a, the new image is much cleaner, free of aberrations. Moreover, the Photon Gear objective's NA=0.44 is significantly larger than the previous one, allowing for a more efficient photon collection for faster quantum state read-

[46] Direct Digital Synthesizer
[47] Minicircuits ZHL-1-2W+, 2W
[48] MiniCircuits TC1-1-T+
[49] Miniciruits ZASWA-2-50DRA+
[50] custom designed, numerical aperture (NA) 0.289, working distance 58 mm

out as well as more tightly focused addressing beams, which will allow for less crosstalk during single-qubit operations[51]. The NA and related to that the diameter of the objective is limited by the available space around the vacuum chamber. Here, the main limitation arises from the optical access required for the laser beams propagating along and perpendicular to the magnetic field axis, at 45 degrees with respect to the main axes. The objective is placed at a working distance of 45 mm on a five-axis control stage which allow precise tilting and displacement in all directions. Besides being designed and anti-reflection coated for the imaging and addressing wavelengths, 397 nm and 729 nm, the objective additionally can be used at 532 nm. The intention for implementing this feature was to open up the possibility for experiments where high-power light at this wavelength is used to perform operations on individual qubits.

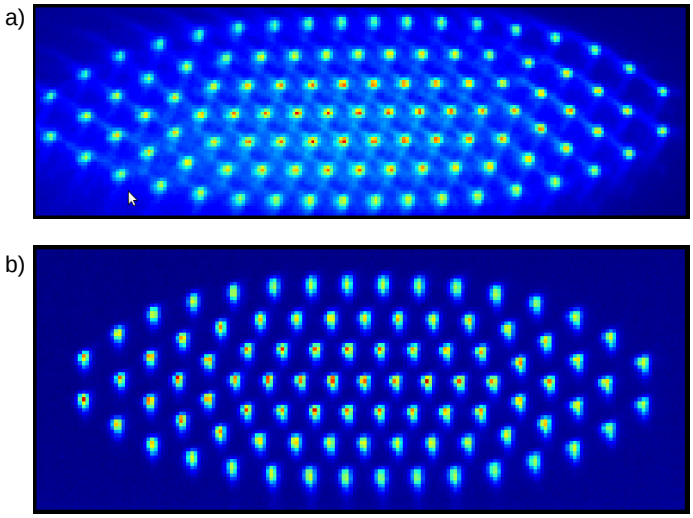

Figure 4.16: EMCCD camera image of a) a 105-ion Coulomb crystal imaged with the Sill Optics objective and b) a 91-ion crystal imaged with the new Photon Gear objective. Most experiments in this thesis were carried out with the Sill Optics objective, the Photon Gear objective, which demonstrates a significant improvement in imaging quality, having been installed only towards the end of this thesis work.

4.6.2 EMCCD Camera and Photomultiplier Tube

The ions' fluorescence light, collected by the objective, is guided, split and focused onto the chip of an EMCCD camera[52] and a photomultiplier tube (PMT)[53]. Narrowband filters[54] in the optical path block any stray light from the other laser beams, in particular the high-power Raman

[51] During this PhD work, the objective was used only to collect fluorescence light. The second purpose of the objective is to focus 729 nm laser beams to diffraction-limited diameters on the order of 1 µm, to address individual ions in the crystal. At the end of writing this thesis, the optical setup for this purpose had been built by Artem Zhdanov.
[52] Andor iXon Ultra 897
[53] Sens-Tech Photodetector module P25PC
[54] Alluxa F97-396 subnanometer bandpass filter, center wavelength 396.92 nm, bandwidth <0.45 nm

beams, such that the camera and PMT are only exposed to light at 397 nm. The camera constitutes the most critical device for data taking, allowing for spatially resolved and thus ion-specific fluorescence detection, to detect quantum states and lattice structure of the ions (see also subsequent section). For high-fidelity detection the imaging time needs to be sufficiently long. While the Sill Optics objective originally necessitated an imaging time of approximately 5 ms, the introduction of the new Photon Gear objective significantly reduced this duration to around 500 µs. This enhancement cannot be solely attributed to the increased Numerical Aperture (NA) of the new objective. Rather, it suggests that the photon collection efficiency of the Sill Optics objective was, for some unknown reason, considerably below the level that should have been achievable. Complementary to the camera, the PMT allows for fast detection of the ions' overall fluorescence signal, useful for calibration purposes, e.g. maximizing fluorescence counts when aligning lasers and optimizing laser parameters, as well as determining e.g. if an ion crystal has melted (see sec. 5.3.1).

4.7 Analysis Tools for Ion Crystal Images

The EMCCD camera allows for the spatially-resolved detection of the ions' fluorescence signal, which is needed for reading out the quantum states of the ions and analyzing the crystal's lattice structure. However, gaining relevant information from such an image requires a variety of analysis tools to be applied to the image data, which are presented in this section. In general, the problem can be described as having N emitters (ions), m pixels of the camera image where each pixel can take on a value in a certain range. The pixel values of a camera image can be stored in a $m \times 1$ vector, and if we consider n camera images, those pixel values can be stored in an $m \times n$ matrix. Then, mathematical tools, described in the following subsection, are applied to this matrix to extract relevant information. In our experiment this information consists of the location of individual ions in a crystal, to count them and classify configurations of the crystal lattice, and to detect if an ion is bright or dark for quantum state analysis. Measuring the quantum state of individual emitters in engineered quantum systems, also in other experimental platforms besides ions, can be particularly challenging. The close spatial proximity of emitters with respect to each other and the necessity for short detection times, associated with few fluorescence counts, can lead to errors. In particular in 2D systems, where an emitter has a higher number of neighbors than in 1D, light scattering crosstalk, where the light from an emitter spills over to the location of another emitter, can be problematic. Thus, a new scheme for quantum state analysis based on unsupervised learning was developed which allows for robust quantum state readout even in the presence of strong light scattering crosstalk resulting from the aberrations in our imaging system[55].

4.7.1 Mathematical Tools for Image Data Processing

Singular Value Decomposition (SVD)

The SVD is one of the most important tools in numerical linear algebra, oftentimes used in the context of dimensionality reduction in data processing and as the foundation of many machine learning applications. The SVD decomposes a matrix into singular values and vectors as described

[55] This issue was minimized by exchanging the Sill Optics objective with the Photon Gear one.

in the following. If we represent the image data as an $m \times n$ matrix $\mathbf{M}$ then the singular value decomposition is given by

$$\mathbf{M} = \mathbf{U}\mathbf{\Sigma}\mathbf{V}^T \tag{4.2}$$

where $\mathbf{U}$ and $\mathbf{V}$[56] are unitary matrices, and $\mathbf{\Sigma}$ is a diagonal matrix, which can be understood in an intuitive way: If columns of $\mathbf{M}$ represent individual images, then columns of $\mathbf{U}$ represent "eigenpictures", a basis in which to represent any image stored in $\mathbf{M}$. $\mathbf{\Sigma}$ stores the coefficients corresponding to these eigenpictures ordered in a hierarchical way, meaning that they are ordered from largest to smallest. These singular values are thus representative of the relative importance of a certain eigenpicture in describing the images in the dataset. That means that the data matrix $\mathbf{M}$ may be approximated by the first N dominant eigenpictures and corresponding singular values while neglecting small values (truncation):

$$\mathbf{M} \approx \mathbf{U}_N\mathbf{\Sigma}_N\mathbf{V}_N^T \tag{4.3}$$

Intuitively this can be understood as reducing a large image into the key features describing it, thereby reducing the data that is needed for its representation. Consequently, the computational complexity can be reduced which enhances an algorithm's speed. To understand the physical significance of $\mathbf{V}$ we consider that the matrix $\mathbf{M}$ also represents a time series of images. $\mathbf{V}$ would then be related to an eigen-timeseries, describing how the individual eigenpictures evolve in time.

Since the SVD naturally captures key features in the data, such as dominant patterns or correlations, it is closely related to an eigenvalue problem involving the data's correlation matrix:

$$\mathbf{M}\mathbf{M}^T = \mathbf{U}\mathbf{\Sigma}^2\mathbf{U}^T \tag{4.4}$$

The columns of $\mathbf{U}$ are consequently at the same time the eigenpictures of $\mathbf{M}$ as well as the eigenvectors of the correlation matrix $\mathbf{M}\mathbf{M}^T$, $\mathbf{U}$ thus capturing correlations in the columns of $\mathbf{M}$[57]. Moreover, the non-zero singular values obtained from SVD are the square roots of the eigenvalues of $\mathbf{M}\mathbf{M}^T$ and $\mathbf{M}^T\mathbf{M}$.

Principal Component Analysis (PCA)

While the SVD is a general matrix factorization technique which can also be used for dimensionality reduction, PCA is an application of the SVD specifically in the context of dimensionality reduction. As discussed in the preceding subsection, high-dimensional data oftentimes contains underlying patterns and correlations that can be distilled into a more compact representation. The PCA focuses on capturing variations in the data by identifying orthogonal directions (principal components) that maximize the variance. It is usually applied to centered data, meaning that in a first step the mean $\bar{\mathbf{M}}$ is subtracted from the data matrix $\mathbf{M}$.

The principal components are again ordered hierarchically, allowing for the determination of suitable cutoffs to approximate the original data. The number of components selected defines the precision of the representation.

[56] Here ^{T} represents the transpose of the matrix $\mathbf{V}$.

[57] Analogously, the columns of $\mathbf{V}$ are the eigenvectors of $\mathbf{M}^T\mathbf{M}$, thus $\mathbf{V}$ capturing correlations in the rows of $\mathbf{M}$.

Independent Component Analysis (ICA)

While PCA focuses on finding correlations by maximizing variance in a data set, ICA focuses on maximize independence in the data. More specifically, ICA is a method for unmixing a dataset representing a composite signal into its constituent signals. A well-known application of ICA is the "cocktail party problem", where a mixture of multiple audio signals such as conversations, music and other noise is recorded by multiple microphones. Then, it is possible via ICA to separate the mixture of audio signals into the individual sources without any prior knowledge about them. This concept is also called blind source separation. Applications of ICA extend beyond audio signals and are also relevant in image processing. An image which is comprised of contributions from different sources can be separated into a set of additive images that are statistically independent from each other. Just as in the audio example, where the different microphones each record a different linear combination of the source signals, here we have a set of images stored in the data matrix $\mathbf{X}$, each representing a different linear combination of statistically independent source images $\mathbf{S}$. These can be mathematically represented as

$$\mathbf{S} = \mathbf{W}\mathbf{X} \tag{4.5}$$

where $\mathbf{W}$ is the transformation ("unmixing") matrix which achieves the separation. An ICA algorithm essentially determines $\mathbf{W}$ and $\mathbf{S}$ simultaneously in an iterative process, adjusting the matrix entries in such a way that the estimated source signals become as statistically independent as possible, quantified by measures such as non-Gaussianity.

Voronoi Tesselation

Voronoi tessellation is a mathematical method used in image analysis for e.g. image segmentation and pattern recognition. It divides a space into different parts, defined by cells, each cell corresponding to a generator or seed point which is placed on a feature of interest within the image. The Voronoi cells are represented as polygons with edges that are equidistant to their neighboring seeds. Any pixel within a cell is thus closer to the cell's respective seed point than to any other seed point in the image.

Density-Based Clustering of Applications with Noise (DBSCAN)

DBSCAN [136] is an algorithm often used in machine learning applications related to pattern recognition or feature extraction, which identifies clusters of datapoints in a dataset. The clusters are defined as dense regions of data points which are separated from other clusters by regions of lower density[58]. Noise points that do not belong to any cluster are identified as outliers. This ability of being able to handle noisy data as well as clusters of different sizes and arbitrary shapes, and especially the ability to automatically determine the number of clusters without user input make DBSCAN an important tool in unsupervised learning applications.

[58] The space in which this algorithm classifies data into clusters is sometimes referred to as the feature space of the dataset, its dimensionality defined by the dimensions of the data points, each dimension corresponding to a feature of the data.

4.7.2 Ion Number Counting

Before any experiment can be performed on an ion crystal, it is necessary to perform a calibration procedure of the camera program. Here, a set of $10^3 - 10^4$ reference images is taken, where ions are randomly prepared in bright or dark states by applying a global $\pi/2$ pulse. These reference images form the basis for automatic ion number counting and quantum state readout, as explained in the following.

For counting the ion number automatically the camera program produces an average image, on which all ions are visible, and identifies the locations of the individual ions. The program then calculates Voronoi cells where the center position of each ion corresponds to a seed point, such that the number of cells corresponds to the number of ions in the image. An example of Voronoi cells partitioning the image of a 91 ion crystal is given in fig. 4.17, demonstrating the number of neighbours of an ion in a graphical way.

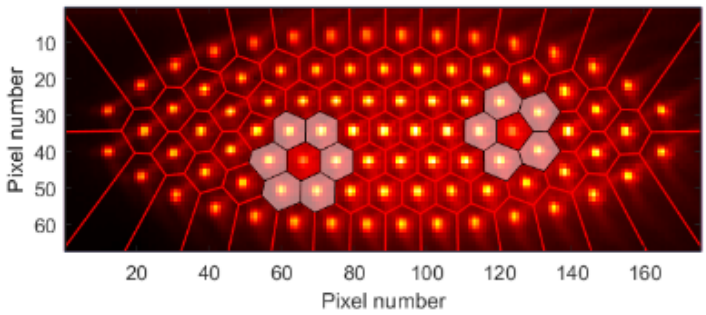

Figure 4.17: Voronoi tesselation partitioning a 91-ion image for automatic determination of the ion number.

4.7.3 Unsupervised Learning for Trapped-Ion Quantum State Readout based on Fluorescence Images

Data analysis for the experiments presented in this thesis requires the ability to measure the quantum state of all individual ions in a Coulomb crystal. In other words, it is necessary to be able to distinguish if a certain ion in a crystal is either bright or dark on a camera image. This is most simply done by dividing the image into regions of interest (ROI) around the locations of each ion, and then defining a threshold of the added pixel values in the ROI, above which an ion is considered as bright. This endeavour is complicated by the necessity to keep illumination times of the crystal for imaging purposes short (on the order of a few hundred microseconds to few milliseconds). Short illumination times are required for several reasons: First, the qubit may decay to the ground state during the detection time which leads to quantum state readout errors. Since each qubit has the potential to decay these errors add up and become particularly problematic in large ion crystals. Second, it is desirable to increase the cycle time, i.e. the number of experiments that can be performed in a certain time. And third, adverse effects such as heating of the ions from scattered photons should be minimized. While a short detection time reduces the chance that the qubit decays during detection, it may also lead to other readout errors: For

example, an ion being wrongly considered dark due to low fluorescence signal, or an ion wrongly considered bright due to background light scattered at the trap, or fluorescence light from a neighboring ion spilling over to pixel values in the region of interest of the ion to be measured. Established methods to minimize such errors in threshold discrimination for trapped ion systems are the use of maximum-likelihood estimation (MLE) techniques [137][59] or supervised learning [138]. However, these methods require complex characterization measurements, which might become unfeasible for large 2D crystals in particular. In our approach we employ unsupervised learning for quantum state readout of trapped ions. The advantages of unsupervised learning are that the algorithm explores the data and identifies underlying patterns by itself without requiring a target output. Our algorithm is presented in detail in a forthcoming publication, the most important steps are given in the subsequent subsections. In summary, the algorithm takes the reference images in which the ions are randomly prepared in bright and dark states as an input and applies SVD, PCA and ICA to construct a set of projectors. These projectors contain information about the contribution of an individual ion to the image of the entire ion crystal, while subtracting fluorescence crosstalk from other ions.

Introduction and Motivation

In the experiment, light is detected by individual pixels of the EMCCD camera chip, as sketched in fig. 4.18a. The detected light is a sum of the fluorescence light scattered by the ions and background light, typically laser light that is scattered on the experimental setup or background counts from the CCD chip. In the simplest case, considering one pixel which only receives fluorescence light from a single ion, the photon counts can be described by a histogram, modeled as a bimodal distribution, as shown in fig. 4.18b. More specifically, this represents the scenario where an ion that may be in one of the two qubit states is detected repeatedly to obtain the statistics represented by this distribution. The left part of the bimodal distribution corresponds to the ion not fluorescing, the signal on the detector only relating to background light. The right part represents the bright state, where background as well as fluorescence light from the ion contributes. The individual distributions can, in a simple model, be described as normally distributed with mean μ and standard deviation $\sigma = \sqrt{\mu}$. A natural way to distinguish the bright and dark states is to place a threshold between the two distributions. Whenever a count rate falls into one of the two regimes below or above the threshold, the state of the ion is counted as dark or bright, respectively. But, the two distributions have some overlap, the counts of a weakly fluorescing ion overlapping with the counts corresponding to strong background light. This can lead to detection errors, where an ion's state can be misclassified. In order to minimize the detection error, the threshold t is set such that

$$t = \frac{\mu_d \sigma_b - \mu_b \sigma_d}{\sigma_b - \sigma_d}, \tag{4.6}$$

[59] Here, the quantum state of neighboring ions is estimated.

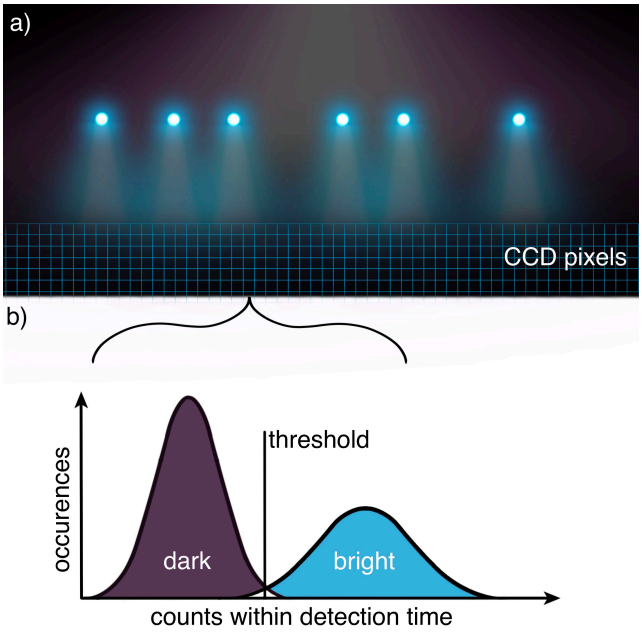

Figure 4.18: Schematic illustration of measuring the quantum states of trapped ions via detection of fluorescence light with an EMCCD camera: a) Ions (shown in blue, for simplicity in one dimension) scatter 397 nm fluorescence light if in the $4^2S_{1/2}$ ground state and remain dark if in the $3^2D_{5/2}$. The fluorescence light is detected by individual pixels of the camera chip, where the light scattered by multiple ions may overlap on certain pixels. Additionally, background light (shown in purple) is detected. b) The detected fluorescence light can be represented as a histogram, the left part of the resulting bimodal distribution corresponding to background light, i.e. the ion is dark on the camera image, and the right part emerging from a combination of background and ion fluorescence light. The two distribution are separated by a threshold to differentiate the count values associated with dark and bright states. Detection errors may occur due to an overlap of the two distributions.

where state detection errors are equal for the bright and dark states[60]. The state detection error here is given by

$$p_{err} = (1 - \mathrm{erf}(Q/\sqrt{2}))/2, \tag{4.7}$$

where erf is the error function and

$$Q = \frac{\mu_b - \mu_d}{\sigma_b + \sigma_d} \tag{4.8}$$

is a quality factor, the discrimination quality, which is a measure for the separation and thus the distinguishability of the two distributions.

[60] More specifically, this is the optimum threshold for a bimodal distribution consisting of two Gaussians. In practice, spontaneous decay modifies the dark-state distribution; the resulting tail of counts extending towards larger count values requires moving the threshold to higher count numbers to achieve an optimal discrimination in a real experimental system. Thus, a slight modification to the equation is necessary to include the effect of spontaneous emission.

It turns out that the achievable detection error can be reduced by taking into account the signal detected by other pixels on the camera chip. However, if these pixels also receive fluorescence light from neighboring ions besides the ion of interest, detection errors may actually increase as the fluorescence from the neighboring ions contributes to the width of the dark and bright state distributions. But if not all pixels are weighted equally, it is possible to reduce detection errors below the level achievable in the original scenario.

Mathematically, the problem can be modelled as follows. The counts, recorded by a detector consisting of m pixels, are stored in a vector $\mathbf{x} = (x_1, x_2, ..., x_m)$, which can be represented as a sum of contributions from the ions' fluorescence and background:

$$\mathbf{x} = \mathbf{qA} + \mathbf{b} \tag{4.9}$$

Here, $\mathbf{q} = (q_1, q_2, ..., q_N)$ is a vector describing the quantum sate of the N ions, where all q_i can take on either the value 1, indicating a bright state, or 0, indicating a dark state. The $N \times m$ matrix $\mathbf{A}$ describes how much each ion contributes to the counts on each pixel of the detector. The vector $\mathbf{b}$ contains the background counts on each pixel. The goal is to find a weight vector $\mathbf{w}_i$ for each ion i, which, multiplied with the original vector of counts $\mathbf{x}$, yields new distributions

$$y_i = \mathbf{x} \cdot \mathbf{w}_i^T. \tag{4.10}$$

Threshold discrimination of y_i should provide a lower detection error for ion i, than discrimination of summed up counts detected by pixels in the region around ion i. Finding weight vectors $\mathbf{w}_i$, however, is not a straightforward task, as it is hard to determine experimentally to which extent certain pixel values are influenced by the ions' quantum states.

Unsupervised-Learning Algorithm

The algorithm presented in this section employs unsupervised learning to assign with high fidelity the quantum state of each individual ion in a camera image that may contain fluorescence crosstalk. The first step is to take a set of reference images. The process of quantum state assignment can then be divided into different steps, the first of which is a dimensionality reduction, to map an m dimensional vector to an N dimensional space. Then the resulting vectors are mapped onto a new basis, where each coordinate is proportional to the fluorescence emitted by a single ion, independent of the other ions' fluorescence signal. The resulting bimodal distributions are then discriminated via thresholds.

Calibration Step 1: Take a set of reference images

The input data for the algorithm, from which the weights are generated, is a set of n reference images, where the N ions are randomly prepared in bright and dark states, which is straight forward to implement experimentally by a global $\pi/2$ pulse. Four examples from a set of reference images for a 91-ion crystal are shown in fig. 4.19a.

Calibration Step 2: Dimensionality reduction

The $m \times n$ matrix $\mathbf{X}$ stores each reference image in a separate column, where again m is the number of pixels of the detector. Due to the fact that specific pixels in the camera image primarily capture fluorescence from a particular ion, quantum-state dependent correlations emerge in the image sequence. These correlations manifest as certain pixels simultaneously exhibiting darkness

or brightness when a specific ion is either dark or bright. They provide an opportunity for dimensionality reduction, and to transform the high-dimensional data into a lower-dimensional space, with the number of dimensions given by the ion number N. For capturing the correlations and performing the dimensionality reduction there are several options available, such as calculating the pixel covariance matrix $\mathbf{X}\mathbf{X}^T$, subtracting the mean counts and finally diagonalizing this matrix, which effectively corresponds to performing a PCA. The correlations we are interested in are then contained in the largest N principal components, i.e. eigenvectors of the covariance matrix. That this is indeed the case is shown in fig. 4.19c for a 91 ion crystal, where only the first 91 eigenvalues of the correlation matrix are significant. Projecting an image onto the corresponding eigenvectors results in the desired dimensionality reduction. However, diagonalization of the covariance matrix is computationally expensive. But from eq. 4.4 we have seen that the eigenvectors obtained via diagonalization of $\mathbf{X}\mathbf{X}^T$ also correspond to the eigenpictures of $\mathbf{X}$ that can be obtained via a SVD. Since we are interested only in the largest N eigenvectors and values which capture the quantum-state dependent correlations, it is sufficient to carry out a truncated singular value decomposition, computationally less involved than the method suggested above. In this way the normalized data $\mathbf{X} - \bar{\mathbf{X}}$ is represented via the N most important eigenvectors and values:

$$\mathbf{X} - \bar{\mathbf{X}} \approx \mathbf{E}_N \mathbf{\Sigma}_N {\mathbf{V}_N}^T, \tag{4.11}$$

To map a camera image into the N dimensional space, it is projected onto $\mathbf{E}_N$, which forms the reduced eigenpicture basis:

$$\tilde{\mathbf{X}} = {\mathbf{E}_N}^T \mathbf{X}, \tag{4.12}$$

Here and in the following, the tilde sign denotes the vectors which are in the reduced state space.

Calibration Step 3: Mapping to a new basis

Determining the N most important eigenpictures $\mathbf{E_N}$ was an essential step for dimensionality reduction, allowing camera images to be mapped to a reduced state space and simplifying the calculation by harnessing the correlations present in the reference images. In a second step, we want to find a projector which, upon multiplication with a camera image provides the contributions of the individual ions to the image while subtracting crosstalk from neighbors. This projector can thus be thought of as the generalization of the weight vector concept, described in the previous section, for all ions in the system. In order to find the projector $\mathbf{K}$ or the projector in the reduced space $\tilde{\mathbf{K}} = {\mathbf{E}_N}^T \mathbf{K}$, it is first necessary to transform into the single-ion picture basis $\mathbf{S}$. This is a rather intuitive representation, where every image in this basis should display the spatial distribution of fluorescence emitted by a single ion. The single-ion picture basis is found via ICA, where eigenpictures $\mathbf{E_N}$ are represented as a linear combination of single-ion pictures.

$${\mathbf{E}_N}^T \approx \mathbf{W}\mathbf{S}^T, \tag{4.13}$$

Examples of single-ion pictures in a 91-ion crystal are given in fig. 4.19e. The disadvantage of this representation is that in the presence of fluorescence crosstalk in the image set, the ICA algorithm isn't able to find independent source signals which form an orthogonal basis set. For a crosstalk-free discrimination we therefore require the introduction of the projector $\mathbf{K}$, where

$$\mathbb{1}_N = \tilde{\mathbf{K}}^T \tilde{\mathbf{S}} = \tilde{\mathbf{K}}^T {\mathbf{E}_N}^T \mathbf{S}. \tag{4.14}$$

The projector forms an orthogonal basis, the orthogonality arising due to the projector constituting a reciprocal basis to the single-ion picture basis. Examples of projector pictures are shown in fig. 4.19f, corresponding to the single-ion pictures shown in 4.19e. The projector pictures have negative entries at the location of neighboring ions whose fluorescence should not be taken into account, to compensate for the fluorescence crosstalk present in the image.

Once the projector has been determined, it is used for calculating the count distributions $\tilde{\mathbf{Y}}$ of the reference pictures, based on which thresholds $\mathbf{t} = (t_i)$ for quantum state discrimination for each ion i are determined:

$$\tilde{\mathbf{Y}} = \tilde{\mathbf{K}}^T \tilde{\mathbf{X}} = (\mathbf{E}_N \tilde{\mathbf{K}})^T \mathbf{X} \equiv \mathbf{K}^T \mathbf{X} \tag{4.15}$$

The projector $\mathbf{K} = \mathbf{E}_N(\mathbf{E}_N{}^T \mathbf{S})^{-1}$ in this equation projects each picture in $\mathbf{X}$ onto an N-dimensional vector whose elements are proportional to the fluorescence emitted by each individual ion. To quantify the success of this calibration procedure, the discrimination quality, as defined in eq. 4.8, is determined for all ions in the crystal. Here, we expect values above ~ 4, corresponding to detection errors below $\sim 3 \cdot 10^{-5}$ according to eq. 4.7. An example of the discrimination quality is shown for all ions in the 91-ion crystal in fig. 4.19g. Here, an average value of $\langle Q_i \rangle \sim 4.8$ was achieved, with Q_i corresponding to ion i.

Application: Discriminating the quantum state in experimental data

The previous steps are carried out usually in the beginning of the day when a new ion crystal is loaded into the trap, to calculate the projectors $\mathbf{K}$ and thresholds $\mathbf{t}$ for a given ion crystal based on a set of reference images. During experimental measurement sequences, ion crystal images are taken at the end of each cycle. These images are then projected and discriminated in order to determine the quantum states of the individual ions.

Practical Challenges and Error Rates

For large ion numbers and high fluorescence crosstalk, the algorithm may sometimes not work reliably, possibly also due to a jitter of the ion positions, melting of the crystal or configuration changes during the calibration. In this case, the algorithm can be run on a subset of pixels, e.g. on the Voronoi cell for an ion and its neighboring Voronoi cells, as illustrated in fig. 4.17[61].

The error rates achievable with this algorithm, dependent on the number of reference images used, was investigated in another experimental setup with long linear ion crystals (QSIM). Here, it was found that a reference set of at least 500 pictures is sufficient for achieving a discrimination quality of above 4 with a 1 ms detection time. Moreover they found state discrimination error probabilities for this illumination time to be $p_{err} = 4.5 \cdot 10^{-6}$[62], not including errors caused by ions spontaneously decaying from the D state which are on the order of $p_{spon} \approx 1.7 \cdot 10^{-4}$.

[61] After installing the Photon Gear objective this strategy was not necessary any longer due to the low level of fluorescence crosstalk with this objective.

[62] A sequence of 52 measurements enabled the identification of erroneous detection of the ions' quantum states. Initially, some ions were prepared in the bright state and others in the dark state. During subsequent experimental cycles, the ions were only laser-cooled and measured, the expectation being that the number of ions in the dark state decreases due to spontaneous decay. Any deviation from the expected behavior, such as an ion switching states for a single experimental cycle and then switching back, indicates a detection error.

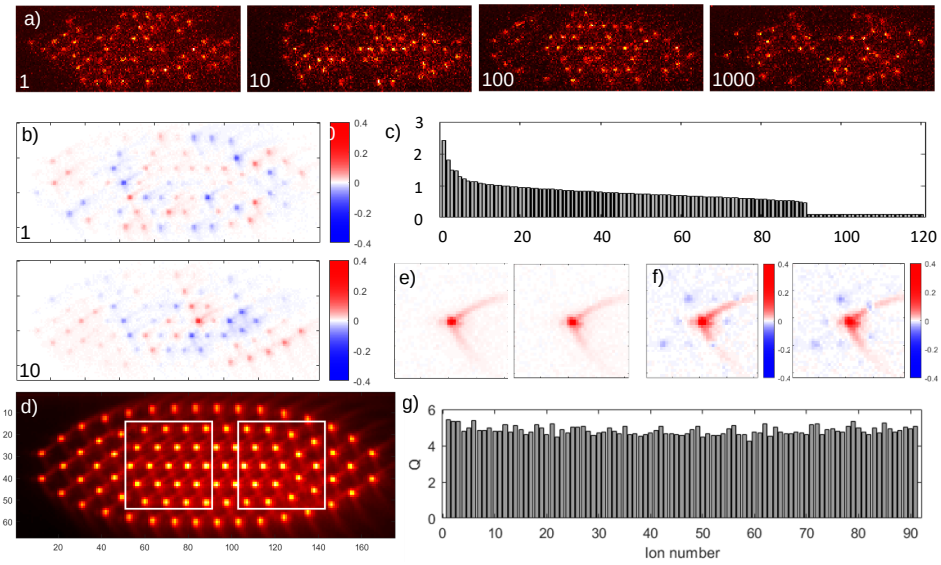

Figure 4.19: Analysis of the quantum state of individual qubits in a 91-ion Coulomb crystal a) Examples of reference images taken with an illumination time of 5 ms (Sill Optics objective), where about half of the ions are in bright and dark states, respectively. b) Examples of eigenpictures found via a PCA of the pixel correlation matrix. c) The first 120 corresponding eigenvalues of the correlation matrix are shown, with only the first 91 values being significant, capturing all relevant quantum-state dependent correlations. d) Average fluorescence of all reference images taken of the 91-ion crystal. e) Single-ion pictures corresponding to the two areas marked in d. f) Projectors for the two ions shown in e. In contrast to the single ion picture basis, here crosstalk from neighboring ions is subtracted. g) Discrimination quality Q for all 91 ions.

4.7.4 Crystal Lattice Configuration Analysis

While taking data it is crucial that the ion crystal remains in a stable lattice configuration as the approach to ion-specific quantum state detection, presented in the previous section, relies on stable ion positions. When tuning the trapping parameters in an optimal way, see sec. 5.3.2, the occurrence of undesired configurations is rare, but still present. Thus, the data, taken during this time when the ions were in a wrong configuration, needs to be removed from the data set. This requires an approach to detect and classify the lattice configuration of the ion crystal, which is briefly summarized in the following, with more details to be found in the thesis of Dominik Kiesenhofer. The classification of different lattice configurations is done in the following way: A time series of images of the ion crystal is taken where all ions are fluorescing, while configuration changes occur due to collisions with background gas or heating effects. The image data is again stored in a matrix and a PCA is applied. Each crystal lattice configuration is represented by a specific linear combination of principal components[63]. Then, DBSCAN can be employed to classify different configurations and visualize them as clusters in the space spanned by the dominant principal components. During experimental sequences, after each quantum state detection,

[63] Typically, for our ion crystals, it is sufficient to use the first 8 principal components for representing all lattice configurations.

an additional image of the ion crystal is taken, where all ions are bright. The experiment control program then computes the principal components of this image and determines which cluster the image belongs to. Should the crystal not be in the correct configuration, the data point taken previously is discarded and the measurement is repeated.

Towards the end of this thesis work another approach to detecting crystal configuration changes was implemented, which eliminates the need for capturing an additional bright ion image subsequent to quantum state detection. The new method is based on monitoring the detection counts. In the event of a configuration change, the projectors may no longer effectively overlap with the ions, such that a bright ion that has shifted away from its original position contributes less light to its own projector but may now contribute to another ion's projector. This manifests in the detection counts, which then tend to be distributed toward the outer edges of the bimodal distribution. To quantify this, an outlier parameter was introduced that considers both the difference of the counts from expected values and the distribution's width. When no configuration change occurs during quantum state detection, the outlier parameter should roughly correspond to the number of ions present. However, if a problem arises, this parameter will significantly deviate from the expected value. This tool not only enables the detection of lattice configuration changes but also the identification of dark or hot (melted) ions without the need to take an additional image of the ion crystal, thus improving cycle time. However, both methods have their limitations. The first method relies on the assumption that the crystal configuration remains unchanged between the imaging for quantum state analysis and lattice configuration analysis. On the other hand, the second method faces challenges when analyzing the configuration of a crystal with a substantial number of ions in the dark state and becomes infeasible when all ions are in the dark state.

4.8 Experiment Control System

The successful operation of the entire apparatus is based on the communication with, control of and interaction between the various individual subsystems. Figure 4.20 provides an overview of the electronic devices controlled via two computers hosting suitable software. The illustration shows aforementioned devices for powering the ion trap, laser light generation and control, and for the detection of the ions' fluorescence light. Additionally shown here are the National Instruments Data Acquisition module (NI-DAQ), used for controlling the power and trigger of the laser ablation for ion loading, and the Sinara system which incorporates modules for generating RF signals (DDSs and AWGs[64]) e.g. to drive AOMs, modules to produce and read digital signals for triggering and counting, and modules for measuring analog signals (ADCs) from e.g. photodiodes for laser intensity stabilization. The control PC runs the main control program named Serles, which coordinates the operation of different components and provides interfaces for device control and data acquisition. The second PC is mainly used to monitor and control the Toptica laser systems.

[64] Arbitrary Waveform Generator

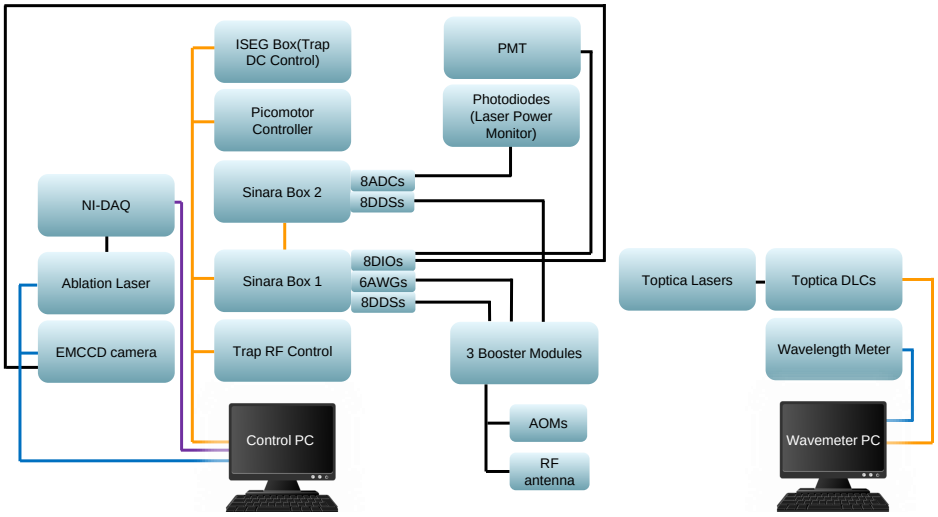

Figure 4.20: Overview of the main parts of the experiment control hardware: Blue, yellow and purple lines represent USB, ethernet and PCIe connections, respectively. Black lines represent connections via BNC or SMA cables. Detailed information on the individual devices and their purpose can be found in the main text.

4.8.1 Avoiding Ground Loops

Controlling the apparatus requires interconnecting many different devices, which can result in the formation of ground loops. Here, the grounds of multiple devices are connected and due to them not being on the same potential current may flow in between them. As a result AC magnetic fields are created in the laboratory environment, oscillating dominantly at 50 Hz, the frequency of the AC mains in Europe, as well as other frequencies. These fields can be detrimental to the qubit, motional and laser coherence in an experimental apparatus and steps need to be taken to minimize them as much as possible. The first step is to supply the whole experiment from a well-controlled number of power sockets and avoid electrical interconnections between them. Since a single socket in our case does not provide enough power for the entire apparatus, devices are connected in multiple star-shaped networks. Communication between different branches is unfortunately sometimes inevitable, which can be realized in the following way: for RF signals, e.g. from a DDS to an AOM, isolation can be established by 1:1 transformers[65]. For TTL signals, Galvanic isolation can be achieved via high speed optocouplers[66] or digital isolators. Devices relying on USB connections are problematic as optical USB cables are rare and not compatible with many devices. Thus, devices based on ethernet connections are preferred. Here, either isolated cables are used or ethernet-to-optical converters[67].

[65] e.g. Minicircuits TC1-1+
[66] e.g. ACPL-064-060E
[67] e.g. TP-Link

4.8.2 Serles Software

The Serles software is the main experiment control program. Its user interface allows control of devices (Sinara Hardware, electronics for controlling the trapping potential and ablation loading) and interprets fluorescence data recorded by the EMCCD camera and PMT. Moreover it incorporates basic data analysis tools such as curve fitting. Serles was mainly developed by Alpine Quantum Technologies GmbH, but is continuously updated and extended in close collaboration with various ion-trapping research teams in Innsbruck to incorporate and accomodate their experiment-specific needs. The most important Serles extensions that the 2D Crystals experiment has developed is the camera program, based on the algorithm presented in sec. 4.7.3.

4.8.3 Sinara Hardware

The main purpose of the experiment control hardware is to create RF signals, which drive acousto-optic elements installed in the optical setups for switching, frequency and phase scanning of laser beams, and TTL[68] signals for triggering devices. Here, timing precision, accuracy, reproducibility and speed are crucial. In terms of speed, all operations created by lasers interacting with the ions have to be performed on timescales much faster than the ion qubits' coherence time, usually on the order of few tens to hundreds of milliseconds. Timing imprecision may lead to over- or under-rotations of the qubit and thus to errors, latency may lead to additional errors. Moreover, typical pulse sequences for quantum experiments oftentimes require many different signals to be generated and processed simultaneously, and pulses to be phase coherent with respect to each other. Experiment control might be further complicated by the necessity for branching, where experimental outputs are processed in real time, and based on the result alterations to the experimental sequence are implemented. This may be particularly relevant for experiments harnessing a variational quantum eigensolver [139] and error correction protocols, but also in a more basic context for e.g. in-sequence re-cooling of a melted ion crystal.

The M-Labs ARTIQ (Advanced Real-Time Infrastructure for Quantum physics) is a commercial open-source system devised for the control of experiments in quantum information science. The hardware, called Sinara, is made in a modular way in order to address different and changing needs in the experiment. The Sinara system in our experiment is comprised of the components listed in tab. 4.2 and discussed in the following. The Kasli-2 module constitutes the core device, a field-programmable gate array with nanosecond timing resolution and sub-microsecond latency, connected via ethernet to the control PC. This module is connected to all other modules described subsequently via the backplane of a crate. RF signals are created via the Urukul or Phaser modules and amplified via Booster modules: The Urukul cards house 4 DDSs which drive AOMs as well as the RF antenna for ground state qubit manipulation. The DDSs work in a frequency range from 1-450 MHz and contain integrated attenuators and RF switches[69]. Urukuls will also be used for steering the tightly-focused addressing beam for manipulation of individual ions' quantum states. However, the Urukul modules don't suffice for all applications where RF pulses are required, as they only generate square pulses. Some applications demand shaped pulses, where the RF power is turned on and off slowly, over a timescale of several microseconds. Shaped pulses optimize the

[68] Transistor–transistor logic

[69] The shortest pulses which can be generated by the hardware are 10 μs

process of inducing transitions between electronic energy levels, while reducing errors from off-resonant excitation. Such errors may arise from the broad frequency profile associated with a short laser pulse. For application where pulse shaping is needed, in particular the 729 nm and Raman beams, acousto-optic elements are driven with a Phaser module, which is a 2 channel AWG that allows for phase-coherent switching. For the bichromatic pulses, the output of two Phaser channels is mixed and then applied to the AOM. After generation of the RF signals, they are amplified by separate Booster racks, 8 channel power amplifiers for a frequency range from 40 to 500 MHz. A Sampler module, which is an 8 channel analog-digital converter (ADC), reads the signals from photodiodes monitoring beam powers and provides feedback to the Urukul and Phasers for laser intensity stabilization. Besides modules for creating and reading analog signals, digital inputs and outputs, are also required. For this purpose 8-channel DIO modules are used. The outputs are used for trigger signals for the EMCCD camera, shutters blocking laser beams, and line trigger[70], as well as TTL signals for switches. A digital input is used for the PMT signal, i.e. for recording the ion fluorescence.

Table 4.2: Overview of Sinara Hardware used in the experiment

Crate	Modules	Channels	Purpose
Master	1 Kasli		central core device
Master	2 Urukul	8	drive AOMs
Master	3 Phaser	6	pulse shaping, bichromat
Master	1 DIO	8	trigger signals, counter
Satellite	1 Kasli		connection to master
Satellite	2 Urukul	8	drive AOMs
Satellite	1 Sampler	8	monitor laser powers

[70] We have the option of using a line trigger in the experiment but after minimizing ground loops in our setup this has not been necessary and doesn't yield an improvement.

CHARACTERIZATION

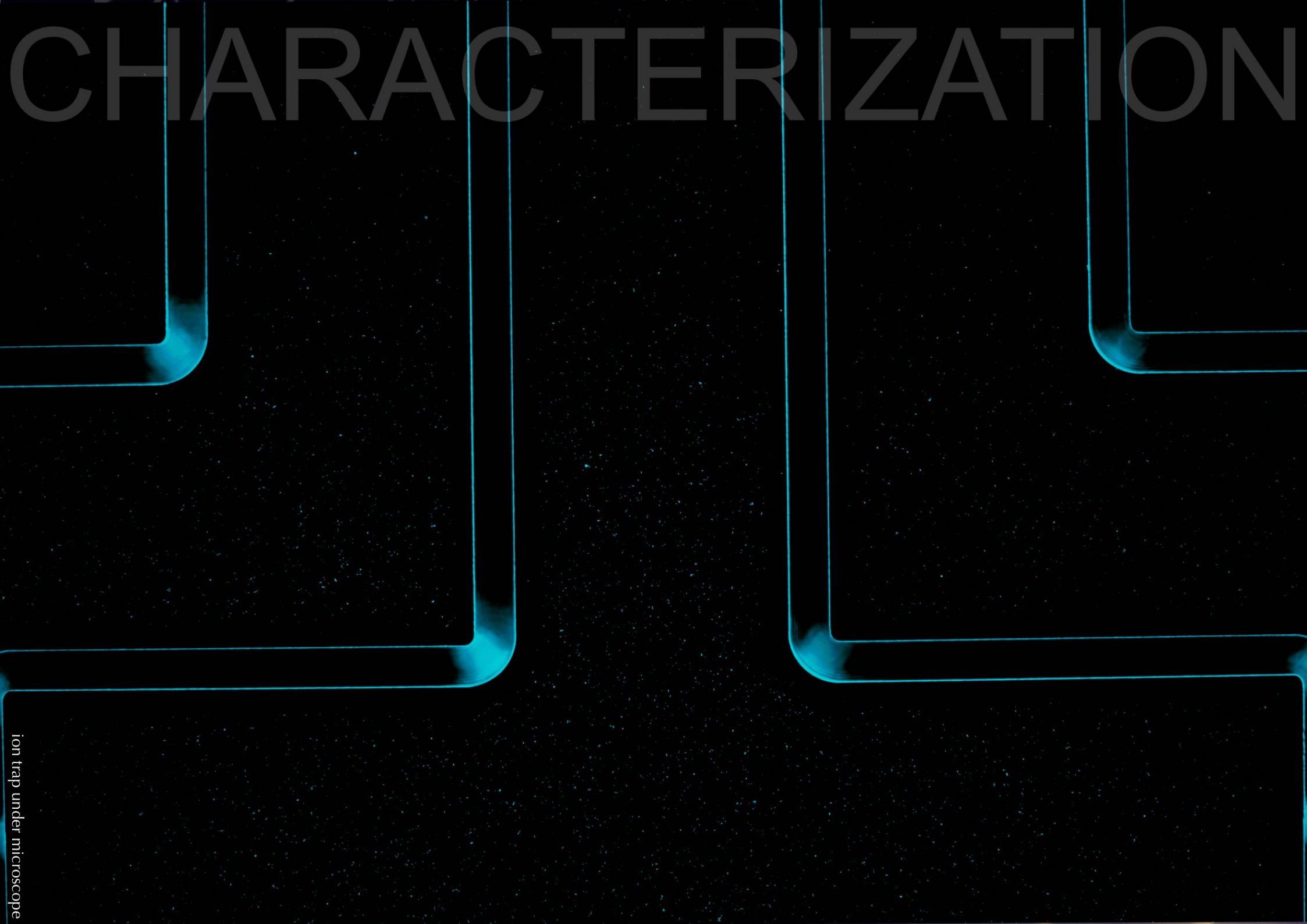

ion trap under microscope

5 Characterization of the Apparatus

This chapter presents characterization measurements, carried out to assess the performance of the apparatus, to explore limitations and capabilities in view of quantum simulation experiments. The technical requirements relevant in this context have been discussed in preceding chapters and are briefly summarized here with an experimental investigation presented in the subsequent sections: The ion trap needs to be able to sustain high enough voltages to allow for secular frequencies on the order of a few MHz in the strongly confined direction and thus allow for efficient laser cooling and sufficiently fast entangling interactions. Furthermore, the heating rate of the trap should be sufficiently low to avoid coupling strength variations and decoherence due to phonon-mode occupation as well as to not put severe limitations on the motional coherence, both allowing for interaction times on the order of tens of ms. The trapping potential should be precisely tunable and low in anharmonicities, resulting in predictable and well controllable ion motion. The lattice of the 2D ion crystals needs to be sufficiently stable for high-fidelity readout and manipulation of the ions' quantum states, and to maintain a consistent structure of the motional modes throughout many experimental repetitions. The ions' out-of-plane motional modes need to be cooled close to the ground state for mediating long-range entangling interactions. These interactions are implemented via global Raman laser beams. Here, it is imperative to achieve high interaction speeds, ideally exceeding 100 rad/s for spins encoded in the $4^2S_{1/2}(m = \pm 1/2)$ ground states, while simultaneously minimizing errors that may arise from factors such as the beams' intensity profiles, aberrations in the focused beam, interferometric instability of the two beams with respect to each other, and spontaneous scattering, as well as undesired polarization components that may lead to Stark shifts.

5.1 Ion Trap

In this section results on ion trap tests are presented. First, the voltage handling capabilities were investigated, putting a bound on the achievable secular frequencies. Here, two different trap chips were tested, the first of which was destroyed in the process, the second of which has remained in operation in the experiment ever since. Moreover, the heating rate of the second trap at the typical operating voltage was determined.

5.1.1 Electrical Testing

Trap 1 in a test setup

Several electrical tests in a UHV environment were performed in order to determine the resilience of the novel trap design during high voltage application. A first trap was installed in a test setup

to explore the voltage limitations via breakdown tests, i.e. slowly increasing the voltage applied to a specific electrode, where eventually, if the voltage becomes too high, the electrode isolation can no longer be sustained. Most segmented DC electrodes of the first trap were tested up to 750 V DC using the ISEG module without observing any breakdown behavior. On one segment the voltage was increased in steps of 100 V up to 1300 V DC, at which point a breakdown occured, characterized by a sudden increase in leakage current to ground. This likely constitutes the limit in DC voltage handling capability for all electrodes.

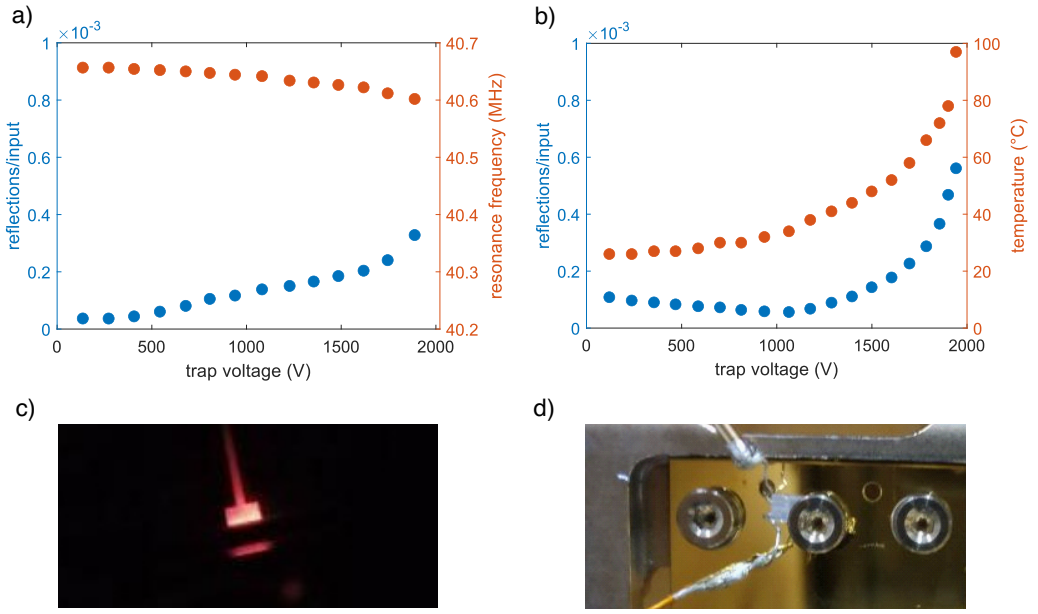

Figure 5.1: Electrical test of the first trap chip in a test setup: In a) the ratio of reflection signal from the helical resonator to input voltage (blue data points) as well as the resonance frequency (orange data points) are plotted as a function of RF voltage applied to one of the central segmented (DC) electrodes. When increasing the voltage to about 2000 V peak-to-peak, the electrode started glowing which is depicted in c. One of the outer segmented electrodes was tested in the same way as the central segemented electrode. The respective data is shown in b. Again blue data points represent the ratio of reflections to input, while here the orange points correspond to temperature values, measured via the sensor shown in d.

In order to estimate the RF voltage handling capability, one of the central segmented electrodes[1] was tested instead of the RF electrode, which unfortunately exhibited a short to the ground plane, likely resulting from handling or wirebonding. RF voltage at a frequency of about 40 MHz was created as described in sec. 4.1.3, with the exception of omitting at this time the RF stabilization module. For estimation of the voltage applied to the trap, a capacitive divider was used, whose splitting ratio was determined beforehand[2]. The RF voltage applied to the central DC electrode

[1] All other electrodes were kept at ground potential during these tests.

[2] The capacitive divider signal provided at that time the most reliable estimation of the trap voltage. For consistency checks the trap voltage was also calculated from the input voltage and helical resonator and amplifier gain. Later on, when ions could be trapped in our setup, measurement of their secular frequencies provided a third method of trap voltage estimation.

was slowly ramped up to 2000 V peak-to-peak, while monitoring the reflections from the helical resonator (with respect to the input voltage) as well as the resonance frequency, both shown in fig. 5.1a[3]. The observed shift in resonance frequency of about 50 kHz over the voltage range is most likely due to thermal effects within the resonating circuit or the capacitive divider. The reflection signal remains low in the beginning, with a deviation emerging at around 500 V peak-to-peak, followed by a rather linear behavior and a stronger increase starting at about 1600 V peak-to-peak. At around 1800 V the wirebonds to the trap started to glow for a few seconds after which the trap electrode started glowing (see fig. 5.1c), which indicates temperatures beyond 1000°C, but only locally near the trap center. The cause for this extreme heating could neither be determined nor understood through calculations estimating the expected temperature increase when applying RF voltage of this frequency and magnitude[4]. Subsequently, a temperature sensor was attached to the trap chip by clamping it down with one of the screws which fix the trap chip at the top to the titanium frame (see fig. 5.1d). This location is not optimal for measuring the temperature, as it is away from the central region of the trap, but it allows the heating behavior of the trap to be investigated qualitatively. Again, 2000 V peak-to-peak were applied, this time on one of the lower outer segmented electrodes. The resonator reflection with respect to input voltage and temperature values as a function of the applied RF voltage are shown in fig.5.1b. The glowing behavior could not be reproduced on this electrode, despite the assumption of identical electrical and thermal behaviour for all electrodes. Rather, a temperature increase of the trap chip of only up to around 100°C was measured, correlated with the curve of reflections. Interestingly, the reflections to input voltage ratio decreases for this electrode up to an input voltage of about 1000 V peak-to-peak, and subsequently increases[5]. When comparing the reflection signals in the two measurements, it seems that a strong non-linear increase in reflections begins roughly at the same RF voltage beyond about 1600 V peak-to-peak, for both the central as well as the outer electrode. This may indicate that the safe regime in which to operate the trap lies below this value.

As the extreme heating of the central electrode during RF voltage application was not reproducible with the outer electrode, it seems unlikely to result from a fundamental problem, e.g. due to RF losses in the fused silica substrate. One possible explanation for the heating could be related to the boundaries of the metal coating on the trap chip. Due to the diffusive nature of the sputtering process, coating which reaches the inside of the trenches for separating electrodes (see fig. 4.2c) does not have a well-defined boundary but becomes progressively thinner, which may exacerbate heating. Compared to before it had glowed, the resistance between the central electrode and ground was lower, which hints at small gold bridges having formed between this electrode and ground. One possible reason might be the coating flaking off partially, which could also play a role in the heating process.

[3] The reflections were measured via a bi-directional coupler (MiniCircuits ZFBDC20), the resonance frequency was determined by finding for each data point the frequency at which reflections were minimized.

[4] These estimations combined heating due to Ohmic power dissipation in the trap electrodes and wire bonds, as well as due to RF losses in the trap's substrate material. Parameters which enter the calculation are the electrical conductivity of the gold, thickness of the gold layer and wire bonds, capacitance of the RF electrode and specified loss tangent of the fused silica material.

[5] The initial decrease may be explained by starting out with a worse impedance match than in the previous case, which gets slightly better as voltage increases due to thermal effects.

Trap 2 inside experimental vacuum chamber

After destroying the first trap, a second trap chip was installed and tested, this time in the experimental vacuum chamber[6], where it remains to this day. All DC electrodes of this trap were subjected to up to 300 V DC with no breakdowns occurring, and the RF electrode was tested analogously to the RF tests performed in the previous section, with the data shown in fig. 5.2a and b. In addition to tracking the reflections from the helical resonator and resonance frequency, the pressure inside the vacuum chamber was monitored via a residual gas analyzer (RGA)[7]. Moreover, in this setup, temperature monitoring was realized via an infrared (IR) camera in combination with a Zinc-Selenide viewport[8]. The IR camera had not been calibrated along with the viewport such that it is not possible to infer absolute temperature values from the measurements. However, the spatial resolution of the camera makes it possible to see where on the trap chip heating occurs, which may correspond to locations where the metal coating boundary causes a problem such as forming a connection to ground or being particularly thin. Two examples of such IR images are shown in fig. 5.2c and d, taken during application of low and high RF voltage, respectively.

During the first ramp-up of RF voltage applied to the RF electrode, the reflections and resonance frequency were monitored, which is shown in fig. 5.2a. Overall, the trap here seems rather unstable when applying voltages higher than 1200 V peak-to-peak. One distinct jump of resonance frequency to a lower value, different from the typical slow frequency drift due to thermalization, could be observed when increasing the voltage from 1200 V to 1300 V peak-to-peak. This was also accompanied by a large hydrogen spike in the RGA spectrum and a sudden increase in resonator reflections. However, since the trap seemed to be able to sustain the applied RF power after this incident, the voltage was further increased to 1700 V peak-to-peak. The data shows some instabilities which may hint at the formation of gold bridges from the RF electrode to ground, changing the impedance matching. Meanwhile, the temperature of the trap chip, monitored via the IR camera, increased only by a few degrees overall. After about 15 minutes of constant RF voltage application at 1700 V peak-to-peak a spontaneous breakdown occurred. The RF breakdown behavior manifests in a huge increase in reflections from the resonator and the emergence of oscillations on the order of kHz in the reflection signal. After switching the trap off and on again, the breakdown behavior could be observed for voltages of 150 V peak-to-peak and higher. However, after leaving the trap switched off over night, it was possible to ramp up the voltage again to 1200 V peak-to-peak before a breakdown occurred. After three days, this recovery effect was again observed, this time with a breakdown occurring at 800 V peak-to-peak. The reason for this recovery effect is not understood. It was suspected that the breakdown occurs on the trap surface, due to gold bridges forming when metallization migrates or flakes off during the application of high voltage. Most likely this happens deep inside the trenches for electrode separation where the coating boundary is diffuse. Indeed, after these voltage breakdowns, a resistance of merely 50 MΩ was measured between the electrical feedthrough connected to the RF electrode, and the vacuum chamber ground, which is connected to the ground plane of the trap. Thereupon, an attempt was

[6] The electrical tests were performed before bake-out.

[7] Stanford Research Systems RGA100, gas analysis up to 100 amu

[8] This IR transmissible viewport was initially installed on the vacuum chamber but later replaced, due to becoming leaky during bake-out. The replacement viewport is of the same type used on most other flanges, i.e. anti-reflection coated for our laser wavelengths, and thus temperature monitoring is no longer possible in our setup.

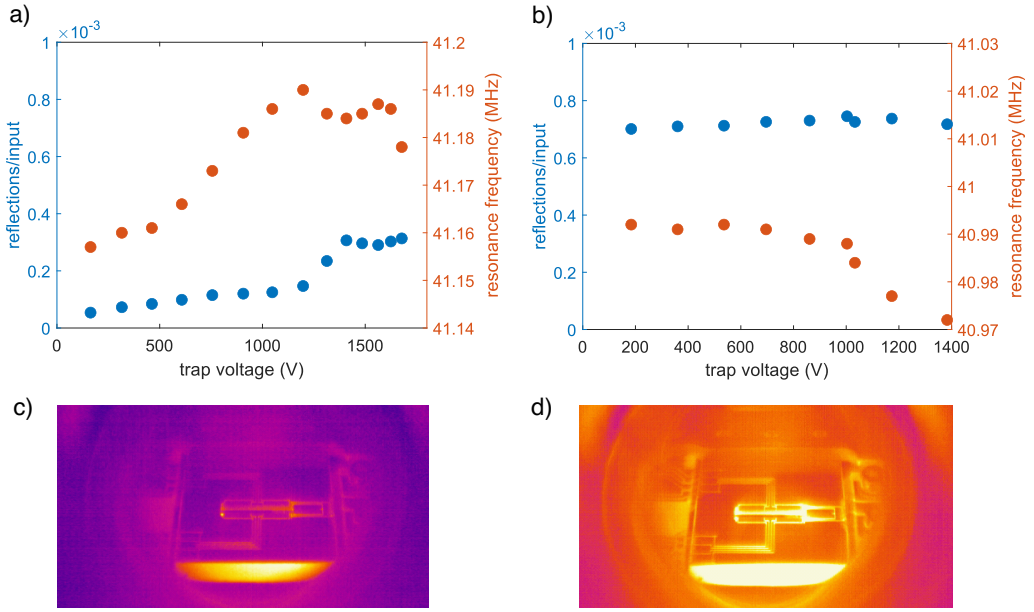

Figure 5.2: Electrical test of the second trap chip inside the experimental vacuum chamber: a) shows the first ramp-up of RF voltage applied to the RF electrode. Blue data points show again the ratio of resonator reflections to input voltage while orange points represent the resonance frequency. b) After several RF voltage breakdowns on the RF electrode and recovering its isolation by burning away potential gold bridges that formed short circuits, the RF voltage was ramped up again. Here, reflections are higher as in a, as we chose to work at a different impedance matching point. c) and d) show IR images taken while applying low and high RF voltage to the RF electrode, respectively. The bare fused silica part on the bottom of the trap chip appears to be hotter, but this is just a visual effect caused by the different emissivities of the two materials (fused silica and gold).

made to burn away the supposed gold bridges creating shorts, by applying a high DC voltage to the RF electrode. When applying DC voltages between 900 and 1200 V, electric discharges were observed on the trap near the outer edges of the RF rails. These may be evidence to gold connections in the coating burning off, which was also reflected in a decreasing leakage current from the RF electrode to ground, observed during this process. In the end, the trap was again able to sustain RF powers up to 1400 V peak-to-peak, as shown in fig. 5.2b. Here, the reflections were generally at a higher level compared to before, due to deliberately worse impedance matching. This approach was implemented based on the suspicion that introducing a less optimal impedance match would improve the system stability. Higher voltages than 1400 V peak-to-peak were not applied in order to prevent a further voltage breakdown. The IR image shown in fig. 5.2d displays hotter areas on the connection lines to the RF rails as well as a spot close to the location where electric discharges were observed during application of high DC voltage, near the ramp connecting the ground plane to the bottom of the trench. It seems that these are problematic locations on the trap, where gold bridges from RF to ground likely emerge.

Conclusion

From these electrical tests it can be concluded that the DC electrodes of the trap can easily sustain voltages of a few hundred V DC, a breakdown occurring only at 1300 V on the one electrode that was tested at this high voltage. The RF electrode has shown to be delicate, with shorts to ground happening more unpredictably[9]. It seems, though, that operating the trap in the regime below 1600 V, before the resonator reflections increase in a non-linear way as a function of the RF voltage, is likely safe. Another important observation was the fact that after an RF voltage breakdown occurred, the trap displayed a recovery effect, whose origin is not understood. Moreover, gold bridges creating shorts could be burned away via the application of high DC voltages, with the trap being in stable operation without any issues since then, i.e. for about 4 years. Since the ion trap apparatus had been installed in the laboratory, different and more temperature-stable pickup electronics have been in use for monitoring the trap voltage and as input for the RF stabilization circuit. As a result, the trap drive frequency used in other measurements presented in this thesis is about 43 MHz, a bit higher than used during the electrical tests. Furthermore, in the experiments described in this thesis the trap is typically operated only around 1000 V peak-to-peak of RF voltage, well within the safe regime and additionally keeping the trap temperature low[10]. The secular frequencies achievable with typical parameters of 1000 V peak-to-peak of RF at 43 MHz and DC voltages of 13 V and 24 V on the central and outer segments, respectively, are on the order of $2\pi(2100, 700, 350)$ kHz.

While it would be beneficial to have a trap with less power dissipation and better insulation between electrodes to be able to safely apply higher RF voltages and thus increase the secular frequencies, this might be challenging to realize in practice. To improve electrical isolation, a redesign of the electrode shapes would likely be necessary, which is not a straight forward task as recognized by Translume during their testing stage. Merely making the gap size between electrodes larger likely does not help as more gold would reach the bottom of the trenches and could lead to more shorts there, necessitating further optimization and testing. To address the power dissipation, a change of substrate material, such as sapphire, may result in better management of heat that is generated. At the moment, it is not yet possible to process sapphire with high enough precision in laser-assisted etching for our purposes, but perhaps this will change in the future [128].

5.1.2 Heating Rate

An important figure of merit for any ion trap is the heating rate. It sets a limit to the motional coherence that can be achieved and is thus critical for experiments, where the motion of the ions mediates entangling interactions. In order to determine the heating rate, the temperature of an ion or ion crystal is measured via thermometry techniques such as the ones discussed in sec. 3.3.3, for different wait times between laser cooling and temperature measurement. The heating rate in our apparatus was determined several times over the last years. For the majority of this PhD work, the best achievable result was a heating rate of about $\dot{\bar{n}} = 15$ quanta/s [119], which lim-

[9] The reason for this may be that, as observed by Translume during the manufacturing stage, it is more challenging to achieve electrical isolation between electrodes on the slanted parts of the trap chip.

[10] This has the benefit of keeping the number of dark ions low as a higher trap temperature corresponds to more contaminants being detached from the trap surface, that can chemically react with the ions or get ionized and caught in the trapping potential.

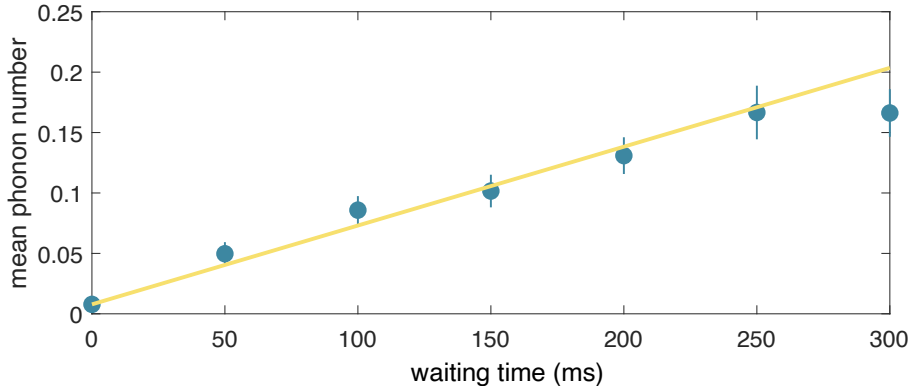

Figure 5.3: Heating rate determined via standard single ion thermometry: The bluegreen data points represent the mean phonon number as a function of waiting time between ground-state cooling and measurement. The mean phonon numbers were determined by relating the height of the red and blue sidebands of the motional mode along the strongly confined trapping direction (trap frequency 2.188 MHz), probed on the ground-state qubit transition via Raman laser light. Error bars stem from uncertainties in the determination of the height of the Gaussian fits applied to the sidebands. The yellow line represents a linear fit, weighted by the uncertainties in $\bar{n}$, the slope of which constitutes a heating rate of 0.65(7) quanta/s.

ited motional coherence of an ion to approximately 40 ms. This heating rate result was obtained after minimizing ground loops around the experiment and thus providing a clean electrical environment for the ions with minimal technical noise[11]. Although not competitive with the best experimental setups, this heating rate was in a reasonable range, comparable with many other ion trap systems [101][12]. However, theory calculations as well as comparison with some of the lowest reported heating rates [123, 140] had indicated that in principle it should be possible to achieve a significantly lower heating rate in our system. After suspecting for a long time that the low-pass filters, which should suppress the noise level on the DC electrodes, were actually responsible for the high heating rate, a modification was made: Here, 100 kΩ resistors were removed which were supposed to be part of a second filter stage but in fact introduced a significant amount of Johnson noise. Merely by removing those resistors on the filter boards, we were able to lower the heating rate to 0.65(7) phonons/s towards the end of this thesis work. This data and experimental details are now presented.

A single ion was trapped at secular frequencies of 2π (2188, 644, 338) kHz, Doppler cooled, with the mode along the strongly confined direction[13] subsequently prepared close to the motional ground state via sideband cooling. The temperature of the ion along the direction of motion along which it is probed is quantified by the mean phonon number $\bar{n}$, which according to eq. 3.64 is related to the ratio of the excitation probability on the red and blue motional sideband of the motional mode along that direction. In order to determine these motional excitation probabilities, sideband spectroscopy was performed on the groud-state qubit transition via the Raman

[11] This value constitutes the heating rate of a single ion along the x direction, or the heating rate per ion in a larger crystal for the center-of-mass mode along x.
[12] In order to compare our heating rate measured at about 2.2 MHz to other systems, we assume a $1/f^2$ scaling.
[13] For an ion crystal this corresponds to the out-of-plane direction.

laser beams, their differential k vector aligned with the strongly confined direction[14]. The mean phonon number is shown in fig. 5.3 as a function of a variable wait time introduced between ground-state cooling and temperature measurement. A linear fit was applied to the data, yielding a heating rate of 0.65(7) phonons/s, which is in excellent agreement with the value presented in the thesis of Dominik Kiesenhofer of 0.64(8) phonons/s, that was found via the alternative thermometry method where mean phonon numbers are determined from excitation dynamics on the motional sidebands [119].

All measurements which are presented in this thesis were carried out with the trap exhibiting the higher heating rate of about 15 phonons/s, with the exception of the last measurements, presented in sec. 6.2. While the higher heating rate did not constitute a limitation for this thesis work, it might have become a problem in future experiments, given our work with large ion crystals. For example, the center-of-mass mode of a 100 ion crystal would heat up by 1500 phonons/s (assuming perfectly correlated electric field noise on the ions), which is quite significant. With entangling interactions in our case requiring a coupling to all motional modes simultaneously, and modes other than the center-of-mass mode heating up significantly less, it is not clear how a very hot center-of-mass mode would adversely affect the overall behavior in specific experiments. In a different experimental setup harnessing such entangling interactions in long strings of trapped ions, a model for the dependence of decoherence effects on the motional mode occupation, Lamb Dicke parameter and laser detuning from the mode is presented [100]. Here, it is shown that the contribution from the center-of-mass mode to decoherence is indeed dominant when compared to the effect of other motional modes.

On the upside, with the new heating rate a factor ~ 30 improvement is achieved. This means that the heating will likely not impose a limit on the time over which dynamics of interacting spins can be observed for in Coulomb crystals of envisioned sizes, and raises the question of what other potential limitations in this context are.

5.2 Trapping Potential

The tunability and quality of the trapping potential play a significant role in the level of control that can be achieved over the trapped ions. The tunability of the trapping potential is defined by how precisely and strongly the potential can be shaped, quantified by parameters such as the achievable secular frequencies[15], translation of the potential minimum, and rotation angles of principal axes. The quality of the trapping potential is affected by the stability of the trap voltages, the presence of stray electric fields as well as anharmonicities in the potential. In essence, these effects diminish the ability to exert precise control over the motion of the ions, which was

[14] Note, that during the previous heating rate measurements sideband spectroscopy was perfomed on the optical qubit transition via the out-of-plane 729 nm laser beam. During these last measurements a sufficiently narrow 729 nm laser was not available but rather only one from the remote AQTION lab with a linewidth broadened by fiber noise to about 10 kHz. Thus, the Raman laser was employed for the new heating rate measurement, which has the advantage of common mode frequency noise affecting both beams equally, thus not having an effect on the measurement as the noise drops out in the Raman process.

[15] Another parameter which quantifies the tunability of the trapping potential is the minimum step size in changing the secular frequencies. This relates mainly to the precision of the RF stabilization unit, allowing us to tune the frequencies with a resolution of a few Hz, and is not discussed further in this chapter.

discussed in sec. 3.1.3 and is summarized here briefly. Unstable trap voltages may lead to configuration changes of the crystal lattice, heating of the ions, motional decoherence as well as coupling strength variations during entangling interactions. Stray fields created from dust particles or similar contamination on the trap surface may give rise to excess micromotion. Anharmonicities in the potential may lead to a modification of the motional mode frequencies and amplitudes of an ion crystal, and give rise to cross-coupling between different modes. As a result the ion motion may become unpredictable, which adversely affects laser cooling and entangling interactions and in the worst case may even lead to the ejection of ions from the trap. Unfortunately, the occurrence of anharmonicities is inevitable when moving away from ideal, hyperbolically-shaped electrodes [86]. With our electrode shapes and arrangement we expect anharmonic contributions to the potential to be stronger than in a standard linear Paul trap design. However, this effect should be predictable via simulations. Additionally, unpredictable anharmonicities could result from a misalignment of the trap electrodes with respect to each other[16], which we expect to be minimal due to the monolithic trap design.

Ultimately, the achievable tunability and quality of the trapping potential must meet specific criteria: The potential needs to confine 100 ions without nonlinear resonances ejecting ions. Additionally, the potential must be tunable enough to trap 100 ions in a single plane, with micromotion restricted to a specific direction within the crystal plane. This demands precise tunability for placing the ion crystal in the trap center and a high-quality potential to prevent uncompensated micromotion along undesired directions. This section explores these challenges as well as methods for extracting relevant information about the potential from images of ion crystals.

5.2.1 Size Limitations of 2D Ion Crystals

The potential created by our ion trap is capable of confining 2D Coulomb crystals of around 100 ions, which fulfills the requirements regarding planarity and ion number. In particular, in our setup we routinely work with planar ion crystals consisting of up to 105 ions. Here, limitations to the number of ions that can be trapped in 2D arise from the limited RF voltage that can be applied to the trap. The planarity condition, as given in eq. 3.14, needs to be maintained. This means that for higher ion numbers the ratio between strong (out-of-plane) and weak (in-plane) confinement needs to be increased. One could assume that it is sufficient to just increase the confinement in the strong direction by raising the DC voltages applied to the middle segments of the ion trap electrodes. Unfortunately, this also introduces negative potential curvatures in other directions. If then the RF confinement is not sufficiently high, the curvatures may add up to be anti-confining along the y direction close to the trap center, reflected by an ion crystal in an "hourglass shape". The only other option for maintaining the planarity condition is to lower the confinement in the weak directions, which at some point becomes critical due to e.g. strong heating effects along those directions.

Besides a redesign of the ion trap to apply higher RF voltages safely, one could instead lower the RF drive frequency which would increase the secular frequencies. While this approach might enable control over a higher number of ions, it comes at the expense of larger micromotion amplitudes which scale with the q parameter and thus inversely with the drive frequency. A careful investigation of this trade-off in the experiment has not yet been done.

[16] Such a misalignment may also cause micromotion which cannot be compensated.

It is difficult to assess at this point the fundamental limit to how many ions can be trapped in 2D with our trap design. However, recent progress [12] has shown that storing several hundreds of ions in a monolithic trap with a similar electrode configuration is indeed feasible. While we establish precise experimental control over the lattice stability of our ion crystals with up to around 100 particles (see sec. 5.3), it remains an open question how well this control can be retained when working with Coulomb crystals of much large size.

5.2.2 Residual Micromotion

The 12 segmented DC electrodes of the trap allow for tuning the DC potential in order to perform certain actions on the ion crystal, such as manipulating the confinement to trap the ions in arbitrary shapes (1D, 2D, 3D) as well as shift the crystals along and rotate it about the principal axes. For this purpose, voltage sets were determined from simulations, which describe the distribution of voltages over the available electrodes, that is needed to decouple one specific action on the ion crystal from other actions. An important application of these voltage sets is micromotion compensation. Micromotion is inevitably present in a 2D crystal, but should be restricted to a single direction within the crystal plane (y direction)[17], in order to control adverse effects on laser-ion interactions. Ideally, a 2D crystal would have to be placed exactly in the center of the trap[18], the axes which span the crystal plane aligned with the trap axes, to constrain micromotion to the y direction. However, stray fields may shift the crystal away from the center or rotate it with respect to the principal axes, giving rise to micromotion along the out-of-plane (x) direction that is homogeneously (in case of shift) or inhomogeneously (in case of rotation) distributed over the ions, respectively. Moreover, micromotion along this direction may be present for an optimally placed crystal in the case that it is not perfectly planar, as then some ions in the center are pushed out of the crystal plane. We quantify micromotion by measuring the micromotion modulation indices of the individual ions along the out-of-plane direction. This is achieved by comparing the coupling strength of the 729 nm laser, which is aligned with the out-of-plane direction, on the micromotion sideband and carrier transition of the optical qubit. After applying appropriate voltage sets to confine the ions to a single plane and place/rotate the crystal in the optimum position, out-of-plane micromotion modulation indices of less than 0.02 are determined for all ions (91 ion-crystal)[19]. In principle, no modulation should be visible from this direction; the limitation stems likely from a small misalignment of the laser beam with respect to the crystal plane, such that they are not perfectly perpendicular to each other.

5.2.3 Extracting Information about the Trapping Potential from Ion Crystal Images

Several properties of the trapping potential can be determined from analysis of the positions of ions in a Coulomb crystal, such as potential anisotropy, anharmonicity, and orientation of its

[17] In practical terms, there is always a minute level of micromotion present along the axial z direction, which poses no issues in experiments.

[18] In reality there may be geometrical imperfections present in the trap chip such that the geometrical center of the trap may not be the location at which micromotion is minimized.

[19] The thesis of Dominik Kiesenhofer presents these results along with data on Coulomb crystals that are rotated or translated from the optimum position.

principal axes. Methods to extract such information from a camera image, as well as the motivation for doing so, are presented in this section. Knowledge of the trap anisotropy $\xi = \omega_y/\omega_z$, may be useful, e.g. for calibration purposes, as specific anisotropy values correspond to enhanced crystal lattice stability in planar crystals, its determination from a crystal picture providing a fast alternative to the use of sideband spectroscopy. There exists a natural relationship between the potential anisotropy and the shape of an ion crystal that is confined by the potential[20]. The shape of an ion crystal is quantified by its aspect ratio, which, considering an elliptical shape, is given by $\zeta = a_2/a_1$, defined as the ratio of the semi-minor axis a_2 and the semi-major axis a_1. The aspect ratio can be determined from a crystal picture by calculating the covariance matrix of the ion positions (y_i, z_i) and diagonalizing it, with the two eigenvalues $\lambda_1 \geq \lambda_2$ relating to the aspect ratio as $\zeta = \sqrt{\lambda_2/\lambda_1}$. This can be understood intuitively, as the covariance matrix captures the relationship between ion positions and is thus a measure for their distribution. A diagonalization then reveals the principal axes of the distribution, with the eigenvalues as a quantitative measure for how much the distribution is stretched along each axis. Once ζ is known, it can be linked to the potential anisotropy ξ: Considering large crystals, that can be modeled as a charged fluid whose shape is determined from potential theory [141], the relationship between anisotropy and aspect ratio is given by

$$\zeta^2 \frac{K - E}{E - \zeta^2 K} = \xi^{-2}. \tag{5.1}$$

Here, $K = K(\sqrt{1-\zeta^2})$ and $E = E(\sqrt{1-\zeta^2})$ are complete elliptic functions of the first and second kinds [142].

Another method to extract information from an ion crystal image is based on modelling a harmonic potential in the crystal plane spanned along the y and z directions as

$$V = \frac{1}{2}\begin{pmatrix} z - z_0, & y - y_0 \end{pmatrix} A \begin{pmatrix} z - z_0 \\ y - y_0 \end{pmatrix} \tag{5.2}$$

where z_0 and y_0 denote the potential minimum and

$$A = \begin{pmatrix} \alpha & \gamma \\ \gamma & \beta \end{pmatrix}$$

is a symmetric matrix. Once the parameters α, β and γ are known, the potential is determined on all points in this plane, making it easy to extract relevant information from it. The parameters α, β and γ are determined from a fit as described in the following: We know that the gradient of V is equal (up to a factor -1) to the force which is exerted by the potential on the ions. The force can easily be determined from an ion crystal image because the ions sit at equilibrium positions, where the confining force exerted on them by the potential is exactly equal to the repelling Coulomb force between them. We gain information about Coulomb forces by observing the distances of

[20] Knowledge of the crystal shape may be additionally useful when performing simulations, providing an intial guess of ion positions in a harmonic potential.

the ions with respect to each other on the camera image[21], as the Coulomb force on an ion at location $\vec{x}'$ is given by

$$F = \frac{e^2}{4\pi\epsilon_0} \frac{\sum_x \vec{x'} - \vec{x}}{|\vec{x'} - \vec{x}|^3}. \tag{5.3}$$

where e is the elementary charge and ϵ_0 the vacuum permittivity. Now we can perform least squares fitting to find values of α, β and γ for which the gradient of the potential matches the Coulomb forces calculated from the ion positions.

Once we have found the entries of A we have determined the potential. As a next step, diagonalization of A yields eigenvectors and eigenvalues that contain information which we want to access. The eigenvalues of A, λ_y and λ_z, are proportional to the squares of the oscillation frequencies ω_y and ω_z, which immediately yields the trap anisotropy as $\xi = \sqrt{\lambda_y/\lambda_z}$. The trap frequencies in the crystal plane can be calculated as $\omega_{y,z} = 2\pi\sqrt{\lambda_{y,z}e^2/(4\pi\epsilon_0 m)}$ where m is the mass of the calcium ion. The eigenvectors are also useful as they provide the direction of the potential's principal axes. These are not necessarily aligned with the axes of the camera image. The crystal's coordinate system can thus be introduced as $z' = z\cos\phi + y\sin\phi$ and $y' = -z\sin\phi + y\cos\phi$, rotated with respect to the coordinate system (z, y) of the image.

Besides determination of the trap anisotropy, individual trap frequencies, and orientation of the potential with respect to the imaging coordinate system, we can use this model to determine anharmonic contributions to the trapping potential. For an ideal harmonic potential we expect the Coulomb force acting on an ion by all other ions to depend linearly on the ion position. Any anharmonic contribution to the potential will then be revealed by fitting a linear gradient to the Coulomb force calculated from the ion positions and determining the deviation between data and fit.

Application on a 91 ion crystal

The methods discussed above are now applied to a 91-ion crystal, whose ion positions are shown as blue points in the top plot of fig. 5.4. First, the aspect ratio and anisotropy are determined: Calculation and diagonalization of the covariance matrix of the ion positions yields an aspect ratio of $\zeta = 0.382$. From this, the trap anisotropy $\xi^{-1} = 0.483$ can be calculated via eq. 5.1. This result can be compared to the anisotropy determined from sideband spectroscopy on the optical qubit transition: For secular frequencies of $\omega_y = 2\pi \times 742$ kHz and $\omega_z = 2\pi \times 370$ kHz, an anisotropy of $\xi^{-1} = 0.499$ is determined, in good agreement with the value obtained by the other method. Determining the potential anisotropy via the third method, taking the square root of the ratio of the eigenvalues of the matrix A, we find a potential anisotropy of $\xi^{-1} = 0.503$, also in good agreement with the result obtained from sideband spectroscopy.

The eigenvectors of A are then used to determine the angle between the principal axes of the crystal and the image. Here we find $\phi = 0.004$ (0.229 degrees), showing that they nearly coincide

[21] In order to calculate the Coulomb forces accurately in physical units, the pixels from the camera image need to be converted into meters. This is achieved by matching the value of the secular frequency ω_z found by crystal image analysis to the one obtained by sideband spectroscopy, yielding a magnification factor of 22.4 in our imaging system (SillOptics objective).

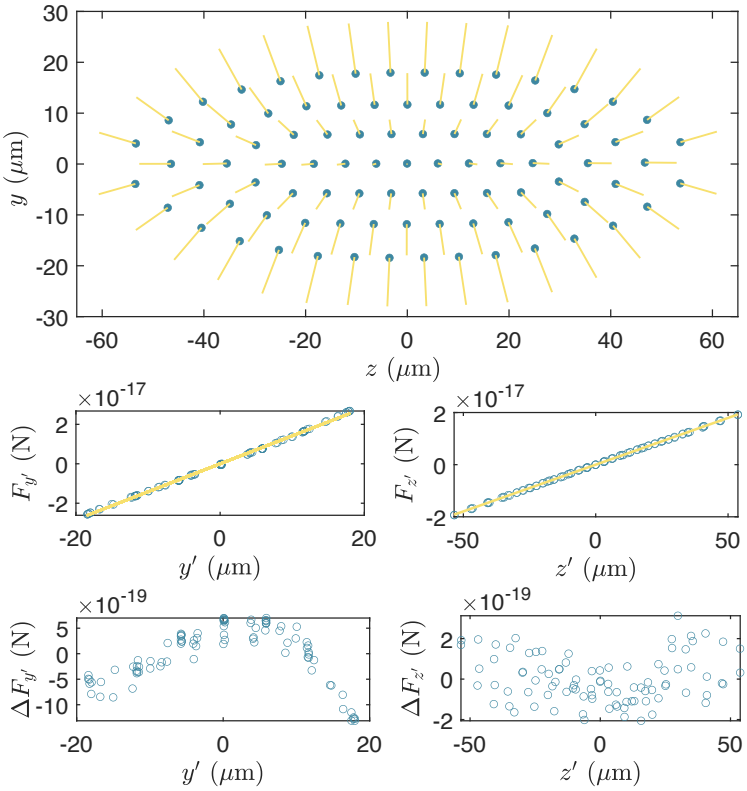

Figure 5.4: Characterization of the trapping potential from a 91-ion crystal image: top: Individual ion positions are illustrated as blue points, the forces exerted on the ions by the trapping potential are illustrated as yellow lines in arbitrary units. The central row shows the force components $F_{y'}$ and $F_{z'}$ along the two directions y' and z' of the rotated (crystal) coordinate system. A linear fit (yellow) is applied to the force components and the residuals $\Delta F_{y'}$ and $\Delta F_{z'}$ with respect to this fit are shown in the bottom row.

in our case. From here on the rotated coordinate system (z', y') is used, that is aligned with the principal axes of the ion crystal.

The forces exerted on the ions (in arbitrary units) are represented by yellow lines in the top image of fig. 5.4. In the middle row, the Coulomb force components in physical units $F_{y'}(z'_i, y'_i)$, $F_{z'}(z'_i, y'_i)$ are plotted along the principal axes. The residuals $\Delta F_{y'}$, $\Delta F_{z'}$ determined from a linear fit are shown in the bottom row and reveal that the trapping potential is not purely harmonic. However, as the deviations from the linear fit are small, we conclude that anharmonic contributions to the trapping potential are rather minor. This observation agrees with the trapping potential simulations presented in sec. 4.1.1, which indicate that anharmonicities in the potential are negligible in a region around the trap center. This region extends about 1 mm along the z direction and 200 µm along the y direction, which is larger than the typical crystal sizes in our setup, e.g. the 91-ion crystal shown in fig. 5.4 with a size of less than 120 µm along z and 40 µm along y. The low presence of anharmonicities in the potential is also a testament to the high alignment precision of the trap electrodes with respect to each other, due to the monolithic design.

5.3 Stability of Large Planar Ion Crystals

Readout and control of the quantum states of individual ions relies on a well-defined and stable crystal lattice structure. This encompasses several requirements: The number of $^{40}Ca^{+}$ ions must remain constant, which can be impaired by Langevin collisions with background gas molecules, either passing kinetic energy to an ion such that it escapes the trapping potential, or leading to a chemical reaction forming a "dark" (molecular) ion. Moreover, dark ions can emerge as particles present inside the vacuum vessel become ionized and caught in the trapping potential. In our setup crystal lifetimes of several hours or even days are observed, indicating excellent vacuum conditions, and enabling continuous data taking over long timescales. Apart from ion loss and chemical reactions, Langevin collisions can also give rise to two other undesirable effects: First, energy transferred to the ions via a collision, potentially in combination with RF heating, can lead to a transition to a non-crystalline phase, where the melted ions are no longer localized in space [31]. This section characterizes the melting behavior of planar crystals of different sizes, as well as the ability to quickly re-crystallize the ions with a far-detuned (330 MHz) Doppler cooling beam. Second, collisions at lower energy may initiate structural phase transitions of the crystal lattice, leading to position changes of the ions. Besides corrupting quantum state readout, lattice configuration changes may lead to a modification of the motional mode structure and thus the entangling interactions in quantum simulation experiments. A brief summary of our approach to minimize the influence of such events on our experiments is presented in this section, with more information available in the thesis of Dominik Kiesenhofer.

5.3.1 Survival in Crystalline Form

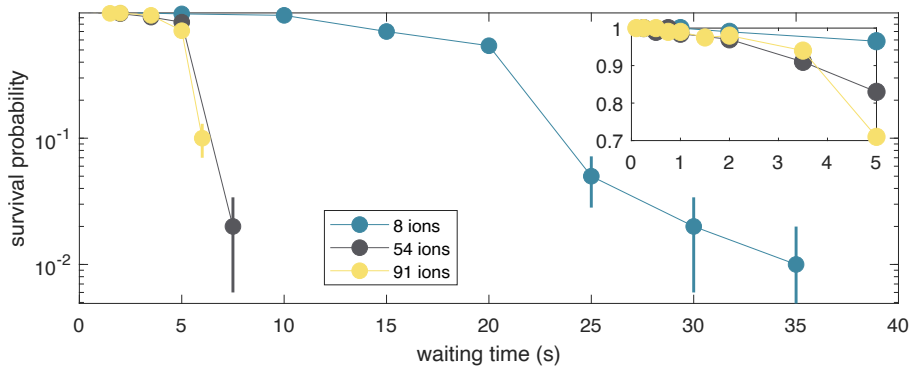

Figure 5.5: Melting dynamics of planar crystals of different sizes: a) shows the probability that a crystal consisting of a certain number of ions has remained crystallized after a waiting time without any laser cooling. The inset shows the probabilities for short waiting times in more detail and on a linear scale. Here, the error bars correspond to the standard error of the mean for a binomial random variable.

During a standard measurement sequence, laser cooling is performed at the beginning, followed by a manipulation of the ions' quantum state and subsequent state readout. This corresponds to one measurement cycle, typically taking a few milliseconds to tens of milliseconds. During the cycle the ions must remain in crystalline form to allow for high-fidelity control and readout.

When a melting event occurs it is critical that first, it is detected automatically, such that data taken during this time can be excluded, and second, that a crystallized state is reinstated as fast as possible such that measurements can continue. On top of that, a melted ion crystal is more prone to ion loss due to RF heating, which also emphasizes the need for fast re-crystallization. In our apparatus, detecting that an ion crystal has melted into a cloud is based on the fluorescence counts recorded during Doppler cooling. These counts are monitored via the PMT, a drop in the signal indicating that the ions are in a non-crystalline phase where they scatter less photons, and that the previous data point is likely corrupted[22]. When such a drop in fluorescence counts occurs, the experiment control system triggers immediate recrystallization of the ions, by switching on the 330 MHz red-detuned Doppler cooling beam (refreeze beam) along with the primary Doppler cooling beam. The following characterization measurements were performed in order to determine on which timescales melting and recrystallization occur.

In a first experiment, to characterize the melting behavior, an ion crystal was Doppler cooled and subsequently subjected to a variable wait time without any laser cooling. After the wait time, the fluorescence signal was measured to determine if the ion crystal had melted or not[23]. This experiment was repeated 100 times each for different crystal sizes and wait times, to collect sufficient statistics in order to reliably estimate the probability of the ions to remain crystallized. Figure 5.5 shows this "survival probability" as a function of wait time for planar ion crystals consisting of 8, 54, and 91 ions. For the smallest crystal the time it takes to melt with 100 percent probability is $\sim$ 40 s. Larger crystals of 54 and 91 ions melt on shorter timescales, however they remain crystallized with high probability even after several seconds, which is significantly longer than the timescale of any envisaged experimental sequences. More quantitatively, the data does not follow a purely exponential decay in time and the dependence on ion number is nonlinear. These two observations indicate that melting events are not exclusively caused by Langevin collisions, but rather a combination of collisions and RF heating, where energy is transferred from the trapping RF field to the ions. Simulations carried out in [143] suggest that RF heating scales in proportion to q^4. Operating our ion trap at a low $q \approx 0.1$ thus mitigates such RF heating effects. For the long time scales investigated in this experiment, however, the heating does become significant.

A second experiment was performed, to estimate the time it takes a melted ion cloud to be recrystallized. Here, a 91 ion crystal[24] was subjected to a fixed waiting time of 1 s without any laser cooling. This represents an upper limit for our planned experiments and mimics a realistic time scale for the free evolution of the ion cloud before application of the recrystallization beam. After the 1 s waiting time, the 91-ion crystal melted in $\sim$ 1% of cases, which is consistent with the data taken during the previous experiment. When the crystal had melted, the recrystallization beam was switched on for a variable time. Subsequently, a camera image of the ions was taken to determine if the crystalline structure had been successfully reinstated. After a time of 70 ms, recrystallization was effective in 101 out of 102 cases. Thus, a refreeze time of 100 ms can be concluded to be sufficient to recrystallize an ion cloud during standard measurement sequences.

[22] Additionally, as explained in sec. 4.7.4, it is also possible to infer if an ion crystal has melted from a camera image.

[23] In case of a melting event the far-detuned Doppler beam is switched on for 100 ms to bring the ions back into crystalline form, which is confirmed by a camera image before the next measurement.

[24] Only a 91 ion crystal was used for this experiment, minimizing the duration required for data collection, as melting events are rare for smaller crystals.

5.3.2 Mitigation of the Influence of Lattice Configuration Changes

In order to practically eliminate the influence of structural phase transitions on experiments, several strategies are combined: First, an anisotropy $\xi^{-1} \approx 0.5$ in the weak directions of the trapping potential is introduced, creating elliptically-shaped ion crystals, elongated along the axial trap direction. Such crystals have shown a more stable lattice structure, compared to rounder crystals, owed to a suppression of librational modes.

Second, ion crystals which possess mirror symmetry with respect to both axes that span the crystal plane are exclusively used in our experiments, such as the 91- and 105-ion crystals shown in fig. 4.16. These crystals demonstrate fewer lattice configuration changes, based on the fact that they possess only a single structural ground state configuration (symmetric "main" configuration). If, on the other hand, a crystal configuration in the ground state lacks symmetry, there exist further configurations with the same energy that could be obtained by flipping the configuration horizontally or vertically, e.g. the two degenerate ground states in zig-zag ion crystals. Very little energy is needed to cause transitions between these structural phases, correlating with frequent lattice configuration changes in these crystals. For a specific trap anisotropy, only crystals consisting of certain numbers of ions allow for the desired mirror symmetry to be achieved. The experiments presented in this thesis are, thus, carried out with crystals of 8, 19, 54, 91 and 105 ions. This is just a selection of the possibilities, which were found empirically, as performing simulations for various anisotropies and ion numbers would be infeasible.

Third, the trapping potential anisotropy ξ is fine-tuned in order to optimize the time that the crystal lattice remains in the main configuration. This process corresponds to maximizing the energy gap between the main configuration and metastable ones, to reduce the probability of transitioning from the ground to energetically-higher structural phases. In particular, the setpoint of the RF voltage is tuned, which predominantly changes the confinement in the y direction and thus tunes the crystal's aspect ratio.

Fourth, the sensitivity of the crystal aspect ratio to RF power fluctuations necessitates power stabilization in order to reduce the number of structural phase transitions[25]. As a result, the probability of the crystal being in the main configuration can be raised to over 99 percent (91-ion crystal).

Fifth, strategies to deal with remaining occurrences of wrong lattice configurations are implemented. Once the previously mentioned steps are taken, the time the crystal spends in wrong configurations is rather short, i.e. on the order of 10 ms. Thus, as the crystal transitions back to the main configuration typically within one measurement cycle, it is not necessary to actively resolve wrong configuration, e.g. by deliberately heating the crystal via changing the frequency of the Doppler cooling beam. However, it is necessary to be able to detect when a wrong lattice configurations has occurred such that data taken during this time can be excluded. For this purpose, an in-sequence detection tool was incorporated into the experiment control program, where data is automatically retaken for experiments in which the ion crystal was found to be in a wrong configuration, similar to the filtering of melting events described above. This tool is based on the analysis

[25] RF instabilities are the dominant effect in this case, as DC voltages are sufficiently stable to not contribute in a noticable way to structural phase transitions.

of camera images, using PCA and clustering to classify images into different configurations[26]. It should be noted, that with this approach we only have the ability to track ions swapping positions when accompanied by a change in crystal lattice structure. However, low energetic collisions may lead to position swapping of ions without melting or reconfiguration of the lattice, which can still affect measurement outcomes. In principle such collisions could be detected by the use of tracer ions[27]. However, it does not seem necessary to monitor all collisions, as the measurement error resulting from these events is estimated to be well below 10^{-3}. The basis of this estimation comes from an experiment performed in the QSIM apparatus, which has a higher background gas collision rate than ours.

5.4 Ground-State Cooling of the Out-of-Plane Motional Modes

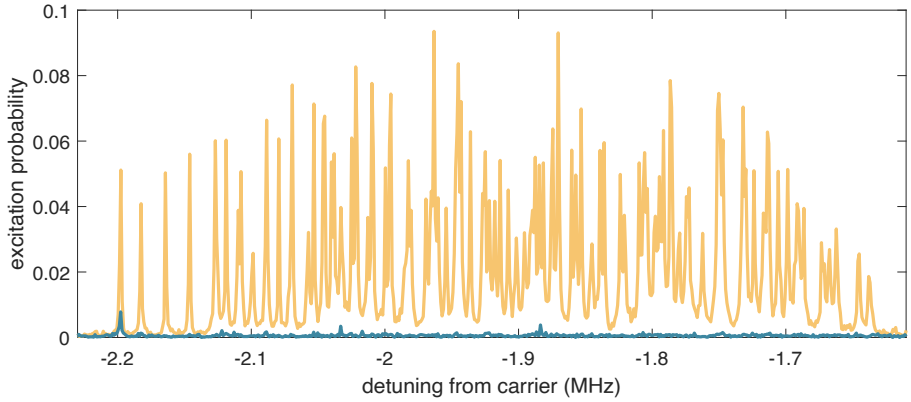

Figure 5.6: Red sideband spectra of the out-of-plane modes of a 105 ion crystal, probed on the optical qubit transition: The yellow data corresponds to the spectrum taken after only Doppler cooling. The bluegreen data is taken after additional EIT cooling for 300 µs.

Ground-state cooling of all out-of-plane motional modes of an ion crystal is a prerequisite when employing these modes to mediate long-range entangling interactions. EIT cooling offers a possibility for fast and multimode ground-state cooling and is thus used routinely on the out-of-plane modes of Coulomb crystals in our apparatus. The concept of EIT cooling had briefly been introduced in sec. 3.3.3, with the laser setup shown in sec. 4.4.4. This section presents our result on EIT cooling of a planar 105-ion crystal, whose crystal structure can be seen in fig. 4.16a. For this measurement presented in this section, the ions were trapped at secular frequencies $\omega_{x,y,z} = 2\pi \times (2188, 528, 248)$ kHz and pre-cooled via Doppler cooling. Before performing EIT cooling a calibration procedure was carried out in order to set the light shift induced by the EIT σ beam equal to the center of the mode spectrum of the given ion crystal [115]. This ensures

[26] In the thesis of Dominik Kiesenhofer more information is given on the algorithm for crystal configuration assignment, as well as simulations reproducing many of the configurations found in the experiment.

[27] For example, one could dedicate some ions in the crystal to probe the temperature in the out-of-plane direction which may indicate a collision event

that all modes are within cooling range and can be cooled efficiently and simultaneously. In order to determine the center of the mode spectrum, the motional sidebands were probed on the optical qubit transition, with the frequency of the 729 nm laser scanned over several hundred kHz. For this specific 105-ion crystal the mode spectrum spans about 550 kHz, with the highest frequency (COM) mode at 2.188 MHz and the lowest frequency out-of-plane mode at 1.637 MHz. The power of the σ beam was adjusted to set the light shift to about 1.95 MHz, approximately equally detuned from both the COM and lowest-frequency mode. EIT cooling beams were applied to the ion crystal for 300 µs, followed by 100 µs optical pumping. While a quantitative investigation of the ions' temperature for such a large Coulomb crystal is not straightforward, a qualitative assessment of the success of ground state cooling can be inferred from a comparison of sideband spectra before and after the application of EIT cooling. This is shown in fig. 5.6, the two curves displaying the red sideband excitation after Doppler (yellow curve) and additional EIT cooling (bluegreen curve). A clear suppression of all out-of-plane modes is visible in the EIT cooled crystal, with some minor excitation remaining for a few modes. The most prominent peak here corresponds to the COM mode, which heats up during the measurement time as $\dot{\bar{n}}N$, in proportion to the original heating rate of 15 phonons/s present in our system at the time of performing these measurements. Modes other than the COM mode generally have a lower heating rate and thus are less prominent in the EIT-cooled spectrum. In order to make a more quantitative estimate of the temperatures achievable in our system, we on one hand consider the mean phonon number $\bar{n} = 0.06$ measured via standard sideband thermometry after applying EIT cooling to a single ion. On the other hand, we presented a new thermometry method to investigate low temperatures in larger ion crystals, based on observing excitation dynamics on the motional sidebands [119]. In this work, our method was applied to a planar 19-ion crystal, yielding results of $\bar{n} = 0.149(3)$ for the COM, and $\bar{n} = 0.081(3)$ for the lowest-frequency out-of-plane mode. In principle, our method could also be used to characterize the temperature of crystals consisting of even more ions, but the calculation of $\bar{n}$ relies on multiplication of large matrices which at some point becomes infeasible as the system scales up. This method may thus be limited to characterizing crystals consisting of a few tens of ions. However, from the study of smaller crystals, we have already obtained an indication of the approximate temperature range to be expected in our apparatus.

5.5 Raman Beam Characteristics and Ground-State Qubit Coherence

Table 5.1: Ground State Qubit Coherence

Probe	Spin Echo	$1/e$ Coherence Time (ms)	$1/e^2$ Coherence Time (ms)
RF Antenna	no	129(14)	183(19)
RF Antenna	yes	379(28)	536(40)
Raman Beams	no	133(12)	188(17)
Raman Beams	yes	361(15)	510(22)

The Raman laser system at 395.8 nm constitutes a crucial tool in our experiments focused on investigating interacting spin-1/2 particles, with detailed information on various aspects, includ-

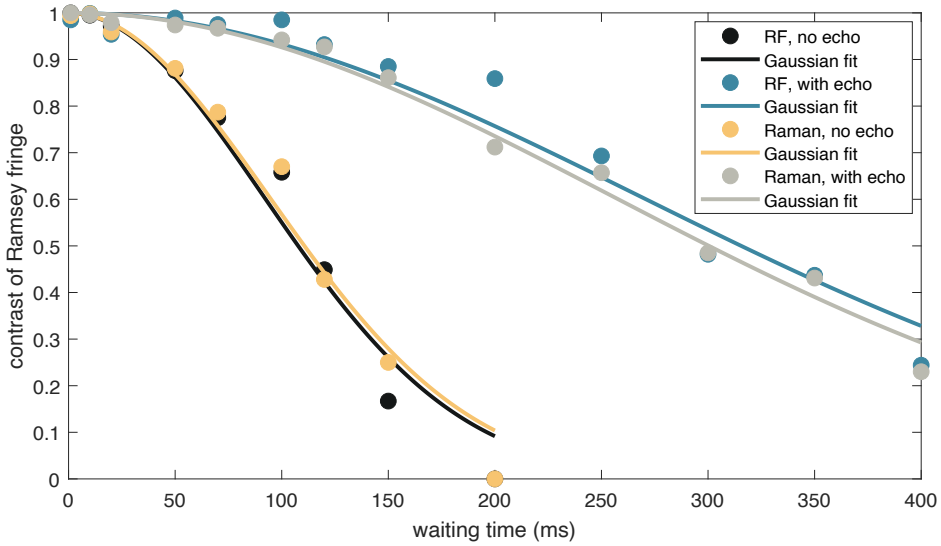

Figure 5.7: Coherence of the ground-state qubit: Black and yellow data represents the contrast of Ramsey fringes without spin-echo as a function of Ramsey wait time, where the Ramsey sequence was carried out with the RF coil and Raman beams, respectively. Blue and grey data was taken with spin-echo and again represents RF coil and Raman beams, respectively. Gaussian fits to the data points allow for the determination the coherence values given in tab. 5.1.

ing theory, motivation, and methodology, provided throughout this thesis: As presented in sec. 3.3.4, laser light at this wavelength is employed for coupling the two levels of the ground-state qubit transition through a Raman process. Beyond performing basic rotations on the qubits, the Raman laser light is also used for mediating entangling interactions via the ion crystals' motional modes, as introduced in sec. 3.3.5. Here, detailed information was given on our approach to implementing Raman transitions in our apparatus, e.g. on the motivation for choosing this route over the use of 729 nm light coupling the optical qubit transition, as well as experimental details such as beam geometry and polarization. In 4.4.5 technical details on the optical setup were presented. And finally, later on in this thesis in sec. 6.1.4, information is provided on how to align the Raman beams optimally with respect to each other and the Coulomb crystal plane, by harnessing correlation spectroscopy.

Now an overview of the key characteristics of the Raman laser beams is given. Note, that as the setup for driving Raman transitions has been under constant development over the past year and the careful investigation of characteristics such as the scattering rates is beyond the scope of this thesis work, only a short summary of current experimental parameters is provided, with more quantitative information on the final setup to be found in the upcoming PhD thesis of Artem Zhdanov. With approximately 300 mW of power available per Raman beam and a beam waist in the trap center of about 500 µm, we achieve Raman Rabi frequencies on the carrier transition of the ground-state qubit of about $2\pi \cdot 200\,\mathrm{kHz}$ and spin-spin interaction strengths on the order of 1000 rad/s (see sec. 6.2). Due to the Gaussian intensity profile of the Raman beams the Rabi frequency is not homogeneously distributed over large ion crystals, with e.g. the outer ions in a 91-ion crystal exhibiting a coupling strength of 93% with respect to the inner ions. This effect would

lead to rotation errors in resonant operations but can be corrected by the use of composite pulse sequences [144], which were applied in experiments presented in sec. 6.2. As for decoherence, we investigated two sources: amplitude damping caused by off-resonant scattering from the P levels during the Raman process, as well as phase damping that can arise from an instability of the interferometer formed by the Raman beams. In the first case, at a Rabi frequency of $2\pi \cdot 200\,\mathrm{kHz}$, the decay rate is on the order of 20 per second, which does likely not constitute a limitation in our experiments in the context of spin squeezing, presented in sec. 6.2. The phase-stability of the Raman beams with respect to each other was investigated in Ramsey experiments. Here, a single ion was probed via Raman light with and without spin-echo. Subsequently, the same experiments were carried out with the Ramsey sequence implemented via a magnetic RF signal applied with the RF antenna, which provides a phase-noise-free reference value. The results of these measurements are summarized in tab. 5.1 and shown in fig.5.7. More specifically, in the figure the Ramsey fringe contrast of the ground-state qubit is shown as a function of Ramsey wait time. From this data, a $1/e^2$ coherence time of 188(17) ms without spin echo is derived when probing the ion with Raman light, which is extended up to 510(22) ms by the use of a standard spin echo sequence. When probing the ion with the RF antenna, values of 183(19) ms and 536(40) ms, respectively, are achieved, which agree within the margin of error with the previous measurement. The overlap of data when probing the ion via the RF coil and Raman laser shows that the Raman optical setup is phase-stable and path-length fluctuation do not introduce significant coherence decay. Using a line trigger did not yield any improvement of the coherence times, reflecting the low level of technical noise in our setup, resulting from the measures described in sec 4.3 and 4.8.1, i.e. enclosing the experiment in a magnetic field shielding box and establishing a clean electrical environment. Nevertheless, the qubit coherence was still limited by magnetic field noise on the ion when those measurements were carried out. Recently, coherence time results of up to 1 s have been achieved, after removing a cable that connected the NEG in the vacuum setup to its controller.

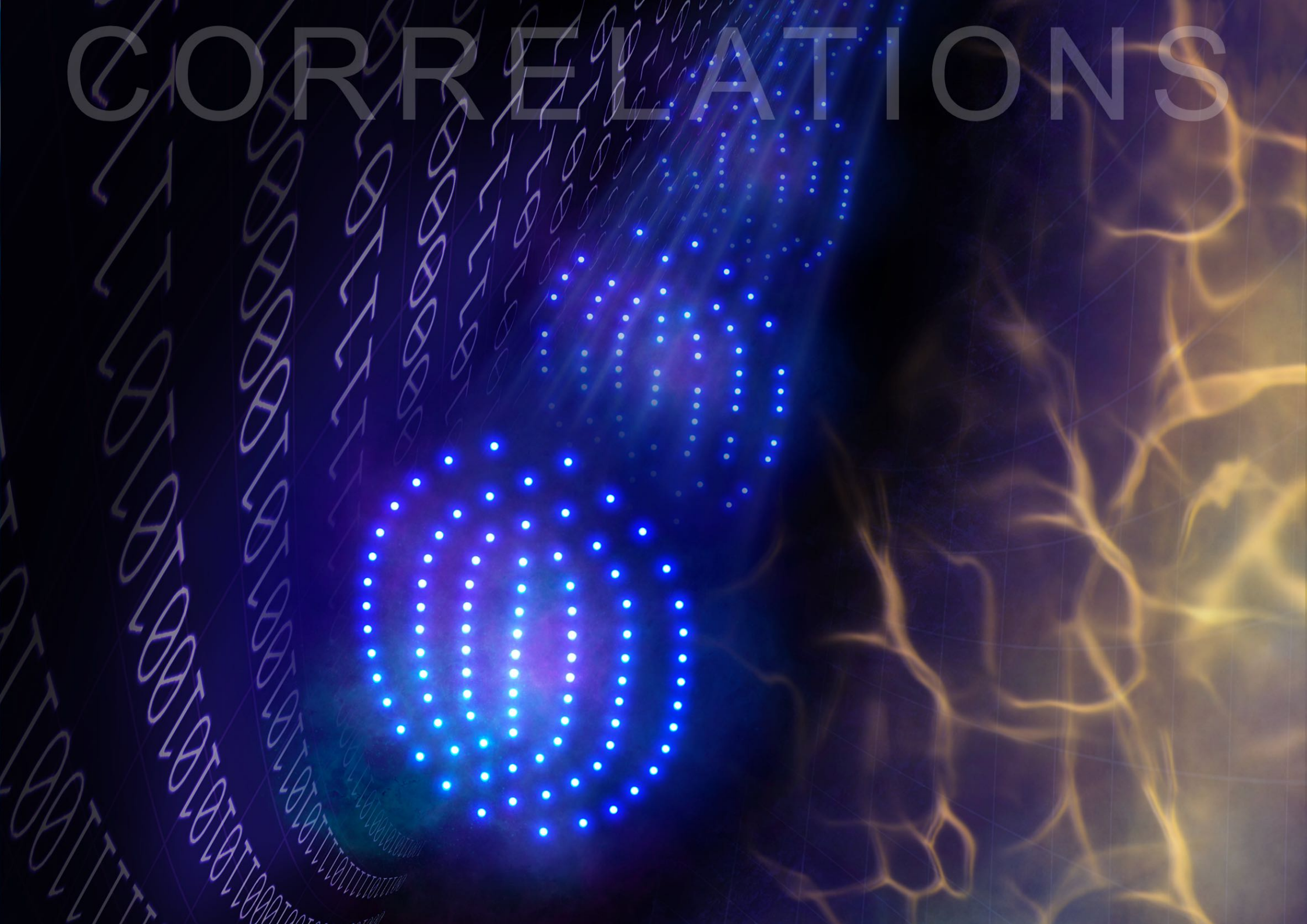
CORRELATIONS

6 Quantum Correlations in Planar Ion Crystals

This chapter presents experiments on observing and harnessing quantum correlations in planar ion crystals. These experiments are set more in the context of quantum sensing and metrology, rather than simulation. However, the tools which are used here allow for characterization and optimization of the experimental setup and for quantifying the interactions created in a system of spins that are encoded in the ions, important steps on the path towards quantum simulation.

In quantum metrology quantum effects such as quantum correlations are harnessed to enhance the precision with which physical observables can be measured. This chapter provides two examples of high-precision metrology, employing two distinct types of quantum correlations. While entanglement constitutes the most well-known type of quantum correlation, it is often fragile and difficult to create in the laboratory. The first part of this chapter is thus concerned with non-entangled states, making use of quantum discord in a large Coulomb crystal of 91 ions, to enhance phase estimation via correlation spectroscopy. As will be shown, correlation spectroscopy represents a versatile tool for the characterization and optimization of our experimental system. In the second part of this chapter, a spin squeezing protocol is applied to a small 19-ion planar crystal, which allows the measurement uncertainty to be reduced below classical limits, at the same time demonstrating the capability of generating entanglement in our experimental apparatus.

6.1 Correlation Spectroscopy with Multi-Qubit-Enhanced Phase Estimation

Employing quantum systems for sensing and metrology has shown great potential in a variety of applications in science and technology [58, 145, 146, 147, 148, 149, 150]. The key idea here is that when quantum objects are used as probes to measure observables, their quantum properties can be harnessed to enhance measurement precision compared to classical measurement devices. While building quantum computers or simulators that provide advantage over classical devices remains an outstanding challenge due to the sensitivity of quantum systems to disturbances from the environment, in sensing applications this property can turn into a benefit, leading to the establishment of quantum sensors as a comparatively mature technology in the NISQ era.

Quantum sensing oftentimes relies on determination of the phase of a quantum system's superposition state, which carries relevant information about the environment. Consequently, phase estimation, with the aim to as precisely as possible extract phase information from measurements on the quantum system, constitutes a central tool in sensing and metrology; a precision enhance-

ment in phase estimation providing a direct path to creating better sensors. However, phase estimation is compromised by decoherence, the loss of well-defined phase relationships, arising from noise processes which the quantum sensor is exposed to. Probing a quantum system for a longer time relates to increased spectral and phase resolution, e.g. in Ramsey experiments, but the coherence time sets a limit on how long the system can be probed for.

In this section our work on multi-qubit enhanced phase estimation is presented theoretically and experimentally, with more details to be found in [38]. Our method harnesses correlation spectroscopy, where multiple qubits are probed simultaneously via Ramsey interferometry and measurement outcomes of the individual qubits are correlated. In experiments where the noise that is leading to coherence decay is common to all qubits, correlation spectroscopy allows the probe time to be extended beyond the coherence time of the individual qubits in the system. While this technique has been demonstrated previously with two ions [151, 152, 153, 154] and has enabled the precise comparison of two atomic clocks, in our work correlation spectroscopy is extended to significantly larger systems of up to 91 qubits, constituting a network of many quantum sensors [155, 156, 157, 158]. Here, we find that analysis of correlations between all particles improves the achievable phase uncertainty compared to the case of only analyzing pair correlations. In our apparatus these correlation spectroscopy techniques are applied in order to determine spatial transition frequency differences as well as track temporal phase fluctuations, allowing for characterization and compensation of a magnetic field gradient across a planar ion Coulomb crystal, optimization of the alignment of Raman laser beams, as well as quantification of the screening performance of our magnetic field shielding. The wide variety of applications is a testament to the versatility of this method, which is further reflected in the fact that it is also applicable to other experimental platforms capable of measuring qubits individually, such as atoms held in optical lattices or tweezers arrays.

Correlation spectroscopy doesn't require the use of entanglement, which is well known to allow for improving precision beyond the standard quantum limit [6, 159, 160] but comes at the expense of being hard to generate and preserve. Thus, the relevant question of how the uncertainties obtained via correlation spectroscopy compare to phase estimation harnessing entangled states is also addressed in this section. Here, we find that for our estimation task entanglement can provide only small advantage that vanishes in the limit of large qubit number.

6.1.1 Phase estimation

Phase estimation plays a central role in metrological and sensing applications. Here, an atomic clock constitutes a prominent example, where the phase of an atomic superposition state is probed by a local oscillator in order to measure time. In this case the energy levels of the atom ideally serve as a stable reference for timekeeping, but in reality may be vulnerable to external perturbances if the atom is not sufficiently shielded form the environment. Quantum sensing applications oftentimes rely on this exact fact of environmental influences leading to phase changes in a quantum system's superposition state. In particular, a qubit's phase with respect to the local oscillator may be sensitive to e.g. magnetic field noise or gravitational changes and tracking phase changes allows for the characterization of the underlying processes giving rise to them.

Ramsey interferometry provides a convenient tool for extracting the phase of a qubit's superposition state. While a typical Ramsey experiment provides information about a qubit's phase

that is averaged over the timescale of the experiment, for some applications more sophisticated parameter estimation tools are required. In this chapter maximum-likelihood and Bayesian estimation is utilized, in order to characterize mechanisms which govern phase variations of qubits either in space or time.

Extracting Phase Information via Ramsey Interferometry

An essential tool in phase estimation is Ramsey interferometry, where the phase of a qubit, encoded in e.g. the electronic states of an atom or ion, with respect to the local oscillator probing the transition, is mapped onto the energy eigenstates of the qubit and can thus be easily read out via projective measurements. Ramsey interferometry was presented in detail in sec. 3.3.4. As described there, the phase ϕ of the qubit with respect to the local oscillator at the end of the Ramsey sequence is a sum of the phase differences between the two Ramsey pulses and acquired phase differences during the free evolution time T. This phase can also be modelled as a sum of temporal and spatial contribution

$$\phi = \phi_T - \phi_R = \Delta T + (\vec{k}_1 - \vec{k}_2)\vec{r} \tag{6.1}$$

where Δ is the frequency detuning between local oscillator and atomic transition, $\vec{k}_1 - \vec{k}_2$ is the difference in k vectors of the two Ramsey fields and $\vec{r}$ represents the position vector of the qubit with respect to some reference position[1]. By expressing the phase in this way it becomes obvious how Ramsey interferometry can be used to gain information about a qubit's environment in sensing applications: One example is the sensing of fields which induce changes in the atomic transition frequency and thus changes in Δ, which can be read out via the phase. While longer free evolution times correlate with increased phase resolution, fast (compared to the timescale set by T) noise processes acting on the qubit or local oscillator may lead to shot-to-shot variations of Δ, which when averaged over many experimental repetitions manifests as dephasing, making it impossible to extract relevant phase information. As will be explained in sec. 6.1.2, correlation spectroscopy constitutes a tool where Ramsey experiments are carried out in parallel on multiple qubits, with the noisy reference common to all qubits dropping out in the analysis such that relevant phase information can be recovered. Moreover, correlation spectroscopy can be applied in the time domain, allowing for characterization of these exact noise processes giving rise to decoherence.

Parameter Estimation Tools

Parameter estimation describes the concept of experimentally determining as accurately as possible the values of certain parameters which govern a system's behavior [161]. As such, parameter estimation combines data analysis with statistical modelling, to describe the distribution of the data and find the most likely model parameters which can produce the experimental observations. The data is gained from probing the system to be studied, e.g. in our case probing the phase of trapped-ion qubits via Ramsey experiments. The method of least squares is an example of a simple and commonly used parameter estimation method which reduces the difference between measured

[1] This equation neglects any deliberately added phase difference between the first and second Ramsey pulse.

data points and a fit function in order to determine fit parameters which best represent the data. However, there exist other and more sophisticated schemes of parameter estimation, such as maximum likelihood (MLE) [162] and Bayesian estimation (BE) [163], which may be more versatile, robust and precise. The basis of both MLE and BE is the likelihood function of the data sample

$$\mathcal{L}(\theta|D) = P(D|\theta) = \prod_{i=1}^{M} P(x_i|\theta) \tag{6.2}$$

where D is the measured data, consisting of M individual measurement outcomes x_i, and θ is the parameter to be estimated. The likelihood function quantifies how likely it is that a possible parameter value has produced D, with $P(x_i|\theta)$ describing the likelihood for an individual measurement outcome. Finding the estimator $\hat{\theta}$ via MLE is based on finding the value of θ which maximizes $\mathcal{L}$:

$$\hat{\theta} = \arg\max_{\theta}(\mathcal{L}(\theta|D)). \tag{6.3}$$

A natural way to determine this maximum is to take the derivative of the likelihood-function with respect to the parameter. However, as it is computationally more challenging to compute the derivative of products compared to sums, oftentimes the logarithm of the likelihood-function is used instead[2].

BE differs from MLE in the sense that instead of finding the single value of θ that maximizes the likelihood, BE is based on considering all possible values of θ, but weighting them according to their likelihood. More specifically, the Bayesian estimate is a weighted average over θ, where the weights are determined by how likely each value is, given the observed data. Mathematically this can be represented as

$$\hat{\theta} = \int \theta P(\theta|D) d\theta, \tag{6.4}$$

where θ is weighted with the *posterior* probability distribution $P(\theta|D)$, which can be derived using Bayes' theorem

$$P(\theta|D) = \frac{P(D|\theta) \cdot P(\theta)}{P(D)}. \tag{6.5}$$

This equation reflects the concept of conditional probability, where beliefs about unknown parameters are updated based on previous information. Here, the posterior consists of the likelihood of observing the data D given θ, represented by the likelihood function $P(D|\theta)$ as before, but also takes into account prior knowledge or believes about the parameter(s) to be estimated, reflected in the *prior* distribution $P(\theta)$. The denominator $P(D) = \int P(D|\theta)P(\theta)d\theta$ represents a normalization factor[3]. By incorporating prior knowledge about the parameter in the estimation process a Bayesian estimator may be less biased in the case that a suitable prior is chosen but may be computationally more complex than MLE. When the data sample size is infinite it is expected that MLE and BE converge.

[2] This does not affect the function argument at which the function is maximized but speeds up the computation.

[3] Note, that instead of explicitly calculating $P(D)$, the posterior is normalized by ensuring the intergral over it equals 1.

Assessing the Performance of Estimators

The outcome of parameter estimation is the estimator $\hat{\theta}$ which can be assessed in terms of accuracy and precision. In this context, the performance of an estimator may depend on a number of factors, such as the quality (e.g. amount of noise) and quantity of the available data, the complexity of the assumed model (how many unknown parameters), and the estimation method. An estimator is considered *unbiased* if the expectation value of the estimator $E(\hat{\theta}) = \theta$, i.e. on average the estimator produces results close to the true value of θ (high accuracy). On the other hand, the estimator may still exhibit significant variance when considering individual repetitions of the estimation process (low precision)[164]. The precision of parameter estimation and related to that also the limitations can be captured by certain statistical tools, such as the Fisher information and Cramer-Rao bound. The Fisher information essentially quantifies the amount of information contained in the data about θ[4][165] and is thus a measure for the precision that can be achieved when estimating θ based on this data. More specifically, the reciprocal of the Fisher information, defined as the Cramer-Rao bound, represents the lower bound for the variance of an unbiased estimator. In the case that the variance of an estimator is close to the Cramer-Rao bound, the estimator is considered *efficient*. In the context of quantum-enhanced parameter estimation, information content in the data about a parameter may exceed classical bounds. This can be quantified by the Quantum Fisher Information, which constitutes the Fisher information optimized over all possible measurement strategies [61, 166]. Related to that, the Quantum Cramer-Rao bound describes the best achievable precision in quantum-enhanced parameter estimation.

6.1.2 Theory on Correlation Spectroscopy

Introduction to Correlation Spectroscopy

When probing a single ionic qubit in the presence of phase noise via Ramsey interferometry, it picks up a random phase during the free evolution time. Consequently, before application of the second Ramsey pulse the Bloch vector points in a different direction within the equatorial plane of the Bloch sphere for each experimental realization. When averaging over these realizations in order to get sufficient measurement statistics, coherence is lost. The phase noise may here result from the atomic energy levels being unstable, e.g. due to magnetic field noise in the ambient environment, or the local oscillator probing the transition being noisy. When considering more that one qubit, the noise processes leading to decoherence oftentimes affect all ions in the same way. Since the ions are manipulated globally, noise on the local oscillator influences all ions probed by it equally. Similarly, magnetic field noise inducing transition frequency fluctuations affects the ions in a collective way due to the ions' close proximity with respect to each other in space. As discussed in sec. 2.4.3 such correlated noise processes may give rise to the emergence of quantum correlations in the form of discord, manifesting as correlations in the outcomes of Ramsey experiments carried out in parallel on the individual particles in the multi-qubit system. While the measurement outcomes of the individual experiments may vary from shot to shot due to dephasing, analysis of correlations in the measurement outcomes allows for an effect subtraction

[4] The Fisher information matrix extends the concept of Fisher information to multiple parameters, providing a complete picture of the information content in the data with respect to all relevant parameters.

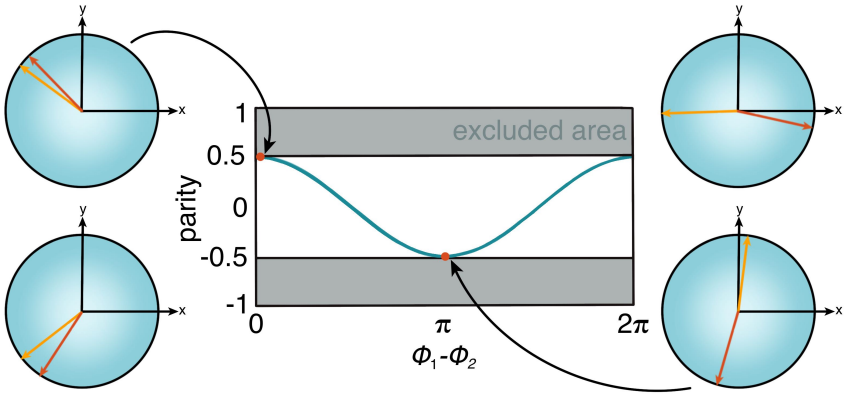

Figure 6.1: Conceptual representation of correlation spectroscopy with two qubits: Two examples of the Bloch vectors of two qubits (yellow and orange) in the equatorial plane pointing in the same direction (left), representing a positive correlation, or opposite directions (right), representing anticorrelation. These correlations depend on the phase difference of the qubits. When measuring the parity signal $\langle \hat{\sigma}_z^{(1)} \hat{\sigma}_z^{(2)} \rangle$ as a function of the phase difference of the two qubits, (anti)correlation emerges as a (minmum) maximum of the parity fringe. The parity fringe has reduced contrast of at most 0.5, as perfect correlation between the qubits can be achieved only via entanglement.

of the noise contribution common to all qubits to uncover other phase differences present between the qubits. In the Bloch sphere picture, this can be visualized as illustrated in fig. 6.1: What is relevant in this case is not the direction in which a Bloch vector is pointing in the equatorial plane, representing an individual measurement outcome, but rather if the Bloch vectors of multiple qubits are pointing in the same (positive correlation) or opposite directions (anticorrelation). This constitutes the key idea of correlation spectroscopy, where phase differences between qubits can be measured precisely even in the presence of strong dephasing, by harnessing the collective nature of the noise processes giving rise to decoherence. The measurement protocol constitutes the determination of parities, for two qubits written as $\hat{\sigma}_z^{(1)} \hat{\sigma}_z^{(2)}$. Upon averaging the individual measurement outcomes over the common random phase φ[5], the parity expectation value is proportional to the cosine of the phase difference between the qubits:

$$C_{12} \equiv \langle \hat{\sigma}_z^{(1)} \hat{\sigma}_z^{(2)} \rangle = \frac{1}{2\pi} \int_0^{2\pi} d\varphi \cos(\phi_1 + \varphi) \cos(\phi_2 + \varphi) = \frac{1}{2} \cos(\phi_1 - \phi_2) \tag{6.6}$$

This parity signal is also illustrated in fig. 6.1. Here, a maximum contrast of the parity fringe of 0.5 can be achieved. Full contrast, i.e. perfect correlation between a pair of qubits, can be achieved only with entangled input states. As a higher contrast corresponds to an increased signal to noise ratio in phase estimation, entanglement provides a benefit compared to the discordant state employed in correlation spectroscopy. However, later on in sec. 6.1.3 a quantitative investigation is presented on how phase uncertainty scales when increasing the qubit number beyond $N = 2$,

[5] Here, φ encodes the fluctuations resulting from collective dephasing, which are assumed to be randomly distributed over 2π.

showing that for the given phase estimation task the advantage of entanglement-enhanced phase estimation over correlation spectroscopy vanishes in large systems.

As shown in sec. 6.1.1, the phase of a trapped-ion qubit contains information about the detuning between the local oscillator and atomic transition frequency as well as about the position of the ion. In correlation spectroscopy phase differences

$$\phi_1 - \phi_2 = (\Delta_1 - \Delta_2)T - (\vec{k}_1 - \vec{k}_2)(\vec{r}_1 - \vec{r}_2) \tag{6.7}$$

are measured. From this expression it is straight forward to see that correlation spectroscopy can be carried out in two distinct ways in order to either access information about detuning or position differences of the ions. In order to access information about detuning differences, the experiment is carried out with two Ramsey pulses from the same spatial direction for which $\vec{k}_1 = \vec{k}_2$ and thus the second term in eq. 6.7 equals zero. Since the frequency of the local oscillator is the same for both ions probed, the measured phase difference results only from transition frequency differences of the qubits, e.g. due to a spatially varying field gradient giving rise to energy level shifts across an ion crystal. On the other hand, carrying out Ramsey experiments with a nonzero k vector difference and free evolution time $T = 0$ makes the phase difference sensitive only to the spatial arrangement of the ions.

In summary, correlation spectroscopy allows for the precise measurement of transition frequency differences and ion-ion distances, even in the presence of strong dephasing, by exploiting the collective nature of the noise. Extending the probe time beyond the limit imposed by single-particle coherence allows for higher phase resolution and measurement precision. These techniques allow e.g. for the characterization of the ions' environment, e.g. magnetic field structure and harmonicity of the potential. As will be shown in the following, measurement outcomes can also be correlated in the time domain to track changes in φ giving rise to dephasing and thus to characterize the noise processes leading to decoherence.

Model for N-Qubit Correlation Spectroscopy

The previous subsection introduced the concept of correlation spectroscopy in the smallest possible system consisting of two qubits. Now these ideas are extended to N qubits, encoded in N trapped ions, which represent a network of quantum sensors [155, 156, 157, 158]. In such larger systems different types of correlations, from pair to N-particle correlations, can be analyzed and harnessed to improve phase estimation. When a Ramsey experiment is carried out in parallel on N qubits, the collective state of the system before the second $\pi/2$ pulse is applied can be written as a product state of the individual ion's states, which are distributed within the equatorial plane of the Bloch sphere:

$$2^{-\frac{N}{2}} \prod_{i=1}^{N} (|0\rangle + e^{i\phi_{im}}|1\rangle), \tag{6.8}$$

This denotes the mth realization of the Ramsey experiment with $m = 1, \ldots, M$. The phase of the individual qubit superposition states can be written as

$$\phi_{im} = \phi_i + \varphi_m, \tag{6.9}$$

a sum of the qubit-specific phase ϕ_i, varying over space, and a random phase φ_m, fluctuating in time but common to all qubits, e.g. stemming from magnetic field or laser noise[6]. As shown in eq. 6.1, the Ramsey phase can be written as a sum of spatial and temporal contribution. Now only the qubit-specific phases are represented in this way, i.e. as $\phi_i = (\vec{k}_1 - \vec{k}_2)\vec{r}_i + \Delta_i T$, with the assumption that this phase remains constant over many experimental repetitions, while shot to shot variations are contained only in φ_m. The outcome of the mth experimental realization of the Ramsey measurement of qubit i is denoted as $q_{im} = 1$ or -1, corresponding to measuring the qubit in state $|0\rangle$ or $|1\rangle$, repectively. The probability of observing the outcome q_{im} is given by

$$p(q_{im}) = \frac{1}{2}(1 + q_{im}\sin(\phi_{im})). \tag{6.10}$$

Given the experimental measurement outcomes of N qubits, one goal is to as precisely as possible extract the phase differences $\phi_i - \phi_j$, with the second goal of characterizing the temporally fluctuating phase φ_m. These goals are achieved by modelling the situation as a multi-parameter phase estimation problem.

For the determination of phase differences $\phi_i - \phi_j$, φ_m is assumed to be uniformly distributed over 2π, which represents a situation where the Ramsey probe time is much longer than the coherence time of the individual qubits. The state of the qubit network after application of the first Ramsey pulse and exposure to this phase noise is given by

$$\begin{aligned} \rho &= \frac{1}{2\pi}\int_0^{2\pi} d\varphi |\Psi(\varphi)\rangle\langle\Psi(\varphi)| \quad \text{with} \\ |\Psi(\varphi)\rangle &= 2^{-\frac{N}{2}} \prod_{i=1}^{N} (|0\rangle_i + e^{i\varphi}|1\rangle_i). \end{aligned} \tag{6.11}$$

This state is clearly separable but does contain quantum discord. The effect of the ion specific phase shifts ϕ_i can be represented by a unitary operation $\hat{U}_{\boldsymbol{\phi}} = \exp(\frac{i}{2}\sum_i \phi_i \hat{\sigma}_z^{(i)})$ acting on ρ. After evolution under $\hat{U}_{\boldsymbol{\phi}}$ the second Ramsey pulse is applied, which can be modelled as $\hat{U}_X = \exp(-i\frac{\pi}{4}\sum_i \hat{\sigma}_x^{(i)})$, followed by a projective measurement to extract measurement outcomes q_{im}. The Ramsey measurement outcome of qubit i is thus described by the expectation value $\langle\hat{\sigma}_z^{(i)}\rangle = \mathrm{Tr}(\hat{U}_X\hat{U}_{\boldsymbol{\phi}}\rho\hat{U}_{\boldsymbol{\phi}}^\dagger\hat{U}_X^\dagger\hat{\sigma}_z^{(i)})$, which results in zero due to dephasing and thus contains no useful information.

Estimating ϕ_i from Pair Correlations

However, analysis of correlations in the measurement outcomes of ions i and j corresponds to performing the parity measurement $C_{ij} \equiv \langle\hat{\sigma}_z^{(i)}\hat{\sigma}_z^{(j)}\rangle = 1/2\cos(\phi_i - \phi_j)$, in analogy to eq. 6.6. Here, it is assumed that no other sources of decoherence besides collective dephasing are present which would lead to an additional decay of the Ramsey contrast. However, later on in sec. 6.1.2, the influence of additional uncorrelated dephasing on the measurement precision is discussed. Pair correlations of measurement outcomes can be represented by a correlation matrix $C = (C_{ij})$,

[6] More specifically, φ_m here is defined as the phase difference between the mth and the first experiment.

a fit of which allows single-qubit phase estimates $\hat{\phi}_i$ to be determined up to an irrelevant global offset phase. From these estimators the single qubit phase differences $\hat{\phi}_i - \hat{\phi}_j$ can be determined, providing information about transition frequency or position differences of the ions.

Estimating ϕ_i and φ_m from N-particle correlations via MLE and Bayesian techniques

It will be shown in sec. 6.1.2 and 6.1.3 that considering higher order correlations provides a precision enhancement for the given phase estimation task, compared to only considering pair correlations. Thus, we employ parameter estimation techniques based on MLE and Bayesian techniques in order to extract the single-qubit phases from N-qubit correlations. Additionally, in this section, Bayesian estimation is employed to characterize noise processes giving rise to decoherence, by tracking the randomly fluctuating phase φ_m in time.

For estimation of the single-qubit phases $\boldsymbol{\phi} = (\phi_1, \phi_2, \ldots)$ the function $P(\mathbf{q}|\boldsymbol{\phi})$ is introduced, describing the likelihood of observing the single-shot measurement outcome $\mathbf{q} = (q_1, \ldots, q_N)$:

$$P(\mathbf{q}|\boldsymbol{\phi}) = \frac{2^{-N}}{2\pi} \int_0^{2\pi} d\varphi \prod_{i=1}^{N} (1 + q_i \sin(\phi_i + \varphi)) \tag{6.12}$$

In order to simplify this expression, the integral over φ can be replaced by an average over $N+1$ evenly distributed phases $\varphi_m = 2\pi m/N$[7]. Evaluation of the log-likelihood function

$$\mathcal{L}(Q|\boldsymbol{\phi}) = \log \prod_{m=1}^{M} P(\mathbf{q}_m|\boldsymbol{\phi}) \tag{6.13}$$

for a set of measurements $Q = (q_{im})$ yields MLE phase estimates $\hat{\phi}_i$.

The phase estimates $\hat{\phi}_i$ may then be used as a basis for estimating the random phase φ_m. As φ_m fluctuates from one experimental realization to the next, single-shot Ramsey interferometry has to be applied in order to extract it. Here, parameter estimation techniques essentially allow a Ramsey fringe to be fitted to single-shot measurement outcomes $\mathbf{q}_m \equiv (q_{im})_{i=1}^{N}$, despite the lack of sinusoidal data, as shown in fig. 6.3d. The position of the single-shot Ramsey fringe with respect to the ion crystal represents the phase φ_m for a given experimental realization. The likelihood function for this estimation task is given by

$$P(\mathbf{q}_m|\{\hat{\phi}_i\}, \varphi) = 2^{-N} \prod_{i=1}^{N} (1 + q_{im} \sin(\hat{\phi}_i + \varphi)), \tag{6.14}$$

[7] This discretization is valid as $2\pi/N$ represents the periodicity of the highest Fourier component of the integral kernel, meaning that essential features of the integral will be preserved.

of similar form to the previous case in eq. 6.12. However, here φ is the parameter to be estimated, with previously determined single-qubit phases $\hat{\phi}_i$ applied in the equation. The Bayesian estimate for the random phase in experimental realization m is given by

$$\hat{\varphi}_m = \arg\left(\int_0^{2\pi} d\varphi e^{i\varphi} P(\mathbf{q}_m|\{\hat{\phi}_i\},\varphi)\right), \tag{6.15}$$

i.e. a weighted average over all possible phases φ with the weight given by the probability of observing the respective measurement outcome[8]. Tracking this phase from shot to shot allows the temporal fluctuations of the local oscillator with respect to the qubit transition frequencies to be characterized, which are either caused by instabilities of the oscillator or of the qubit energy levels due to magnetic field noise.

Once estimates $\hat{\varphi}_m$ are available it is also possible to perform BE in order to estimate single-qubit phases $\boldsymbol{\phi}$. Here, the likelihood function is of the form

$$P(\mathbf{q}_i|\phi_i,\{\hat{\varphi}_m\}) = 2^{-N}\prod_{m=1}^{M}(1+q_{im}\sin(\phi_i+\hat{\varphi}_m)), \tag{6.16}$$

where $\mathbf{q}_i \equiv (q_{im})_{m=1}^{M}$. The Bayesian estimate for $\hat{\phi}_i$ is given by

$$\hat{\phi}_i = \arg\left(\int_0^{2\pi} d\phi e^{i\phi} P(\mathbf{q}_i|\{\hat{\varphi}_m\},\phi)\right). \tag{6.17}$$

In sec. 6.1.3 a comparison of the phase uncertainty using MLE vs. BE is provided, showing that while the Bayesian approach is computationally fast, it is less precise when estimating single-ion phases $\boldsymbol{\phi}$.

Precision Limits in Estimating Phase Differences

This subsection is concerned with the fundamental limits of precision that can be achieved in our phase estimation task when considering no dephasing, correlated dephasing and uncorrelated dephasing. Moreover, the precision limit when considering entangled input states is given.

Noiseless precision bound

In a first step a situation is considered where neither correlated nor uncorrelated dephasing is acting on the qubits. Here, an N-qubit system can be modelled as a pure product state

$$2^{-\frac{N}{2}}\prod_{i=1}^{N}(|0\rangle_i + e^{i\phi_i}|1\rangle_i), \tag{6.18}$$

[8] Here, the prior is the assumed uniform probability distribution of φ over 2π, where all values of φ are considered equally likely before observing the data.

where the precision in estimating phase ϕ_i, given M measurements, is defined by quantum projection noise

$$\sigma_{\phi_i} = \frac{1}{\sqrt{M}}. \tag{6.19}$$

This expression is derived from the projection noise defined in eq. 2.12, where we model $p = 0.5(1 + \sin(\phi_i))$ and consider the condition

$$\sigma_p = |dp/d\phi_i|\sigma_{\phi_i}. \tag{6.20}$$

As each phase is estimated independently from the M measurements, the minimum uncertainty when estimating a phase difference $\Delta\phi = \phi_2 - \phi_1$ is simply given by

$$\sigma_{\Delta\phi} = \sqrt{\sigma_{\phi_1}^2 + \sigma_{\phi_2}^2} = \sqrt{\frac{2}{M}}, \tag{6.21}$$

which represents the *noiseless precision bound*, i.e. the best precision that can be achieved with a product input state in the absence of dephasing.

Bounds in the Presence of Correlated Dephasing

In the scenario where correlated dephasing is present, the uncertainties σ_{ϕ_i} in the individual phases will not be independent. This has to be considered when applying error propagation of quantum projection noise in order to find the uncertainty in the phase difference of two qubits

$$\sigma_{\Delta\phi}^{N=2} = \frac{\sqrt{4 - \cos^2(\phi_i - \phi_j)}}{\sqrt{M}|\sin(\phi_i - \phi_j)|}. \tag{6.22}$$

This expression diverges at phase differences approaching values 0 and π, where the parity fringe reaches an extremum, as illustrated in fig. 6.1, and becomes minimal at $\Delta\phi = \pi/2$. At the minimum, the uncertainty in $\Delta\phi$ is given by

$$\min \sigma_{\Delta\phi}^{N=2} = \frac{2}{\sqrt{M}}, \tag{6.23}$$

larger by a factor of $\sqrt{2}$ than the noiseless precision bound derived in eq. 6.21, due to the reduced contrast of at most 0.5 in correlation spectroscopy.

In our work we demonstrate that it is possible to beat this threshold by analysing higher-order correlations in multi-qubit systems, eventually approaching the noiseless precision bound in eq. 6.21 in the limit of $N \to \infty$. The improvement can be understood intuitively by recognizing that estimating all single-qubit phase differences $\Delta\phi_{ij} = \phi_i - \phi_j$ allows for estimation of the random phases φ_m for each experimental shot m, with higher precision the more particles are in the system (see eq. 6.27). While this fluctuating random phase is the reason for necessitating the use of correlation spectroscopy with reduced parity fringe contrast, its complete reconstruction in time allows access to the full phase information. Instead of basing the analysis on a parity fringe with reduced contrast we therefore harness single-shot Ramsey fringes with close to full contrast, which essentially represents the noiseless limit. In sec. 6.1.3 this intuition is verified experimentally: By analyzing $N = 91$ particle correlations of measurement outcomes an improvement in

phase uncertainty is obtained compared to considering only pair correlations, approaching the noiseless precision bound.

Bound in the Presence of Additional Uncorrelated Dephasing

So far the influence of only correlated dephasing on this phase estimation task was investigated. In reality, however, there may be additional uncorrelated dephasing present in the experiment. The aforementioned precision bound can be generalized to include this contribution by introducing a finite contrast C_0. The following derivations are provided in more detail in [38], here just the most important steps are discussed. As a first step the *finite contrast precision bound* is defined, describing a situation where only uncorrelated dephasing and no correlated dephasing is present. The input state is here no longer the product state in 6.18 but becomes mixed according to

$$\frac{1}{2^N}\prod_i \left(\mathrm{I} + C_0 \hat{R}_{\phi_i}\right) \tag{6.24}$$

where $\hat{R}_{\phi_i} = \cos(\phi_i)\hat{\sigma}_x^{(i)} + \sin(\phi_i)\hat{\sigma}_y^{(i)}$. Here, in analogy to the previously given derivations, and assuming that the phase ϕ_i is drawn from a uniform distribution, the uncertainty of estimating ϕ_i is given by

$$\sigma_{\phi_i} = \frac{1}{\sqrt{M(1-\sqrt{1-C_0^2})}} \tag{6.25}$$

which results in an uncertainty in estimating $\Delta\phi = \phi_i - \phi_j$ of

$$\sigma_{\Delta\phi} = \frac{\sqrt{2}}{\sqrt{M}\sqrt{1-\sqrt{1-C_0^2}}}. \tag{6.26}$$

As a second step correlated dephasing is included in the model. This derivation is based on first determining the uncertainty in estimating the common random phase φ_m

$$\sigma_{\varphi_m} = \frac{1}{\sqrt{N(1-\sqrt{1-C_0^2})}}, \tag{6.27}$$

which is dependent on particle number N. This expression is derived analogously as eq. 6.25, with the exception of replacing M with N. The contrast of the single-shot Ramsey fringes is limited by this uncertainty to

$$C_{\text{unscr.}} = C_0 \exp\left(-\frac{1}{2N(1-\sqrt{1-C_0^2})}\right). \tag{6.28}$$

Here, unscr. represents “unscrambled", referring to the fact that by tracking the random phase φ_m the Ramsey fringes that are scrambled by decoherence processes are effectively reconstructed. The contrast derived in 6.28 contains C_0, reduced from full contrast of 1 by uncorrelated dephas-

ing, as well as a further reduction from the finite precision achievable when estimating φ_m. The uncertainty in the phase difference $\Delta\phi$ is given by

$$\sigma_{\Delta\phi}(N, C_0) = \frac{\sqrt{2}}{\sqrt{M(1-\sqrt{1-C_{\text{unscr.}}^2})}}, \tag{6.29}$$

where C_0 in eq. 6.26 was simply replaced by the further reduced contrast $C_{\text{unscr.}}$, to arrive at this simple analytical model incorporating the effect of uncorrelated and correlated dephasing in correlation spectroscopy. In fig. 6.4b the dark blue theory line represented by eq. 6.29 is compared to experimental data. Besides this simple model, ref. [38] provides information on how the Fisher information can be used alternatively, in order to determine precision bounds achievable for pair correlations as well as N-particle correlations. As the states generated in our experiments do not contain any entanglement, the classical Fisher information suffices for these analyses.

Precision Bound Using Entangled Input States or Nonlocal Measurements

As discussed in sec. 6.1.1 the quantum Fisher information provides insight into the precision achievable in entanglement-enhanced phase estimation. While our experiments do not involve the preparation of entangled states, these bounds are explored theoretically. In the case of two qubits, phase estimation harnessing a Bell state would provide an advantage compared to the correlation spectroscopy approach, due to the factor of 2 larger contrast of the parity signal and the corresponding improved signal to noise ratio. This section summarizes how this advantage scales with increasing particle number, with details to be found in [38] and its appendices. In order to quantify the superiority in estimating phases offered by entangled states and nonlocal measurements, the theoretical analysis has to be optimized over all possible input states and measurement strategies. This optimization is achieved by minimizing the variance between any pair of qubits via minimization of

$$\frac{1}{\binom{N}{2}}\sum_{j>k}\text{Var}(\phi_j - \phi_k), \tag{6.30}$$

yielding

$$\sigma_{\Delta\phi} = \sqrt{\frac{N-1}{N}}\sqrt{\frac{2}{M}}, \tag{6.31}$$

with an analysis based on the quantum Fisher information matrix confirming this as the ultimate precision limit for our estimation task. In fig. 6.4b the expression in eq. 6.31 is plotted as a red line, illustrating this precision bound as a function of qubit number in comparison to experimental data and the bound derived in eq. 6.29. The entanglement-enhanced limit can be reached via several strategies based on initializing entangled input states and employing local measurements in the x or y basis: One option is to prepare symmetric Dicke states of N particles with $N/2$ excitations[9], which when measured in the x basis result in the quantum Cramer-Rao bound given in eq. 6.31. A second option is to probabilistically[10] prepare the qubits in products of anti-parallel Bell states. From eq. 6.31 it becomes evident that the advantage of using entangled states decreases

[9] Symmetric Dicke states are quantum states of an N qubit system which are symmetric under permutation of any particles.

[10] Here, different pairs of qubits are entangled for each experimental realization.

with increasing qubit number, with the phase uncertainty eventually approaching the noiseless precision bound for large N. The reason for this increase in uncertainty is frustration, prohibiting the preparation of all pairs of qubits in anti-parallel states.

6.1.3 Experimental Implementation

In this section the implementation of correlation spectroscopy on a 91-ion planar crystal is demonstrated. In particular, the measurement protocol for N-qubit correlation spectroscopy is presented along with experimental data from which phase uncertainties are determined.

Measurement Protocol

The N-qubit correlation spectroscopy measurement protocol, used for most measurements carried out within this thesis work, is illustrated in fig. 6.2. Here, the ground state qubit transition is probed in Ramsey experiments using a magnetic RF signal produced by the antenna described in sec. 4.5. The first Ramsey $\pi/2$ pulse prepares the ions' Bloch vectors in the equatorial plane. Subsequently, the qubits' superposition states undergo free evolution for a duration T, during which correlated noise imprints a fluctuating collective phase φ onto the ions. Additionally, individual ions within the crystal acquire ion-specific phase shifts ϕ_i. After the free evolution time, the second Ramsey $\pi/2$ pulse maps information about these accumulated phases into the measurement basis, where it is read out via projective measurements. In data analysis the single-shot measurement outcomes are correlated, which can be done in two distinct ways: One option is to correlate the measurement outcomes of different ions probed at the same time, illustrated in blue. Alternatively, correlations in the time domain can be investigated, by correlating outcomes of consecutive measurements of a specific ion, illustrated in orange.

Quantum Correlations within a 91 Ion Planar Crystal

This subsection presents data on correlation spectroscopy according to the protocol shown in fig. 6.2 performed on a planar Coulomb crystal consisting of 91 ions trapped in a potential characterized by the trap frequencies 2π (2196, 680, 343) kHz. In these experiments the Ramsey wait time was chosen as $T = 10\,\mathrm{ms}$, which at the time exceeded the coherence time of the qubit[11]. The correlations of measurement outcomes of all pairs of ions are visualized as a correlation matrix, shown in fig. 6.3a. More specifically, this matrix shows if the qubits are measured to be in the same qubit state (yellow) or different states (green) at the end of the Ramsey sequence. Here, the ion numbering is chosen to increase from the left to the right side of the crystal. A fringe pattern can be observed, alternating between positive and negative correlation, with anticorrelations of -0.5 indicating a phase difference of π between ions. A fit of the correlation matrix allows the single ion phases ϕ_i to be reconstructed[12]. As only relative phases, not absolute phases, can be

[11] While now the coherence time of the ground state qubit in our apparatus is significantly longer (see sec. 5.5), the measurements presented in this section were taken before the apparatus was enclosed in a magnetic field shielding. Thus, when those measurements were carried out, after a Ramsey time of 5 ms already no single-particle coherences were remaining.

[12] Note that this reconstruction is based only on pair correlations and can be further improved by harnessing N-particle correlations.

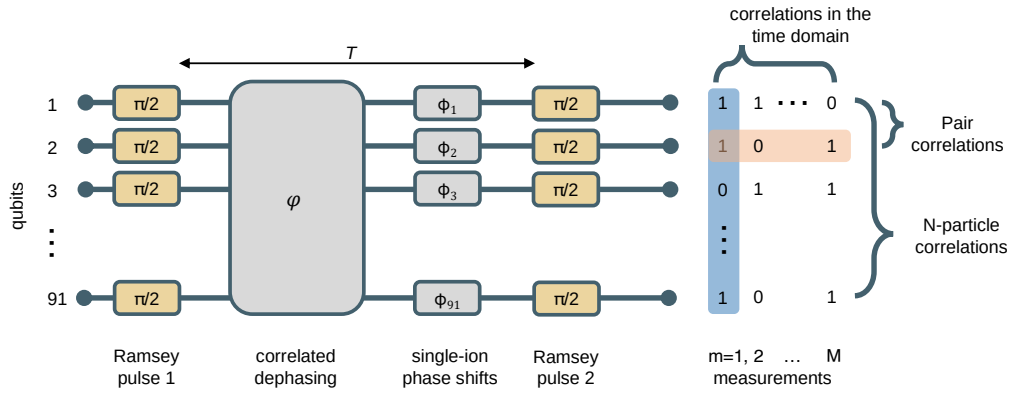

Figure 6.2: Measurement protocol of correlation spectroscopy: N qubits are simultaneously probed in Ramsey experiments. The first $\pi/2$ pulse prepares all qubits in the equatorial plane of the Bloch sphere. During the free evolution time T of the Ramsey experiment the qubits pick up a collective random phase φ, representing correlated dephasing, as well as ion-specific phase shifts ϕ_i. The second $\pi/2$ maps the phase information back into the measurement basis. Finally, the outcomes of projective measurements are correlated, either of different qubits probed at the same time (column vector q_m) or of the same qubit at different times (row vector q_n). In this way phase differences between qubits and the temporal evolution of phases can be characterized, respectively.

measured, the phase ϕ_1 of qubit 1 is set to zero, with all other qubit phases considered relative to ϕ_1. The phases ϕ_i for all 91 ions are shown, modulo 2π, in fig. 6.3b. Here, a phase shift between ϕ_{91} and ϕ_1 of a bit more than 2π is observed, which results from a magnetic field inhomogeneity across the ion crystal, giving rise to qubit-specific transition frequency shifts, described in detail in sec. 6.1.4. While it would be possible to reduce this magnetic field gradient to a small value, for the measurements presented here it was intentionally left larger as phases spanning over at least 2π facilitates data fitting. From the single ion phases ϕ_i, phase differences $\phi_i - \phi_j$between two qubits are reconstructed, and in fig. 6.3c the correlations between pairs of qubits i and j are plotted as a function of the phase difference between them. Despite the lack of single particle coherence due to fluctuating φ, the result is a parity fringe with a contrast of 0.5, which represents full contrast in the context of this measurement technique.

Besides analyzing correlations of measurement outcomes of different ions probed simultaneously, the outcomes can also be studied and correlated in the time domain. In fig. 6.3d the measurement outcomes of all 91 ions from a single experimental shot are plotted as a function of single ion phases ϕ_i (yellow points). This representation allows for the reconstruction of single-shot Ramsey fringes. Despite the absence of sinusoidal data due to considering only a single experimental repetition and corresponding projective measurement outcomes of 0 or 1, it is possible to identify the structure of a Ramsey fringe: For some phases the measurement outcomes are mostly in the upper state, indicating the location of a fringe maximum, while for other phases outcomes are mostly in the lower state, indicating a minimum. This reflects the concept that different ions can be considered to occupy different locations within a single Ramsey fringe. The position of the Ramsey fringe for a certain experimental cycle depends on the random phase φ_m at that moment. For example, the green circles in the figure represent a different measurement cycle, where

the Ramsey fringe is roughly out of phase by π with respect to the yellow data[13]. In order to reconstruct the most likely position of the single-shot Ramsey fringe, given the available data, a Bayesian estimation is carried out, as described in eq. 6.15. This estimation finds the most likely value of φ_m to have produced the observed outcomes of measurement m. Carrying out such an estimation for each experimental cycle allows φ to be tracked over time, which in turn allows the noise giving rise to decoherence to be characterized. In fig. 6.3e, two single-qubit Ramsey fringes with nearly full contrast are displayed. These are obtained by binning the data into sets of similar phase φ_m and then plotting the expectation value $\langle \hat{\sigma}_z^{(i)} \rangle$ as a function of this phase.

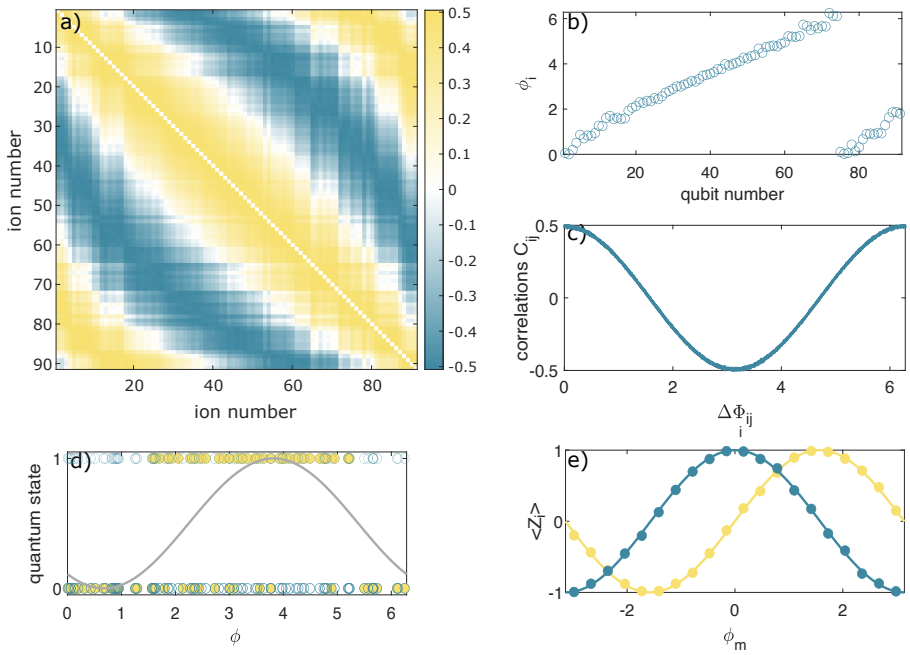

Figure 6.3: Correlation spectroscopy of a 91-ion planar crystal with $M = 26852$ experimental repetitions: a) Correlation matrix visualizing pair correlations between all N qubits. These correlations are limited to $\leq 1/2$ due to the reduced contrast in correlation spectroscopy. b) A fit of the correlation matrix allows the ion-specific phases $\hat{\phi}_i$ to be estimated. c) Correlations between ions are plotted as a function of the phase difference $\phi_i - \phi_j$ obtained by analysis of N-qubit correlations. d) The yellow points and green circles represent measurement outcomes of two different experimental realizations, plotted as a function of the single-qubit phase estimates. The black curve represents a single-shot Ramsey fringe, fitted to the yellow data points via Bayesian estimation, in order to determine the common random phase $\hat{\varphi}_m$. e) By binning the data into sets of similar $\hat{\varphi}_m$, single-qubit Ramsey fringes with nearly full contrast can be constructed. Here, two out of the 91 single-qubit fringes are shown. Note that here $\langle Z_i \rangle = \langle \hat{\sigma}_z^{(i)} \rangle$.

[13] From this example it becomes clear that averaging over multiple measurement outcomes would eliminate any contrast in the signal.

Uncertainty in the Estimated Phases

This subsection investigates experimentally how the uncertainty in measuring phase differences scales in N qubit correlation spectroscopy, with a comparison of the results made to theory derived in sec. 6.1.2[14]. Here, different types of correlations can be considered for analysis. Besides solely correlating the measurement outcomes of the two qubits, whose phase difference should be determined, one can take into account pair correlations of other qubits in the system that were simultaneously recorded. Moreover, higher-order correlations can be analyzed up to the full counting statistics of N-qubit correlations. In sec. 6.1.2 it was derived that considering higher-order correlations in the analysis leads to an improvement in phase estimation for a finite number of experimental repetitions. In order to demonstrate this experimentally, the data presented in sec. 6.1.3 is divided into 134 subsets of 200 samples each, representing independent experiments. For each subset, the single qubit phase difference estimates $\hat{\phi}_i - \hat{\phi}_j$ are reconstructed. This essentially results in 134 realizations of each phase difference, with the phase uncertainty estimated from the spread of these values, quantified by the standard deviation. The phase uncertainty as a function of the phase difference is shown in fig. 6.4a. Here, yellow points correspond to the case where two-qubit correlations are considered. These points do not span the full range of phases as points with contrast higher than 0.5 are omitted. For these pair correlations the phase uncertainty becomes lowest at phase difference $\pi/2$ as the slope of the parity fringe is steepest here, which is expected from eq. 6.22. The experimentally observed uncertainty is well described by this expression, shown as an orange line in fig.6.4a, which represents the limit imposed by quantum projection noise (under correlated dephasing). Carrying out MLE of the observed N-bit strings as described in sec. 6.1.2 allows the phase uncertainty when considering N-qubit correlations to be determined. These uncertainties are represented by the green points in fig. 6.4a, with the white line illustrating the average over all points, demonstrating a clear improvement compared to the case of considering only two-particle correlations. The black dashed line in the figure represents the noiseless precision bound $\sigma_{\Delta\phi} = \sqrt{2/M}$. Notably, our data comes within about 10 percent of this limit.

Having shown that the analysis of higher-order correlations is advantageous in the context of measurement precision, the question remains how the uncertainties scale with the number of qubits in the sensor network. In order to investigate this, the data is split into subsets of specific qubit number, with each subset containing single-qubit phases approximately evenly distributed over 2π. As before, in order to estimate the phase uncertainty, the data subsets are split and analyzed in partitions of 200 experimental realizations. While for the previous analysis only MLE was employed, here both MLE and BE are used for determining the single-ion phases, which allows for a comparison of the two methods. The resulting phase uncertainties are shown in fig. 6.4b. With increasing qubit number, the uncertainty decreases, asymptotically approaching the black line representing the noiseless precision bound for $N \to \infty$. The theoretical prediction of the finite contrast precision bound, as derived in eq. 6.29, is shown as a dark blue line. The experimental results obtained via MLE (dark blue points) agree well with this model, while the uncertainties obtained via BE approach the ones obtained via MLE only in the limit of large qubit number. Thus, it can be concluded that BE provides a more imprecise result, compared to MLE,

[14] Note, that as the measurement results on which the uncertainties are based on are assumed to be normally distributed, the estimator is considered to be unbiased [167].

for this estimation task. Additionally, the dependence of phase uncertainty on data sample size was investigated for a fixed number of $N = 91$ qubits, shown in the inset of fig. 6.4b. The phase uncertainty reduces with increasing sample size, with the data agreeing well with the noiseless precision bound, illustrated as a black line, which means that the uncertainty is still projection-noise limited at $M = 10^4$ samples. Finally, in order to illustrate how the uncertainties achievable in correlation spectroscopy compare to entangled input states, the bound derived in eq. 6.31 is shown as a red line in fig. 6.4b. While in the case of few qubits an initial advantage of precision is visible, it vanishes for large qubit numbers, with the entanglement-based bound also approaching the noiseless precision limit.

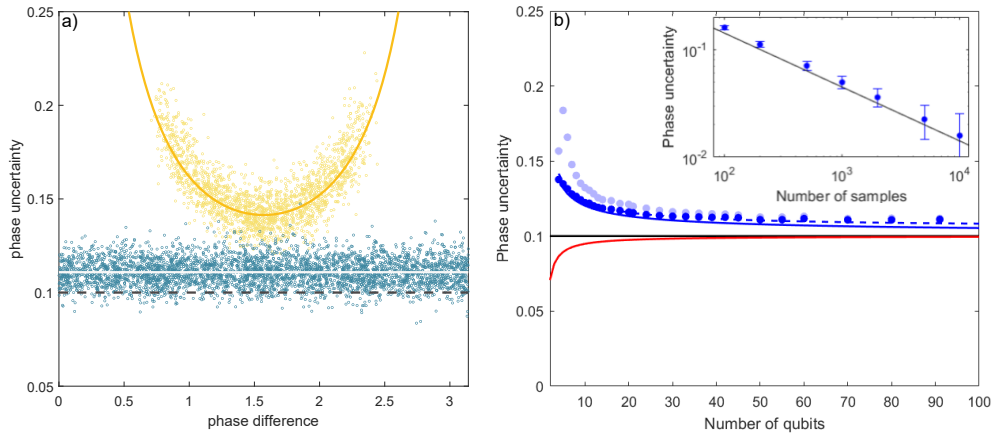

Figure 6.4: Uncertainty in phases estimated from N-qubit correlation spectroscopy, based on the data presented in fig. 6.3: a) The phase uncertainty is calculated for pair correlations (yellow data points) and 91-qubit correlations (green data points), with the solid white line representing the average of the green data points. The yellow points do not span the full range of phases as data which produces correlations exceeding 0.5 is omitted. Grey dashed and solid yellow lines represent the noiseless precision bound in eq. 6.21 and the two-qubit limit under correlated dephasing in eq. 6.22, respectively. b) The phase uncertainty is investigated in dependence of qubit number and sample size. The data is analyzed in samples of $M = 200$ experimental realizations. Here, phase estimation is carried out via MLE (dark blue data points) and BE (light blue points), which allows for a comparison of the two methods. The theoretical prediction for phase uncertainty as a function of qubit number, derived in eq. 6.29, is shown as a solid dark blue line ($C_0 = 1$) and a dashed blue line ($C_0 = 0.995$), with the finite contrast C_0 determined from a fit to the experimental data. The black line represents the noiseless precision bound. The optimum uncertainty achievable with entangled input states, given in eq. 6.31, is illustrated as a red line. The figure inset displays the phase uncertainty achievable when harnessing 91 qubit correlations, as a function of the sample size, with the black line representing the noiseless precision bound.

6.1.4 Applications

Correlation spectroscopy is a useful and versatile tool which can be applied in different ways, e.g. for the determination of spatial transition frequency differences, relative ion positions and to characterize noise processes (giving rise to decoherence) in the time domain. In the context of this

thesis this tool is predominantly used on large planar ion crystals in order to characterize and optimize our experimental setup in a variety of ways. First, a magnetic field gradient, giving rise to transition frequency shifts across the ion crystal, is determined and compensated. As a second application, the screening performance of our magnetic field shielding in the low frequency domain is characterized. As a third application, the alignment of our Raman laser beams with respect to the ion crystal plane is optimized. In this way, coupling to the out-of-plane motional modes is maximized while undesired coupling to in-plane modes is minimized. Additionally, an overview of further applications is presented that were realized in experiments with long strings of ions in a separate experimental apparatus.

Characterizing a Magnetic Field Gradient

In this section the spatial arrangement of reconstructed qubit-specific phases ϕ_i is used to quantify transition frequency shifts across a 91-ion crystal, that arise from a magnetic field gradient. A visual representation of these phases, plotted as a function of position, is shown in the top image of fig. 6.5. Here, a linear fit function is applied to the data, shown as colored lines that represent contour lines of constant phase. The fit parameters thus represent the phase gradient that emerges over the timescale of the Ramsey experiment ($T = 5$ ms), which can be related to the spread in qubit transition frequencies across the ion crystal. Here, the expression

$$\gamma \mu_B B_{\text{grad}} = \frac{\hbar a}{T} \tag{6.32}$$

can be used, connecting the observed phase gradient, quantified by fit parameter a, to the expected energy splitting due to the Zeeman effect. Here, $\gamma = m_1 g_1 - m_2 g_2$ represents the difference of the product of magnetic quantum number and Landé factor of the ground states, μ_B is the Bohr magneton and B_{grad} is the magnetic field gradient to be determined. From this analysis a magnetic field gradient of 0.85(1) G/m is extracted, which has an angle of 38.6(4) degrees with respect to the horizontal direction of the camera image. The transition frequency difference from one side of the ion crystal to the other corresponds to $(\phi_{max} - \phi_{min})/(2\pi T) = 218.2(8)$ Hz. Residuals, which remain after subtracting the dominant linear contribution from the phase gradient, are shown in the central image of fig. 6.5. Here, we observe a small quadratic contribution, indicating higher order terms in the magnetic field structure. After subtracting a quadratic fit function from the data only minor residuals on the order of 1 Hz remain, shown in the bottom row of the figure. This measurement demonstrates that small magnetic field gradients giving rise to transition frequency differences across an ion crystal can be measured precisely with probe times exceeding the single-particle coherence. Precise measurement of such a gradient allows it to be minimized: In our apparatus, correlation measurements were carried out for various configurations of permanent magnets and currents applied to the pair of gradient-compensation coils placed around the ion trap, until the optimum configuration was found, with the gradient reduced to 10 Hz across the 91-ion crystal (see also sec. 4.3).

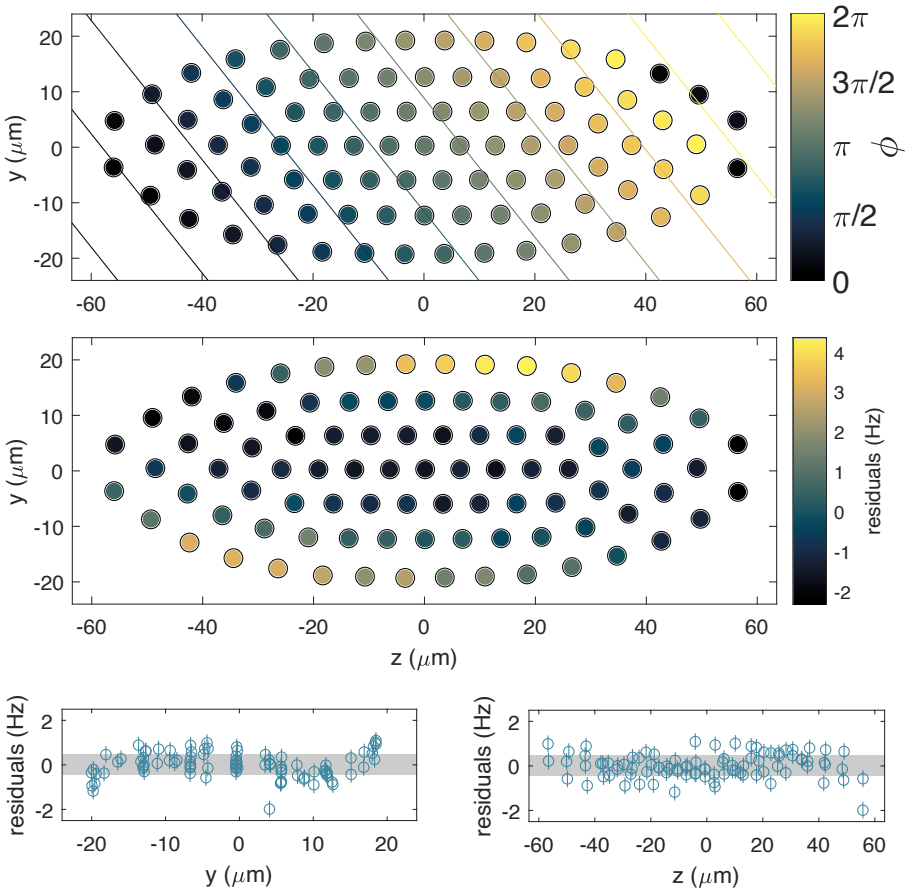

Figure 6.5: Magnetic field gradient across a 91-ion crystal giving rise to transition frequency shifts: Phase differences were determined via correlation spectroscopy techniques considering 19736 experimental realizations. Here, the ground-state qubit transition was probed in Ramsey experiments with a probe time of $T = 5$ ms. Top: Single-ion phase estimates are plotted as a function of position within the 91-ion crystal, with contour lines indicating constant phases. Center: Subtracting the dominant linear gradient determined from a fit uncovers a small quadratic contribution to the field gradient. Bottom: The residuals from a quadratic fit along both axes of the camera image are shown, with a small contribution of a linear and cubic function in y and no visible systematic structure along the z direction. Grey rectangles represent a measurement uncertainty of one standard deviation as expected from quantum projection noise.

Measuring Fluctuations of the Earth's Magnetic Field

After enclosing our experimental apparatus inside a magnetic field shielding, the coherence time on the ground state transition increased to about 130 ms (without spin echo). In this section correlation spectroscopy is thus not used to extend the probe time of the ions beyond the coherence time, but only to temporally track phase changes emerging in a 91 ion crystal. In this way, the earth's magnetic field can be used as a tool to determine the screening performance of our magnetic shield at low frequencies. In these measurements, the ions were again probed via Ramsey experiments on the ground state transition, here with a free evolution time of 20 ms. From the

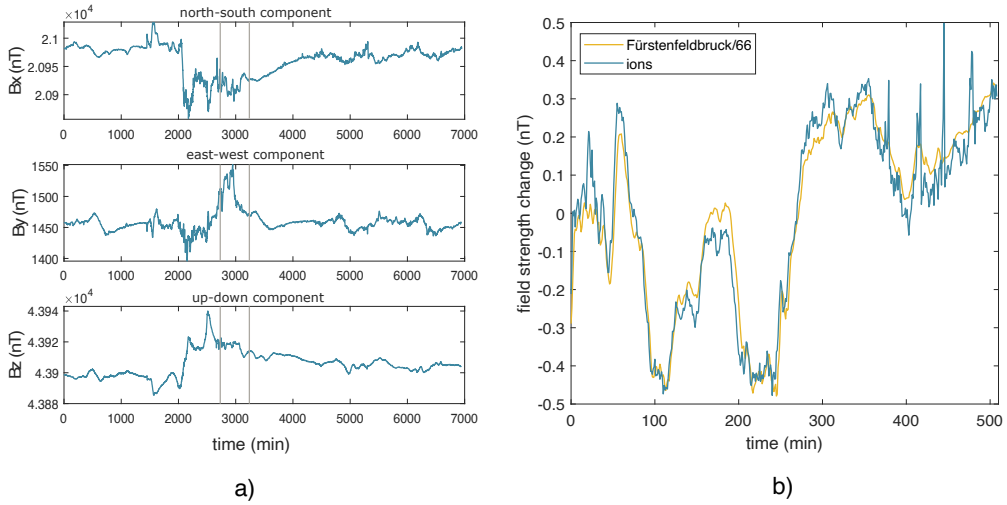

Figure 6.6: Measurement of the earth magnetic field fluctuations on the night of december 1st to 2nd 2023: a) The magnetic field along three spatial directions is shown, with the data provided by the geophysical observatory Fürstenfeldbruck near Munich. b) The data from the observatory is shown in blue, with the two horizontal directions weighted to represent the magnetic field change along the quantization axis in our experiment. The orange curve represents the magnetic field changes seen by our ions, determined via correlation spectroscopy. In order to overlap the two data curves, the observatory data was divided by a factor of 66, representing the screening performance of the magnetic shield. In the ion signal peaks can be observed towards the end of the night, resulting from trams going by the building again after the overnight break.

single-shot measurement outcomes, the temporally varying phase φ_m is extracted, these phase changes converted to magnetic field variations via the methods described in the previous subsection. These measurements were carried out over a timescale of about 8 hours during a geomagnetic storm, leading to particularly strong variations of the earth's magnetic field during that time. Our results are compared with data taken at the same time in the geophysical observatory Fürstenfeldbruck near Munich, the closest observatory for magnetic field sensing to our location in Innsbruck. They provide data of the earth's magnetic field along three directions as shown in fig. 6.6a. As the ions in our apparatus are only sensitive to magnetic field variations along the quantization axis, its orientation with respect to the reference directions of the observatory has to be determined in order to compare the two data sets. Here, the two (mean subtracted) horizontal magnetic field components from the observatory, stored in matrix $\mathbf{X} = (\mathbf{B}_x, \mathbf{B}_y)$ are weighted to fit the data measured in our apparatus, stored in vector $\mathbf{y}$. Estimation of the weight vector $\mathbf{w}$ is performed via

$$\mathbf{w} = \mathbf{X}^{+}\mathbf{y} = (\mathbf{X}^T\mathbf{X})^{-1}\mathbf{X}^T\mathbf{y} \tag{6.33}$$

where $\mathbf{X}^{+}$ represents the pseudoinverse of $\mathbf{X}$. The norm of the weight vector relates to the attenuation factor of our magnetic field shielding at low frequencies, which was determined to be about 66. This value is consistent with the measurements of shielding performance carried out by the manufacturer that were shown in fig. 4.8. The ratio of the weights describes the angle of our quantization axis with respect to the east-west direction of the observatory via $\arctan(w_1/w_2) =$

38.11 degrees. The two data curves are shown in fig. 6.6b, with the data from our experiment displaying additional structure starting at about 380 min into the measurement, which coincides with the schedule of trams going by the building in which our laboratory is located.

Further Applications of Correlation Spectroscopy on Linear Ion Crystals

Besides correlation measurements carried out on large planar ion crystals, in our work presented in [38] additional data was shown where correlation spectroscopy techniques were applied on long linear ion chains in a different experimental setup (QSIM). Here, ion positions as well as quadrupole and Zeeman shifts were determined, and laser phase noise characterized. In these measuremens the optical qubit in $^{40}Ca^{+}$ was manipulated with laser light at 729 nm, with the option of probing ions from two different directions, i.e. along the symmetry axis and perpendicular to it. Instabilities of the magnetic field as well as laser phase noise are no limitations as here again only correlations in the measurement outcomes are analyzed.

In a first experiment, transition frequency differences were investigated in a linear ion crystal of 51 ions. Here, aside from Zeeman shifts arising from a magnetic field inhomogeneity across the ion crystal, electric quadrupole shifts cause additional transition frequency variations. Ramsey experiments were carried out with a wait time of $T = 40$ ms with the two laser pulses illuminating the ions from the same direction. In this way, the phase differences of the qubits are not related to the position of the ions, but, as in the previous subsections, only arise from transition frequency differences. Correlation spectroscopy allows these cumulative transition frequency variations to be measured precisely. Moreover, a separation of contributions from Zeeman and quadrupole shift is achieved by probing the two stretch-state transitions $4^2S_{1/2}(m_j = \pm 1/2) \longleftrightarrow 3^2D_{5/2}(m_j = \pm 5/2)$, for which the Zeeman shift has an opposite sign while the quadrupole shift does not.

In order to measure ion-position differences, a linear ion string of 62 ions was probed in Ramsey experiments with each Ramsey pulse coming from a different direction. Here, the free evolution time between the Ramsey pulses was chosen as short as possible to prevent the qubits from picking up a phase due to transition frequency differences. Ion-position differences can be inferred from the measured phase differences as in this case they stem only from the $(\vec{k}_1 - \vec{k}_2)\vec{r}$ term in eq. 6.1. Once the ion-position differences have been determined, anharmonicities in the trapping potential, giving rise to non-uniform spacing between the ions, can be characterized, their effect well visible over the macroscopic length of the ion string of 200 µm.

Furthermore, correlations in the time domain were analyzed in order to track the position of an elevator giving rise to magnetic field changes, to characterize low-frequency noise of the 729 nm laser and differential path length fluctuations within two optical fibers which guide the laser light to the ions.

Hybrid-Ramsey Correlation Spectroscopy for Raman-Beam Alignment

In this section another application example of correlation spectroscopy is demonstrated: for aligning the Raman laser beams optimally with respect to the ion crystal plane. Theory on Raman beams coupling off-resonantly to the out-of-plane motional modes of the ion crystal in order to mediate entangling interactions was presented in sec. 3.3.5. Here, an optimal alignment of the beams is crucial in order to maximize the coupling between the laser field and ion motion, and in

turn maximize the spin-spin interaction strength, while avoiding coupling to in-plane motional modes. Piezo-controlled mirror holders provide the ability to precisely tune the position and angle of the Raman beams with respect to the ion crystal. For the first Raman beam, propagating perpendicular to the magnetic field axis, alignment is optimized by minimizing Stark shifts that arise when this beam has undesired overlap with the quantization axis. Correlation spectroscopy is subsequently applied in order to align the second Raman beam, which propagates along the quantization axis, with respect to the first beam[15]. More specifically, phase difference across the ion crystal arising from the differential k vector not being aligned perpendicularly to the ion crystal plane, are made accessible via correlation spectroscopy techniques.

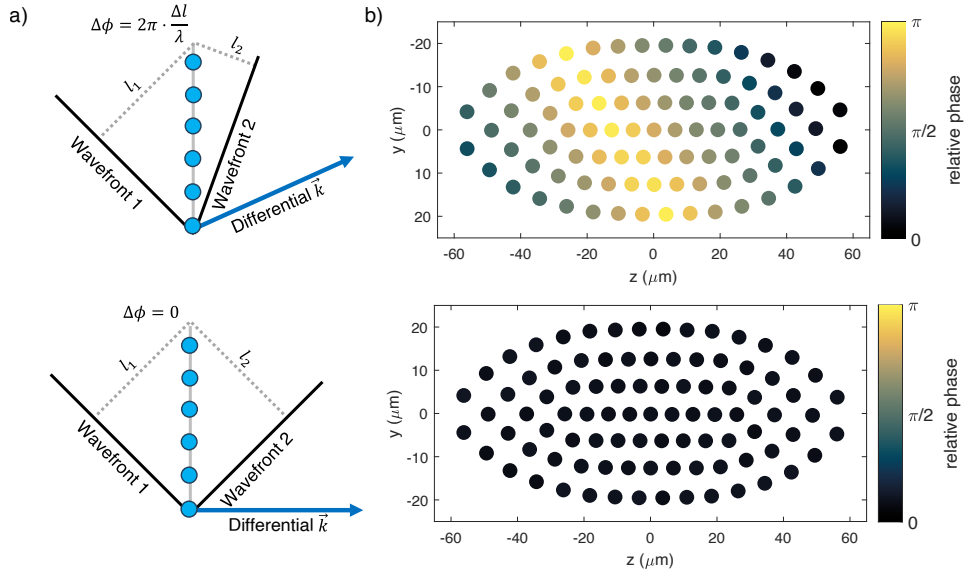

Figure 6.7: Optimizing the alignment of the Raman laser beams by applying correlation spectroscopy to a 91-ion planar crystal: The top and bottom images relate to imperfect ($\Delta\phi \neq 0$) and perfect ($\Delta\phi = 0$) beam alignment, respectively. a) A schematic representation of the Raman beams with respect to the ion crystal plane (top view) is shown. b) Experimental data showing the phase distribution across the ion crystal.

Measurement protocol

The correlation spectroscopy protocol for this measurement is slightly modified compared to the one applied in previous subsections, as here a hybrid-Ramsey experiment is required. The definition of hybrid-Ramsey in this context is that the first Ramsey pulse is applied via the RF antenna, whereas the second Ramsey pulse is applied via the Raman laser beams (in counter-propagating configuration). The first Ramsey pulse imprints the same phase to all ions in the crystal due to the large wavelength of the RF field. The second Ramsey pulse imprints its spatial phase distribution on the ions which is directly related to the orientation of the differential k vector with respect to

[15] Note, that this correlation spectroscopy method is combined in an iterative way with measurements probing the ions' micromotion along the out-of-plane direction via the Raman beams. This ensures not only correct alignment of the Raman beams with respect to the crystal plane but also correct alignment of the crystal plane within the trapping potential.

the crystal plane. Since there is no phase coherence between the first and second Ramsey pulse due to mechanical drifts of the optical setup leading to shot-to-shot variations of the phase of the Raman light field, we rely on correlation spectroscopy to extract information about the spatial phase distribution. In order to prevent the ions from picking up any other phase differences, the free evolution time is set to $T = 0$. In these experiments, a phase gradient $\Delta\phi = 2\pi\Delta l/\lambda$ across the ion crystal is dependent on the Raman light wavelength λ as well as the length difference $\Delta l = l_1 - l_2$, with the lengths l_1 and l_2 relating to the angles between the respective Raman beam wave vector and the crystal plane, as shown in 6.7a. The sketches illustrate two scenarios in which the Raman beams are imperfectly (top) and perfectly (bottom) aligned, respectively. In the first case of bad alignment a phase gradient across the ion crystal is present as $\Delta l \neq 0$, while in the second case, where k_{eff} is aligned optimally with respect to the ion crystal plane, $\Delta\phi$ equates to zero. Figure 6.7b shows examples of the ion-dependent phases across a 91-ion crystal in the case of imperfect and optimized alignment of the Raman beams. The position-dependent phases ϕ_i are extracted from the outcomes of the hybrid-Ramsey experiments analogously to previous subsections. In the optimized case, $l_1 - l_2$ is minimized to 40 nm across the 91-ion crystal.

6.2 Spin Squeezing and Entanglement Generation

While the previous section presented results on harnessing quantum correlations in the form of discord, the work in this section demonstrates the ability to create stronger quantum correlations, i.e. entanglement, in our apparatus. While entanglement constitutes a fundamentally interesting phenomenon to be studied, it can also be used as a tool for enhancing sensitivity in metrological applications. Indeed, one example of this concept was already demonstrated theoretically in the previous section, with entanglement providing a benefit in the investigated phase estimation task for small qubit numbers. More generally, it has been shown that maximally-entangled states allow for approaching the ultimate Heisenberg limit of precision [160, 168]. While long-range entangling interactions lead to stronger correlations between distant parts of a quantum system, which intuitively results in enhanced sensitivity in sensing tasks, in our experiments we demonstrate that the shorter-range interactions available in our experimental apparatus can provide metrological advantage as well. Here, we investigate spin squeezing, which has recently been implemented in long strings of $^{40}Ca^{+}$ ions, representing up to 51 spin [40]. Our work extends these experiments to a planar 19-ion crystal, with spins here not encoded in the optical but the ground state qubit transition. The finite-range interactions employed for spin squeezing are well-approximated by the one-axis twisting model [39] yielding a highly-squeezed state quantified by a Wineland parameter of below -6 dB. This serves as evidence of successfully creating multi-partite entanglement within a planar ion Coulomb crystal in our apparatus.

6.2.1 Introduction to Spin Squeezing

Squeezing constitutes an important tool in the context of quantum metrology, allowing for measurement precision defined by the SQL to be surpassed. As briefly introduced in sec. 2.4.4, the key idea of squeezing is to manipulate the variances of a pair of complementary variables, such that the variance of one of them is reduced while the variance of the other increases. A measurement of the squeezed variable will thus be more precise than would be possible classically. Here, squeezed

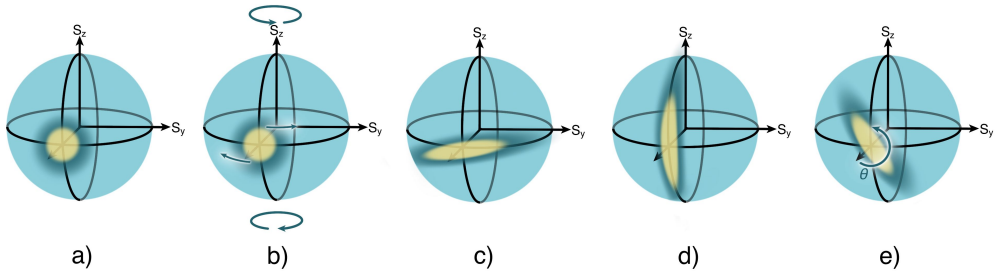

Figure 6.8: Spin Squeezing illustrated on a collective Bloch sphere: a) A coherent spin state (CSS), representing a system of N spins, is aligned with the x axis of the Bloch sphere. b) The action of the one-axis twisting (OAT) Hamiltonian can be visualized by a sheering effect which results in the spin-squeezed state (SSS) shown in c. d) Aligning the SSS in this way, where the direction along which variance is minimized lays within the equatorial plane of the Bloch sphere, allows the best achievable precision in phase sensing. e) In order to determine the minimum variance (axis) of the SSS, the angle θ is scanned by performing a rotation around the x axis.

light is a prominent example, e.g. used to enhance the sensitivity of gravitational wave detectors. In the experiments carried out in this thesis, squeezing is instead employed on a system of spin-1/2 particles, each spin represented by an ion within a planar $N = 19$ ion Coulomb crystal. Here, a collective spin vector $\hat{\mathbf{S}}$ of the system is defined, initially prepared in an uncorrelated coherent spin state (CSS), with all spins prepared in the equatorial plane of the Bloch sphere, aligned along the x axis:

$$|\mathbf{x}\rangle = \otimes_{i=1}^{N} |+\rangle_i \tag{6.34}$$

This state is useful for phase sensing, as demonstrated in our work on correlation spectroscopy, but since it is not an eigenstate of the measurement basis, it exhibits a coherent spread set by the SQL. The uncertainties of the CSS are isotropic, i.e. equal for both spin components normal to the spin vector, represented by the circular quasiprobability distribution shown in fig. 6.8a. This classical noise distribution can be sheared into a spin squeezed state (SSS) by the interactions described in the subsequent subsection. The SSS has a smaller variance along the squeezed axis of the spin and, as the Heisenberg uncertainty principle

$$\langle (\Delta \hat{\mathbf{S}}_i)^2 \rangle \langle (\Delta \hat{\mathbf{S}}_j)^2 \rangle \geq \frac{1}{4} |\langle \hat{\mathbf{S}}_k \rangle|^2 \tag{6.35}$$

has to hold [39], with $i \neq j \neq k \in (x, y, z)$, the orthogonal axis to the squeezed axis is anti-squeezed. This manifests in an elliptical shape of the quasiprobability distribution, as illustrated in fig. 6.8c. As such, squeezing can increase measurement precision, e.g in phase sensing when the direction along which variance is minimized lays within the equatorial plane of the Bloch sphere (as in fig. 6.8d). While for the CSS the phase uncertainty scales as $\Delta\phi_{SQL} = 1/\sqrt{N}$ it is possible to achieve a Heisenberg scaling of $1/N$ in a SSS [56][16]. Spin squeezing and thus the sensitivity

[16] Note, that for the one-axis twisting protocol used in our experiment rather a $N^{-2/3}$ reduction in uncertainty with the particle number is expected, as discussed below.

enhancement in measurements can be quantified by the Wineland parameter [56, 159]. It can be expressed in the form

$$\xi^2 = (\frac{\Delta\phi}{\Delta\phi_{SQL}})^2 \tag{6.36}$$

describing the metrological gain in phase sensitivity by comparing the phase uncertainty $\Delta\phi$ of the SSS with the uncertainty achievable with a CSS. An alternative form in which to express the Wineland parameter is given by

$$\xi^2 = \frac{N\langle(\Delta\hat{S}_{\mathbf{n}_\perp})^2\rangle}{|\langle\hat{\mathbf{S}}\rangle|^2} \tag{6.37}$$

which compares the minimized variance to the collective Bloch vector's length. Here, $\mathbf{n}_\perp$ is the axis transverse to the collective Bloch vector, along which the variance $\langle(\Delta\hat{S}_{\mathbf{n}_\perp})^2\rangle = \langle(\hat{S}_{\mathbf{n}_\perp} - \langle\hat{S}_{\mathbf{n}_\perp}\rangle)^2\rangle$ is minimized. These quantities are measured in our experiments via global rotations of the spin system as described in sec. 6.2.3. In a spin squeezed state the individual spins are more tightly correlated with each other than would be possible in a classical system. Due to this natural connection between squeezing and entanglement, the Wineland parameter witnesses entanglement when its value is $\xi^2 < 1$.

6.2.2 Entangling Interactions for the Creation of Spin Squeezing

Establishing the strong correlations required to generate a squeezed state in a system of spins, necessitates the use of entangling interactions. Here, the one-axis twisting (OAT) model is a well known example, with dynamics under the Hamiltonian

$$\hat{H}_{\mathrm{OAT}} = \frac{\chi}{2}\sum_{i<j}^{N}\hat{\sigma}_z^{(i)}\hat{\sigma}_z^{(j)} \tag{6.38}$$

allowing for the generation of spin squeezed states[17] [39]. The action of this Hamiltonian can be imagined by considering the Bloch sphere to be twisted along the z direction, with the north and south poles being rotated in opposite directions, as illustrated in fig. 6.8b. This process shears the isotropic quasiprobability distribution of the CSS into an elliptical one. The Hamiltonian in eq. 6.38 is of analogous structure to the MS Hamiltonian introduced in sec. 3.2.3. As such, the OAT model describes an infinite-range interaction which produces all-to-all connectivity within the spin system. Within this model, the Wineland parameter ideally scales as $N^{-2/3}$ [39]. It is thus beneficial to prepare spin squeezed states in large systems in order to produce more strongly squeezed states. While establishing all-to-all connectivity is difficult or impossible in many experimental systems, trapped ions in principle offer this possibility, e.g. by mediating long-range interactions in linear ion chains via a single axial motional mode of the ion crystal. However, as the system scales up it becomes increasingly challenging to maintain sufficient control for carrying out such an operation with high fidelity, e.g. due to heating effects. In that sense, the finite-range interactions available in our experimental system, where entanglement is mediated by many motional

[17] Moreover, such dynamics can also produce other states when the system is oversqueezed during long evolution times, such as multi-headed cat states.

modes of the ion crystal simultaneously, constitute a more scalable type of interaction and indeed in [40] it has been demonstrated that these interactions can also reliably create spin-squeezed states.

As presented in sec. 3.2.3, certain spin Hamiltonians can be realized within an ion crystal by illuminating the ions with a bichromatic laser field that couples off-resonantly to the out-of-plane motional modes of the ion crystal, where the interaction strength between particles follows the power law in eq. 3.63, the interaction range dependent on the parameter α. This parameter relates to the detuning of the laser field from the motional modes. By introducing an additional centerline detuning, the transverse field Ising Hamiltonian in eq. 3.59 can be implemented. In the context of spin squeezing the use of the transverse-field Ising Hamiltonian is not ideal because it does not suppress collective spin flips, meaning that the collective spin vector of the system may rotate out of the equatorial plane of the Bloch sphere. This, in turn, reduces the sensitivity of the measurement and should thus be avoided. The XY Hamiltonian, on the other hand, conserves the number of spin excitations and thus stabilizes collective behavior. As discussed in sec. 3.2.3 this Hamiltonian emerges from the transverse field Ising model in the limit of strong transverse B field, i.e. operating at large centerline detuning. The resulting power-law XY Hamiltonian

$$\hat{H}_{PL-XY} = \sum_{i<j} J_{ij}\left(\hat{\sigma}_+^{(i)}\hat{\sigma}_-^{(j)} + \hat{\sigma}_-^{(i)}\hat{\sigma}_+^{(j)}\right) \tag{6.39}$$

is employed for the creation of squeezing in our apparatus. In order for this Hamiltonian to approximate the scaling of the OAT model, the condition $\alpha < 2D/3$ must be satisfied [169], where D is the spatial dimensionality of the spin system, which in our case equals 2.

6.2.3 Spin Squeezing in a 19-Ion Planar Crystal

A planar 19-ion crystal is stored in a potential characterized by the secular frequencies 2π (2223, 697, 360) kHz[18], each ion encoding a spin-1/2 particle whose basis states are represented by the Zeeman states of the $4S_{1/2}$ ground state manifold. The experimental sequence for creating and probing spin squeezed states is described in the following. First, the spins are brought into the equatorial plane of the Bloch sphere via a resonant global $\pi/2$ Raman pulse, aligning the collective spin vector with the x axis (see fig. 6.8a). Subsequently, bichromatic Raman laser light is applied for a certain time τ, which induces dynamics under the Hamiltonian 6.39[19]. These entangling Raman beams have a detuning to the highest frequency out-of-plane (COM) mode of 80 kHz with an additional center line detuning of 15 kHz, resulting in an interaction strength between spins quantified by $J_0 \approx 1000$ rad/s[20] and $\alpha \approx 1$. The Wineland parameter is determined for different values of τ in order to find the interaction time for which squeezing is maximized.

[18] The spatial structure of the 19-ion crystal as well as the structure of a few of its motional modes can be seen in fig. 3.2.

[19] In order to mitigate dephasing during the entangling interaction, a spin echo pulse is applied which splits the interaction into two laser pulses of length $\tau/2$. This spin echo operation constitutes a π rotation along the x axis, leading to a rephasing during the second half of the interaction while increasing the spin squeezing in the state.

[20] J_0 represents the maximum value of the spin-spin coupling strength J_{ij}, which can be modeled as $J_{ij} = J_0/|i-j|^\alpha$.

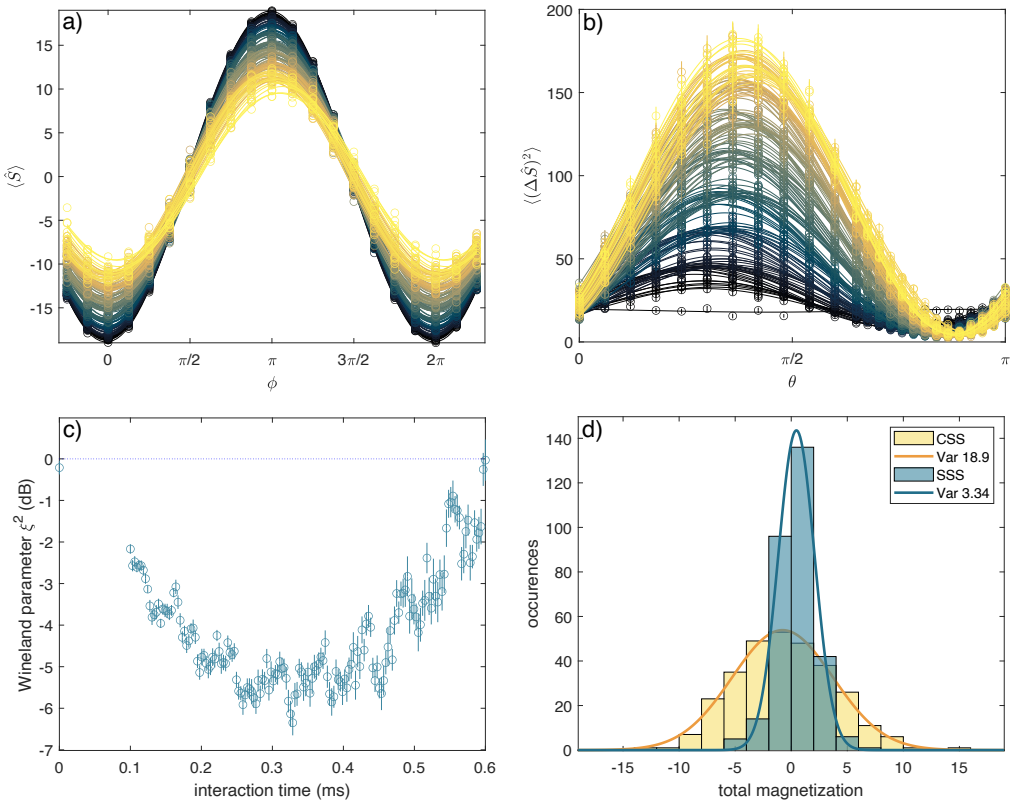

Figure 6.9: Results on squeezing a spin system represented by a 19-ion planar Coulomb crystal: a) The phase ϕ is scanned in order to determine the collective Bloch vector's length which is given by the contrast of the fringe. The duration τ of the entangling interaction pulse was varied from 0 (black data points) to 600 µs (yellow data points). The length of the Bloch vector shrinks as interaction time increases. b) In order to find the minimum variance (axis), the readout angle θ is scanned. For a CSS a straight line is observed as the spin vector rotates which transforms into a fringe as interaction time increases. The minimum of the fringe is used in the calculation of the Wineland parameter. c) The Wineland parameter is plotted as a function of the interaction time. A minimum of -6.3(3) dB is observed at about 330 µs. The Wineland parameter subsequently rises again due to oversqueezing of the state. The dotted line represents the classical bound, above which the spin state shows no evidence of entanglement and metrological gain over classical strategies. d) A histogram of the total magnetization is shown, measured along the axis of minimal variance for the SSS. Gaussian fits are applied to the data in order to determine the variance of the distributions.

Measurement of the Wineland parameter according to eq. 6.37 only requires collective rotations[21] on the spin states, generally described by

$$\hat{R}(\tilde{\theta}, \tilde{\phi}) = \prod_j e^{-i\frac{\tilde{\theta}}{2}\left(\hat{\sigma}_x^{(j)} \cos\tilde{\phi} + \hat{\sigma}_y^{(j)} \sin\tilde{\phi}\right)}, \tag{6.40}$$

[21] Note that resonant laser pulses are comprised of a composite pulse sequence [144] in order to compensate coupling strength inhomogeneities arising from the Gaussian intensity profile of the beams.

where j denotes the individual spins and $\theta = \tilde{\theta}$ and $\phi = \tilde{\phi} + \pi/2$ are the polar and azimuthal angles of the Bloch vector. While a projective measurement determines the expectation value of $\hat{S}_z$, i.e. the collective spin state in the z basis, it is possible to perform measurements in arbitrary bases

$$\hat{S}_{\theta,\phi} = \hat{R}^{\dagger}(\tilde{\theta}, \tilde{\phi})\, \hat{S}_z\, \hat{R}(\tilde{\theta}, \tilde{\phi}) \tag{6.41}$$

by applying global rotations before measurement. Determining the Wineland parameter necessitates measurement of the collective Bloch vector's length as well as the minimized variance along the direction $n_{\perp}$. In a first step, in order to find the Bloch vector length, measurements on the spin system were carried out in different bases within the equatorial plane of the Bloch sphere, effectively scanning the parameter $\tilde{\phi}$. For interaction times between 0 and 600 µs this phase scan is shown in fig. 6.9a. Here, the presence of a small offset phase ϕ_0 of the fringe minimum from 0 indicates the Bloch vector not being perfectly aligned with the x axis of the Bloch sphere, which may result from Stark shifts and must be taken into account in subsequent measurements. The contrast of the observed fringes represents the Bloch vector length, which decreases as interaction time increases. Note, that a shrinking of the Bloch vector is expected in squeezing, with the average of the spin projection along the measurement axis reducing as the spins spread out across the Bloch sphere in the antisqueezed direction, and is not necessarily an effect related to decoherence. In a second step, in order to determine the minimum variance of the SSS, the measurement basis was aligned with ϕ_0, and the angle θ is scanned via a resonant Raman pulse, which rotates the Bloch vector around the measurement axis[22]. When performing projective measurements, this effectively allows the variance to be scanned in the plane orthogonal to the spin vector, to find its minimum. These measurements are illustrated in fig. 6.8e with data presented in fig 6.9b, again for interaction times between 0 and 600 µs. Here, as expected, a flat line is observed when probing a CSS with an isotropic probability distribution. In the case of a SSS, however, oscillations can be observed, as the variance changes when rotating the spin vector. The angle at which the fringe minimum occurs corresponds to the minimum variance axis with the minimum of the fringe constituting the lowest achievable uncertainty.

The Wineland parameter is shown in fig. 6.9c, as a function of the entangling interaction time τ. Here, the lowest point at -6.3(3) dB is observed after only about 330 µs of interaction time and comes close to the noiseless limit for squeezing under the XY model of about -7 dB. After reaching the minimum value the Wineland parameter rises for longer interaction times due to overqueezing. Here, both a reduction in Bloch vector length as well as an increase in variance occurs as states other than a SSS are created. Oscillations are visible in the data which stem from that fact that the XY interaction realized in the experiment is imperfect, with off-resonant terms of the transverse-field Ising model not being negligible[23]. Figure 6.9d presents another, more intuitive visualization of the squeezing results. Here, the spin magnetization is plotted for the CSS (yellow) and the most sensitive SSS (green), respectively, showing that the latter exhibits a variance lower by more than a factor of 5 compared to the CSS.

The limitations in these measurements which prevent us from reaching the noiseless precision bound may stem from decoherence processes. Here, it is assumed that spontaneous scattering of

[22] This Raman pulse has a phase that is offset by $\pi/2$ from the first Raman pulse which prepared the spins along x.

[23] The frequency of the oscillations relates to the centerline detuning. In recent measurements it was shown that it is indeed possible to remove these oscillations by laser pulse shaping of one Raman beam.

the Raman laser light does not impose a restriction to the achievable Wineland parameter. First of all, scattering represents an uncorrelated decoherence process, which is in general less harmful in experiments where entangling interactions are harnessed [46]. Secondly, the interaction timescale is comparatively short, such that scattering as well as heating of the motional modes, which constituted a limit to the coherence in [40], do not become relevant in our experiment. On the other hand, collective decoherence from magnetic field instabilities, differential changes in optical path length between the Raman beams, and laser light reflections illuminating the ion crystal may be dominant sources of decoherence.

6.2.4 Outlook on Variational Optimization of Spin-Squeezing in Large Planar Crystals

In the aforementioned experiments, the interaction time and readout angle were scanned in order to find out which system parameters would prepare the spin system in the most sensitive SSS. In a recent collaboration with theorists an algorithm for optimal parameter search was developed and implemented in our apparatus in order to automatize this process. Here, a feedback loop is established between a classical computer and our experimental system, which performs two-parameter optimization of τ and θ to minimize the Wineland parameter. These measurements were carried out with up to 91 ions in a planar crystal, with the results subject to a future publication.

CONCLUSION

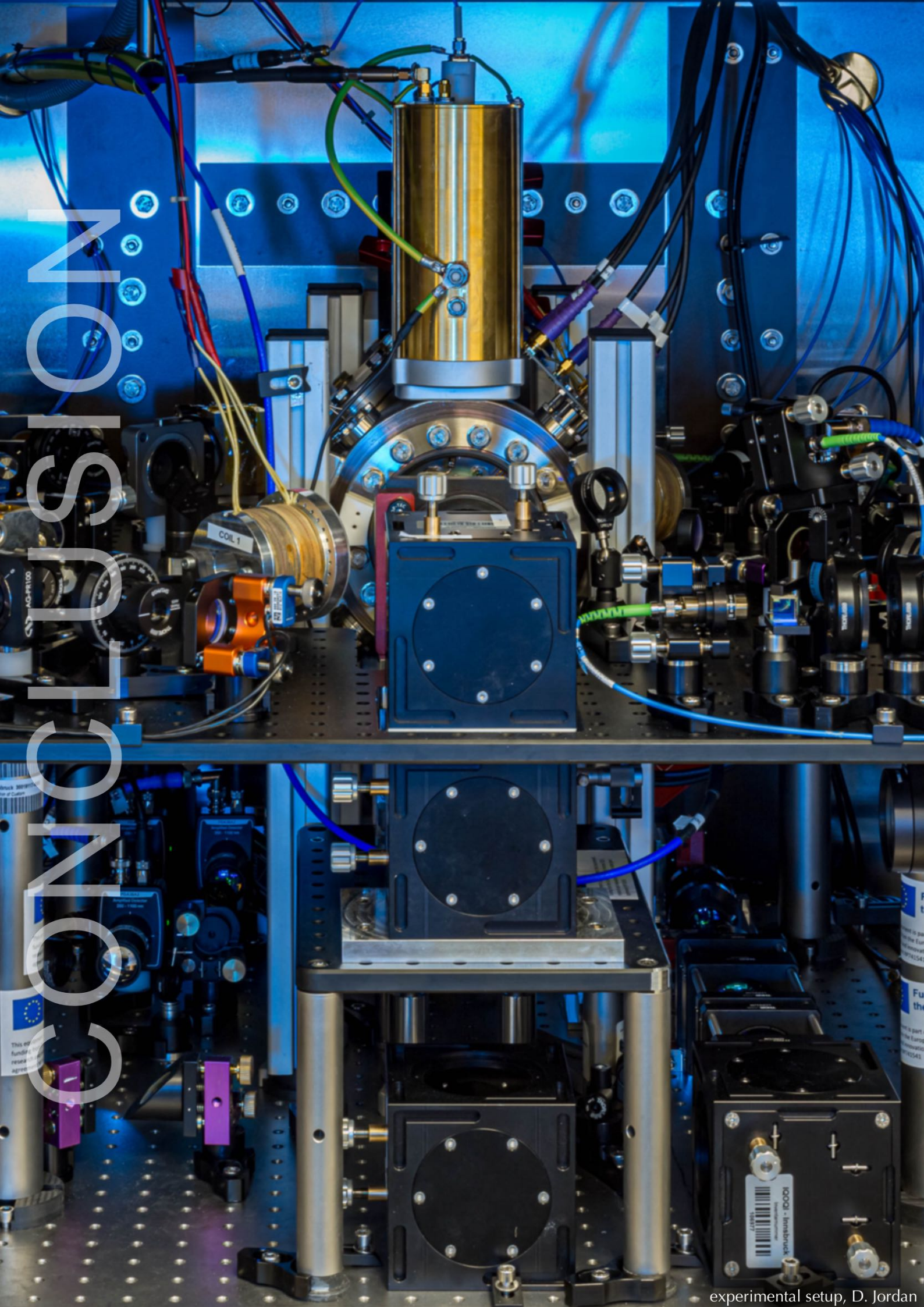

experimental setup, D. Jordan

7 Summary and Outlook

This thesis presented the development of a new ion trap apparatus for controlling planar ion Coulomb crystals of up to 105 ions in a RF trap. In ch. 2 and 3 relevant theory background was given on quantum information science, in particular with respect to the trapped ion platform. In ch. 4 technical details on the key components comprising the apparatus were discussed. This includes the design, setup and control of a monolithic linear Paul trap that allows for creation of the anisotropic potentials required for storing 2D ion crystals while offering excellent optical access for imaging and laser-addressing of the ions to first order free of micromotion. The chapter furthermore presented the vacuum setup, magnetic field control, optical setups for ion creation, laser cooling, coherent quantum state manipulation and entanglement generation, a RF antenna for ground-state qubit manipulation and experiment control hard- and software. Here, in particular, our work on an unsupervised learning algorithm for high-fidelity readout of the ions' quantum states from fluorescence images was reported, constituting a novel feature of the experiment control software.

Characterization measurements provided in ch. 5 demonstrated the high level of control achievable in our setup. Here, characteristics of the ion trap were investigated: The RF voltage handling capability of the monolithic trap allows for a trap frequency of more than 2 MHz along the out-of-plane direction of the ion Coulomb crystals, giving rise to a limit in ion number on the order of 100 particles that can be trapped in a plane. Furthermore, a low heating rate of the trap of 0.56 quanta/s per ion was found, which, considering crystal sizes of 100 ions, does not impose severe limitations on the planned experiments[1]. Furthermore, the trapping potential was characterized: Precise tunability of the potential was confirmed by verifying ions can be confined to a single plane that is optimally placed (via DC trap electrode control) within the trap center, with the optimum reflected in low micromotion indices for all ions along the out-of-plane direction. A fluorescence image of a 91-ion crystal was used to determine trapping potential characteristics such as the trap anisotropy and frequencies, providing a fast alternative to the use of sideband spectroscopy. Image analysis also showed that potential anharmonicities, which could lead to unpredictable ion motion, are dominant along the direction spanned by the RF electrodes of the trap but are in general small and should not lead to experimental complications. Typical ion crystal lifetimes of several hours or even days were observed in our apparatus, indicating excellent vacuum conditions in a room temperature environment. Ion crystal stability was quantified by determining how long the ions stay crystallized in the absence of laser cooling. Here, it was shown that even large crystals of 91 ions typically remain cold for several seconds, significantly longer than the timescales of our experimental sequences, which demonstrates that RF heating is not a limiting factor in our exper-

[1] Limitations would arise e.g. if the heating rate restricts motional or electronic coherence time to below the desired interaction times.

iments. Furthermore, in case a melting event does occur, the ions can be recrystallized in a fast and automatized way. The chapter also presented strategies for eliminating the influence of structural phase transitions on experiments, by reducing their occurrence and detecting them in sequence, which solves a major technical challenge in experiments with large planar ion crystals. Entangling interactions across the ion crystal are mediated via its out-of-plane motional modes. Here, a requirement is that all of these modes are laser-cooled close to the motional ground state, which was achieved in a 105-ion crystal via electromagnetically-induced transparency cooling. Furthermore, characteristics of the Raman laser system for creating entangling interactions were presented, such as coherence, achievable coupling strengths and scattering rates.

The last thesis chapter 6 presented experiments where quantum correlations, in particular discord and entanglement, were harnessed for applications in the context of quantum metrology and sensing. The first part of the chapter described measurements on correlation spectroscopy, a technique where multiple qubits that are exposed to the same phase noise are probed simultaneously via Ramsey interferometry. Analyzing correlations in the measurement outcomes allowed phase differences between qubits to be resolved with high precision, despite employing Ramsey probe times exceeding the coherence time of the individual qubits. Moreover, correlation spectroscopy allowed the present phase noise to be characterized in the time domain. While this technique had been demonstrated previously e.g. to compare two atomic clocks, in our work it was extended to large planar Coulomb crystals consisting of up to 91 ions, essentially constituting a network of 91 quantum sensors. Several applications of correlation spectroscopy were presented, such as the determination and minimization of transition frequency differences arising from a magnetic field gradient across the ion crystal, precise alignment of the Raman laser beams as well as characterization of the attenuation performance of the magnetic field shielding enclosing our apparatus. Our work presented novel features of correlation spectroscopy in the sense that analyzing N-particle correlations was found to reduce phase uncertainty in comparison to considering only pair correlations. It was also demonstrated that for our estimation task the use of entanglement-enhanced phase sensing would only provide an advantage in the case of small sensor networks, becoming negligible for large systems. The last part of the chapter presented results on spin squeezing in a 19-ion planar crystal, where measurement uncertainty was reduced below the classical limit, quantified by a Wineland parameter of $\xi^2 = -6.3(3)$ dB. This result represents a factor of 5 improvement compared to the standard quantum limit and comes close to the noiseless limit of the model of about -7 dB. Besides demonstrating non-classical metrological gain, these results also showcase the ability of implementing spin Hamiltonians of transverse-field Ising and XY type in our experimental system, the basis for performing quantum simulation of interacting spin 1/2 particles in 2D.

While the spin squeezing measurements presented in this thesis were carried out on a comparatively small planar ion crystal, these experiments are already being extended to larger systems of up to 91 ions and more sophisticated protocols. On one hand, this allows for reaching even lower Wineland parameters, which, for the interactions employed in our system, follows a scaling of approximately $N^{-2/3}$. Additionally, by harnessing a variational optimization algorithm, the optimum experimental parameters for generating the most sensitive spin squeezed state are determined in an automatized way. All experiments in this thesis framework were carried out only via global interactions on the ion crystal, with single-ion addressability still missing for the establishment of full quantum control. This upgrade will allow us to also simulate out-of-equilibrium

phenomena in 2D in our apparatus. Optics and electronics comprising the individual-ion addressing unit have already been installed as this dissertation is finalized. In this addressing unit, which will be presented in the upcoming PhD thesis of Artem Zhdanov, a laser beam is tightly focused by the objective, also used for imaging the ions, to a spot size on the order of a micrometer, thus enabling the manipulation of an individual ion within the Coulomb crystal with low crosstalk to neighboring ions. The addressing laser beam will be steered within the crystal plane via two acousto-optic deflectors, producing vertical and horizontal displacement, respectively, to sequentially rotate the quantum state of the addressed qubits via AC Stark shifts. Furthermore, resonant addressed operations will allow for shelving ions into metastable states that do not couple to the laser field creating entangling interactions. In this way, the natural triangular lattice of the ion Coulomb crystals can be artificially structured into different geometries, such as honeycomb or Kagome. These single-ion operations will be carried out around the optical qubit transition wavelength of 729 nm. On a longer time-scale, however, we aim to implement far-detuned single-ion operations at 532 nm for which a 50 W laser system has been purchased. Fully controlled quantum systems of around 100 particles may already allow for demonstrating quantum advantage in quantum simulation experiments, exceeding the capabilities of classical computation. While it has been shown in this thesis work that ion crystals of such size can be precisely controlled in our apparatus, the question arises what the upper limit on the number of ions is, which can be trapped in a plane. It is likely that a significant increase, compared to the Coulomb crystals controlled in this thesis, will require the development of a new ion trap. Here, a smaller model may be suitable, which produces stronger confinement at the RF voltages proven safe in this thesis, or a trap of similar or larger size to which higher RF voltages can be applied. Very recently it was demonstrated that storing 2D Coulomb crystals of up to 512 ions is indeed feasible in a monolithic linear Paul trap with a similar structure to the one developed and characterized in this thesis work, but installed in a cryogenic environment. It remains an open question how well control over structural phase transitions and RF heating can be retained when increasing the system to even larger size, with these effects possibly becoming limiting factors at some point.

Bibliography

1. R. Blatt and C. F. Roos. "Quantum simulations with trapped ions". *Nat. Phys.* 8:4, 2012, pp. 277–284. ISSN: 1745-2481. DOI: 10.1038/nphys2252. URL: https://doi.org/10.1038/nphys2252.
2. C. Figgatt et al. "Parallel entangling operations on a universal ion-trap quantum computer". *Nature* 572:7769, 2019, pp. 368–372. ISSN: 1476-4687. DOI: 10.1038/s41586-019-1427-5. URL: https://doi.org/10.1038/s41586-019-1427-5.
3. S. M. Brewer et al. "$^{27}Al^{+}$ Quantum-Logic Clock with a Systematic Uncertainty below 10^{-18}". *Phys. Rev. Lett.* 123, 3 2019, p. 033201. DOI: 10.1103/PhysRevLett.123.033201. URL: https://link.aps.org/doi/10.1103/PhysRevLett.123.033201.
4. C. Monroe et al. "Programmable quantum simulations of spin systems with trapped ions". *Rev. Mod. Phys.* 93, 2021, p. 025001. DOI: 10.1103/RevModPhys.93.025001.
5. L. Postler et al. "Demonstration of fault-tolerant universal quantum gate operations". *Nature* 605:7911, 2022, pp. 675–680. ISSN: 1476-4687. DOI: 10.1038/s41586-022-04721-1. URL: https://doi.org/10.1038/s41586-022-04721-1.
6. C. D. Marciniak et al. "Optimal metrology with programmable quantum sensors". *Nature* 603:7902, 2022, pp. 604–609. ISSN: 1476-4687. DOI: 10.1038/s41586-022-04435-4. URL: https://doi.org/10.1038/s41586-022-04435-4.
7. J. G. Bohnet et al. "Quantum spin dynamics and entanglement generation with hundreds of trapped ions". *Science* 352:6291, 2016, pp. 1297–1301. DOI: 10.1126/science.aad9958.
8. J. Zhang et al. "Observation of a many-body dynamical phase transition with a 53-qubit quantum simulator". *Nature* 551:7682, 2017, pp. 601–604. ISSN: 1476-4687. DOI: 10.1038/nature24654. URL: https://doi.org/10.1038/nature24654.
9. C. Kokail et al. "Self-verifying variational quantum simulation of lattice models". *Nature* 569:7756, 2019, pp. 355–360. ISSN: 1476-4687. DOI: 10.1038/s41586-019-1177-4. URL: https://doi.org/10.1038/s41586-019-1177-4.
10. M. K. Joshi et al. "Observing emergent hydrodynamics in a long-range quantum magnet". *Science* 376:6594, 2022, pp. 720–724. DOI: 10.1126/science.abk2400.
11. B.-W. Li et al. "Probing Critical Behavior of Long-Range Transverse-Field Ising Model through Quantum Kibble-Zurek Mechanism". *PRX Quantum* 4, 2023, p. 010302. DOI: 10.1103/PRXQuantum.4.010302.
12. S.-A. Guo et al. *A Site-Resolved 2D Quantum Simulator with Hundreds of Trapped Ions under Tunable Couplings*. 2023. arXiv: 2311.17163 [quant-ph].

13. R. Islam et al. "Emergence and Frustration of Magnetism with Variable-Range Interactions in a Quantum Simulator". *Science* 340:6132, 2013, pp. 583–587. DOI: 10.1126/science.1232296. eprint: https://www.science.org/doi/pdf/10.1126/science.1232296. URL: https://www.science.org/doi/abs/10.1126/science.1232296.

14. C. Maier et al. "Environment-Assisted Quantum Transport in a 10-qubit Network". *Phys. Rev. Lett.* 122, 5 2019, p. 050501. DOI: 10.1103/PhysRevLett.122.050501. URL: https://link.aps.org/doi/10.1103/PhysRevLett.122.050501.

15. F. Kranzl et al. "Controlling long ion strings for quantum simulation and precision measurements". *Phys. Rev. A* 105, 5 2022, p. 052426. DOI: 10.1103/PhysRevA.105.052426. URL: https://link.aps.org/doi/10.1103/PhysRevA.105.052426.

16. M. Block et al. "Crystalline ion structures in a Paul trap". *J. Phys. B* 33:11, 2000, p. L375. DOI: 10.1088/0953-4075/33/11/101. URL: https://dx.doi.org/10.1088/0953-4075/33/11/101.

17. S. Fishman et al. "Structural phase transitions in low-dimensional ion crystals". *Phys. Rev. B* 77, 6 2008, p. 064111. DOI: 10.1103/PhysRevB.77.064111. URL: https://link.aps.org/doi/10.1103/PhysRevB.77.064111.

18. A. M. Polloreno, A. M. Rey, and J. J. Bollinger. "Individual qubit addressing of rotating ion crystals in a Penning trap". *Phys. Rev. Research* 4, 3 2022, p. 033076. DOI: 10.1103/PhysRevResearch.4.033076. URL: https://link.aps.org/doi/10.1103/PhysRevResearch.4.033076.

19. B. J. McMahon et al. *Individual-Ion Addressing and Readout in a Penning Trap*. 2024. arXiv: 2404.02105 [physics.atom-ph].

20. S. Jain et al. "Scalable Arrays of Micro-Penning Traps for Quantum Computing and Simulation". *Phys. Rev. X* 10, 3 2020, p. 031027. DOI: 10.1103/PhysRevX.10.031027. URL: https://link.aps.org/doi/10.1103/PhysRevX.10.031027.

21. S. Jain et al. "Penning micro-trap for quantum computing". *Nature*, 2024. ISSN: 1476-4687. DOI: 10.1038/s41586-024-07111-x. URL: https://doi.org/10.1038/s41586-024-07111-x.

22. R. C. Sterling et al. "Fabrication and operation of a two-dimensional ion-trap lattice on a high-voltage microchip". *Nat. Commun.* 5:1, 2014, p. 3637. ISSN: 2041-1723. DOI: 10.1038/ncomms4637. URL: https://doi.org/10.1038/ncomms4637.

23. M. Mielenz et al. "Arrays of individually controlled ions suitable for two-dimensional quantum simulations". *Nat. Commun.* 7:1, 2016, p. 11839. ISSN: 2041-1723. DOI: 10.1038/ncomms11839. URL: https://doi.org/10.1038/ncomms11839.

24. P. C. Holz et al. "2D Linear Trap Array for Quantum Information Processing". *Adv. Quantum Technol.* 3:11, 2020, p. 2000031. DOI: https://doi.org/10.1002/qute.202000031.

25. B. Yoshimura et al. "Creation of two-dimensional Coulomb crystals of ions in oblate Paul traps for quantum simulations". *EPJ Quantum Technol.* 2:1, 2015, p. 2. ISSN: 2196-0763. DOI: 10.1140/epjqt14. URL: https://doi.org/10.1140/epjqt14.

26. Y. Wang et al. "Coherently Manipulated 2D Ion Crystal in a Monolithic Paul Trap". *Adv. Quantum Technol.* 3:11, 2020, p. 2000068. DOI: https://doi.org/10.1002/qute.202000068.

27. Y. Xie et al. "An open-endcap blade trap for radial-2D ion crystals". *Quantum Sci. Technol.* 6:4, 2021, p. 044009. DOI: 10.1088/2058-9565/ac1e38. URL: https://doi.org/10.1088/2058-9565/ac1e38.

28. D. J. Berkeland et al. "Minimization of ion micromotion in a Paul trap". *Journal of Applied Physics* 83:10, 1998, pp. 5025–5033. ISSN: 0021-8979. DOI: 10.1063/1.367318. eprint: https://pubs.aip.org/aip/jap/article-pdf/83/10/5025/18699946/5025_1_online.pdf. URL: https://doi.org/10.1063/1.367318.

29. R. Blümel et al. "Chaos and order of laser-cooled ions in a Paul trap". *Phys. Rev. A* 40, 2 1989, pp. 808–823. DOI: 10.1103/PhysRevA.40.808. URL: https://link.aps.org/doi/10.1103/PhysRevA.40.808.

30. R. Blümel et al. "Phase transitions of stored laser-cooled ions". *Nature* 334:6180, 1988, pp. 309–313. ISSN: 1476-4687. DOI: 10.1038/334309a0. URL: https://doi.org/10.1038/334309a0.

31. M. W. van Mourik et al. "rf-induced heating dynamics of noncrystallized trapped ions". *Phys. Rev. A* 105, 3 2022, p. 033101. DOI: 10.1103/PhysRevA.105.033101. URL: https://link.aps.org/doi/10.1103/PhysRevA.105.033101.

32. M. G. Bertsch. "Optical Clocks with Trapped Ions". PhD thesis. University of Innsbruck, 2023. URL: https://quantumoptics.at/images/publications/dissertation/Thesis_Milena_Guevara_Bertsch.pdf.

33. M. Qiao et al. "Double-Electromagnetically-Induced-Transparency Ground-State Cooling of Stationary Two-Dimensional Ion Crystals". *Phys. Rev. Lett.* 126, 2 2021, p. 023604. DOI: 10.1103/PhysRevLett.126.023604. URL: https://link.aps.org/doi/10.1103/PhysRevLett.126.023604.

34. M. Qiao et al. "Tunable quantum simulation of spin models with a two-dimensional ion crystal". *Nature Physics*, 2024. ISSN: 1745-2481. DOI: 10.1038/s41567-023-02378-9. URL: https://doi.org/10.1038/s41567-023-02378-9.

35. S.-A. Guo et al. "A site-resolved two-dimensional quantum simulator with hundreds of trapped ions". *Nature* 630:8017, 2024, pp. 613–618. ISSN: 1476-4687. DOI: 10.1038/s41586-024-07459-0. URL: https://doi.org/10.1038/s41586-024-07459-0.

36. Y.-H. Hou et al. *Individually Addressed Entangling Gates in a Two-Dimensional Ion Crystal*. 2024. arXiv: 2406.13999 [quant-ph]. URL: https://arxiv.org/abs/2406.13999.

37. J. Preskill. "Quantum Computing in the NISQ era and beyond". *Quantum* 2, 2018, p. 79. DOI: 10.22331/q-2018-08-06-79.

38. H. Hainzer et al. "Correlation Spectroscopy with Multiqubit-Enhanced Phase Estimation". *Phys. Rev. X* 14, 1 2024, p. 011033. DOI: 10.1103/PhysRevX.14.011033. URL: https://link.aps.org/doi/10.1103/PhysRevX.14.011033.

39. M. Kitagawa and M. Ueda. "Squeezed spin states". *Phys. Rev. A* 47, 6 1993, pp. 5138–5143. DOI: 10.1103/PhysRevA.47.5138. URL: https://link.aps.org/doi/10.1103/PhysRevA.47.5138.

40. J. Franke et al. "Quantum-enhanced sensing on optical transitions through finite-range interactions". *Nature* 621:7980, 2023, pp. 740–745. ISSN: 1476-4687. DOI: 10.1038/s41586-023-06472-z. URL: https://doi.org/10.1038/s41586-023-06472-z.

41. V. Giovannetti, S. Lloyd, and L. Maccone. "Quantum-Enhanced Measurements: Beating the Standard Quantum Limit". *Science* 306:5700, 2004, pp. 1330–1336. DOI: 10.1126/science.1104149. eprint: https://www.science.org/doi/pdf/10.1126/science.1104149. URL: https://www.science.org/doi/abs/10.1126/science.1104149.

42. P. Zoller et al. "Quantum information processing and communication". *The European Physical Journal D - Atomic, Molecular, Optical and Plasma Physics* 36:2, 2005, pp. 203–228. ISSN: 1434-6079. DOI: 10.1140/epjd/e2005-00251-1. URL: https://doi.org/10.1140/epjd/e2005-00251-1.

43. M. A. Nielsen and I. L. Chuang. *Quantum Computation and Quantum Information: 10th Anniversary Edition*. Cambridge University Press, 2010. ISBN: 9781107002173. URL: https://www.cambridge.org/highereducation/books/quantum-computation-and-quantum-information/01E10196D0A682A6AEFFEA52D53BE9AE.

44. B. Yan and W. H. Zurek. "Decoherence factor as a convolution: an interplay between a Gaussian and an exponential coherence loss". *New Journal of Physics* 24:11, 2022, p. 113029. DOI: 10.1088/1367-2630/ac9fe8. URL: https://dx.doi.org/10.1088/1367-2630/ac9fe8.

45. N. F. Ramsey. "Experiments with Separated Oscillatory Fields and Hydrogen Masers". *Science* 248:4963, 1990, pp. 1612–1619. DOI: 10.1126/science.248.4963.1612. eprint: https://www.science.org/doi/pdf/10.1126/science.248.4963.1612. URL: https://www.science.org/doi/abs/10.1126/science.248.4963.1612.

46. T. Monz et al. "14-Qubit Entanglement: Creation and Coherence". *Phys. Rev. Lett.* 106, 13 2011, p. 130506. DOI: 10.1103/PhysRevLett.106.130506. URL: https://link.aps.org/doi/10.1103/PhysRevLett.106.130506.

47. P. R. Bevington and D. K. Robinson. *Data Reduction and Error Analysis for the Physical Sciences*. McGraw-Hill, New York, 1969.

48. J. A. Rice. *Mathematical Statistics and Data Analysis.* Third. Belmont, CA: Duxbury Press., 2006.

49. H. Ollivier and W. H. Zurek. "Quantum Discord: A Measure of the Quantumness of Correlations". *Phys. Rev. Lett.* 88, 1 2001, p. 017901. DOI: 10.1103/PhysRevLett.88.017901. URL: https://link.aps.org/doi/10.1103/PhysRevLett.88.017901.

50. A. Datta. *A Condition for the Nullity of Quantum Discord*. 2011. arXiv: 1003.5256 [quant-ph].

51. K. Modi et al. "The classical-quantum boundary for correlations: Discord and related measures". *Rev. Mod. Phys.* 84, 4 2012, pp. 1655–1707. DOI: 10.1103/RevModPhys.84.1655. URL: https://link.aps.org/doi/10.1103/RevModPhys.84.1655.

52. R. Jozsa and N. Linden. "On the Role of Entanglement in Quantum-Computational Speed-Up". *Proceedings of the Royal Society of London. Series A. Mathematical, Physical and Engineering Sciences* 459, 2036 2003, pp. 2011–2032. DOI: https://doi.org/10.1098/rspa.2002.1097. URL: https://royalsocietypublishing.org/doi/10.1098/rspa.2002.1097.

53. A. R. Calderbank and P. W. Shor. "Good quantum error-correcting codes exist". *Phys. Rev. A* 54, 2 1996, pp. 1098–1105. DOI: 10.1103/PhysRevA.54.1098. URL: https://link.aps.org/doi/10.1103/PhysRevA.54.1098.

54. J. Preskill. "Reliable Quantum Computers". *Proceedings: Mathematical, Physical and Engineering Sciences* 454:1969, 1998, pp. 385–410. ISSN: 13645021. URL: http://www.jstor.org/stable/53172 (visited on 12/19/2023).

55. A. Kay. "Degree of quantum correlation required to speed up a computation". *Phys. Rev. A* 92, 6 2015, p. 062329. DOI: 10.1103/PhysRevA.92.062329. URL: https://link.aps.org/doi/10.1103/PhysRevA.92.062329.

56. J. Ma et al. "Quantum spin squeezing". *Physics Reports* 509:2, 2011, pp. 89–165. ISSN: 0370-1573. DOI: https://doi.org/10.1016/j.physrep.2011.08.003. URL: https://www.sciencedirect.com/science/article/pii/S0370157311002201.

57. G. Tóth et al. "Spin squeezing and entanglement". *Phys. Rev. A* 79, 4 2009, p. 042334. DOI: 10.1103/PhysRevA.79.042334. URL: https://link.aps.org/doi/10.1103/PhysRevA.79.042334.

58. M. Tse et al. "Quantum-Enhanced Advanced LIGO Detectors in the Era of Gravitational-Wave Astronomy". *Phys. Rev. Lett.* 123, 23 2019, p. 231107. DOI: 10.1103/PhysRevLett.123.231107. URL: https://link.aps.org/doi/10.1103/PhysRevLett.123.231107.

59. M. Cramer et al. "Efficient quantum state tomography". *Nature Communications* 1:1, 2010, p. 149. ISSN: 2041-1723. DOI: 10.1038/ncomms1147. URL: https://doi.org/10.1038/ncomms1147.

60. M. Lewenstein et al. "Optimization of entanglement witnesses". *Phys. Rev. A* 62, 5 2000, p. 052310. DOI: 10.1103/PhysRevA.62.052310. URL: https://link.aps.org/doi/10.1103/PhysRevA.62.052310.

61. J. Liu et al. "Quantum Fisher information matrix and multiparameter estimation". *J. Phys. A Math. Theor.* 53:2, 2019, p. 023001. DOI: 10.1088/1751-8121/ab5d4d.

62. D. J. Wineland et al. "Squeezed atomic states and projection noise in spectroscopy". *Phys. Rev. A* 50, 1 1994, pp. 67–88. DOI: 10.1103/PhysRevA.50.67. URL: https://link.aps.org/doi/10.1103/PhysRevA.50.67.

63. P. Shor. "Proceedings of the 35th Annual Symposium on the Foundations of Computer Science, IEEE", 1994.

64. L. K. Grover. "A fast quantum mechanical algorithm for database search". In: *Proceedings of the Twenty-Eighth Annual ACM Symposium on Theory of Computing*. STOC '96. Association for Computing Machinery, Philadelphia, Pennsylvania, USA, 1996, pp. 212–219. ISBN: 0897917855. DOI: 10.1145/237814.237866. URL: https://doi.org/10.1145/237814.237866.

65. R. P. Feynman. "Simulating physics with computers". *International Journal of Theoretical Physics* 21:6, 1982, pp. 467–488. ISSN: 1572-9575. DOI: 10.1007/BF02650179. URL: https://doi.org/10.1007/BF02650179.

66. I. Buluta and F. Nori. "Quantum simulators". *Science* 326, 2009, p. 108. DOI: 10.1126/science.1177838.

67. I. M. Georgescu, S. Ashhab, and F. Nori. "Quantum simulation". *Rev. Mod. Phys.* 86, 1 2014, pp. 153–185. DOI: 10.1103/RevModPhys.86.153. URL: https://link.aps.org/doi/10.1103/RevModPhys.86.153.

68. F. Arute et al. "Quantum supremacy using a programmable superconducting processor". *Nature* 574:7779, 2019, pp. 505–510. ISSN: 1476-4687. DOI: 10.1038/s41586-019-1666-5. URL: https://doi.org/10.1038/s41586-019-1666-5.

69. Y. Kim et al. "Evidence for the utility of quantum computing before fault tolerance". *Nature* 618:7965, 2023, pp. 500–505. ISSN: 1476-4687. DOI: 10.1038/s41586-023-06096-3. URL: https://doi.org/10.1038/s41586-023-06096-3.

70. D. Bluvstein et al. "Logical quantum processor based on reconfigurable atom arrays". *Nature*, 2023. ISSN: 1476-4687. DOI: 10.1038/s41586-023-06927-3. URL: https://doi.org/10.1038/s41586-023-06927-3.

71. A. D. King et al. *Computational supremacy in quantum simulation*. 2024. arXiv: 2403.00910 [quant-ph].

72. Y. Cao, J. Romero, and A. Aspuru-Guzik. "Potential of quantum computing for drug discovery". *IBM Journal of Research and Development* 62:6, 2018, 6:1–6:20. DOI: 10.1147/JRD.2018.2888987.

73. R. Santagati et al. "Drug design on quantum computers". *Nature Physics* 20:4, 2024, pp. 549–557. ISSN: 1745-2481. DOI: 10.1038/s41567-024-02411-5. URL: http://dx.doi.org/10.1038/s41567-024-02411-5.

74. M. Reiher et al. "Elucidating reaction mechanisms on quantum computers". *Proceedings of the National Academy of Sciences* 114, 2016, pp. 7555–7560. URL: https://api.semanticscholar.org/CorpusID:19039145.

75. A. M. Dalzell et al. *Quantum algorithms: A survey of applications and end-to-end complexities*. 2023. arXiv: 2310.03011 [quant-ph].

76. I. Buluta and F. Nori. "Quantum Simulators". *Science* 326:5949, 2009, pp. 108–111. DOI: 10.1126/science.1177838. eprint: https://www.science.org/doi/pdf/10.1126/science.1177838. URL: https://www.science.org/doi/abs/10.1126/science.1177838.

77. A. J. Daley et al. "Practical quantum advantage in quantum simulation". *Nature* 607:7920, 2022, pp. 667–676. ISSN: 1476-4687. DOI: 10.1038/s41586-022-04940-6. URL: https://doi.org/10.1038/s41586-022-04940-6.

78. H. F. Trotter. "On the product of semi-groups of operators". In: 1959. URL: https://api.semanticscholar.org/CorpusID:35277671.

79. D. G. Cory et al. "Experimental Quantum Error Correction". *Phys. Rev. Lett.* 81, 10 1998, pp. 2152–2155. DOI: 10.1103/PhysRevLett.81.2152. URL: https://link.aps.org/doi/10.1103/PhysRevLett.81.2152.

80. X. Yuan et al. "Theory of variational quantum simulation". *Quantum* 3, 2019, p. 191. ISSN: 2521-327X. DOI: 10.22331/q-2019-10-07-191. URL: https://doi.org/10.22331/q-2019-10-07-191.

81. R. Moessner and A. P. Ramirez. "Geometrical frustration". *Physics Today* 59:2, 2006, pp. 24–29. ISSN: 0031-9228. DOI: 10.1063/1.2186278. eprint: https://pubs.aip.org/physicstoday/article-pdf/59/2/24/16665199/24_1_online.pdf. URL: https://doi.org/10.1063/1.2186278.

82. L. Balents. "Spin liquids in frustrated magnets". *Nature* 464:7286, 2010, pp. 199–208. ISSN: 1476-4687. DOI: 10.1038/nature08917. URL: https://doi.org/10.1038/nature08917.

83. D. J. Wineland. "Nobel Lecture: Superposition, entanglement, and raising Schrödinger's cat". *Rev. Mod. Phys.* 85, 3 2013, pp. 1103–1114. DOI: 10.1103/RevModPhys.85.1103. URL: https://link.aps.org/doi/10.1103/RevModPhys.85.1103.

84. C. D. Bruzewicz et al. "Trapped-ion quantum computing: Progress and challenges". *Applied Physics Reviews* 6:2, 2019, p. 021314. ISSN: 1931-9401. DOI: 10.1063/1.5088164. eprint: https://pubs.aip.org/aip/apr/article-pdf/doi/10.1063/1.5088164/14577412/021314_1_online.pdf. URL: https://doi.org/10.1063/1.5088164.

85. D. P. DiVincenzo. "The Physical Implementation of Quantum Computation". *Fortschritte der Physik* 48:9-11, 2000, pp. 771–783. DOI: https://doi.org/10.1002/1521-3978(200009)48:9/11<771::AID-PROP771>3.0.CO;2-E. eprint: https://onlinelibrary.wiley.com/doi/pdf/10.1002/1521-3978%28200009%2948%3A9/11%3C771%3A%3AAID-PROP771%3E3.0.CO%3B2-E. URL: https://onlinelibrary.wiley.com/doi/10.1002/1521-3978(200009)48:9/11%3C771::AID-PROP771%3E3.0.CO;2-E.

86. W. Paul. "Electromagnetic traps for charged and neutral particles". *Rev. Mod. Phys.* 62, 3 1990, pp. 531–540. DOI: 10.1103/RevModPhys.62.531. URL: https://link.aps.org/doi/10.1103/RevModPhys.62.531.

87. P. Ghosh and P. Ghosh. *Ion Traps*. International Series of Monogr. Clarendon Press, 1995. ISBN: 9780198539957. URL: https://books.google.at/books?id=YX95QgAACAAJ.

88. D. J. Wineland et al. "Experimental issues in coherent quantum-state manipulation of trapped atomic ions". *Journal of research of the National Institute of Standards and Technology* 103:3, 1998, p. 259.

89. D. Leibfried et al. "Quantum dynamics of single trapped ions". *Rev. Mod. Phys.* 75:1, 2003, p. 281. DOI: 10.1103/RevModPhys.75.281.

90. S. Earnshaw. "On the Nature of the Molecular Forces which Regulate the Constitution of the Luminiferous Ether". *Transactions of the Cambridge Philosophical Society* 7, 1848, p. 97.

91. M. G. Raizen et al. "Ionic crystals in a linear Paul trap". *Phys. Rev. A* 45, 9 1992, pp. 6493–6501. DOI: 10.1103/PhysRevA.45.6493. URL: https://link.aps.org/doi/10.1103/PhysRevA.45.6493.

92. D. H. E. Dubin. "Theory of structural phase transitions in a trapped Coulomb crystal". *Phys. Rev. Lett.* 71, 1993, pp. 2753–2756. DOI: 10.1103/PhysRevLett.71.2753.

93. A. Steane. "The ion trap quantum information processor". *Applied Physics B* 64:6, 1997, pp. 623–643. ISSN: 1432-0649. DOI: 10.1007/s003400050225. URL: https://doi.org/10.1007/s003400050225.

94. C. Hempel. "Digital quantum simulation, Schrödinger cat state spectroscopy and setting up a linear ion trap". PhD thesis. University of Colorado, 2010. URL: https://www.nist.gov/system/files/documents/2017/05/09/blakestad2010thesis.pdf.

95. D. F. V. James. "Quantum dynamics of cold trapped ions with application to quantum computation". *Applied Physics B* 66:2, 1998, pp. 181–190. ISSN: 1432-0649. DOI: 10.1007/s003400050373. URL: https://doi.org/10.1007/s003400050373.

96. R. B. Blakestad. "Transport of Trapped-Ion Qubits within a Scalable Quantum Processor". PhD thesis. University of Colorado, 2010. URL: https://www.nist.gov/system/files/documents/2017/05/09/blakestad2010thesis.pdf.

97. J. P. Home et al. "Normal modes of trapped ions in the presence of anharmonic trap potentials". *New J. Phys.* 13, 2011, p. 073026. DOI: 10.1088/1367-2630/13/7/073026.

98. F. v. Busch and W. Paul. "Über nichtlineare Resonanzen im elektrischen Massenfilter als Folge von Feldfehlern". *Z. Phys.* 164:5, 1961, pp. 588–594. ISSN: 0044-3328. DOI: 10.1007/BF01378433. URL: https://doi.org/10.1007/BF01378433.

99. R. Alheit et al. "Higher order non-linear resonances in a Paul trap". *Int. J. Mass Spectrom.* 154:3, 1996, pp. 155–169. ISSN: 0168-1176. DOI: https://doi.org/10.1016/0168-1176(96)04380-7. URL: https://www.sciencedirect.com/science/article/pii/0168117696043807.

100. L. K. Joshi et al. *Observing the quantum Mpemba effect in quantum simulations*. 2024. arXiv: 2401.04270 [quant-ph].

101. M. Brownnutt et al. "Ion-trap measurements of electric-field noise near surfaces". *Rev. Mod. Phys.* 87, 4 2015, pp. 1419–1482. DOI: 10.1103/RevModPhys.87.1419. URL: https://link.aps.org/doi/10.1103/RevModPhys.87.1419.

102. P. C. Müller. "Raman Scattering of Single Photons and its Use for Quantum Networks and High-Precision Measurements". PhD thesis. Universität des Saarlandes, 2021. URL: https://d-nb.info/1251313094/34.

103. C. F. Roos et al. "Experimental demonstration of ground state laser cooling with electromagnetically induced transparency". *Phys. Rev. Lett.* 85:26, 2000, p. 5547. DOI: 10.1103/PhysRevLett.85.5547.

104. M. S. Gulley, A. G. White, and D. F. V. James. *A Raman approach to quantum logic in Calcium-like ions*. 2001. arXiv: quant-ph/0112117 [quant-ph].

105. D. J. Wineland et al. "Quantum information processing with trapped ions". *Philosophical Transactions of the Royal Society of London. Series A: Mathematical, Physical and Engineering Sciences* 361:1808, 2003, pp. 1349–1361. DOI: 10.1098/rsta.2003.1205. eprint: https://royalsocietypublishing.org/doi/pdf/10.1098/rsta.2003.1205. URL: https://royalsocietypublishing.org/doi/abs/10.1098/rsta.2003.1205.

106. R. Ozeri et al. "Errors in trapped-ion quantum gates due to spontaneous photon scattering". *Phys. Rev. A* 75, 4 2007, p. 042329. DOI: 10.1103/PhysRevA.75.042329. URL: https://link.aps.org/doi/10.1103/PhysRevA.75.042329.

107. B. C. Sawyer and K. R. Brown. "Wavelength-insensitive, multispecies entangling gate for group-2 atomic ions". *Phys. Rev. A* 103, 2 2021, p. 022427. DOI: 10.1103/PhysRevA.103.022427. URL: https://link.aps.org/doi/10.1103/PhysRevA.103.022427.

108. C. J. Foot. *Atomic Physics*. Oxford University Press, 2005. ISBN: 9780198506966. URL: https://global.oup.com/academic/product/atomic-physics-9780198506966?cc=at&lang=en&.

109. B. Wilhelm. "Coherent control of a $^{40}Ca^{+}$ Ground State Qubit". MA thesis. University of Innsbruck, 2021. URL: https://ulb-dok.uibk.ac.at/ulbtirolhs/content/pagetext/6449523.

110. A. Sørensen and K. Mølmer. "Entanglement and quantum computation with ions in thermal motion". *Phys. Rev. A* 62, 2 2000, p. 022311. DOI: 10.1103/PhysRevA.62.022311. URL: https://link.aps.org/doi/10.1103/PhysRevA.62.022311.

111. P. Jurcevic. "Quantum Computation and Many-Body Physics with Trapped Ions". PhD thesis. University of Innsbruck, 2017. URL: https://quantumoptics.at/images/publications/dissertation/Jurcevic_Dissertation.pdf.

112. C. Maier. "A quantum simulator with long strings of trapped ions". PhD thesis. University of Innsbruck, 2020. URL: https://quantumoptics.at/images/publications/dissertation/ChristineMaier_Dissertation.pdf.

113. P. A. Barton et al. "Measurement of the lifetime of the $3d^2D_{5/2}$ state in $^{40}Ca^{+}$". *Phys. Rev. A* 62, 3 2000, p. 032503. DOI: 10.1103/PhysRevA.62.032503. URL: https://link.aps.org/doi/10.1103/PhysRevA.62.032503.

114. J. Jin and D. A. Church. "Precision lifetimes for the Ca^{+} 4p ^{2}P levels: Experiment challenges theory at the 1% level". *Phys. Rev. Lett.* 70, 21 1993, pp. 3213–3216. DOI: 10.1103/PhysRevLett.70.3213. URL: https://link.aps.org/doi/10.1103/PhysRevLett.70.3213.

115. R. Lechner. "Multi-mode cooling techniques for trapped ions". PhD thesis. University of Innsbruck, 2016. URL: https://quantumoptics.at/images/publications/dissertation/lechner_diss.pdf.

116. J. Eschner et al. "Laser cooling of trapped ions". *J. Opt. Soc. Am. B* 20:5, 2003, pp. 1003–1015. DOI: 10.1364/JOSAB.20.001003. URL: https://opg.optica.org/josab/abstract.cfm?URI=josab-20-5-1003.

117. R. Lechner et al. "Electromagnetically-induced-transparency ground-state cooling of long ion strings". *Phys. Rev. A* 93, 5 2016, p. 053401. DOI: 10.1103/PhysRevA.93.053401. URL: https://link.aps.org/doi/10.1103/PhysRevA.93.053401.

118. E. Jordan et al. "Near Ground-State Cooling of Two-Dimensional Trapped-Ion Crystals with More than 100 Ions". *Phys. Rev. Lett.* 122, 5 2019, p. 053603. DOI: 10.1103/PhysRevLett.122.053603. URL: https://link.aps.org/doi/10.1103/PhysRevLett.122.053603.

119. I. Vybornyi et al. "Sideband Thermometry of Ion Crystals". *PRX Quantum* 4, 4 2023, p. 040346. DOI: 10.1103/PRXQuantum.4.040346. URL: https://link.aps.org/doi/10.1103/PRXQuantum.4.040346.

120. W. Nagourney, J. Sandberg, and H. Dehmelt. "Shelved optical electron amplifier: Observation of quantum jumps". *Phys. Rev. Lett.* 56, 26 1986, pp. 2797–2799. DOI: 10.1103/PhysRevLett.56.2797. URL: https://link.aps.org/doi/10.1103/PhysRevLett.56.2797.

121. J. C. Bergquist et al. "Observation of Quantum Jumps in a Single Atom". *Phys. Rev. Lett.* 57, 14 1986, pp. 1699–1702. DOI: 10.1103/PhysRevLett.57.1699. URL: https://link.aps.org/doi/10.1103/PhysRevLett.57.1699.

122. T. Sauter et al. "'Quantum jumps' observed in the fluorescence of a single ion". *Optics Communications* 60:5, 1986, pp. 287–292. ISSN: 0030-4018. DOI: https://doi.org/10.1016/0030-4018(86)90152-5. URL: https://www.sciencedirect.com/science/article/pii/0030401886901525.

123. D. An et al. "Distance scaling and polarization of electric-field noise in a surface ion trap". *Phys. Rev. A* 100, 2019, p. 063405. DOI: 10.1103/PhysRevA.100.063405.

124. S. Ragg et al. "Segmented ion-trap fabrication using high precision stacked wafers". *Rev. Sci. Instrum.* 90:10, 2019, p. 103203. DOI: 10.1063/1.5119785.

125. C. Decaroli et al. "Design, fabrication and characterization of a micro-fabricated stacked-wafer segmented ion trap with two X-junctions". *Quantum Sci. Technol.* 6:4, 2021, p. 044001. DOI: 10.1088/2058-9565/ac07ee. URL: https://doi.org/10.1088/2058-9565/ac07ee.

126. G. Araneda et al. "The Panopticon device: An integrated Paul-trap–hemispherical mirror system for quantum optics". *Rev. Sci. Instrum.* 91:11, 2020, p. 113201. DOI: 10.1063/5.0020661.

127. P. Bado, C. R. Monroe, and W. C. Campbell. "Fused Silica Ion Trap Chip with Efficient Optical Collection System for Timekeeping, Sensing, and Emulation". In: 2015.

128. A. Butkutė et al. "Sapphire Selective Laser Etching Dependence on Radiation Wavelength and Etchant." eng. *Micromachines* 14, 1 2022.

129. A. Butkutė et al. "Optimization of selective laser etching (SLE) for glass micromechanical structure fabrication". *Opt. Express* 29:15, 2021, pp. 23487–23499. DOI: 10.1364/OE.430623. URL: https://opg.optica.org/oe/abstract.cfm?URI=oe-29-15-23487.

130. J. D. Siverns et al. "On the application of radio frequency voltages to ion traps via helical resonators". *Appl. Phys. B* 107:4, 2012, pp. 921–934. ISSN: 1432-0649. DOI: 10.1007/s00340-011-4837-0. URL: https://doi.org/10.1007/s00340-011-4837-0.

131. M. W. van Mourik et al. "Coherent rotations of qubits within a surface ion-trap quantum computer". *Phys. Rev. A* 102, 2 2020, p. 022611. DOI: 10.1103/PhysRevA.102.022611. URL: https://link.aps.org/doi/10.1103/PhysRevA.102.022611.

132. J. A. Fedchak et al. "Outgassing rate comparison of seven geometrically similar vacuum chambers of different materials and heat treatments". *Journal of Vacuum Science & Technology B* 39:2, 2021, p. 024201. DOI: 10.1116/6.0000657. eprint: https://doi.org/10.1116/6.0000657. URL: https://doi.org/10.1116/6.0000657.

133. T. Brydges. "Randomised Measurements with Strings of Trapped Ions". PhD thesis. University of Innsbruck, 2021. URL: https://quantumoptics.at/images/publications/dissertation/brydges_diss.pdf.

134. J. Franke. "Magnetic field noise cancellation for quantum simulation experiment with trapped ions". MA thesis. University of Innsbruck, 2021. URL: https://ulb-dok.uibk.ac.at/ulbtirolhs/download/pdf/6770176.

135. A. Winkler. "Frequency Stabilization of a 729 nm Ti:Sa Laser for Qubit Manipulation in Trapped Calcium Ions". MA thesis. University of Innsbruck, 2023. URL: https://ulb-dok.uibk.ac.at/ulbtirolhs/download/pdf/8398078.

136. M. Ester et al. "A Density-Based Algorithm for Discovering Clusters in Large Spatial Databases with Noise". In: *Proceedings of the Second International Conference on Knowledge Discovery and Data Mining*. KDD'96. AAAI Press, Portland, Oregon, 1996, pp. 226–231. DOI: 10.5555/3001460.3001507.

137. A. H. Burrell et al. "Scalable simultaneous multiqubit readout with 99.99 % single-shot fidelity". *Phys. Rev. A* 81, 4 2010, p. 040302. DOI: 10.1103/PhysRevA.81.040302. URL: https://link.aps.org/doi/10.1103/PhysRevA.81.040302.

138. A. Seif et al. "Machine learning assisted readout of trapped-ion qubits". *Journal of Physics B: Atomic, Molecular and Optical Physics* 51:17, 2018, p. 174006. DOI: 10.1088/1361-6455/aad62b. URL: https://dx.doi.org/10.1088/1361-6455/aad62b.

139. J. Tilly et al. "The Variational Quantum Eigensolver: A review of methods and best practices". *Physics Reports* 986, 2022. The Variational Quantum Eigensolver: a review of methods and best practices, pp. 1–128. ISSN: 0370-1573. DOI: https://doi.org/10.1016/j.physrep.2022.08.003. URL: https://www.sciencedirect.com/science/article/pii/S0370157322003118.

140. I. Pogorelov et al. "Compact Ion-Trap Quantum Computing Demonstrator". *PRX Quantum* 2, 2 2021, p. 020343. DOI: 10.1103/PRXQuantum.2.020343. URL: https://link.aps.org/doi/10.1103/PRXQuantum.2.020343.

141. O. D. Kellogg. *Foundations of potential theory*. Springer, Berlin [u.a.], 1929. URL: http://eudml.org/doc/203661.

142. D. H. E. Dubin and T. M. O'Neil. "Trapped nonneutral plasmas, liquids, and crystals (the thermal equilibrium states)". *Rev. Mod. Phys.* 71, 1999, pp. 87–172. DOI: 10.1103/RevModPhys.71.87.

143. V. L. Ryjkov, X. Zhao, and H. A. Schuessler. "Simulations of the rf heating rates in a linear quadrupole ion trap". *Phys. Rev. A* 71, 3 2005, p. 033414. DOI: 10.1103/PhysRevA.71.033414. URL: https://link.aps.org/doi/10.1103/PhysRevA.71.033414.

144. H. L. Gevorgyan and N. V. Vitanov. "Ultrahigh-fidelity composite rotational quantum gates". *Phys. Rev. A* 104, 1 2021, p. 012609. DOI: 10.1103/PhysRevA.104.012609. URL: https://link.aps.org/doi/10.1103/PhysRevA.104.012609.

145. A. D. Ludlow et al. "Optical atomic clocks". *Rev. Mod. Phys.* 87, 2 2015, pp. 637–701. DOI: 10.1103/RevModPhys.87.637. URL: https://link.aps.org/doi/10.1103/RevModPhys.87.637.

146. M. A. Taylor and W. P. Bowen. "Quantum metrology and its application in biology". *Physics Reports* 615, 2016. Quantum metrology and its application in biology, pp. 1–59. ISSN: 0370-1573. DOI: https://doi.org/10.1016/j.physrep.2015.12.002. URL: https://www.sciencedirect.com/science/article/pii/S0370157315005001.

147. Y.-J. Chen et al. "Single-Source Multiaxis Cold-Atom Interferometer in a Centimeter-Scale Cell". *Phys. Rev. Appl.* 12, 1 2019, p. 014019. DOI: 10.1103/PhysRevApplied.12.014019. URL: https://link.aps.org/doi/10.1103/PhysRevApplied.12.014019.

148. E. Pedrozo-Peñafiel et al. "Entanglement on an optical atomic-clock transition". *Nature* 588:7838, 2020, pp. 414–418. ISSN: 1476-4687. DOI: 10.1038/s41586-020-3006-1. URL: https://doi.org/10.1038/s41586-020-3006-1.

149. C. A. Casacio et al. "Quantum-enhanced nonlinear microscopy". *Nature* 594:7862, 2021, pp. 201–206. ISSN: 1476-4687. DOI: 10.1038/s41586-021-03528-w. URL: https://doi.org/10.1038/s41586-021-03528-w.

150. N. Aslam et al. "Quantum sensors for biomedical applications". *Nature Reviews Physics* 5:3, 2023, pp. 157–169. ISSN: 2522-5820. DOI: 10.1038/s42254-023-00558-3. URL: https://doi.org/10.1038/s42254-023-00558-3.

151. M. Chwalla et al. "Precision spectroscopy with two correlated atoms". *Applied Physics B* 89:4, 2007, pp. 483–488. ISSN: 1432-0649. DOI: 10.1007/s00340-007-2867-4. URL: https://doi.org/10.1007/s00340-007-2867-4.

152. C. W. Chou et al. "Quantum Coherence between Two Atoms beyond $Q = 10^{15}$". *Phys. Rev. Lett.* 106, 16 2011, p. 160801. DOI: 10.1103/PhysRevLett.106.160801. URL: https://link.aps.org/doi/10.1103/PhysRevLett.106.160801.

153. R. Shaniv et al. "Quadrupole Shift Cancellation Using Dynamic Decoupling". *Phys. Rev. Lett.* 122, 22 2019, p. 223204. DOI: 10.1103/PhysRevLett.122.223204. URL: https://link.aps.org/doi/10.1103/PhysRevLett.122.223204.

154. E. R. Clements et al. "Lifetime-Limited Interrogation of Two Independent $^{27}Al^{+}$ Clocks Using Correlation Spectroscopy". *Phys. Rev. Lett.* 125, 24 2020, p. 243602. DOI: 10.1103/PhysRevLett.125.243602. URL: https://link.aps.org/doi/10.1103/PhysRevLett.125.243602.

155. T. J. Proctor, P. A. Knott, and J. A. Dunningham. "Multiparameter estimation in networked quantum sensors". *Phys. Rev. Lett.* 120:8, 2018, p. 080501. DOI: 10.1103/PhysRevLett.120.080501.

156. W. Ge et al. "Distributed quantum metrology with linear networks and separable inputs". *Phys. Rev Lett.* 121:4, 2018, p. 043604. DOI: 10.1103/PhysRevLett.121.043604.

157. Z. Eldredge et al. "Optimal and secure measurement protocols for quantum sensor networks". *Phys. Rev. A* 97:4, 2018, p. 042337. DOI: 10.1103/PhysRevA.97.042337.

158. J. Rubio et al. "Quantum sensing networks for the estimation of linear functions". *J. Phys. A Math. Theor.* 53:34, 2020, p. 344001. DOI: 10.1088/1751-8121/ab9d46.

159. D. J. Wineland et al. "Spin squeezing and reduced quantum noise in spectroscopy". *Phys. Rev. A* 46, 11 1992, R6797–R6800. DOI: 10.1103/PhysRevA.46.R6797. URL: https://link.aps.org/doi/10.1103/PhysRevA.46.R6797.

160. J. J. . Bollinger et al. "Optimal frequency measurements with maximally correlated states". *Phys. Rev. A* 54, 6 1996, R4649–R4652. DOI: 10.1103/PhysRevA.54.R4649. URL: https://link.aps.org/doi/10.1103/PhysRevA.54.R4649.

161. J. Beck and K. Arnold. *Parameter Estimation in Engineering and Science*. Probability and Statistics Series. Wiley, 1977. ISBN: 9780471061182. URL: https://books.google.at/books?id=_qAYgYN87UQC.

162. I. J. Myung. "Tutorial on maximum likelihood estimation". *Journal of Mathematical Psychology* 47:1, 2003, pp. 90–100. ISSN: 0022-2496. DOI: https://doi.org/10.1016/S0022-2496(02)00028-7. URL: https://www.sciencedirect.com/science/article/pii/S0022249602000287.

163. M. J. Zyphur and F. L. Oswald. "Bayesian Estimation and Inference: A User's Guide". *Journal of Management* 41:2, 2015, pp. 390–420. DOI: 10.1177/0149206313501200. eprint: https://doi.org/10.1177/0149206313501200. URL: https://doi.org/10.1177/0149206313501200.

164. D. Braun et al. "Quantum-enhanced measurements without entanglement". *Rev. Mod. Phys.* 90, 3 2018, p. 035006. DOI: 10.1103/RevModPhys.90.035006. URL: https://link.aps.org/doi/10.1103/RevModPhys.90.035006.

165. J. M. E. Fraisse. "New concepts in quantum-metrology: From coherent averaging to Hamiltonian extensions". PhD thesis. Universität Tübingen, 2018. URL: https://publikationen.uni-tuebingen.de/xmlui/handle/10900/80877?show=full.

166. S. L. Braunstein and C. M. Caves. "Statistical distance and the geometry of quantum states". *Phys. Rev. Lett.* 72:22, 1994, p. 3439. DOI: 10.1103/PhysRevLett.72.3439.

167. W. H. Holtzman. "The Unbiased Estimate of the Population Variance and Standard Deviation". *The American Journal of Psychology* 63, 1950, p. 615. DOI: 10.2307/1418879.

168. D. Leibfried et al. "Toward Heisenberg-Limited Spectroscopy with Multiparticle Entangled States". *Science* 304:5676, 2004, pp. 1476–1478. DOI: 10.1126/science.1097576. eprint: https://www.science.org/doi/pdf/10.1126/science.1097576. URL: https://www.science.org/doi/abs/10.1126/science.1097576.

169. M. Foss-Feig et al. *Entanglement and spin-squeezing without infinite-range interactions*. 2016. arXiv: 1612.07805 [cond-mat.quant-gas].

Acknowledgements

Despite not having a Gazebo available in which to write this thesis during the summer months, I finally managed to complete it. My PhD journey has probably been the most rewarding as well as challenging thing I've ever done and I am grateful for how this research project has developed and for the resilience I've gained along the way. Of course, this work would not have been possible without the help and support of many people, and I would like to take the opportunity to convey my sincere gratitude to them:

First of all, I would like to thank my supervisor Christian Roos for believing in me and allowing me to be part of his team, for his great ideas that he always explains patiently, and for providing a well-funded and cutting-edge research project for me to work on. I'm also very grateful for the freedom he gave us, such as when letting me write this thesis in the way I imagined it, even if it took literally forever…

I thank Rainer Blatt for his continuous encouragement over the years and for creating the supportive environment that makes it possible to carry out top level research. Without the support of the entire Innsbruck ion-trapping community, with its wonderfully collaborative and friendly culture, it would not have been possible to develop our work in this capacity.

My team deserves unending thanks for all the support they have given me at work and also personally. I consider myself lucky to have been surrounded by such kind, patient and smart people. I will greatly miss our lunch breaks during which I could always bring up the strange topics and (start-up) ideas I was preoccupied with on a given day, and will fondly remember all the pranks we played, such as the ones related to mustard, cucumbers or unplugging cables. Officina Aperitivo also deserves a mention, the best tradition that has ever been established at work. Special thanks goes of course to Dominik Kiesenhofer (Domsi), who has been there from the beginning and with whom I shared basically every single day for 5 and a half years. For the first 2.5 years it was just the two of us working on this project and the planning and building of this new experimental setup seemed like an overwhelming task. I almost can't believe it but somehow we managed to pull this off and build the tightest vacuum setup since Goethe (despite playing Russian roulette in the vacuum room as well as dealing with language barriers – fermez la bride!), which eventually allowed us to defeat the Bizarro 2dQs. There is nobody I would have rather shared this experience with because besides the fact that you're an extremely competent colleague, your friendship is invaluable to me. I'm really happy that all you do was recognized by others as well; you really deserved that Werner-Welzig award for your contribution to the internal cohesion as well as the public reputation of our team! I guess I still owe you about 132 (vegan) iced coffees for all the bets I've lost and I hope that we will drink them together during the next 50 years. Tuomas Ollikainen was the next person to join our team. He taught us about Finnish culture and most importantly, as a great hacker, has taught me a thing or two about programming, which is also documented in the internationally-known video we have produced together. Matthias Bock deserves special thanks for being the most hardcore postdoc, always pushing the experiment forward with full

gas. Thank you for all your hard work that made this experimental setup run so smoothly, and for always patiently explaining physical concepts and technical details. Artem Zhdanov is the newest member of our team and I could not be happier that the experiment is left in his hands. While he has contributed great improvements to the setup, I hope he can take on the most important responsibility of the 2D Crystals experiment, i.e. checking if that heat paste has finally dried.

I am deeply grateful to the Innsbruck ion-trapping groups, who have supported us countless times. I want to mention a few people in particular: The QSim Team (Christine Maier, Manoj Joshi, Florian Kranzl, Johannes Franke and Tiff Brydges) has provided a lot of support to us over the years, whether it was laser light, equipment or knowledge they shared with us. Thanks to the Quantum Fried Chicken and AQTION teams for providing laser light to our experimental setup. I also want to take the opportunity to thank Thomas Monz, who, despite his demanding schedule, always found time to offer support and advice. I am also grateful to his team at Alpine Quantum Technologies GmbH (AQT). The synergy between the research groups and spin-off company constitutes an invaluable resource that leads to great progress. From AQT I want to acknowledge a few people in particular who have provided support at work and/or personally: Philip Holz, Alexander Erhard, Josef Schupp, Georg Jacob and Max Hettrich.

My office mates Christine Maier and Armin Winkler have greatly contributed to an enjoyable work environment. Christine shared an office with Dominik and me in IQOQI and deserves a mention, not only because she's the ghost whisperer, which quantifies our special friendship, but also because of all the support she has given us at work. Being the knowledgeable senior PhD student at QSim she gave us valuable advice countless times when we were planning our experimental setup and was never too busy to help us out. Armin has also contributed to a great atmosphere at the university office, always up for interesting fundamental discussions from physics to politics to, most importantly, memes.

An additional thank you goes out to Christian, Matthias, Artem, Armin and Manoj for giving me comments on this thesis.

I want to express my gratitude to the administrative staff for dealing with, among other things, what feels like at least a million orders. Here, I want to mention Markus Knabl, Elisabeth Huck and Klaus Falschlunger from IQOQI, and Claudia Mevenkamp from the university. Thanks to Valentin Staubmann for IT support, to the guys from the mechanical workshops, in particular Stefan Haslwanter, Berhard Öttl, Andreas Strasser, and Manuel Presslaber, for machining numerous custom parts for our setup, as well as Gerhard Hendl from the electronic workshop at IQOQI.

I would like to express my gratitude to all my friends who have accompanied me during the last years. I am grateful to Lea and Jessy, who have been there with me since the very first day of the Bachelor studies. I would like to thank the "fit chicks" (Christine, Lata and Milena) for nice ladies' lunches (including Martin of course) and other fun activities, and the running group (Brandon, Christian M. and Max), obvi, for enhancing my physical fitness, which has been much needed. I also want to thank my non-physicist friends and my family for all the support.

Finally, I would like to thank you, the reader, for your interest in this work. I hope you find something of value to you in this thesis.